Photons & Phonons: A room-temperature diamond quantum memory

by

Kent Fisher

A thesis
presented to the University of Waterloo
in fulfillment of the
thesis requirement for the degree of
Doctor of Philosophy
in
Physics

Waterloo, Ontario, Canada, 2016

I hereby declare that I am the sole author of this thesis. This is a true copy of the thesis, including any required final revisions, as accepted by my examiners.

I understand that my thesis may be made electronically available to the public.

Abstract

This thesis presents demonstrations of the storage and manipulation of single photons in a room-temperature diamond quantum memory using a Raman memory protocol. We report on results from four experiments.

In the first we demonstrate single photon storage and, upon retrieval, verify the quantum nature of the light with a Hanbury Brown Twiss measurement of $g^{(2)}(0) = 0.65 \pm 0.07$. A measurement of $g^{(2)}(0) < 1$ is indicative of quantum light. This is the first demonstration of single photon storage where the bandwidth of the stored light is greater than 1 THz. The diamond memory stores light for over 13 times the duration of the input wavepacket. In the second experiment, we report the storage and retrieval of polarization-encoded qubits and demonstrate qubit storage above a classical bound. We also verify that entanglement between the input photon and an auxiliary persists through storage and retrieval.

We then turn to additional uses of a Raman quantum memory. We demonstrate that a photon stored in the diamond memory can, upon retrieval, have its frequency and bandwidth converted. We report frequency conversion over a range of 4.2 times the bandwidth of the input photon (4.1 nm, 2.3 THz), and bandwidth modulation between 0.5 to 1.9 times the bandwidth of the input. We verify that the output light from storage and spectral manipulation is still non-classical in nature.

Finally, we demonstrate both single- and two-photon quantum interference mediated by the diamond memory, where the memory acts as a beamsplitter between photon and optical phonon modes in the diamond lattice. In a first experiment, a single photon is split into two time-bins. The first time-bin is stored in the memory, then recalled and made to interfere with the second time-bin producing fringes. In a second experiment, a photon from a weak coherent state is stored in the memory and, upon retrieval, undergoes Hong-Ou-Mandel interference with a second photon. We measure Hong-Ou-Mandel interference with a visibility of 59% giving a signature of non-classical interference ($> 50\%$).

This collection of experiments establishes the diamond memory as a prime candidate for certain quantum communication and processing applications. These results demonstrate the potential for the diamond memory to be an integrated platform for photon storage, spectral conversion, and information processing.

Acknowledgements

First, I would like to thank my supervisor Dr. Kevin Resch. It has been an absolute pleasure to study, research, and grow as a scientist under his guidance. I will always value my time in his group. I also thank the members of my advisory committee, Drs. Raymond Laflamme, Thomas Jennewein, and Chris Wilson for their feedback and direction throughout my PhD program, and Dr. Todd Pittman for serving as my external examiner.

I have been very fortunate to have received funding during my PhD, and so I am grateful to the agencies that provided this: NSERC, OGS, IQC, and the Department of Physics and Astronomy at the University of Waterloo.

The Institute for Quantum Computing is a marvel, and I treasure my time as a part of it. I am thankful to all the scientists and staff who make IQC such a special place to learn, research, and be involved in scientific outreach. I am also grateful to the staff of the Department of Physics and Astronomy, especially Judy McDonnell, for support and guidance in progressing through the PhD program.

The experiments in this thesis were performed at the National Research Council of Canada in Ottawa. As such, I am very thankful to the NRC, and everyone that comprises it, for hosting me during my many visits. My time there, in both the lab and the lunch room, will be remembered with fondness. The NRC staff, especially the ever-helpful Lise Chabot, deserve many thanks for steering me through the various hoops for working in a government lab.

While at NRC, I worked under the guidance of Dr. Ben Sussman in the Quantum Technologies group. I am very grateful for my time working with Dr. Sussman, my supervisor away from home. I have benefited from his wisdom on many occasions, ranging from advice on the experiment to my introduction to Pili Pili Grilled Chicken.

Physics is a team sport, and so I am filled with gratitude for my fellow group members. My office mates John Donohue and Mike Mazurek have helped make our work environment full of good conversation, encouragement, balloons, foliage, various trinkets, and trophies for very meaningful accomplishments. When our conversations occasionally touch on physics, I am enlightened by their fruitful insights. This, of course, extends to the other

members of the QOQI group: JP Maclean, Jeff Salvail and Matt Brown, as well as my fellow quantum optics enthusiasts Aimee Gunther, Chris Pugh and Dr. Evan Meyer-Scott. JP Maclean deserves special thanks for his partnership in performing experiments in this thesis, as well as accompanying me on trips to Ottawa. He is a talented physicist and his apartment-finding skills are top-notch, not to mention his cooking and taste for fine wines. Past QOQI group members also deserve recognition. Drs. Jonathan Lavoie and Deny Hamel taught me much of what I know about quantum optics experiments. I am also thankful to Megan Agnew, Lydia Vermeyden, Drs. Chris Erven, Krister Shalm, Robert Prevedel and Rainer Kaltenbaek.

I am greatly indebted to the members of the Quantum Technologies group at NRC. Drs. Duncan England, Philip Bustard and Khabat Heshami welcomed me as one of their own and helped make my time in Ottawa a wonderful experience. Duncan England, in particular, deserves all the thanks I can muster. In addition to enduring my sub-standard cross-country skiing and table tennis skills, he also put up with my occasionally obnoxious lab songs. He is an adept experimentalist, smoked-meat enthusiast, and a good friend. I am glad to have been able to collaborate closely with him for the experiments in this thesis. I am also very grateful to Doug Moffatt, Denis Guay and Rune Lausten for their technical assistance in the NRC lab.

Lastly, I am forever thankful to my roommates, close friends, my wonderful parents, sister, brother, my amazing partner and her family. All these people have walked in solidarity with me through both triumphs and failures, serious times and plenty of silly ones. I am more than fortunate to be blanketed with such support and joy. I cherish their love.

For now we see only a reflection as in a mirror;
then we shall see face to face.
Now I know in part; then I shall know fully,
even as I am fully known.
1 Corinthians 13:12

Table of Contents

List of Figures

Chapter 1

Quantum information

> Very simply... normal computers work, either there's power going through a wire or not — a one, or a zero. They're binary systems. What quantum states allow for is much more complex information to be encoded into a single bit...
>
> Right Honourable Justin Trudeau,
> 23rd Prime Minister of Canada

For over a century now, quantum mechanics has both baffled and dazzled scientists. The quantum theory challenges our intuition of how the world around us works like no other, and yet is also the most accurate description of the physical world ever produced. As intuition has developed, scientists have transitioned from observing the bizarre features of quantum systems to harnessing them. On the coattails of massive developments in information technology in the past century, quantum information theory has emerged as powerhouse of potential. Quantum computing, which promises solutions to problems current computers find entirely intractable; quantum cryptography, which offers information security guaranteed by the laws of physics; along with quantum simulators and quantum sensors are all consequences of quantum information theory.

In many emerging quantum technologies it is a prerequisite to distribute fragile quantum states between two parties. These parties can be distant people trying to communicate, or nearby components in a quantum computer. In either scenario, single photons are a natural choice for carrying the information. In many cases, buffering qubits is necessary to synchronize events. This task is performed by an optical quantum memory which stores photonic qubits, releasing them on demand as a faithful recreation of the input.

In this thesis I present experimental results showing room-temperature diamond as such a quantum memory. I show that diamond is capable of storing photonic qubits with THz bandwidths, three orders of magnitude higher than any previous memory demonstration. I also present results showing additional features of the diamond quantum memory, namely spectral manipulation and mediating two-photon interference. I believe this work firmly establishes the diamond quantum memory as the candidate for many applications in quantum information.

The thesis has nine chapters. In the first we will overview concepts of quantum information that are relevant for the main results. In Chapter 2 we discuss quantum optics in some detail, especially pertaining to the production and manipulation of single photons. Next, we will look at concepts of quantum communication and carve out the role that an optical quantum memory can play in quantum networks. We will also discuss different quantum memory implementations. In Chapter 4 we discuss diamond, its properties and potential as a quantum memory. We then turn to the experiments. Chapter 5 shows that a high-bandwidth single photon can be stored and retrieved from the diamond memory while retaining its quantum nature. Chapter 6 shows the storage of a photonic qubit, including the case when the stored qubit is entangled with another. Chapters 7 and 8 experimentally explore additional features of the diamond memory: Chapter 7 presents results on frequency and bandwidth conversion of the stored photon; and Chapter 8 shows results of two-photon interference mediated by the quantum memory. Finally, we conclude in Chapter 9 with some suggestions for further developments.

Let us begin then with some basic notions of quantum information. In this chapter we will cover quantum states that are used in quantum information, namely qubits and entangled states, how they evolve, and how we measure them. We begin with the qubit.

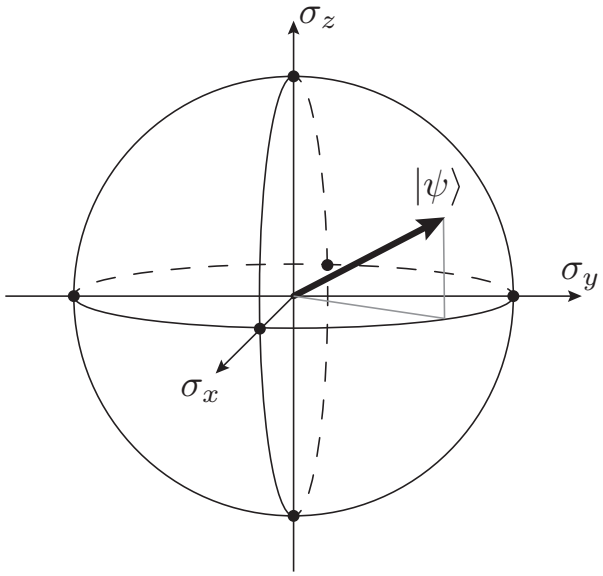

Figure 1.1: The Bloch sphere can be used to visualize a qubit. The black dots on the x, y, and z axes correspond to the ± 1 eigenvectors of the Pauli operators σ_x, σ_y and σ_z. A qubit state is represented as a vector from the origin to a point in the sphere.

1.1 The qubit

Modern computers function by processing bits of information. A bit can occupy one of the two binary states: 0 or 1. However, the state of a quantum bit, or "qubit", has far more possibilities. A two-level quantum system, for example, the spin of an electron, can be used as a qubit since it is not restricted to being 0 or 1 but can be any superposition of the two. We call the quantum states $|0\rangle$ and $|1\rangle$ the computational basis, where the "kets" are defined as vectors

$$|0\rangle \equiv \begin{pmatrix} 1 \\ 0 \end{pmatrix}, \quad |1\rangle \equiv \begin{pmatrix} 0 \\ 1 \end{pmatrix} \tag{1.1}$$

Physically, the qubits in this thesis are the polarization of a single photon, with $|0\rangle$ defined as the horizontal polarization and $|1\rangle$ as the vertical polarization. A superposition of the two computational basis states gives a state of the form

$$|\psi\rangle = \alpha|0\rangle + \beta|1\rangle \tag{1.2}$$

where α and β are complex amplitudes which have the constraint $|\alpha|^2 + |\beta|^2 = 1$. However, Equation 1.2 does not encapsulate the whole essence of a qubit. In general, a qubit ρ is defined as a probabilistic mixture of two-level states like those in Equation 1.2,

$$\rho = \sum_i p_i |\psi_i\rangle\langle\psi_i| \tag{1.3}$$

where the probabilities $p_i \geq 0$ and $\sum_i p_i = 1$. The operator ρ is called the *density matrix* which is Hermitian and has trace equal to one. The diagonal entries of the density matrices directly correspond to measurement probabilities in the expressed basis. We can visualize a qubit as vector $\vec{r}$ on the Bloch sphere (Fig. 1.1),

$$\rho \quad = \quad \frac{\mathbb{1}}{2} + \frac{1}{2}\vec{r} \cdot \vec{\sigma} \tag{1.4}$$

where $\mathbb{1}$ is the two-dimensional identity matrix, and $\vec{\sigma} = \sigma_x \hat{x} + \sigma_y \hat{y} + \sigma_z \hat{z}$ is the vector of Pauli matrices

$$\sigma_x = \begin{pmatrix} 0 & 1 \\ 1 & 0 \end{pmatrix}, \quad \sigma_y = \begin{pmatrix} 0 & -i \\ i & 0 \end{pmatrix}, \quad \sigma_z = \begin{pmatrix} 1 & 0 \\ 0 & -1 \end{pmatrix}. \tag{1.5}$$

Each component of $\vec{r}$ is then the overlap of the density matrix with a Pauli matrix, $r_i = \mathrm{Tr}(\rho\sigma_i)$. States with vectors reaching to the surface of the Bloch sphere, $|\vec{r}| = 1$, are called *pure* states. These are the states that can be expressed as in Equation 1.2, while *mixed* states, $|\vec{r}| < 1$, fill the volume of the Bloch sphere.

1.2 Entanglement

Quantum entanglement is perhaps where our classical intuition of how the world works breaks down the most. When two particles are entangled we can no longer think of them as separate entities – each particle can be indefinite while the state as a whole is entirely definite. This means that the two particles can share correlations – even if separated by a long distance – beyond what is possible in a solely classical physics world [1, 2, 3, 4].

Because of these strong correlations, entanglement is the work horse of quantum computing. Universal quantum computing can be achieved with single qubit control and an

entangling operation between qubits [5]. Conversely, with multi-particle entanglement as a resource, universal quantum computing can be achieved with measurement and feedforward techniques [6, 7]. In this thesis we will be interested in entanglement in the context of quantum communication between two parties. We will elaborate on this in Chapter 3, but for know let us introduce some key concepts. An example of a pure two-qubit entangled state is

$$|\Phi^+\rangle = \frac{1}{\sqrt{2}}\left(|0\rangle^A \otimes |0\rangle^B + |1\rangle^A \otimes |1\rangle^B\right) \tag{1.6}$$

Notice that we can not factor the state into the form of a state describing system A and one describing system B, i.e. $|\psi\rangle^A \otimes |\phi\rangle^B$. Formally, we say that a state is entangled when it is not separable, where a separable state can be written as a sum of its individual subsystems

$$\rho^{AB} = \sum_{i,j} p_{ij}\rho_i^A \otimes \rho_j^B, \qquad p_{ij} \geq 0 \tag{1.7}$$

In this thesis we will be concerned with two-photon states entangled in their polarization degree of freedom. Perhaps the most common examples of two-qubit entangled states are the "Bell" basis states:

$$|\Phi^\pm\rangle = \frac{1}{\sqrt{2}}(|00\rangle \pm |11\rangle) \tag{1.8}$$

$$|\Psi^\pm\rangle = \frac{1}{\sqrt{2}}(|01\rangle \pm |10\rangle) \tag{1.9}$$

where we have dropped the superscripts and tensor product symbols to write the multi-qubit state vector in a more compact way, $|00\rangle = |0\rangle^A \otimes |0\rangle^B$. The Bell states form an orthonormal basis for two qubits.

We are interested in quantifying the amount of entanglement between two qubits. In Chapter 6 we will explore the storage of one qubit of a two-qubit entangled state in a quantum memory. Since the storage process in the quantum memory is inherently noisy, the quality of the entangled state will degrade. We would therefore like to measure the difference in the quality of entanglement between the qubits, both before and after the storage process.

One way to quantify entanglement is to measure how indeterminate one subsystem of the entangled state is when the others are ignored. This is done mathematically by performing a partial trace. For example, if we have a state ρ comprised of subsystems A and B, taking the partial trace over subsystem B gives $\rho_A = \mathrm{Tr}\left[\sum_k (\mathbb{1} \otimes |k\rangle\langle k|)\rho\right]$. For maximally entangled states, such as the one in Eq. 1.6, one can verify that taking the partial trace of over one subsystem leaves the remaining system in the maximally mixed state, i.e. $\rho_A = \mathbb{1}/2$ for qubits. For less than maximal entanglement, the remaining subsystem will not be totally mixed. This can be quantified using the von Neumann entropy defined as

$$S(\rho) = -\mathrm{Tr}\left(\rho \log_2 \rho\right). \tag{1.10}$$

For a pure entangled state $|\psi\rangle$, the entanglement of formation [8] is given by

$$E(|\psi\rangle) = -\mathrm{Tr}\left(\rho_A \log_2 \rho_A\right) = -\mathrm{Tr}\left(\rho_B \log_2 \rho_B\right) \tag{1.11}$$

where ρ_B has the parallel meaning to ρ_A. For a mixed state ρ, the entanglement of formation involves a minimization over all possible decompositions $\rho = \sum_i p_i |\psi_i\rangle\langle\psi_i|$,

$$E(\rho) = \min \sum_i p_i E(|\psi\rangle_i). \tag{1.12}$$

Following Ref. [9], in the two-qubit case this minimization reduces to a simpler formula shown below.

1.2.1 Concurrence

The concurrence of a two-qubit state ρ is defined as $\mathcal{C}(\rho) = \max\{0, \lambda_1 - \lambda_2 - \lambda_3 - \lambda_4\}$, where λ_i are the eigenvalues, in decreasing order, of the matrix $R = \sqrt{\sqrt{\rho}\tilde{\rho}\sqrt{\rho}}$; here $\tilde{\rho} = (\sigma_y \otimes \sigma_y)\rho^*(\sigma_y \otimes \sigma_y)$. Maximally entangled states have $\mathcal{C} = 1$, whereas separable states have $\mathcal{C} = 0$. The entanglement of formation is related to concurrence in the following way: $E(\rho) = \mathscr{E}\left(\mathcal{C}(\rho)\right)$, where $\mathscr{E}(\mathcal{C}) = h\left((1 + \sqrt{1 - \mathcal{C}^2})/2)\right)$, with $h(x)$ being the binary entropy function, $h(x) = -x \log_2 x - (1 - x)\log_2(1 - x)$. However, for our use it will suffice to just quote the concurrence of a quantum state.

Let's look at an example for concurrence. In Chapter 6 we will model the output from our quantum memory as a so-called Werner state [10]. A Werner state $\rho_{\mathrm{W}}(p)$ is defined as the probabilistic mixture of a maximally entangled state — we usually use the $|\Phi^+\rangle$ Bell state — and white noise represented by the maximally mixed state $\mathbb{1}/4$. The Werner state is written as

$$\rho_{\mathrm{W}}(p) = p|\Phi^+\rangle\langle\Phi^+| + (1-p)\mathbb{1}/4 \tag{1.13}$$

where p is a probability, i.e. it has a value between 0 and 1. The fidelity of a Werner state $\rho_{\mathrm{W}}(p)$ with the maximally entangled state $|\Phi^+\rangle$ is $(1+3p)/4$. (As a side note, the fidelity between two Werner states $\rho_{\mathrm{W}}(p_1)$ and $\rho_{\mathrm{W}}(p_2)$ is equal to $(\sqrt{(1+3p_1)(1+3p_2)} + 3\sqrt{(1-p_1)(1-p_2)})^2/16$.) It turns out that for the Werner state in Eq. 1.13 we can analytically evaluate the concurrence. Since $\rho_{\mathrm{W}}(p)$ is entirely real and since $|\Phi^+\rangle$ is an eigenstate of $\sigma_y \otimes \sigma_y$, we get that $\tilde{\rho}_{\mathrm{W}}(p) = \rho_{\mathrm{W}}(p)$. The matrix R is then equal to $\rho_{\mathrm{W}}(p)$, which is diagonal in the Bell state basis $\{|\Phi^+\rangle, |\Phi^-\rangle, |\Psi^+\rangle, |\Psi^-\rangle\}$ with eigenvalues $\{(3p-1)/4, (1-p)/4, (1-p)/4, (1-p)/4\}$ respectively. The concurrence is then simply $\mathcal{C}(\rho_{\mathrm{W}}) = \max\{0, (3p-1)/2\}$. We see here that as p decreases below $1/3$ the entanglement "breaks" and $\rho_{\mathrm{W}}(p)$ becomes separable.

1.3 Measurement

Measuring a quantum state disturbs it in such a way that complete information can never be obtained. In general, a quantum measurement is defined by a set of measurement operators $\{M_k\}$, such that the probability of measuring the k^{th} outcome is

$$P(k) = \mathrm{Tr}(M_k^\dagger M_k \rho) \tag{1.14}$$

We require here that the set of measurement operators have the property $\sum_k M_k^\dagger M_k = \mathbb{1}$. This is to ensure that the probabilities of outcomes across all measurements sum to 1, meaning that something must happen when we perform a measurement.

While measurements are in general described theoretically as positive operator-valued measures (POVMs) [5], we will restrict ourselves to a subset of measurement operators that

describe projective measurements. A projective measurement is associated with a physical observable $\mathcal{M}$ which is a Hermitian operator with spectral decomposition

$$\mathcal{M} = \sum_k \lambda_k P_k \tag{1.15}$$

where P_k projects the state $|\psi\rangle$ onto the eigenstates of $\mathcal{M}$ with associated eigenvalues m_k. The probability of getting the measurement result m_k is then

$$p(m_k) = \langle\psi|P_k|\psi\rangle \tag{1.16}$$

There is then some measurement $\mathcal{M}$ where $P_k = |\psi\rangle\langle\psi|$, giving $p(m_k) = 1$ for one value of k and 0 otherwise. Let's look at an example. Suppose we wish to measure the physical observable σ_x. By its spectral decomposition we have that $\sigma_x = (+1)|+\rangle\langle+| + (-1)|-\rangle\langle-|$, meaning the projectors are $|+\rangle\langle+|$ and $|-\rangle\langle-|$ with respective eigenvalues $+1$ and -1. The probability of measuring the $+1$ eigenvalue is then $p(+1) = |\langle+|\psi\rangle|^2$. In Chapter 2 we will see how to perform projective measurements on polarization-encoded qubits in single photons. Finally, we can measure the expectation value of an observable by summing over its eigenvalues with their associated probabilities $\langle\mathcal{M}\rangle = \sum_k m_k p_k$.

1.3.1 Quantum State Tomography

One cannot characterize an unknown quantum state with a single measurement. However, in many experiments we wish to know the final state of our qubit(s) after some quantum process has occurred. We can use *quantum state tomography*. By running the experiment many times and assuming each run is identical, we can measure the output qubit in different bases to reconstruct the density matrix describing the state.

Recall our picture of a single qubit in Fig. 1.1. The density matrix of the qubit, ρ, is a vector from the origin to some point within the Bloch sphere, expressed as

$$\begin{aligned} \rho &= \frac{1}{2}\left[\mathbb{1} + \mathrm{Tr}(\rho\sigma_x)\sigma_x + \mathrm{Tr}(\rho\sigma_y)\sigma_y + \mathrm{Tr}(\rho\sigma_z)\sigma_z\right] \\ &= \frac{1}{2}\sum_{i=\{0,x,y,z\}} \mathrm{Tr}(\rho\sigma_i)\sigma_i \end{aligned} \tag{1.17}$$

where the Pauli matrices are the unit vectors in the x, y, and z directions, and we have used the label σ_0 to signify the identity matrix $\mathbb{1}$. This also extends to higher dimensions. The two-qubit version is simply

$$\rho = \frac{1}{4} \sum_{i,j=\{0,x,y,z\}} \mathrm{Tr}\left[\rho(\sigma_i \otimes \sigma_j)\right] \sigma_i \otimes \sigma_j \tag{1.18}$$

We won't consider any more than two-qubit states in this thesis. Thinking about the single qubit case again, determining the state ρ is akin to finding the projection of the state vector onto each of the three axes, given by $\mathrm{Tr}(\rho\sigma_i)$. We will describe in more detail how these measurements work with photons in Chapter 2, but for now it will suffice to say that we project the state onto the $+1$ and -1 eigenstates of σ_i and measure the number of "counts" over a given time. In the single qubit case we have six projective measurements $\{|0\rangle, |1\rangle, |+\rangle, |-\rangle, |+_y\rangle, |-_y\rangle\}$, producing a set of six measured counts $\{N_0, N_1, N_+, N_-, N_{+y}, N_{-y}\}$, respectively. (Note: this is a tomographically over-complete set of measurements. In the two-qubit case we typically perform 36 measurements.)

Following Ref. [11] we use a maximum likelihood technique to reconstruct ρ. We do this by first parametrizing the density matrix with a vector $\vec{t}$ using the Cholesky decomposition of a Hermitian matrix as follows

$$\rho(\vec{t}) = T^\dagger T, \quad \text{where } T = \begin{pmatrix} t_1 & 0 \\ t_2 + it_3 & t_4 \end{pmatrix}, \tag{1.19}$$

$$\rho(\vec{t}) = T^\dagger T, \quad \text{where } T = \begin{pmatrix} t_1 & 0 & 0 & 0 \\ t_2 + it_3 & t_8 & 0 & 0 \\ t_4 + it_5 & t_9 + it_{10} & t_{13} & 0 \\ t_6 + it_7 & t_{11} + it_{12} & t_{14} + it_{15} & t_{16} \end{pmatrix} \tag{1.20}$$

for the one- and two-qubit cases respectively. We can enforce $\rho(\vec{t})$ to have a trace of one by restricting the parameters along the diagonal. We assume that each measured count is an independent event so that with sufficiently large counts we can estimate the probability of measuring N_k given a density matrix $\rho(\vec{t})$ as a normal distribution

$$p(N_k) = \exp\left\{-\frac{(N_k/\mathcal{N} - \bar{n}_k)^2}{2\sigma_k^2}\right\} \tag{1.21}$$

where $\bar{n}_k = \langle\psi_k|\rho(\vec{t})|\psi_k\rangle$, such that a projective measurement $|\psi_k\rangle$ taken from the set above results in N_k counts. Also here σ_k is the standard deviation for the k$^{\text{th}}$ measurement. Assuming Poissonian error statistics, $\sigma_k = \sqrt{\bar{n}_k}$. Lastly, $\mathcal{N}$ is the total number of measured counts in the respective basis, e.g., for N_+ we take $\mathcal{N} = N_+ + N_-$. The likelihood that a density matrix $\rho(\vec{t})$ could result in a set of counts $\{N_1, ..., N_6\}$ (for two qubits $\{N_1, ..., N_{36}\}$) is

$$p(N_1, ..., N_6) = \prod_{k=1}^{6} \exp\left\{-\frac{(N_k/\mathcal{N} - \langle\psi_k|\rho(\vec{t})|\psi_k\rangle)^2}{2\langle\psi_k|\rho(\vec{t})|\psi_k\rangle}\right\} \tag{1.22}$$

To find the truest representation of ρ from the experiment we maximize this likelihood function over parameters $\vec{t}$. It is mathematically equivalent to instead maximize the logarithm of this above equation which, since the logarithm brings down the minus sign from the exponential, is equivalent to minimizing the following function

$$f(N_1, ..., N_6) = \sum_{k=1}^{6} \exp\left\{-\frac{(N_k/\mathcal{N} - \langle\psi_k|\rho(\vec{t})|\psi_k\rangle)^2}{2\langle\psi_k|\rho(\vec{t})|\psi_k\rangle}\right\} \tag{1.23}$$

We perform this minimization numerically, and for the work in this thesis we used the NMinimize function in Wolfram Mathematica 10. The resulting $\rho(\vec{t})$ is what we take to be the experimental density matrix. To extend this routine to two-qubit state reconstruction we sum over all 36 measurement settings which for each qubit are again chosen from the ± 1 eigenstates of the Pauli operators.

We quantify the uncertainty in the reconstructed density matrix using a Monte Carlo error estimation [12, 13, 14, 15]. We first assume that the measured counts in our experiment can be described with Poissonian error, which goes as the square root of the number of counts. We then sample from Gaussian probability distributions for each measurement, and for each set of samples perform a density matrix reconstruction. We repeat this process numerous times (in this thesis we use on the order of 100 iterations) to find a standard deviation from the measured density matrix.

1.3.2 State Fidelity

In this section we discuss a method for comparing the density matrix we reconstruct from experiment with the ideal state we expect. While there exist a few ways of quantifying distances between two quantum states [5], we will use the state fidelity [16]. A natural way to compare to pure quantum states $|\psi\rangle$ and $|\phi\rangle$ is to calculate their overlap $|\langle\phi|\psi\rangle|^2$. In any realistic scenario, the quantum state we measure is mixed. However, in many cases the ideal state we wish to compare to is still pure. The overlap between pure and mixed states $|\psi\rangle$ and ρ is given by $\langle\psi|\rho|\psi\rangle$.

To compare to mixed states ρ_1 and ρ_2 we use the formula from Ref. [16], originally introduced in Ref. [17], which gives the state fidelity as

$$\mathcal{F}(\rho_1, \rho_2) = \left(\mathrm{Tr}\sqrt{\sqrt{\rho_1}\rho_2\sqrt{\rho_1}}\right)^2 \tag{1.24}$$

One can verify that if one, or both, of ρ_1 and ρ_2 are pure that $\mathcal{F}(\rho_1, \rho_2)$ reduces to the overlaps stated above.

1.4 Quantum processes

How a quantum system evolves in time is determined by its Hamiltonian. The Hamiltonian is a Hermitian operator, meaning it has orthogonal eigenvectors and real eigenvalues. For a Hamiltonian $\mathcal{H}$, the time evolution of a state $|\psi\rangle$ (where we assume the system is closed) is governed by the Schrödinger equation

$$i\hbar\frac{d|\psi\rangle}{dt} = \mathcal{H}|\psi(t)\rangle \tag{1.25}$$

After evolving under the Hamiltonian for a time t, an initial quantum state $|\psi(0)\rangle$ is then unitarily mapped to

$$|\psi(t)\rangle = U(t)|\psi(0)\rangle \tag{1.26}$$

$$\text{where } U(t) = \exp\left\{\frac{-i}{\hbar}\int_0^t dt'\mathcal{H}(t')\right\} \tag{1.27}$$

The fact that $\mathcal{H}$ is Hermitian ensures that U is unitary, i.e., $U^\dagger U = \mathbb{1}$. Unitary processes describe reversible quantum evolution. A unitary operation has the important property that it conserves the magnitude of a state's Bloch vector. That is to say, a unitary operation will maintain the purity of the state it acts on.

However, unitaries alone do not tell us the complete picture of how quantum states can evolve. For that we need to define the quantum channel. Here, channel and process are synonymous terms. In general, a quantum channel is a completely-positive and trace-preserving (CPTP) map [5], which is to say that it transforms a density matrix to another density matrix. Recall that to describe a physical state a density matrix ρ must have all eigenvalues greater than or equal to zero, and must have trace equal to one. A positive map is one that takes a positive semi-definite matrix, like ρ, to another positive semi-definite matrix. However, we require that a quantum channel, $\mathcal{E}(\rho)$ be *completely* positive. This extra condition means that regardless of how many auxiliary systems we add, the resulting output must still be positive semi-definite — i.e., $(\mathcal{E} \otimes \mathbb{1}_d)(\rho \otimes \rho'_d) \geq 0$ for any dimension d of the auxiliary system. Second, the quantum channel must be trace-preserving, meaning that since the input to the channel is a density matrix with trace one, the output must also have trace one.

There are a few different ways to represent the action of a quantum channel $\mathcal{E}$ on a density matrix ρ: the Kraus decomposition [18]; the Choi matrix [19, 20]; and the Stinespring dilation [21] (Ref. [22] is a useful resource for showing the relationships between all of these). Here we will focus on the Kraus representation since it will influence our subsequent discussion on reconstructing experimental quantum processes. The Kraus decomposition models a quantum channel as the probabilistic sum of operations on a density matrix ρ, much in the same way that a mixed quantum state is the probabilistic sum of pure states. In this description, the channel is defined by a non-unique set of d-dimensional square Kraus operators $\{A_1, ..., A_{d^2}\}$, where d is the dimension of the quantum system ($d = 2$ for a single qubit). A quantum channel is then given by

$$\mathcal{E}(\rho) = \sum_i A_i \rho A_i^\dagger \tag{1.28}$$

Complete positivity of the channel is ensured by the fact that both the left- and right-acting

operators are the same. Trace preservation is ensured by the additional criterion

$$\sum_i A_i^\dagger A_i = \mathbb{1}_d \tag{1.29}$$

In general, a set of up to d^2 operators are sufficient to describe any process. One quantum process we will be particularly interested in is the partially depolarizing channel, in which a qubit ρ with probability p remains unchanged, but with probability $(1-p)$ is mapped to the maximally mixed state,

$$\rho \to p\rho + (1-p)\,\mathbb{1}/2 \tag{1.30}$$

One Kraus representation of this channel is given by the Pauli operators with appropriate scalings,

$$A_1 = \frac{\sqrt{1+3p}}{2}\mathbb{1}, \quad A_2 = \frac{\sqrt{1-p}}{2}\sigma_x, \quad A_3 = \frac{\sqrt{1-p}}{2}\sigma_y, \quad A_4 = \frac{\sqrt{1-p}}{2}\sigma_z. \tag{1.31}$$

It is straightforward to verify that the trace preservation criterion stated above is satisfied for these operators. In Chapter 6 we will be interested in characterizing the quantum process that our quantum memory performs on a stored qubit. In order to do this we must do something similar to state tomography but for a whole process, which leads us to our next discussion.

1.4.1 Quantum Process Tomography

In order to reconstruct a quantum state using tomography, as discussed in Section 1.3.1, we needed to perform a complete set of measurements. Now in order to determine a quantum process, i.e., how states get transformed, we will need to input each state from a complete basis set to the process and again measure each output with a complete set of measurements. Then we will have all the information needed to reconstruct how the process transforms an unknown state. This is called *quantum process tomography* [5].

For our purpose in this thesis, we will prepare and measure states in the Pauli basis. For a single-qubit quantum process, we input the ± 1 eigenstates of the σ_x, σ_y, and σ_z operators. Upon output from the process we project onto the same ± 1 eigenstates, the same we used for quantum state tomography.

The process matrix χ

We mentioned above that the Kraus decomposition for a quantum process is not unique. Now we will use that fact to express a process in the Pauli basis. A good resource for this is Chapter 8 of Ref. [5]. The Pauli operators $\{\sigma_0 = \mathbb{1}, \sigma_x, \sigma_y, \sigma_z\}$ form an orthogonal basis, meaning that $\mathrm{Tr}(\sigma_i \sigma_j) = 2\delta_{ij}$. Because of this each Kraus operator A_i can be expressed as linear combination of Paulis

$$A_i = \sum_m c_{i,m} \sigma_m. \tag{1.32}$$

We then write the whole process as

$$\begin{aligned} \mathcal{E}(\rho) &= \sum_i \left(\sum_m c_{i,m} \sigma_m \right) \rho \left(\sum_n c^*_{i,n} \sigma_n \right) && (1.33) \\ &= \sum_{m,n} \left(\sum_i c_{i,m} c^*_{i,n} \right) \sigma_m \rho \sigma_n && (1.34) \\ &= \sum_{m,n} \chi_{m,n} \sigma_m \rho \sigma_n && (1.35) \end{aligned}$$

$\chi_{mn} = \sum_i c_{i,m} c^*_{i,n}$ is called the process matrix. It is a $d^2 \times d^2$ square matrix with the rows and columns labelled by the Pauli operators. It is also Hermitian and has trace equal to one (Note: some definitions take χ to have trace equal to d^2). These properties are very similar to those of a density matrix, and we will draw upon this connection soon. It is the goal of quantum process tomography to reconstruct the experimental χ using many copies of the input states.

An example χ matrix may be of use here. In the previous section we looked at the partially depolarizing channel. The Kraus representation we wrote down, Eq.1.31, for the channel was conveniently already in the basis of Pauli operators. Since the Kraus representation models the process as a probabilistic sum of unitaries, the corresponding χ matrix will be "mixed" in the same fashion that a mixed quantum state is a probabilistic sum of pure states. If we think about the Pauli operators as vectors in the operator space, then χ is given by a sum of the outer products of its Kraus operators – just as a density matrix $\rho = \sum_i p_i |\psi_i\rangle\langle\psi_i|$. For example, the first Kraus operator is $\sqrt{1+3p}/2 \cdot \mathbb{1}$,

so its corresponding outer product will give a matrix with just one non-zero entry: $\chi_{11} = (1+3p)/4$. The total process matrix for the partially depolarizing channel is

$$\chi(p) = \frac{1}{4}\begin{pmatrix} 1+3p & 0 & 0 & 0 \\ 0 & 1-p & 0 & 0 \\ 0 & 0 & 1-p & 0 \\ 0 & 0 & 0 & 1-p \end{pmatrix} \tag{1.36}$$

Experimentally, we can reconstruct χ with a complete set of d^2 input states, each measured in a complete set (d^2 measurements). As was the case for quantum state tomography, in this work we use over-complete sets of inputs and measurements, giving a total of $6 \times 6 = 36$ total measurements for a single-qubit process. We should mention here that other quantum process tomography techniques exist, which can be advantageous depending on available resources. For example, ancilla-assisted quantum process tomography [23, 24] uses one qubit from a two-qubit entangled state as the input to the process. We could then reconstruct χ by performing two-qubit state tomography on the output. This still requires d^2 measurements, but the work is shifted from preparation and measurement to solely measurement. In thesis we use the method of preparing 6 inputs states and measuring each with 6 projections.

Maximum likelihood revisited

In very much the same fashion as Section 1.3.1 we use a maximum likelihood method for reconstructing the process matrix χ [25]. We will make the same assumptions, namely that we have many identical copies the input states ρ_i which give output states $\mathcal{E}(\rho_i)$, and that our measured "counts" are independent events allowing us to use Poissonian statistics. We will parametrize the χ matrix for a single-qubit process in the same way as we did for the density operator,

$$\chi(\vec{t}) = \begin{pmatrix} t_1 & t_2+it_3 & t_4+it_5 & t_6+it_7 \\ t_2-it_3 & t_8 & t_9+it_{10} & t_{11}+it_{12} \\ t_4-it_5 & t_9-it_{10} & t_{13} & t_{14}+it_{15} \\ t_6-it_7 & t_{11}-it_{12} & t_{14}-it_{15} & t_{16} \end{pmatrix} \tag{1.37}$$

Then, in analogy to what we did in the state tomography case, we look at the square of the difference between expected and measured counts for each input state $|\psi_a\rangle$ and measurement setting $|\phi_b\rangle$,

$$\sum_{a,b} \frac{\left[N_{ab}/\mathcal{N} - \langle\phi_b| \left(\sum_{m,n} \chi(\vec{t})_{mn}\sigma_m|\psi_a\rangle\langle\psi_a|\sigma_n\right)|\phi_b\rangle\right]^2}{2\langle\phi_b| \left(\sum_{m,n} \chi(\vec{t})_{mn}\sigma_m|\psi_a\rangle\langle\psi_a|\sigma_n\right)|\phi_b\rangle} \tag{1.38}$$

where we divide the counts by $\mathcal{N}$, the total counts across a basis, to convert to probabilities. At this point the method does deviate from quantum state tomography as we need to add another term to form our likelihood function. Since the Kraus representation of a channel requires that $\sum_i A_i^\dagger A_i = \mathbb{1}$, we need to add a term that to our likelihood function that will enforce trace preservation. By switching to the Pauli basis this condition becomes

$$\sum_{mn} \chi_{mn}(\vec{t})\sigma_n\sigma_m = \mathbb{1}. \tag{1.39}$$

We can add a constraint to the likelihood function of the form $[\mathrm{Tr}(\sum_{mn} \chi_{mn}(\vec{t})\sigma_n\sigma_m) - \mathrm{Tr}(\mathbb{1})]^2$. However, including exactly this in the likelihood function would only address the diagonal entries of $\chi(\vec{t})$. Instead, we can multiply both sides of Eq. 1.40 by a sum over the Paulis giving

$$\sum_k \sigma_k \sum_{mn} \chi_{mn}(\vec{t})\sigma_n\sigma_m = \sum_k \sigma_k. \tag{1.40}$$

We then take the trace of both sides and take the square of the difference between them. Our likelihood function is now

$$f(\vec{t}) = \sum_{a,b} \frac{\left[N_{ab}/\mathcal{N} - \langle\phi_b| \left(\sum_{m,n} \chi(\vec{t})_{mn}\sigma_m|\psi_a\rangle\langle\psi_a|\sigma_n\right)|\phi_b\rangle\right]^2}{2\langle\phi_b| \left(\sum_{m,n} \chi(\vec{t})_{mn}\sigma_m|\psi_a\rangle\langle\psi_a|\sigma_n\right)|\phi_b\rangle} \tag{1.41}$$

$$+\lambda \sum_k \left[\sum_{mn} \chi_{mn}(\vec{t})\mathrm{Tr}(\sigma_n\sigma_m\sigma_k) - \mathrm{Tr}(\sigma_k)\right]^2 \tag{1.42}$$

where λ is a Lagrange multiplier term to give more weight to the trace preservation and complete positivity constraints. For the process matrix reconstructions in this thesis we

use $\lambda = 10^3$. As with state tomography, we perform a numerical minimization of $f(\vec{t})$ using the NMinimize function in Wolfram Mathematica 10.

To quantify the uncertainty in the reconstructed process matrix, we again use a Monte Carlo technique. Recall that in the state tomography case we assumed that the measured counts in our experiment can be described with Poissonian error. We do the same thing here. We sample from Gaussian probability distributions for each preparation and measurement, using each set of samples to perform a maximum likelihood process matrix reconstruction. We repeat this process numerous times (in this thesis we use 100 iterations) to find a standard deviation from the measured process matrix.

1.4.2 Process Fidelity

We wish to compare the quantum process we measure in experiment to the expected, or ideal, process from theory. There are multiple ways to quantify the distance between two processes (e.g., the maximum trace distance [5]). Here we look at the process fidelity. We use the same formula for the process fidelity as for the state fidelity, discussed in Section 1.3.2, given by

$$\mathcal{F}(\chi_1, \chi_2) = \left(\mathrm{Tr} \sqrt{\sqrt{\chi_1}\chi_2\sqrt{\chi_1}} \right)^2 \tag{1.43}$$

In analogy to the state fidelity we can think of the process fidelity to be an overlap between two processes.

Chapter 2

Quantum optics

In this chapter we will introduce the photon, what it is and how we generate, manipulate and measure photons for uses in quantum information. We'll begin with the polarization of light, since it is how we will encode quantum information in a photon. We then move on to some important quantum states of light and how to discriminate between them, before discussing interference effects between single photons and weak laser pulses. We'll finish this chapter by discussing the generation of single photon states using nonlinear optics, specifically the photon source used for the experiments in this thesis.

2.1 Polarization

In later chapters of this thesis we will encode a qubit in the polarization of a single photon, by which we mean the transverse direction of its electric field. There are multiple reasons for using polarization qubits. First, optical elements such as waveplates and polarizing beamsplitters are readily available and make state preparation, local gates, and measurements very straightforward. Secondly, the polarization of light propagating in free space is very stable over time. In the polarization encoding we define the computational basis

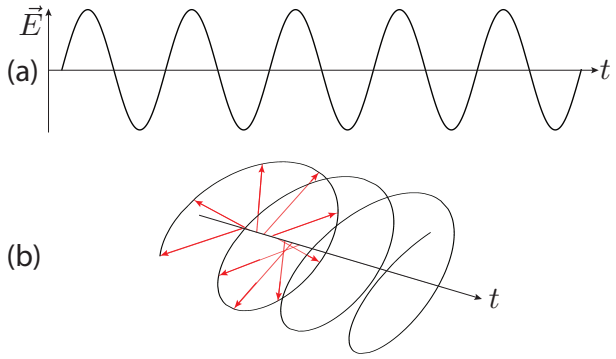

Figure 2.1: Visualization of (a) linearly and (b) circularly polarized light.

$\{|0\rangle, |1\rangle\}$ using the horizontal ($|H\rangle$) and vertical ($|V\rangle$) polarizations,

$$|H\rangle = |0\rangle, \tag{2.1}$$
$$|V\rangle = |1\rangle. \tag{2.2}$$

To be clear, horizontally polarized light looks like a wave wiggling parallel to the floor; vertically polarized light wiggles perpendicular to the floor, like water waves. Having defined the eigenstates of the Pauli σ_z operator we can move on to the eigenstates of σ_x and σ_y. We take the diagonal (D) and anti-diagonal (A) linear polarizations to be the $+1$ and -1 eigenstates of σ_x respectively, and the left- (L) and right-circular (R) polarizations to be the $+1$ and -1 eigenstates of σ_y, giving

$$|D\rangle = \frac{1}{\sqrt{2}}(|H\rangle + |V\rangle), \tag{2.3}$$
$$|A\rangle = \frac{1}{\sqrt{2}}(|H\rangle - |V\rangle), \tag{2.4}$$
$$|L\rangle = \frac{1}{\sqrt{2}}(|H\rangle + i|V\rangle), \tag{2.5}$$
$$|R\rangle = \frac{1}{\sqrt{2}}(|H\rangle - i|V\rangle). \tag{2.6}$$

2.1.1 Manipulating polarization

A general unitary operation on a polarization qubit can be achieved using birefringent waveplates (WP). Birefringence, the difference in refractive indices for ordinary and extraordinary polarizations in a material, allows us to delay one polarization with respect to the other resulting in a rotation in the Bloch sphere. Here, the terms ordinary and extraordinary refer to the polarizations aligned perpendicular to, and along the material's optic axis, respectively. The Jones matrix, which maps between initial and final polarization states, for an arbitrary waveplate with birefringent phase ϕ and its optic axis at angle θ to the horizontal plane is

$$\mathrm{WP}(\phi,\theta) = \begin{pmatrix} \cos^2\theta + e^{i\phi}\sin^2\theta & (1-e^{i\phi})\cos\theta\sin\theta \\ (1-e^{i\phi})\cos\theta\sin\theta & e^{i\phi}\cos^2\theta + \sin^2\theta \end{pmatrix}. \tag{2.7}$$

The two most common waveplates are the half-waveplate (HWP) and the quarter-waveplate (QWP). A half-waveplate delays one polarization by half a wavelength with respect to the other, meaning that $\phi = \pi$. The Jones matrix for a half-waveplate is then

$$\mathrm{HWP}(\theta) = \mathrm{WP}(\pi,\theta) = \begin{pmatrix} \cos 2\theta & \sin 2\theta \\ \sin 2\theta & -\cos 2\theta \end{pmatrix}. \tag{2.8}$$

A quarter-waveplate is similar except that it delays one polarization by a quarter wavelength, meaning that $\phi = \pi/2$. The Jones matrix for a quarter-waveplate is then

$$\mathrm{QWP}(\theta) = \mathrm{WP}(\frac{\pi}{2},\theta) = \begin{pmatrix} \cos^2\theta + i\sin^2\theta & (1-i)\cos\theta\sin\theta \\ (1-i)\cos\theta\sin\theta & i\cos^2\theta + \sin^2\theta \end{pmatrix}. \tag{2.9}$$

It will be useful to describe some of the important cases of half- and quarter-waveplates we use in later chapters. Two of the Pauli gates, σ_x and σ_z, can be achieved using a half-waveplate at $\theta = \pi/4$ and $\theta = 0$, respectively. The σ_y operation can be performed by using σ_z and σ_x gates in succession. In general, any rotation on the Bloch sphere can be achieved by the combination QWP-HWP-QWP.

We are also interested in using waveplates in perform measurements for quantum state tomography. When a half- and quarter-waveplate are used in conjunction with a polarizing

Measurement basis	HWP angle	QWP angle
σ_x	$\frac{\pi}{4}$	0
σ_y	0	$-\frac{\pi}{4}$
σ_z	0	0

Table 2.1: Waveplate settings for tomographic measurements. An incoming photon passes through the HWP, QWP and then the PBS.

beamsplitter, we can perform an arbitrary projective measurement on a single qubit. We will return to the beamsplitter later in this chapter, but for this purpose it will suffice to know that a polarizing beamsplitter will transmit horizontally polarized light and reflect vertically polarized light. By itself, the polarizing beamsplitter can be used for projective measurements in the computational basis: with detectors at both the transmitted and reflected outputs of the beamsplitter we can collect statistics to obtain the expectation value $\langle\sigma_z\rangle$.

To perform a measurement in the σ_x basis, we use a half-waveplate at $\theta = \pi/4$ which maps $|D\rangle \to |H\rangle$ and $|A\rangle \to |V\rangle$. For the σ_y basis, we use a quarter-waveplate at $\theta = \pi/4$ which maps $|L\rangle \to |H\rangle$ and $|R\rangle \to |V\rangle$. However, since in practice we will always have a HWP-QWP combination, and since for any angle the half-waveplate maps $|R\rangle \to |L\rangle$, we take $\theta = -\pi/4$ to make measurements in the σ_y basis. These settings are summarized in Table 2.1.

2.2 Quantum states of light

In this section we will introduce some important states of light in quantum optics. To do this we must first review the quantum harmonic oscillator and the ladder operators. The quantum harmonic oscillator has the Hamiltonian, with mass $m = 1$,

$$\mathcal{H} = \frac{\hat{p}^2}{2} + \frac{1}{2}\omega^2\hat{x}^2 \tag{2.10}$$

$$= \hbar\omega\left(\hat{a}^\dagger\hat{a} + \frac{1}{2}\right), \tag{2.11}$$

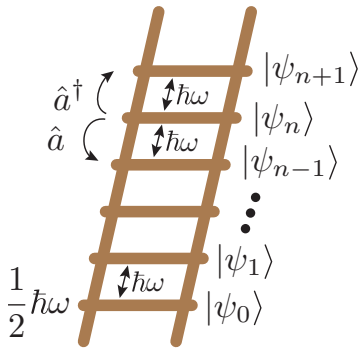

Figure 2.2: The energy levels of the harmonic oscillator with frequency ω. The energy eigenstates $|\psi_n\rangle$ are equally spaced by $\hbar\omega$. The lowest state on the ladder, $|\psi_0\rangle$, has energy $\hbar\omega/2$, and the n^{th} state, $|\psi_n\rangle$, has energy $(n+1/2)\hbar\omega$. The raising and lowering operators, $a^\dagger$ and a, map between the eigenstates of the oscillator.

where $\hat{a}$ and $\hat{a}^\dagger$ are the raising and lowering operators, defined as

$$\hat{a} = \frac{1}{\sqrt{2\hbar\omega}}\left(i\hat{p} + \omega\hat{x}\right), \tag{2.12}$$

$$\hat{a}^\dagger = \frac{1}{\sqrt{2\hbar\omega}}\left(-i\hat{p} + \omega\hat{x}\right). \tag{2.13}$$

Note that the operators $\hat{a}$ and $\hat{a}^\dagger$ have the commutation relation $[\hat{a}, \hat{a}^\dagger] = 1$. We label the eigenstates of the harmonic oscillator are $|\psi_n\rangle$, such that $\mathcal{H}|\psi_n\rangle = E_n|\psi_n\rangle$. Using the commutation relation it can be shown that $\hat{a}|\psi_n\rangle$ and $\hat{a}^\dagger|\psi_n\rangle$ are also eigenstates of $\mathcal{H}$ with energy eigenvalues $E_n - \hbar\omega$ and $E_n + \hbar\omega$ respectively. The eigenstates are then energetically separated by $\hbar\omega$, and the raising and lowering operators map between eigenstates as follows

$$\hat{a}^\dagger|\psi_n\rangle = \sqrt{n+1}|\psi_{n+1}\rangle, \quad \hat{a}|\psi_n\rangle = \sqrt{n}|\psi_{n-1}\rangle \tag{2.14}$$

We enforce $|\psi_0\rangle$ as the lowest energy state by setting $\hat{a}|\psi_0\rangle = 0$. The "ladder" structure of the harmonic oscillator is shown in Fig. 2.2.

We write the quantized electric field in a single mode k and single frequency ω_k as

$$\vec{E}_k = i\sqrt{\frac{\hbar\omega_k}{2\epsilon_0 V}}\left(\hat{a}_k e^{i(\vec{k}\cdot\vec{r}-\omega_k t)} + \hat{a}_k^\dagger e^{-i(\vec{k}\cdot\vec{r}-\omega_k t)}\right)\vec{\varepsilon}_k. \tag{2.15}$$

where the field propagates along $\vec{r}$ with polarization defined by $\vec{\varepsilon}_k$, and V is the mode volume. See Appendix B for a somewhat involved treatment of the quantization. Later in this chapter we will refer to the positive and negative frequency components of $\vec{E}_k$ separately. We'll define them here, respectively, as

$$\vec{E}_k^{(+)} = i\sqrt{\frac{\hbar\omega_k}{2\epsilon_0 V}}\hat{a}_k e^{i(\vec{k}\cdot\vec{r}-\omega_k t)}\vec{\varepsilon}_k, \tag{2.16}$$

$$\vec{E}_k^{(-)} = i\sqrt{\frac{\hbar\omega_k}{2\epsilon_0 V}}\hat{a}_k^\dagger e^{-i(\vec{k}\cdot\vec{r}-\omega_k t)}\vec{\varepsilon}_k. \tag{2.17}$$

We also note that the ladder operator commutation relation across modes k and j is

$$[\hat{a}_j, \hat{a}_k^\dagger] = \delta_{j,k}. \tag{2.18}$$

The definition of the ladder operators leads us to a discussion of a few important states of light in quantum optics: namely the Fock state, the coherent state, and the thermal state. From this point on we will refer to the eigenstates of the harmonic oscillator using the number, or Fock, states $|n\rangle$. The ladder operators work in exactly the same fashion:

$$\hat{a}^\dagger|n\rangle = \sqrt{n+1}|n+1\rangle, \tag{2.19}$$

$$\hat{a}|n\rangle = \sqrt{n}|n-1\rangle, \tag{2.20}$$

$$\hat{a}|0\rangle = 0. \tag{2.21}$$

Here we define the vacuum state $|0\rangle$ as the lowest rung on the harmonic oscillator ladder. Note that the vacuum state still has nonzero energy, $E_0 = \hbar\omega/2$. A single *photon*, one quantum of light, is the first excitation of the electric field above the vacuum, $|1\rangle = \hat{a}^\dagger|0\rangle$. A state with n identical photons is written as $|n\rangle$.

2.2.1 Single photon states

So far we have limited our discussion to single modes. In reality, the single photon states we produce will be a superposition of many modes, say time and frequency, or position and momentum. In the experiments we'll discuss in later chapters we are able isolate single

spatial modes using fibre optic cables with small cores. However, since the main results in this thesis are that we store and manipulate single photons with THz bandwidths, i.e., very large spreads of frequencies, we will need to express a single photon as a superposition of frequencies .

Suppose that a single photon $\hat{a}^\dagger|0\rangle$ is in a superposition of multiple frequencies ω_j each with an amplitude weighting $f(\omega_j)$,

$$|\psi\rangle = \sum_j f(\omega_j)\hat{a}^\dagger(\omega_j)|0\rangle, \tag{2.22}$$

where to be normalized we require $\sum_j |f(\omega_j)|^2 = 1$. The frequency-specific ladder operator $\hat{a}^\dagger(\omega_j)$ follows the commutation relation $[\hat{a}(\omega_i), \hat{a}^\dagger(\omega_j)] = \delta_{i,j}$. Since we are dealing with a spread of densely packed frequencies, instead of distinct single frequencies, we take the continuum limit of this sum to obtain

$$|\psi\rangle = \int d\omega_j f(\omega_j)\hat{a}^\dagger(\omega_j)|0\rangle, \tag{2.23}$$

where the integration is taken over all frequencies, and we have the same normalization condition $\int d\omega_j |f(\omega_j)|^2 = 1$.

2.2.2 Coherent states

Next we look at the eigenstate of the lowering operator $\hat{a}$, the coherent state. A coherent state $|\alpha\rangle$ can be expressed as an infinite sum in the number basis:

$$|\alpha\rangle = e^{-|\alpha|^2/2} \sum_{n=0}^{\infty} \frac{\alpha^n}{\sqrt{n!}}|n\rangle, \tag{2.24}$$

where one can verify that Eq. 2.24 is indeed the eigenstate of the lowering operator, $\hat{a}|\alpha\rangle = \alpha|\alpha\rangle$. We can also check what the average number of photons in the coherent state is by evaluating the expectation value of the number operator $n = \hat{a}^\dagger\hat{a}$,

$$\langle n\rangle = \langle\alpha|\hat{a}^\dagger\hat{a}|\alpha\rangle \tag{2.25}$$

$$= |\alpha|^2. \tag{2.26}$$

Coherent states are often used in quantum memory experiments [26, 27, 28, 29, 30, 13, 31, 32] since they are easy to produce: the output of a laser can be described by a coherent state.

2.2.3 Thermal states

We also discuss the thermal state, which is defined as being in thermal equilibrium with a bath. Following Ref. [34], we express this as the mixed state:

$$\rho_{\text{th}} = \sum_n \frac{\bar{n}^n}{(\bar{n}+1)^{n+1}} |n\rangle\langle n|, \tag{2.27}$$

where the average photon number $\bar{n}$ can be connected to the temperature of the bath by $\bar{n} = (e^{\frac{\hbar\omega}{k_B T}} - 1)^{-1}$, where T is the bath temperature and k_B is Boltzmann's constant. For a fixed amount of energy, this state has the highest entropy. One example of a thermal state of light is the output from a blackbody emitter such as an incandescent light bulb. However, examples of thermal states more relevant to the work in this thesis are spontaneous Stokes and anti-Stokes emission, and the state output from spontaneous parametric downconversion when only one of the downconverted modes is observed.

2.3 The beamsplitter

Now that we have a good understanding of what a single photon state in a single mode looks like, we want to know how to map it into other modes. Such an operation can be achieved with a beamsplitter, which can be thought of as a partial mirror: it reflects a portion of a light beam and transmits the rest. The beamsplitter then has two input "ports" and two output ports which can be used to overlap different spatial modes of light. The same formalism applies to mapping between modes of any kind, temporal or otherwise.

If an input state of light has complex amplitudes α and β in modes a and b respectively, then a lossless beamsplitter that reflects an amount R (and transmits $1 - R$) of the light

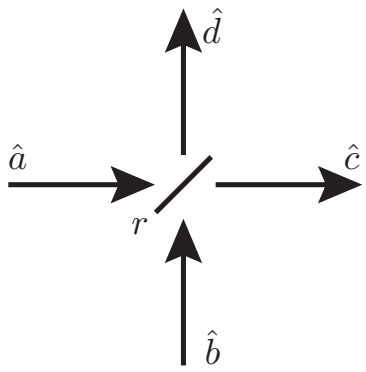

Figure 2.3: A beamsplitter with reflectivity r and transmittivity t, such that $|r|^2+|t|^2 = 1$, maps an input mode $\hat{a} \rightarrow t\hat{c}+r\hat{d}$, and an input mode $\hat{b} \rightarrow t\hat{d}-r\hat{c}$. Alternatively, the relations can be written as $\hat{a} \rightarrow t\hat{c} + ir\hat{d}$, and $\hat{b} \rightarrow t\hat{d} + ir\hat{c}$.

will map the input amplitudes to output amplitudes γ and δ in respective spatial modes c and d such that

$$\gamma \rightarrow \sqrt{1-R}e^{i\phi_{ac}}\alpha + \sqrt{R}e^{i\phi_{bc}}\beta \tag{2.28}$$

$$\delta \rightarrow \sqrt{R}e^{i\phi_{ad}}\alpha + \sqrt{1-R}e^{i\phi_{bd}}\beta \tag{2.29}$$

We want a lossless beamsplitter to be a unitary transformation, meaning that it must preserve the total population of the inputs,

$$\begin{aligned} |\alpha|^2 + |\beta|^2 &\rightarrow |\gamma|^2 + |\delta|^2 && (2.30)\\ &= R|\alpha|^2 + (1-R)|\beta|^2 \\ &+ 2\sqrt{R(1-R)}\mathrm{Re}\{\alpha\beta^* e^{i(\phi_{ac}-\phi_{bc})}\} \\ &+ (1-R)|\alpha|^2 + R|\beta|^2 \\ &+ 2\sqrt{R(1-R)}\mathrm{Re}\{\alpha\beta^* e^{i(\phi_{ad}-\phi_{bd})}\}. && (2.31) \end{aligned}$$

To be unitary we then require $e^{i(\phi_{ac}-\phi_{bc})}+e^{i(\phi_{ad}-\phi_{bd})} = 0$. One choice of phases that satisfies this is $\phi_{ac} = \phi_{ad} = \phi_{bd} = 0$ and $\phi_{bc} = \pi$. Turning to the quantum context, the beamsplitter will then map input mode ladder operators $\hat{a}$ and $\hat{b}$ to output operators $\hat{c}$ and $\hat{d}$ as

$$\hat{a} \rightarrow t\hat{c} + r\hat{d}, \tag{2.32}$$

$$\hat{b} \rightarrow t\hat{d} - r\hat{c} \tag{2.33}$$

where r and t are the reflection and transmission amplitudes such that $|r|^2 + |t|^2 = 1$. We will take r and t to be real numbers from here on. We will apply the beamsplitter to different scenarios soon, but first we need to introduce photon detection.

2.4 Photon detection and statistics

In this section we will discuss a model for how we detect photons, and how the different quantum states of light can be differentiated via their detection statistics. Glauber's model for photodetection [33] is based upon an atom coupled to the optical field to be detected. When, through the optical coupling, the atom transitions to one of its excited states, we assume that free electrons are generated, which are subsequently amplified and measured as a current. Glauber's treatment uses first-order perturbation theory to arrive at the probability of the atom transitioning to its excited state as

$$P(t) = \frac{2\pi}{\hbar^2} \sum_{\mu,\nu} s_{\mu,\nu} \int_{t_0}^{t} dt' \mathrm{Tr}\left(\rho E_\mu^{(-)}(\vec{r},t') E_\nu^{(+)}(\vec{r},t')\right) \tag{2.34}$$

where ρ is the input state of the optical field and $E_\nu^{(+)}(\vec{r},t')$ and $E_\mu^{(-)}(\vec{r},t')$ are the positive and negative frequency components of the quantized electric field (Eqs. 2.16 and 2.17 respectively). The subscripts μ and ν label the polarization modes of the electric field and $s_{\mu,\nu}$ is the detector sensitivity. The integral over time marks how long the interaction Hamiltonian which drives the dipole transition is active for. This can be thought of as a shutter for the detector that opens at time t_0 and closes at t. This implies that the photodetector measures the expectation value of the intensity operator $\hat{I} = 2c\epsilon_0 E^{(-)} E^{(+)}$.

By using Eq. 2.34 we are making a number of assumptions. First, we are assuming that only the positive frequency components of the electric field contribute to the transition amplitude. This is generally a safe assumption since the negative frequency portions result in oscillations which average out very quickly. This is called the rotating wave approximation. Second, we are assuming the detector sensitivity $s_{\mu,\nu}$ is constant over the excited states of the atom, meaning that the excited states are inherently broad band.

We can simplify the detection probability for the two extremes of shutter speeds. When the shutter speed is very fast compared to the wavepacket envelope, the transition probability can be taken as the instantaneous value $P_{\text{fast}}(t) \propto \text{Tr}(\rho E^{(-)}(\vec{r},t)E^{(+)}(\vec{r},t))$. However, we will be primarily concerned with the other extreme. When the shutter speed is very slow the transition probability becomes

$$P_{\text{slow}} \propto (2\pi)^4 \frac{\hbar\omega_k}{2\epsilon_0 V} \text{Tr}\left(\rho \sum_k \hat{a}_k^\dagger \hat{a}_k\right) \tag{2.35}$$

where we are making a few more assumptions. After substituting the positive and negative frequency electric field components (Eqs. 2.16 and 2.17) into the transition probability (Eq. 2.34) we integrated over the detector volume by assuming it to be much larger than the field mode volume ($\sim \lambda^3$). We also pulled ω_k out of the sum over all modes k by assuming that the bandwidth of the light is much smaller than its frequency ($\Delta\omega \ll \omega$); in this thesis we use photons with a central wavelength of 723 nm ($\omega \approx 415$ THz) with bandwidths $\Delta\omega \approx 2.3$ THz. Eq. 2.35 tells us that a slow detector measures the expectation value of the number operator summed over all modes k.

2.4.1 Photon statistics

How can one verify that they are observing single photons, i.e., Fock states $|n\rangle$ with $n = 1$, rather than a coherent state $|\alpha\rangle$ with a small average photon number $|\alpha|^2 \approx 1$, or even a thermal state? We would like a way to differentiate between these different states of light and, following Glauber's work [33], it turns out that correlations in their intensities will provide a way to do just that.

The second-order coherence function $g^{(2)}(\tau)$ is defined classically using average intensities

$$g^{(2)}(\tau) = \frac{\langle I(t)I(t+\tau)\rangle}{\langle I(t)\rangle^2} \tag{2.36}$$

$$= \frac{\langle E^*(t)E^*(t+\tau)E(t)E(t+\tau)\rangle}{\langle E^*(t)E(t)\rangle \langle E^*(t+\tau)E(t+\tau)\rangle} \tag{2.37}$$

We can place a lower bound on $g^{(2)}(\tau)$ in the following way [34]

$$\left(\frac{1}{N}\sum_{i=1}^{N} I(t_i)\right)^2 = \frac{1}{N^2}\sum_{i=1}^{N} I(t_i)^2 + \frac{2}{N^2}\sum_{i=1}^{N}\sum_{j>i}^{N} I(t_i)I(t_j) \tag{2.38}$$

$$\leq \frac{1}{N^2}\sum_{i=1}^{N} I(t_i)^2 + \frac{N-1}{N^2}\sum_{i=1}^{N} I^2(t_i) \tag{2.39}$$

$$\leq \frac{1}{N}\sum_{i=1}^{N} I^2(t_i) \tag{2.40}$$

where in the 2nd step we used $I^2(t_i) + I^2(t_j) \geq 2I(t_i)I(t_j)$. Eq. 2.40 implies that the expectation value of the intensity follows

$$\langle I(t)\rangle^2 \leq \left\langle I^2(t)\right\rangle \tag{2.41}$$

which in turn tells us that $g^{(2)}(0) \geq 1$. As we will see next, quantum states of light can give $g^{(2)}(0)$ values that violate this inequality giving us a contrast between quantum and classical theories of light.

In the quantum case we define $g^{(2)}(\tau)$ in an analogous way

$$g^{(2)}(\tau) = \frac{\left\langle E^{(-)}(t)E^{(-)}(t+\tau)E^{(+)}(t)E^{(+)}(t+\tau)\right\rangle}{\langle E^{(-)}(t)E^{(+)}(t)\rangle \left\langle E^{(-)}(t+\tau)E^{(+)}(t+\tau)\right\rangle} \tag{2.42}$$

where following from our discussion on photodetection, we use just the positive frequency component of the electric field. We also write the electric field operators normally ordered in the expectation value, i.e., all the raising operators $\hat{a}^\dagger$ precede the lowering operators $\hat{a}$. Normally ordering the ladder operators prevents unphysical events in our detection model like driving the atom transition when the optical field is strictly vacuum.

For the following discussion we will assume we have a single-mode state of light. Then, substituting the electric field terms for a single mode into Eq. 2.42 we get

$$g^{(2)}(\tau) = \frac{\left\langle \hat{a}^\dagger(t)\hat{a}^\dagger(t+\tau)\hat{a}(t)\hat{a}(t+\tau)\right\rangle}{\langle \hat{a}^\dagger(t)\hat{a}(t)\rangle \left\langle \hat{a}^\dagger(t+\tau)\hat{a}(t+\tau)\right\rangle} \tag{2.43}$$

For the $\tau = 0$ case, which is what we are interested in here, we get

$$g^{(2)}(0) = \frac{\langle \hat{a}^\dagger \hat{a}^\dagger \hat{a}\hat{a} \rangle}{\langle \hat{a}^\dagger \hat{a} \rangle^2} \tag{2.44}$$

Let's work out $g^{(2)}(0)$ for the important states of light we discussed in Section 2.2. We will start with the number state $|n\rangle$. We simplify the algebra with the commutation relation for the raising and lower operators, $[\hat{a}, \hat{a}^\dagger] = 1$, and using the fact that the number state is an eigenstate of the number operator $\hat{n} = \hat{a}^\dagger \hat{a}$,

$$g_n^{(2)}(0) = \frac{\langle n|\hat{a}^\dagger \hat{a}^\dagger \hat{a}\hat{a}|n\rangle}{\langle n|\hat{a}^\dagger \hat{a}|n\rangle^2} \tag{2.45}$$

$$= \frac{\langle n|\hat{a}^\dagger \hat{a}\hat{a}^\dagger \hat{a}|n\rangle - \langle n|\hat{a}^\dagger \hat{a}|n\rangle}{\langle n|\hat{a}^\dagger \hat{a}|n\rangle^2} \tag{2.46}$$

$$= \frac{\langle n|\hat{n}^2|n\rangle - \langle n|\hat{n}|n\rangle}{\langle n|\hat{n}|n\rangle^2} \tag{2.47}$$

$$= 1 - \frac{1}{n} \tag{2.48}$$

Importantly, for a pure number state $0 < g_n^{(2)}(0) < 1$ for all $|n\rangle$. This is a firm departure from the lower bound of 1 in the classical case. For a single photon $n = 1$, we get that $g_n^{(2)}(0) = 0$.

The coherent state $|\alpha\rangle$ value of $g^{(2)}(0)$ is very straightforward since it is the eigenstate of the lowering operator,

$$g_\alpha^{(2)}(0) = \frac{\langle \alpha|\hat{a}^\dagger \hat{a}^\dagger \hat{a}\hat{a}|\alpha\rangle}{\langle \alpha|\hat{a}^\dagger \hat{a}|\alpha\rangle^2} \tag{2.49}$$

$$= \frac{|\alpha|^4}{|\alpha|^4} \tag{2.50}$$

$$= 1 \tag{2.51}$$

Regardless of the strength of the coherent state we get the same result, the lowest possible classical value of $g^{(2)}(0)$. This means the coherent state can be viewed as a classical state of light.

Lastly, we look at thermal states. Recall that a thermal state has an average photon number $\bar{n}$. We begin with calculating the expectation value of $\hat{n}^2$,

$$\begin{aligned} \langle \hat{n}^2 \rangle &= \mathrm{Tr}(\hat{n}^2 \rho_{\mathrm{th}}) && (2.52) \\ &= \sum_n \frac{\bar{n}^n}{(\bar{n}+1)^{n+1}} n^2 && (2.53) \\ &= \bar{n} + 2\bar{n}^2 && (2.54) \end{aligned}$$

Then substituting this into the formula for the $g^{(2)}(0)$,

$$\begin{aligned} g^{(2)}_{\mathrm{th}}(0) &= \frac{\langle \hat{n}^2 \rangle - \langle \hat{n} \rangle}{\langle \hat{n} \rangle^2} && (2.55) \\ &= \frac{\bar{n} + 2\bar{n}^2 - \bar{n}}{\bar{n}^2} && (2.56) \\ &= 2 && (2.57) \end{aligned}$$

The $g^{(2)}(0)$ function then allows us to distinguish between these states based on their underlying statistical nature. We can gain some intuition into the physical meaning behind these statistical differences if we rewrite $g^{(2)}(0)$ in terms of the mean and variance of the number operator,

$$g^{(2)}(0) = 1 + \frac{\Delta \hat{n}^2 - \langle \hat{n} \rangle}{\langle \hat{n} \rangle^2} \quad (2.58)$$

where $\Delta \hat{n}^2 = \langle \hat{n}^2 \rangle - \langle \hat{n} \rangle^2$ is the variance. The coherent state $|\alpha\rangle$ then offers an intuitive explanation: its variance is equal to its mean $|\alpha|^2$, cancelling out the second term. This is characteristic of Poissonian statistics, and so the coherent state can be thought of as a collection of identical and independent photons. The thermal state ρ_{th} has the property that its variance is greater than its mean $\bar{n}$, indicative of a chaotic light source. Lastly, the photon number state $|n\rangle$ has a variance strictly equal to zero. This behaviour is often referred to as sub-Poissonian [35].

Hanbury Brown and Twiss (HBT) arrangement

Next, we will discuss how we can measure $g^{(2)}(0)$ in experiment. We use a Hanbury Brown and Twiss (HBT) configuration [36], which splits an incoming light beam into two, with

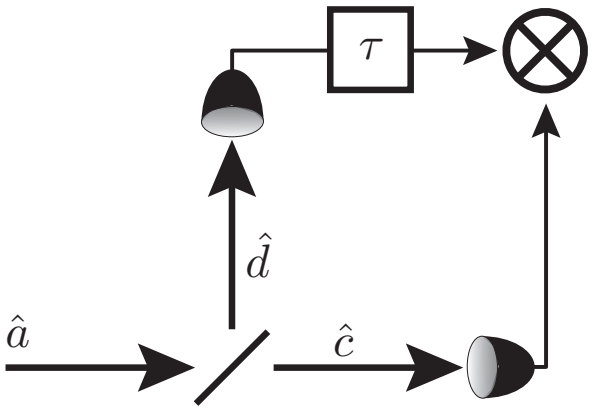

Figure 2.4: A 50:50 beamsplitter splits an incoming light beam in mode a. The two output ports, c and d, are each detected and coincidence detections, as a function of a time delay τ in one arm, are counted.

equal intensities, which are then incident on two detectors. This is shown in Figure 2.4. When the output ports, labelled with ladder operators $\hat{c}$ and $\hat{d}$, are detected, we look at coincidence detections as a function of a timing delay τ in one arm. The experiment then measures the expectation value $\langle \hat{c}^\dagger \hat{d}^\dagger(\tau)\hat{c}\hat{d}(\tau)\rangle$. Propagating this backwards through the beamsplitter we can find an expression in terms of the input mode $\hat{a}$,

$$\left\langle \hat{c}^\dagger \hat{d}^\dagger(\tau)\hat{c}\hat{d}(\tau)\right\rangle \rightarrow \left\langle \frac{(\hat{a}^\dagger - \hat{b}^\dagger)}{\sqrt{2}}\frac{(\hat{a}^\dagger(\tau) + \hat{b}^\dagger(\tau))}{\sqrt{2}}\frac{(\hat{a} - \hat{b})}{\sqrt{2}}\frac{(\hat{a}(\tau) + \hat{b}(\tau))}{\sqrt{2}}\right\rangle \tag{2.59}$$

$$= \frac{1}{4}\left\langle \hat{a}^\dagger \hat{a}^\dagger(\tau)\hat{a}\hat{a}(\tau)\right\rangle \tag{2.60}$$

where in the second step we have dropped any term with $\hat{b}$ or $\hat{b}^\dagger$ since we are assuming that the b mode is the vacuum. Eq. 2.60 gives us the numerator of the $g^{(2)}(\tau)$ function. A single photon, for which $g^{(2)}(0) = 0$, will never produce a coincidence detection. We can normalize it by dividing the coincidence rate by the number of single detections in each arm, $\langle \hat{c}^\dagger \hat{c}\rangle \rightarrow \langle \hat{a}^\dagger \hat{a}\rangle/2$, and $\langle \hat{d}^\dagger(\tau)\hat{d}(\tau)\rangle \rightarrow \langle \hat{a}^\dagger(\tau)\hat{a}(\tau)\rangle/2$. The measured $g^{(2)}(0)$ is then

$$g^{(2)}(0) = \frac{N_{c\&d}}{N_c N_d} \tag{2.61}$$

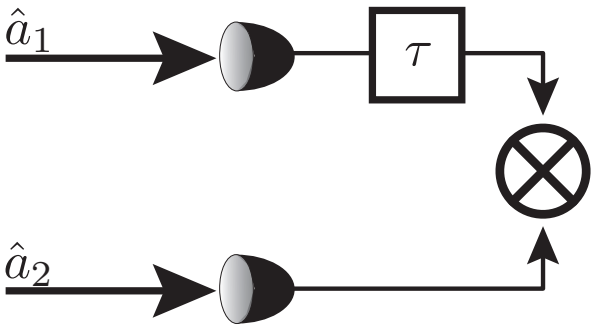

Figure 2.5: Using coincident photon detections in modes 1 and 2, we can tell if the statistical correlations between two light fields is beyond what is allowed classically.

where N_i is the number of detections in mode i. In our experiments we produce photons in pairs, detecting one of them to trigger the experiment. We then incorporate the trigger detection into our $g^{(2)}(0)$ calculation as

$$g^{(2)}(0) = \frac{N_{c\&d\&t} N_t}{N_{c\&t} N_{d\&t}} \tag{2.62}$$

In order to accumulate statistically significant results we must measure many three-fold coincidences, which can take a long time. There is another, faster avenue.

Cross-correlation between two light fields

There is another distinction we can make between classical and quantum states of light. As we will explore further in an upcoming section, pairs of photons generated by spontaneous parametric downconversion possess strong timing correlations. By detecting the pair of photons in coincidence, shown in Figure 2.5, we can determine if a cross-correlative version of the $g^{(2)}$ function lies outside of a classical limit.

We define the normalized cross-correlative second-order coherence function between light fields in modes 1 and 2 as

$$g^{(2)}_{1,2}(\tau) = \frac{\langle I_1(t+\tau) I_2(t) \rangle}{\langle I_1(t) \rangle \langle I_2(t) \rangle}, \tag{2.63}$$

where τ is a timing delay between the two detection events. Clauser [37] showed that classically the numerator of this function obeys a Cauchy-Schwarz inequality. In general, the Cauchy-Schwarz inequality requires that inner products obey $\langle f|g\rangle^2 \leq \langle f|f\rangle\langle g|g\rangle$. We then have that

$$\langle I_1(t)I_2(t)\rangle^2 \leq \langle I_1(t)I_1(t)\rangle \langle I_2(t)I_2(t)\rangle . \tag{2.64}$$

Notice that the right side of this inequality has the numerators of the $g^{(2)}(0)$ functions for modes 1 and 2. Dividing each side by $\langle I_1(t)\rangle \langle I_2(t)\rangle$ we find a classical upper bound for $g^{(2)}_{1,2}(0)$,

$$g^{(2)}_{1,2}(0) \leq \sqrt{g^{(2)}_1(0)g^{(2)}_2(0)} \tag{2.65}$$

where the subscripts on the right side of the inequality refer to the $g^{(2)}(0)$ function, as defined in the previous section, for modes 1 and 2. The quantum version of this function is

$$g^{(2)}_{1,2}(\tau) = \frac{\left\langle \hat{a}^\dagger_1(\tau)\hat{a}_1(\tau)\hat{a}^\dagger_2\hat{a}_2 \right\rangle}{\left\langle \hat{a}^\dagger_1\hat{a}_1 \right\rangle \left\langle \hat{a}^\dagger_2\hat{a}_2 \right\rangle} \tag{2.66}$$

which is unbounded from above. In terms of measured counts, we get that $g^{(2)}_{1,2}(0) = N_{1,2}/N_1N_2$. As an example, let's consider a photon pair generated by spontaneous parametric downconversion. The joint quantum state of the two light fields produced takes the form $|00\rangle + \xi|11\rangle + \xi^2|22\rangle + ...$ (as we will see in Section 2.6), but if one of the two modes is ignored the other takes the form of a thermal state ρ_{th}. The classical limit, or right-hand-side of the inequality, would then be 2, since $g^{(2)}_{\text{th}}(0) = 2$. In contrast, the output of a realistic SPDC photon source can easily have $g^{(2)}_{1,2}(0) \sim 100$. Because this measurement only requires two coincident detections, rather than three, statistically significant results can be collected much quicker. As such, this measurement is frequently used over the "three-click" version [38, 39, 40].

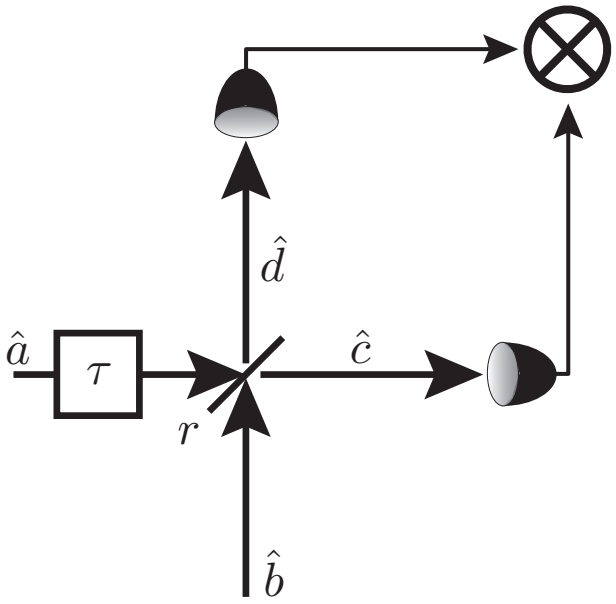

Figure 2.6: Hong-Ou-Mandel (HOM) interference occurs between two indistinguishable photons arriving at the beamsplitter, with reflectivity r, from input ports a and b. Signatures of HOM interference can be observed by measuring coincident detections in output ports c and d.

2.5 Hong-Ou-Mandel (HOM) interference

Hong-Ou-Mandel (HOM) interference occurs when two indistinguishable photons from different input ports are incident on a beamsplitter. If we measure coincidence detections between the two output ports, we find that coincidence detections drop to zero when the two photons hit the beamsplitter at the same time. Classically, in this context, only a 50% drop can be attained, making HOM interference one of the hallmark quantum optical effects. Making two photons interact with one another is generally very difficult, so this type of two-photon interference is the basis for many linear optical quantum computing protocols [41].

2.5.1 HOM dip

Suppose the two-photon state $|\psi\rangle = \iint d\omega_1 d\omega_2 f(\omega_1,\omega_2) e^{i\omega_1\tau}|\omega_1\rangle_a|\omega_2\rangle_b$ is incident on a beamsplitter of reflectivity r (transmittivity t, such that $r^2+t^2=1$), where $f(\omega_1,\omega_2)$ is the joint spectral function, there is a time delay of τ on photon 1, and where the photons are initially in spatial modes a and b. Here we have shifted notation. Instead of showing the numbers of photons in the signal and idler modes, the kets now refer to single photons with frequencies ω_s and ω_i. The state is transformed as

$$
\begin{aligned}
|\psi\rangle &= \iint d\omega_1 d\omega_2 f(\omega_1,\omega_2) e^{i\omega_1\tau}\hat{a}^\dagger(\omega_1)\hat{b}^\dagger(\omega_2)|00\rangle && (2.67)\\
&\rightarrow \iint d\omega_1 d\omega_2 f(\omega_1,\omega_2) e^{i\omega_1\tau}[t\hat{c}^\dagger(\omega_1)+r\hat{d}^\dagger(\omega_1)][t\hat{d}^\dagger(\omega_2)-r\hat{c}^\dagger(\omega_2)]|00\rangle && (2.68)\\
&= \iint d\omega_1 d\omega_2 f(\omega_1,\omega_2) e^{i\omega_1\tau}(t^2|\omega_1\rangle_c|\omega_2\rangle_d - r^2|\omega_2\rangle_c|\omega_1\rangle_d \\
&\qquad\qquad -rt|\omega_1,\omega_2\rangle_c|0\rangle_d + rt|0\rangle_c|\omega_1,\omega_2\rangle_d) && (2.69)
\end{aligned}
$$

The term $|\omega_1,\omega_2\rangle_c|0\rangle_d$ implies that there are two photons in the same spatial mode with different frequencies. The probability of a coincidence measurement in ports c and d has the form

$$
P_{c\&d} = \iint d\omega d\omega' \langle \hat{c}^\dagger(\omega)\hat{c}(\omega)\hat{d}^\dagger(\omega')\hat{d}(\omega')\rangle \qquad (2.70)
$$

We can evaluate it, noticing that the last two terms in Equation 2.69 are will not contribute,

$$P_{c\&d} = \iint d\omega d\omega' \langle\psi| \iint d\omega_1 d\omega_2 f(\omega_1,\omega_2) e^{i\omega_1\tau} \tag{2.71}$$
$$\times \left[t^2\delta(\omega-\omega_1)\delta(\omega'-\omega_2)|\omega_1\rangle_c|\omega_2\rangle_d - r^2\delta(\omega-\omega_2)\delta(\omega'-\omega_1)|\omega_2\rangle_c|\omega_1\rangle_d\right]$$
$$= \iint d\omega_1 d\omega_2 f(\omega_1,\omega_2) e^{i\omega_1\tau}\langle\psi| \left(t^2|\omega_1\rangle_c|\omega_2\rangle_d - r^2|\omega_2\rangle_c|\omega_1\rangle_d\right) \tag{2.72}$$

Substituting in $\langle\psi|$ we continue,

$$P_{c\&d} = \iiiint d\omega_1' d\omega_2' d\omega_1 d\omega_2 f^*(\omega_1',\omega_2') f(\omega_1,\omega_2) e^{i(\omega_1-\omega_1')\tau} \tag{2.73}$$
$$\times \left(t^2\langle\omega_1'|_c\langle\omega_2'|_d - r^2\langle\omega_2'|_c\langle\omega_1'|_d\right) \times \left(t^2|\omega_1\rangle_c|\omega_2\rangle_d - r^2|\omega_2\rangle_c|\omega_1\rangle_d\right)$$

$$= \iiiint d\omega_1' d\omega_2' d\omega_1 d\omega_2 f^*(\omega_1',\omega_2') f(\omega_1,\omega_2) e^{i(\omega_1-\omega_1')\tau} \tag{2.74}$$
$$\times \left[(t^4+r^4)\delta(\omega_1'-\omega_1)\delta(\omega_2'-\omega_2) - 2r^2t^2\delta(\omega_1'-\omega_2)\delta(\omega_2'-\omega_1)\right]$$

$$= \iint d\omega_1 d\omega_2 \left[(t^4+r^4)|f(\omega_1,\omega_2)|^2 - 2r^2t^2 f^*(\omega_2,\omega_1) f(\omega_1,\omega_2) e^{i(\omega_1-\omega_2)\tau}\right] \tag{2.75}$$

We will assume that the joint spectral amplitude is invariant under exchange of its arguments, $f(\omega_1,\omega_2) = f(\omega_2,\omega_1)$. This simplifies the coincidence rate to

$$P_{c\&d} = t^4 + r^4 - 2r^2t^2 \iint d\omega_1 d\omega_2 |f(\omega_1,\omega_2)|^2 e^{i(\omega_1-\omega_2)\tau} \tag{2.76}$$

where we have used the fact that $\iint d\omega d\omega' |f(\omega,\omega')|^2 = 1$. We note that both integrations are over all frequencies, meaning that each pair of frequencies ω_1 and ω_2 is counted twice. We group these re-occurring pairs together, and divide the whole integral by 2 to compensate for double counting. We find that

$$P_{c\&d} = t^4 + r^4 - r^2t^2 \iint d\omega_1 d\omega_2 |f(\omega_1,\omega_2)|^2 (e^{i(\omega_1-\omega_2)\tau} + e^{-i(\omega_1-\omega_2)\tau}) \tag{2.77}$$
$$= t^4 + r^4 - 2r^2t^2 \iint d\omega_1 d\omega_2 |f(\omega_1,\omega_2)|^2 \cos[(\omega_1-\omega_2)\tau] \tag{2.78}$$
$$= (t^2-r^2)^2 + 4r^2t^2 \iint d\omega_1 d\omega_2 |f(\omega_1,\omega_2)|^2 \sin^2\left[\frac{(\omega_1-\omega_2)}{2}\tau\right] \tag{2.79}$$

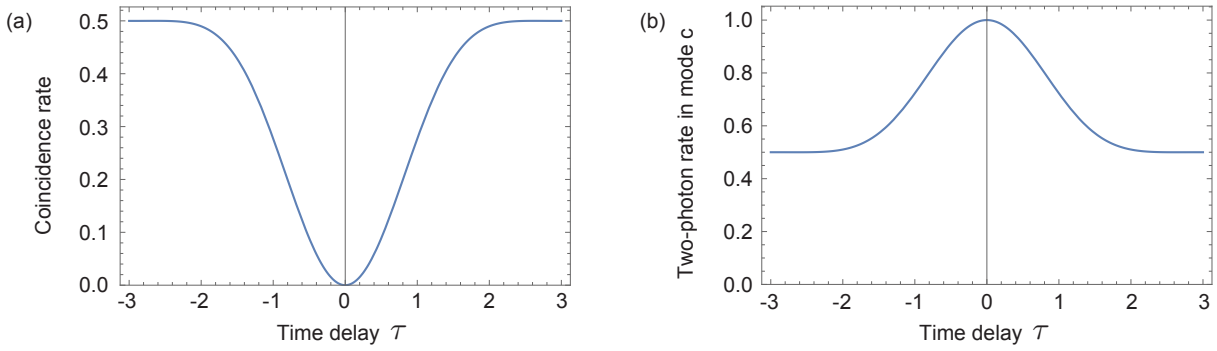

Figure 2.7: (a) The coincidence detection rate between output modes c and d as a function of the delay between the photon arrival times at the beamsplitter, τ. The dip in coincidences is due to Hong-Ou-Mandel interference. (b) The two-photon detection rate in one of the output modes, c, as a function of the difference between photon arrival times, τ. The peak in two-photon events is also due to Hong-Ou-Mandel interference. Both (a) and (b) are calculated using a 50-50 beamsplitter, and separable Gaussian spectral functions.

where in the last step we used the trigonometric identity $\cos 2\theta = 1 - 2\sin^2\theta$. When the delay τ is away from zero, we observe a constant coincidence rate of $t^4 + r^4$. When the delay τ equals zero, the integral term disappears leaving just the $(t^2 - r^2)^2$ term. This produces the characteristic HOM dip, see Figure 2.7(a). For a 50-50 beamsplitter, i.e., $r = t$, the whole coincidence rate goes to zero at $\tau = 0$. We also see that in order for complete destructive interference to occur, the joint spectral function of the input state, $f(\omega_1, \omega_2)$ must be compatible. We will discuss this more in Section 2.6.4.

A figure of merit for the quality of interference between two photons is the visibility of the HOM dip. Ideally, the visibility reaches 100% for a perfectly indistinguishable single photons. As we will see here though, the visibility of the dip also depends on the reflectivity of the beamsplitter. We define the dip visibility as the amplitude of the dip divided by the baseline coincidence rate when the delay is far from zero. Note that this is different than the traditional definition of visibility in signal analysis: the signal amplitude divided by the average. As we can see from Eq. 2.79, when $|\tau| \gg 0$, the integral evaluates to $1/2$ and the baseline coincidence rate is $t^4 + r^4$. At $\tau = 0$ the integral term is zero and so the

amplitude of the dip is $t^4 + r^4 - (t^2 - r^2)^2 = 2r^2t^2$. The dip visibility is then

$$V = \frac{2r^2t^2}{t^4 + r^4} \tag{2.80}$$

which equals 1 for $t = r$, but falls off as the beamsplitter deviates from 50-50. This is not usually a concern since beamsplitters can be manufactured with reflectivities close to 50%. However, in Chapter 8 we will explore the quantum memory in analogy to a beamsplitter between photon and phonon modes. We use it to observe HOM interference between a stored photon and a second incoming photon, however the "reflectivity" of the memory beamsplitter falls short of 50%. In the next section we will look at another way to observe HOM interference that does not depend on the beamsplitter reflectivity.

2.5.2 HOM peak

Suppose we only had access to one of the output ports from the beamsplitter, say the c mode. We would then no longer be able to observe HOM interference using coincidence counting. Fortunately though we can still observe HOM interference by looking for an increase in two-photon events in our lone output port. This can be done using a photon-number resolving detector. As the input photons become indistinguishable and interference occurs, there will be an increase in the amplitudes of the $|20\rangle$ and $|02\rangle$ states. The evidence of HOM interference would then no longer be a dip, but a peak.

We will go through similar math to the above section on the HOM dip, but this time look at two-photon events in mode c. The two-photon detection rate, P_{2c}, can be found

using the state of Equation 2.69,

$$
\begin{aligned}
P_{2c} &= \iint d\omega d\omega' \langle \hat{c}^\dagger(\omega)\hat{c}^\dagger(\omega')\hat{c}(\omega)\hat{c}(\omega')\rangle && (2.81)\\
&= -rt \iint d\omega d\omega' \langle\psi| \iint d\omega_1 d\omega_2 f(\omega_1,\omega_2)e^{i\omega_1\tau} && (2.82)\\
&\quad \times \left[\delta(\omega-\omega_1)\delta(\omega'-\omega_2)+\delta(\omega'-\omega_1)\delta(\omega-\omega_2)\right]|\omega_1,\omega_2\rangle_c|0\rangle_d \\
&= -2rt\langle\psi| \iint d\omega_1 d\omega_2 f(\omega_1,\omega_2)e^{i\omega_1\tau}|\omega_1,\omega_2\rangle_c|0\rangle_d && (2.83)\\
&= 2r^2t^2 \iiiint d\omega_1 d\omega_2 d\omega_1' d\omega_2' f^*(\omega_1',\omega_2')f(\omega_1,\omega_2)e^{i(\omega_1-\omega_1')\tau} && (2.84)\\
&\quad \times \langle\omega_1',\omega_2'|\omega_1,\omega_2\rangle_c\langle 0|0\rangle_d \\
&= 2r^2t^2 \iiiint d\omega_1 d\omega_2 d\omega_1' d\omega_2' f^*(\omega_1',\omega_2')f(\omega_1,\omega_2)e^{i(\omega_1-\omega_1')\tau} && (2.85)\\
&\quad \times \left[\delta(\omega_1'-\omega_1)\delta(\omega_2'-\omega_2)+\delta(\omega_1'-\omega_2)\delta(\omega_2'-\omega_1)\right] \\
&= 2r^2t^2 \iint d\omega_1 d\omega_2 |f(\omega_1,\omega_2)|^2 \times \left[1+e^{i(\omega_1-\omega_2)\tau}\right] && (2.86)
\end{aligned}
$$

where in the last step we made the same assumption about the invariance of the joint spectral function as for the HOM dip calculation. Next, just as for the HOM dip, we collect terms with the same pairs of frequencies and account for double counting with a 1/2 factor,

$$
\begin{aligned}
P_{2c} &= 2r^2t^2 + 2r^2t^2 \iint d\omega_1 d\omega_2 |f(\omega_1,\omega_2)|^2 \cos\left[(\omega_1-\omega_2)\tau\right] && (2.87)\\
&= 4r^2t^2 \iint d\omega_1 d\omega_2 |f(\omega_1,\omega_2)|^2 \cos^2\left[\frac{(\omega_1-\omega_2)}{2}\tau\right] && (2.88)
\end{aligned}
$$

where in the last step we used the trigonometric identity $\cos 2\theta = 2\cos^2\theta - 1$. What we see here is very similar to the HOM dip. Away from $\tau = 0$ there is baseline two-photon detection rate of $2r^2t^2$. At $\tau = 0$ the integral evaluates to 1 giving a two-photon rate of $4r^2t^2$, and producing the HOM peak. This is shown in Figure 2.7(b). We can see that the visibility of the peak, using the same definition as for the dip, is

$$
\begin{aligned}
V &= \frac{4r^2t^2 - 2r^2t^2}{2r^2t^2} \\
&= 1 && (2.89)
\end{aligned}
$$

Importantly, the visibility of the HOM peak is always 1 regardless of the reflectivity of the beamsplitter, assuming perfect spectral overlap. This means that the two-photon rate will always double at $\tau = 0$. In this scenario there is also a 50% limit on the interference visibility of classical light.

2.5.3 Interference between a single photon and a coherent state

In Chapter 8 we investigate HOM interference between a single photon and a coherent state of phonons stored in the quantum memory. For a weak coherent state with average photon $|\alpha|^2 \ll 1$, the single photon component of $|\alpha\rangle$ dominates and HOM interference can be observed [42]. In Appendix C we derive both the HOM dip and peak for interference between a single photon and a coherent state. Here, we will look at the two limiting cases for interference, i.e., when $\tau = 0$ and when τ is far from zero. We expect to find that both the dip and peak visibilities depends on the average photon number of the coherent state, $|\alpha|^2$, with decreasing visibility as $|\alpha|^2$ increases.

HOM dip with a photon and coherent state

When a coherent state $|\alpha\rangle_b$ is incident from mode b onto a beamsplitter, the state is split into modes c and d as $|-r\alpha\rangle_c|t\alpha\rangle_d$, where the output amplitudes are determined by the beamsplitter reflectivity r and transmittivity t. A single photon $|1\rangle_a$ entering the beamsplitter from mode a is transformed in the usual way giving the joint state

$$|1\rangle_a|\alpha\rangle_b \quad \rightarrow \quad (t\hat{c}^\dagger + r\hat{d}^\dagger)|-r\alpha\rangle_c|t\alpha\rangle_d. \tag{2.90}$$

For the HOM dip we look at coincidence detections between modes c and d,

$$\begin{aligned}
\langle \hat{c}^\dagger \hat{c} \hat{d}^\dagger \hat{d} \rangle &= \langle -r\alpha|_c \langle t\alpha|_d \left(t\hat{c} + r\hat{d}\right) \hat{c}^\dagger \hat{c} \hat{d}^\dagger \hat{d} \left(t\hat{c}^\dagger + r\hat{d}^\dagger\right) |-r\alpha\rangle_c |t\alpha\rangle_d && (2.91) \\
&= \langle -r\alpha|_c \langle t\alpha|_d \left[t^2 \hat{c}\hat{c}^\dagger \hat{c}\hat{c}^\dagger \hat{d}^\dagger \hat{d} + rt(\hat{c}\hat{c}^\dagger \hat{c}\hat{d}^\dagger \hat{d}\hat{d}^\dagger + \hat{c}^\dagger \hat{c}\hat{c}^\dagger \hat{d}\hat{d}^\dagger \hat{d}) + r^2 \hat{c}^\dagger \hat{c} \hat{d}\hat{d}^\dagger \hat{d}\hat{d}^\dagger\right] \\
&\qquad \times |-r\alpha\rangle_c |t\alpha\rangle_d && (2.92)
\end{aligned}$$

Using the commutation relations $[\hat{c}, \hat{c}^\dagger] = 1$ and $[\hat{d}, \hat{d}^\dagger] = 1$, we find the normal ordering of each term

$$
\begin{aligned}
t^2\hat{c}\hat{c}^\dagger\hat{c}\hat{c}^\dagger\hat{d}^\dagger\hat{d} &= t^2(1 + 3\hat{c}^\dagger\hat{c} + \hat{c}^\dagger\hat{c}^\dagger\hat{c}\hat{c})\hat{d}^\dagger\hat{d} && (2.93)\\
rt\hat{c}\hat{c}^\dagger\hat{c}\hat{d}^\dagger\hat{d}\hat{d}^\dagger &= rt(\hat{c} + \hat{c}^\dagger\hat{c}\hat{c})(\hat{d}^\dagger + \hat{d}^\dagger\hat{d}^\dagger\hat{d}) && (2.94)\\
rtc^\dagger\hat{c}\hat{c}^\dagger\hat{d}\hat{d}^\dagger\hat{d} &= rt(\hat{c}^\dagger + \hat{c}^\dagger\hat{c}^\dagger\hat{c})(\hat{d} + \hat{d}^\dagger\hat{d}\hat{d}) && (2.95)\\
r^2\hat{c}^\dagger\hat{c}\hat{d}\hat{d}^\dagger\hat{d}\hat{d}^\dagger &= r^2\hat{c}^\dagger\hat{c}(1 + 3\hat{d}^\dagger\hat{d} + \hat{d}^\dagger\hat{d}^\dagger\hat{d}\hat{d}) && (2.96)
\end{aligned}
$$

The coincidence rate becomes

$$
\begin{aligned}
\langle\hat{c}^\dagger\hat{c}\hat{d}^\dagger\hat{d}\rangle &= t^2\left(t^2|\alpha|^2 + 3r^2t^2|\alpha|^4 + r^4t^2|\alpha|^6\right)\\
&\quad + r^2\left(r^2|\alpha|^2 + 3r^2t^2|\alpha|^4 + r^2t^4|\alpha|^6\right)\\
&\quad + rt\left(-r\alpha - r^3\alpha|\alpha|^2\right)\left(t\alpha^* + t^3\alpha^*|\alpha|^2\right)\\
&\quad + rt\left(-r\alpha^* - r^3\alpha^*|\alpha|^2\right)\left(t\alpha + t^3\alpha|\alpha|^2\right) && (2.97)\\
&= \left(t^2 - r^2\right)^2|\alpha|^2 + r^2t^2|\alpha|^4 && (2.98)
\end{aligned}
$$

where all the $|\alpha|^6$ terms cancel out. Here we see that the HOM interference occurs due to the single-photon term of the coherent state, $\propto |\alpha|^2$, matching our intuition. Again, for $r = t$ this term disappears. Also, we see the coincidence rate increases as the average photon number of the coherent state increases.

Let's now consider the case where no interference occurs, e.g., if the single photon and coherent state arrive at the beamsplitter at different times. We take the coherent state and single photon to be in separate modes, marked by the subscripts 1 and 2 on the ladder operators, such that $\hat{c}_1^\dagger|0,0\rangle = |1,0\rangle_c$ and $\hat{c}_2^\dagger|0,0\rangle = |0,1\rangle_c$. The state after the beamsplitter is

$$
|\psi\rangle = t|1, -r\alpha\rangle_c|0, t\alpha\rangle_d + r|0, -r\alpha\rangle_c|1, t\alpha\rangle_d. \quad (2.99)
$$

To calculate the coincidence rate we sum over the different detection modes

$$
\begin{aligned}
\sum_{i,j}\langle\hat{c}_i^\dagger\hat{c}_i\hat{d}_j^\dagger\hat{d}_j\rangle &= \langle\hat{c}_1^\dagger\hat{c}_1\hat{d}_1^\dagger\hat{d}_1\rangle + \langle\hat{c}_1^\dagger\hat{c}_1\hat{d}_2^\dagger\hat{d}_2\rangle + \langle\hat{c}_2^\dagger\hat{c}_2\hat{d}_1^\dagger\hat{d}_1\rangle + \langle\hat{c}_2^\dagger\hat{c}_2\hat{d}_2^\dagger\hat{d}_2\rangle && (2.100)\\
&= 0 + t^4|\alpha|^2 + r^4|\alpha|^2 + r^2t^2|\alpha|^4 && (2.101)\\
&= (r^4 + t^4)|\alpha|^2 + r^2t^2|\alpha|^4 && (2.102)
\end{aligned}
$$

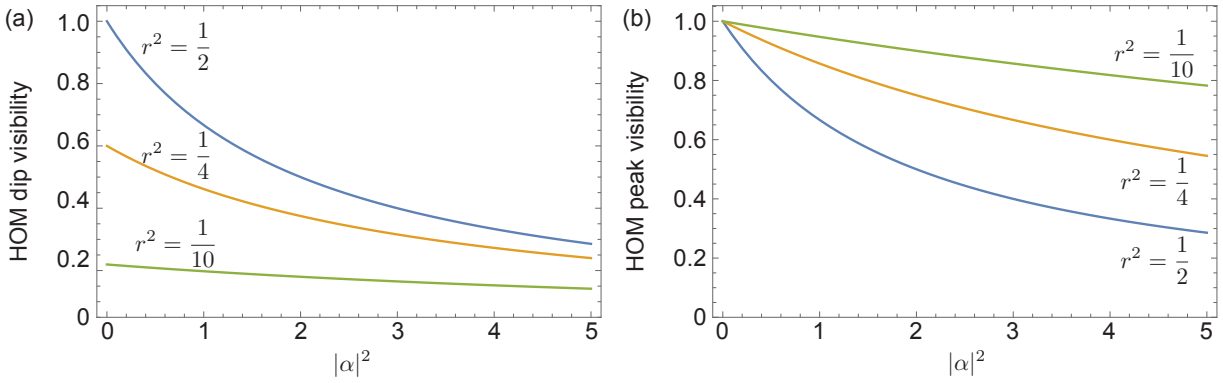

Figure 2.8: The HOM dip (a) and peak (b) visibilities for different beamsplitter reflectivities as a function of the coherent state strength.

We can now evaluate the dip visibility as dip amplitude over the baseline rate,

$$V = \frac{2r^2t^2|\alpha|^2}{(r^4+t^4)|\alpha|^2 + r^2t^2|\alpha|^4} \tag{2.103}$$

For $|\alpha|^2 \ll 1$ we can ignore the $|\alpha|^4$ term and the visibility returns to the same as for the photon-photon case. As we would expect, a higher average photon number in the coherent state degrades the visibility. Figure 2.8(a) shows HOM dip visibility as a function of the average photon number in the coherent state, $|\alpha|^2$, for a few different beamsplitter reflectivities.

HOM peak with a photon and coherent state

We can do the same treatment for the HOM peak. The two-photon detection rate is

$$\langle \hat{c}^\dagger \hat{c}^\dagger \hat{c}\hat{c} \rangle = \langle -r\alpha|_c \langle t\alpha|_d \left(t\hat{c} + r\hat{d}\right) \hat{c}^\dagger \hat{c}^\dagger \hat{c}\hat{c} \left(t\hat{c}^\dagger + r\hat{d}^\dagger\right) | -r\alpha\rangle_c |t\alpha\rangle_d \tag{2.104}$$

$$= \langle -r\alpha|_c \langle t\alpha|_d \left[t^2 \hat{c}\hat{c}^\dagger \hat{c}^\dagger \hat{c}\hat{c}\hat{c}^\dagger + rt(\hat{c}\hat{c}^\dagger \hat{c}^\dagger \hat{c}\hat{c}\hat{d}^\dagger + \hat{c}^\dagger \hat{c}^\dagger \hat{c}\hat{c}\hat{c}^\dagger \hat{d}) + r^2 \hat{c}^\dagger \hat{c}^\dagger \hat{c}\hat{c}\hat{d}\hat{d}^\dagger\right] \times | -r\alpha\rangle_c |t\alpha\rangle_d \tag{2.105}$$

Using commutation relations we can find the normal ordering of each term

$$
\begin{aligned}
t^2\hat{c}\hat{c}^\dagger\hat{c}^\dagger\hat{c}\hat{c}\hat{c}^\dagger &= t^2(4\hat{c}^\dagger\hat{c} + 5\hat{c}^\dagger\hat{c}^\dagger\hat{c}\hat{c} + \hat{c}^\dagger\hat{c}^\dagger\hat{c}^\dagger\hat{c}\hat{c}\hat{c}) && (2.106)\\
rt\hat{c}\hat{c}^\dagger\hat{c}^\dagger\hat{c}\hat{c}\hat{d}^\dagger &= rt(2\hat{c}^\dagger\hat{c}\hat{c} + \hat{c}^\dagger\hat{c}^\dagger\hat{c}\hat{c}\hat{c})\hat{d}^\dagger && (2.107)\\
rt\hat{c}^\dagger\hat{c}^\dagger\hat{c}\hat{c}\hat{c}^\dagger\hat{d} &= rt(2\hat{c}^\dagger\hat{c}^\dagger\hat{c} + \hat{c}^\dagger\hat{c}^\dagger\hat{c}^\dagger\hat{c}\hat{c})\hat{d} && (2.108)\\
r^2\hat{c}^\dagger\hat{c}^\dagger\hat{c}\hat{c}\hat{d}\hat{d}^\dagger &= r^2\hat{c}^\dagger\hat{c}^\dagger\hat{c}\hat{c}(1 + \hat{d}^\dagger\hat{d}) && (2.109)
\end{aligned}
$$

Substituting this into the two-photon rate we get

$$
\begin{aligned}
\langle\hat{c}^\dagger\hat{c}^\dagger\hat{c}\hat{c}\rangle &= t^2\left(4r^2|\alpha|^2 + 5r^4|\alpha|^4 + r^6|\alpha|^6\right) - 2r^4t^2\left(2|\alpha|^4 + r^2|\alpha|^6\right)\\
&\qquad + r^6|\alpha|^4\left(1 + t^2|\alpha|^2\right) && (2.110)\\
&= 4r^2t^2|\alpha|^2 + r^4|\alpha|^4 && (2.111)
\end{aligned}
$$

where the $|\alpha|^6$ term has cancelled out. We see here that the one-photon portion of the coherent state offers us the same interference term as for the photon-photon interference case. We also see that the two-photon rate increases quickly with the higher-order coherent state term, which matches our intuition. Finally, we look at the case where the photon and coherent state do not interfere. To calculate the coincidence rate we sum over the different detection modes to find

$$
\sum_{i,j}\langle\hat{c}_i^\dagger\hat{c}_j^\dagger\hat{c}_i\hat{c}_j\rangle = 2r^2t^2|\alpha|^2 + r^4|\alpha|^4 \qquad (2.112)
$$

This gives a HOM peak visibility of

$$
V = \frac{2r^2t^2|\alpha|^2}{2r^2t^2|\alpha|^2 + r^4|\alpha|^4} \qquad (2.113)
$$

We see again that for low average photon numbers in the coherent state we can ignore the $|\alpha|^4$ term, and the visibility returns to the photon-photon case where the beamsplitter reflectivity does not matter. As the coherent state strength increases the reflectivity of the beamsplitter does become important. This makes sense since a higher reflectivity will introduce more of the coherent state to the detector. In our setup then, a lower reflectivity will preserve the HOM peak visibility for higher coherent state amplitudes. This can be seen in Figure 2.8(b).

2.6 Spontaneous parametric downconversion

In this section we turn to a discussion on nonlinear optics [43] and how we can generate single photons in the lab. In general, nonlinear optics deals with cases where light fields travel through a medium which has a nonlinear response. From Maxwell's equations in a medium we know that the electric field $\vec{E}(z,t)$ is related to the material polarization $\vec{P}(t)$ by

$$\frac{\partial^2}{\partial z^2}E(z,t) - \frac{n^2}{c^2}\frac{\partial^2}{\partial t^2}E(z,t) = \frac{1}{\epsilon_0 c^2}\frac{\partial^2}{\partial t^2}P(z,t). \tag{2.114}$$

where n is the index of refraction in the medium, and where we are only considering beams co-propagating along the z axis. The polarization of the medium has a series expansion in terms of the incident electric field $\vec{P}(t) = \epsilon_0[\chi^{(1)}\vec{E}(t) + \chi^{(2)}\vec{E}^2(t) + \chi^{(3)}\vec{E}^3(t) + ...]$. The quantities $\chi^{(i)}$ are the i^{th}-order susceptibilities which govern the strengths of the linear and nonlinear optics processes. If the electric field incident on the medium is comprised of multiple frequency components, $E(z,t) = \sum_i E_i(z,t)$, where each $E_i(z,t) = A_i e^{ik_i z}e^{-i\omega_i t} +$ c.c., various optical processes can occur. Similarly, the polarization $P(z,t)$ can include different frequency components. In this thesis we will be concerned with both $\chi^{(2)}$ and $\chi^{(3)}$ nonlinear processes. Second-order ($\chi^{(2)}$) materials in our photon source facilitate three-wave mixing such as sum-frequency generation (SFG, sometimes called "upconversion") and spontaneous parametric downconversion (SPDC). The third-order nonlinearity $\chi^{(3)}$ in diamond is responsible for the memory storage process, which we will explore more in Chapter 4. We begin with a discussion on three-wave mixing.

2.6.1 Three-wave mixing

While third-order nonlinearities are very common, second-order nonlinearities only arise in materials, bulk crystals in our context, that are non-centrosymmetric; their crystal lattices lack an inversion centre. The polarization of the medium $\vec{P} = \epsilon_0\chi^{(2)}\vec{E}^2(t)$, and in a centrosymmetric material if we flip the sign of the electric field the polarization must also change sign, $-\vec{P} = \epsilon_0\chi^{(2)}(-\vec{E}(t))^2$. This leads us to $\vec{P} = -\vec{P}$, which requires that

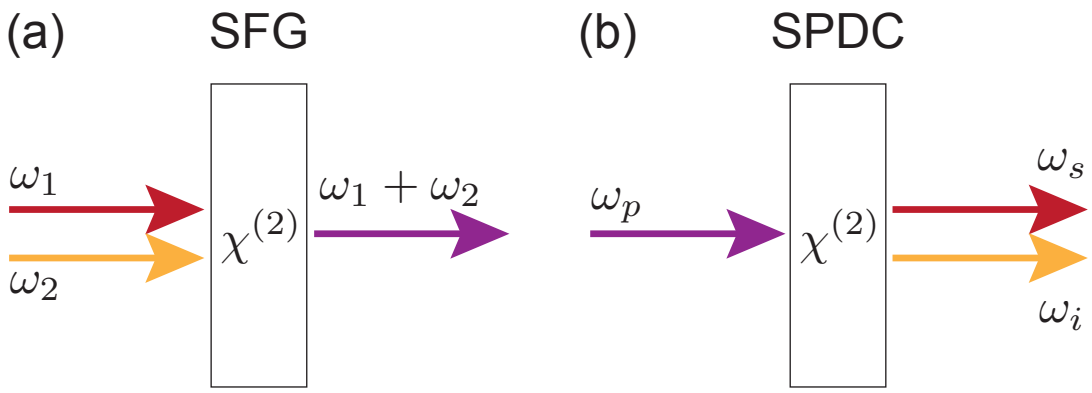

Figure 2.9: (a) Sum-frequency generation (SFG) between two fields of frequencies ω_1 and ω_2 in a $\chi^{(2)}$ nonlinear material produces a field at a third frequency, $\omega_3 = \omega_1 + \omega_2$. (b) Spontaneous parametric downconversion (SPDC) occurs when a higher energy pump photon, frequency ω_p, "splits" into two lower energy photons, called the *signal* and *idler*, with frequencies ω_s and ω_i. Energy conservation requires that $\omega_p = \omega_s + \omega_i$.

$\chi^{(2)} = 0$. (A fuller discussion on this can be found in Chapter 1 of Ref. [43].) The second-order susceptibility tensor, $\chi^{(2)}$, is a 3×6 matrix which maps terms from the expansion of $[E_x(\omega_1) + E_y(\omega_1) + E_z(\omega_1)] \times [E_x(\omega_2) + E_y(\omega_2) + E_z(\omega_2)]$ to the x, y, and z components of the material polarization. Based on the crystal lattice symmetries of a given material the tensor simplifies greatly, and we can consider an effective nonlinearity $\chi^{(2)}_{\text{eff}}$ based on the direction of the propagation in the material.

In sum-frequency generation (see Fig. 2.9(a)) two incident fields at frequencies ω_1 and ω_2 produce a third field at frequency $\omega_3 = \omega_1 + \omega_2$. We take $P(\omega_3) = 2\epsilon_0 \chi^{(2)}_{\text{eff}} E(\omega_1) E(\omega_2)$. Since Eq. 2.114 must hold for each frequency component of the electric field, we first look at the ω_3 equation,

$$\left(\frac{\partial^2}{\partial z^2} - \frac{n^2}{c^2}\frac{\partial^2}{\partial t^2}\right)(A_3 e^{i(k_3 z - \omega_3 t)} + \text{c.c.}) = \frac{2\chi^{(2)}_{\text{eff}}}{c^2}\frac{\partial^2}{\partial t^2}(A_1 e^{i(k_1 z - \omega_1 t)} + \text{c.c.})(A_2 e^{i(k_2 z - \omega_2 t)} + \text{c.c.}) \tag{2.115}$$

This wave equation must also independently hold for the complex conjugate terms, so we

drop them from here on. Working out the partial derivatives we get

$$\left(\frac{\partial^2 A_3}{\partial z^2} + 2ik_3\frac{\partial A_3}{\partial z} - k_3^2 A_3 + \frac{n^2\omega_3^2}{c^2}A_3\right)e^{ik_3 z}e^{-i\omega_3 t} = -\frac{2\chi^{(2)}_{\text{eff}}\omega_3^2}{c^2}A_1 A_2 e^{i(k_1+k_2)z}e^{-i\omega_3 t} \tag{2.116}$$

$$\left(\frac{\partial^2 A_3}{\partial z^2} + 2ik_3\frac{\partial A_3}{\partial z}\right) = -\frac{2\chi^{(2)}_{\text{eff}}\omega_3^2}{c^2}A_1 A_2 e^{i\Delta k z} \tag{2.117}$$

where the A_3 terms cancelled due to the fact that $k = n\omega/c$. We have also defined the phase mismatch $\Delta k = k_1 + k_2 - k_3$. Lastly, we make the slowly varying envelope approximation, $|\frac{\partial^2 A_3}{\partial z^2}| \ll |k_3\frac{\partial A_3}{\partial z}|$, reducing the coupled-wave equation even further. As mentioned above, the wave equation is satisfied for each frequency component of the electric field independently. We then have coupled-wave equations for A_1 and A_2 as well. The collection of all three coupled-wave equations is:

$$\frac{\partial A_1}{\partial z} = \frac{i\chi^{(2)}_{\text{eff}}\omega_1^2}{k_1 c^2}A_3 A_2^* e^{-i\Delta k z} \tag{2.118}$$

$$\frac{\partial A_2}{\partial z} = \frac{i\chi^{(2)}_{\text{eff}}\omega_2^2}{k_2 c^2}A_3 A_1^* e^{-i\Delta k z} \tag{2.119}$$

$$\frac{\partial A_3}{\partial z} = \frac{i\chi^{(2)}_{\text{eff}}\omega_3^2}{k_3 c^2}A_1 A_2 e^{i\Delta k z} \tag{2.120}$$

These equations tell us that the amplitude of the field at frequency ω_3 increases over the length of the material in proportion to the strength of the other two fields at frequencies ω_1 and ω_2. Correspondingly, the amplitudes of the ω_1 and ω_2 components will decrease over the length of the material. Importantly, we can also see from the above coupled-wave equations why the reverse process, spontaneous parametric downconversion, is not possible in the classical theory of nonlinear optics. Downconversion (see Fig.2.9) is the time-reversed version of sum-frequency generation. A pump field with frequency, $\omega_p = \omega_3$, will "split" into two fields of lower frequency components, $\omega_s = \omega_1$ and $\omega_i = \omega_2$, such that $\omega_s + \omega_i = \omega_p$. Here the subscripts s and i refer to the traditional names *signal* and *idler*. (In this thesis the names *idler* and *herald* are used interchangeably.) Initially there is vacuum in the signal and idler modes. Looking at first two coupled-wave equations it is impossible for the signal and idler amplitudes to build up when they depend on non-zero initial amplitudes from one another. We require a new approach.

2.6.2 Downconversion Hamiltonian

A quantum mechanical description for the SPDC has the Hamiltonian

$$\mathcal{H}_{\text{SPDC}} = \int_V d^3r\chi^{(2)}\left\{E_p^{(+)}E_s^{(-)}E_i^{(-)} + E_p^{(-)}E_s^{(+)}E_i^{(+)}\right\} \tag{2.121}$$

$$= -\frac{\chi^{(2)}\hbar\sqrt{\omega_s\omega_i}}{2\epsilon_0 V}\int_V d^3r\tilde{\alpha}_p(t)e^{i\vec{k_p}\cdot\vec{r}} \times\int_0^\infty d\omega_s\hat{a}^\dagger(\omega_s)e^{-i(\vec{k_s}\cdot\vec{r}-\omega_s t)}\times\int_0^\infty d\omega_i\hat{a}^\dagger(\omega_i)e^{-i(\vec{k_i}\cdot\vec{r}-\omega_i t)} + \text{h.c.} \tag{2.122}$$

where the Hamiltonian integrates over the interaction volume, i.e., the nonlinear crystal, and where we have substituted in Eqs. 2.16 and 2.17 in the signal and idler modes. We have also pulled the slowly varying envelope portion of the photon fields, $\hbar\sqrt{\omega_s\omega_i}/2\epsilon_0 V$, out of the integral. We take the pump field to be a classical transform-limited Gaussian pulse with envelope $\tilde{\alpha}_p(t) = e^{-t^2/4\sigma_p^2}$. The interaction time of the Hamiltonian is therefore determined by the temporal length of the pump pulse [44]. We will also assume that the pump field is undepleted by the downconversion process.

2.6.3 Phase matching

In order for the downconversion process to be efficient we must also have momentum conservation, or phase matching, between the pump and downconverted fields,

$$\vec{k}_p \approx \vec{k}_s + \vec{k}_i \tag{2.123}$$

When this condition is met the phases of the three waves involved will constructively interfere as the pump field propagates through the nonlinear medium. This condition allows for downconverted photons to be emitted in a conical pattern about the pump propagation axis [45]. Here we are interested in a simple case for the generated photons' directions: we would like them to be emitted collinearly in the same direction as the input pump pulse. We take the pump, signal and idler momenta to be solely in the z direction:

$\vec{k}_j = k_j \hat{z}$. The Hamiltonian then simplifies to

$$\mathcal{H}_{\text{SPDC}} = -\frac{\chi^{(2)}\hbar\sqrt{\omega_s\omega_i}}{2\epsilon_0 V}\iint_0^\infty d\omega_s d\omega_i \int_0^L dz e^{i\Delta kz}\tilde{\alpha}_p(t)e^{i(\omega_s+\omega_i)t}\hat{a}^\dagger(\omega_s)\hat{a}^\dagger(\omega_i) + \text{h.c.} \tag{2.124}$$

where the integration over the interaction region is limited by the crystal dimension, length L in the z direction. We have also re-written the phase mismatch as $\Delta k = k_p - k_s - k_i$, and define a phase matching function $\phi(\omega_p, \omega_s, \omega_i)$ as

$$\phi(\omega_p, \omega_s, \omega_i) = \int_0^L dz e^{i\Delta kz} \tag{2.125}$$

$$= Le^{i\Delta kL/2}\text{sinc}\frac{\Delta kL}{2}. \tag{2.126}$$

Each momentum term incorporates the dispersion in the nonlinear medium, $k_j = n(\omega_j)\omega_j/c$. We can also begin to see the important role that the medium length plays in our photon source. The width of the $\text{sinc}(\Delta kL/2)$ function will determine the bandwidth of our downconverted photons. Shorter crystals (small L) result in a broader photon spectrum. However, a greater medium length will increase the amplitude of the downconverted state and increase our photon rates.

Due to material dispersion, phase matching does not come for free. One way to engineer a phase-matched process is to use a birefringent medium to compensate for the dispersion relation. The photon source in this work employs collinear type-I phase matching, meaning that an extraordinarily-polarized pump photon downconverts to two ordinarily-polarized daughter photons. We will find that for the photon frequencies we are interested in that we can use a very common nonlinear material, a β-barium borate crystal.

β-Barium Borate

BBO is a *negative* uniaxial crystal, meaning that the ordinary index of refraction $n_o > n_E$, the extraordinary index. This implies that extraordinary polarized light will travel faster through the medium than ordinary polarized light. Figure 2.10 shows an example of a

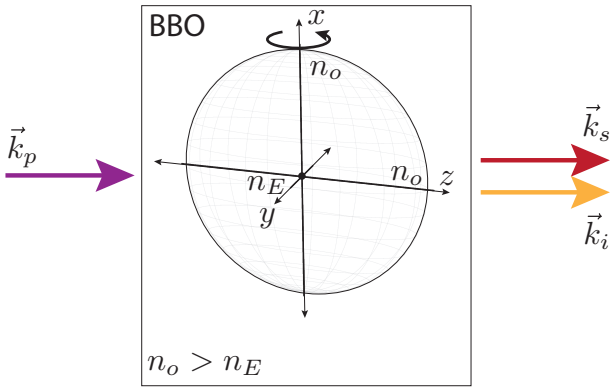

Figure 2.10: The pump field enters the nonlinear crystal BBO with wavevector momentum $\vec{k}_p$. Inside the box shows the refractive index ellipsoid for a negative uniaxial crystal, such as BBO. The indices of refraction in the x and z directions are ordinary, n_o, while the index in the y direction is extraordinary, n_E. Phase matching conditions be achieved by rotating the crystal about the x-axis producing the output fields marked by $\vec{k}_s$ and $\vec{k}_i$.

negative uniaxial crystal. For an incident beam propagating along the z-axis, we can tune the effective extraordinary index by tilting the crystal about the x-axis. For a rotation by an angle θ, the effective extraordinary index, $n_e(\theta)$ follows

$$\frac{1}{n_e^2} = \frac{\cos^2\theta}{n_o^2} + \frac{\sin^2\theta}{n_E^2}. \tag{2.127}$$

The ordinary and extraordinary indices at the relevant wavelengths can be found using the Sellmeier equation,

$$n_i^2 = A_i + \frac{B_i}{\lambda^2 - C_i} + D_i\lambda^2 \tag{2.128}$$

where the coefficients for the ordinary and extraordinary indices of refraction shown in Table 2.6.3 were provided by the crystal manufacturer (Newlight Photonics [46]). The relevant wavelengths for our photon source are 400 nm (pump), 723 nm (signal), 895 nm (idler). By substituting in the values of the refractive index for each wavelength, we find that a crystal angle of $\theta = 29.1°$ minimizes Δk.

	Ordinary	Extraordinary
A	2.7359	2.3753
B	0.01878	0.01224
C	0.01822	0.01667
D	0.01354	0.01516

Table 2.2: Sellmeier coefficients for BBO.

2.6.4 Downconverted state

The quantum state coming out of downconversion is shown below. We take the interaction Hamiltonian, Eq. 2.124, and evaluate the evolution of the signal and idler modes, which we initially take to be the vacuum.

$$|\Psi(t)\rangle = e^{-\frac{i}{\hbar}\int_0^t dt' \mathcal{H}_{\text{SPDC}}(t')}|\Psi(0)\rangle \tag{2.129}$$

$$= \left(\mathbb{1} - \frac{i}{\hbar}\int_0^t dt' \mathcal{H}_{\text{SPDC}}(t') + ...\right)|0_s\rangle|0_i\rangle \tag{2.130}$$

We will only be interested in the second term. Our experimental results depend on photon detection, and so the vacuum component is removed. While higher-order terms involving two or more photons do occur, in the experiments we discuss in this thesis the photon rates are sufficiently low such that multi-pair emissions from the photon sources are not a dominating source of error. The second-order term is then

$$|\Psi^{(2)}(t)\rangle = i\frac{\chi^{(2)}\sqrt{\omega_s\omega_i}}{2\epsilon_0 V}\int_0^t dt' \iint_0^\infty d\omega_s d\omega_i \phi(\omega_s,\omega_i)\tilde{\alpha}_p(t')e^{i(\omega_s+\omega_i)t'}|\omega_s\rangle|\omega_i\rangle \tag{2.131}$$

Since the Hamiltonian is a function of the pump envelope timing, the interaction only occurs when the pump envelope is nonzero. This allows us to expand the limits of the temporal integral to be over all time [44]. We also take the Fourier transform of the pump envelope $\tilde{\alpha}_p(t') = \int d\omega_p \alpha_p(\omega_p)e^{-i\omega_p t}$. The state becomes

$$|\Psi^{(2)}(t)\rangle = i\frac{\chi^{(2)}\sqrt{\omega_s\omega_i}}{2\epsilon_0 V}\iiint_0^\infty d\omega_p d\omega_s d\omega_i \alpha_p(\omega_p)\phi(\omega_s,\omega_i)\int_{-\infty}^\infty dt' e^{-i(\omega_p-\omega_s-\omega_i)t'}|\omega_s\rangle|\omega_i\rangle \tag{2.132}$$

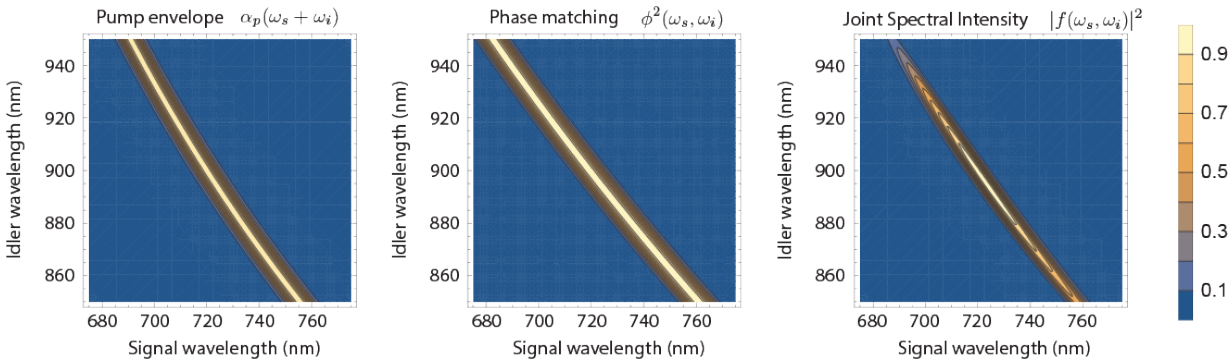

Figure 2.11: The calculated pump envelope, phase matching function, and joint spectral intensity about the relevant signal (723 nm) and idler (895 nm) wavelengths in our photon source. The 400 nm pump beam has a 1.3 nm bandwidth. The phase matching function is calculated for type-I collinear downconversion in a 1 mm BBO crystal. The resulting joint spectrum has strong anti-correlations between the signal and idler wavelengths.

The time integral in Eq. 2.134 can be evaluated to give $2\pi\delta(\omega_p - \omega_s - \omega_i)$. Physically, this enforces the conservation of energy in the downconversion process. The energies of the signal and idler photons must add to a frequency that is within the spectrum of the pump pulse. This leads to an anti-correlation between signal and idler frequencies that is stronger for narrow bandwidth pump fields. Next we perform the integration over the pump frequency which gives the state

$$|\Psi^{(2)}\rangle = i\frac{\pi\chi^{(2)}\sqrt{\omega_s\omega_i}}{\epsilon_0 V}\iint_0^\infty d\omega_s d\omega_i \alpha_p(\omega_s+\omega_i)\phi(\omega_s,\omega_i)|\omega_s\rangle|\omega_i\rangle \tag{2.133}$$

$$= \mathcal{N}\int d\omega_s d\omega_i f(\omega_s,\omega_i)|\omega_s,\omega_i\rangle \tag{2.134}$$

where we have rewritten the coefficients as a normalization factor $\mathcal{N}$. The function $f(\omega_s,\omega_i) = \alpha_p(\omega_s+\omega_i)\times\phi(\omega_s,\omega_i)$ is the joint spectral amplitude (JSA). In Fig. 2.11 we show the pump envelope, phase matching, and joint spectral intensity (the square of the amplitude) using the relevant parameters for our experiment.

As can be seen from the joint spectral intensity in Fig. 2.11, the signal and idler wavelengths in the downconverted state are anti-correlated. This means that a higher energy

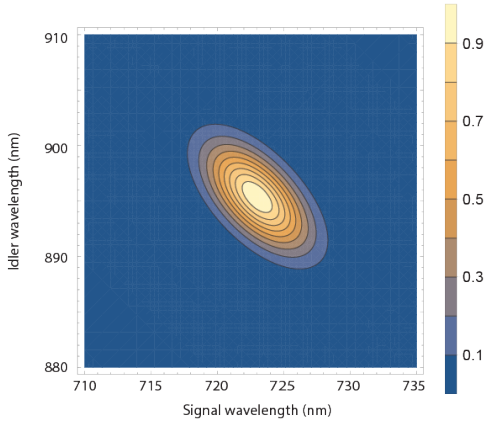

Figure 2.12: The joint spectral intensity when 5 nm wide Gaussian-shaped frequency filters have been applied to both photons. The wavelength anti-correlations are reduced from the unfiltered case.

signal photon is paired with a low energy idler photon, and vice versa. This is an indication that the two photons are entangled in the frequency-time degrees of freedom. These anti-correlations in wavelength (or frequency) also indicate that the times-of-arrival for the signal and idler are correlated: an earlier signal photon is paired with an earlier idler photon. This has a negative effect on our experiment. The time-of-arrival of the signal photon at the quantum memory must be accurate to within ~ 100 fs, and strong timing correlations introduce timing jitter which would degrade the storage efficiency in the quantum memory. It will also degrade the quality of our polarization-entangled states since it adds a distinguishing feature. We are therefore interested in eliminating this spectral entanglement in our downconverted state. This can be accomplished through frequency filtering. Of course filtering will also reduce our photon rates. (It is rare to find a nonlinear medium that can produce spectrally separable states at the relevant wavelengths for your experiment, though it is an active field of research [47].) Fig. 2.12 shows the theoretical joint spectral intensity (using experimental parameters) when 5 nm wide Gaussian-shaped frequency filters have been applied to both photons. While some wavelength anti-correlation still exists it is clearly reduced from the unfiltered case in Fig. 2.11.

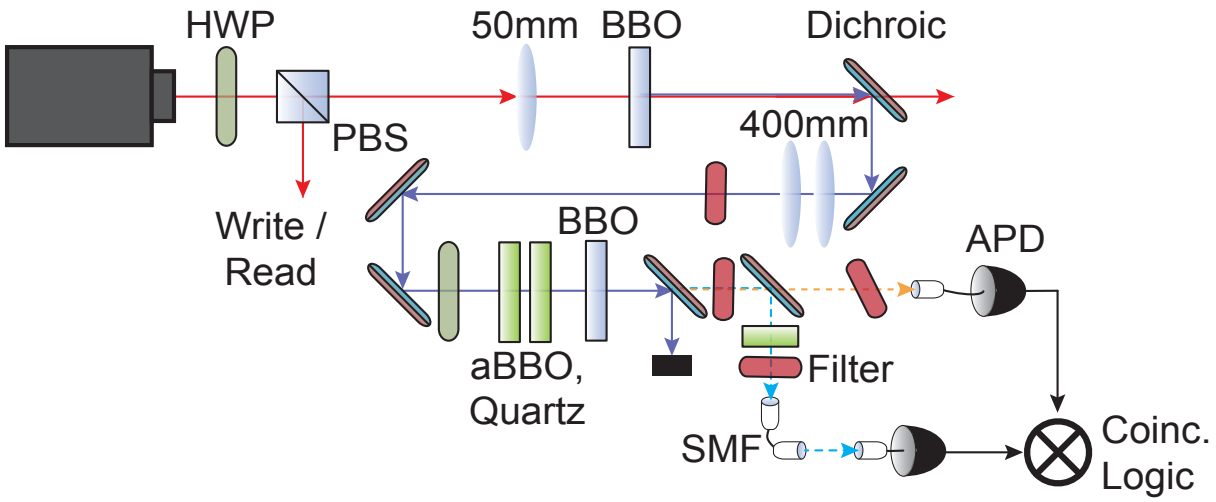

Figure 2.13: The SPDC photon source. Laser light is frequency-doubled in β-barium borate (BBO) and refocussed onto a second BBO crystal for type-I collinear downconversion. The signal and idler photons are filtered from the pump and split into their respective spatial modes by a dichroic mirror, frequency filtered and collected in single mode fibres (SMF). Photons are detected on avalanche photodiodes (APD) and measured in coincidence. See the text for more details. (HWP – half-waveplate; PBS – polarizing beamsplitter; aBBO – α-barium borate).

2.6.5 Our photon source

The laser we use to pump the photon source is a Coherent Chameleon Ultra II. Initially, some laser light is taken for the control beams in the memory experiment. Light for the source, 190 fs pulses at 800 nm, is tightly focussed, with 50 mm focal length, on a BBO crystal for type-I second harmonic generation (a special case of sum-frequency generation where pump light is frequency doubled). The power conversion efficiency to 400 nm light is approximately 15%. For the experiments in this thesis we produce approximately 190 mW of 400 nm light. The resulting 400 nm light is filtered from leftover 800 nm light using dichroic mirrors and a 440 nm short-pass filter. It is refocussed using two 400 mm

cylindrical lenses onto a second BBO crystal for downconversion. The focal length of the cylindrical lenses was used to give a focussed beam waist of approximately 100 μm.

Before it reaches the BBO crystal, the 400 nm pump pulse passes through a half-waveplate, which either leaves the pump polarization vertical or rotates it to diagonal for entangled pair generation. The pump then also travels through birefringent α-BBO and quartz crystals for temporal compensation between horizontal and vertical polarization of the downconverted light (Newlight Photonics [46]). This is vital for producing polarization entanglement. The crystal in which SPDC occurs is actually two 1 mm BBO crystals sandwiched together such that their optical axes are 90° with respect to each other in the transverse direction. When the first crystal is tilted by 29.1° with respect to the incident pump beam, and the pump vertically polarized, 400 nm pump light downconverts to signal and idler photons with centre wavelengths of 723 nm and 895 nm respectively. The same process occurs in the second crystal when the pump is vertically polarized.

After the BBO, 400 nm pump light is filtered with a dichroic mirror and a long-pass 715 nm filter (Semrock [48]). The signal and idler photons are generated in the same spatial mode, but since there is a sizeable frequency difference between them they can be split into separate spatial modes with a 801 nm long-pass dichroic mirror (Semrock [48]). Both photons then pass through ~5 nm bandpass filters (Foreal Spectrum Inc. [49]) and are coupled into single mode fibres. Plugging each fibre into an avalanche photodiode (APD), with detection efficiency ~60% at 723 nm (Excelitas [50]), we can measure the coincidence detection rate by matching detection delay times. Note that in this thesis we define a coincidence as being two detections that occur within a window of 3 ns, unless otherwise stated.

If we instead plug the signal fibre into a 50-50 fibre beamsplitter (Gooch & Housego [51]) and then into the APDs, we can measure the triggered $g^{(2)}(0)$ of the signal photon. We find that the $g^{(2)}(0)$ depends near-linearly on the amount of 400 nm pump power used, see Fig. 2.14. For a two-photon downconverted state of the form $|\psi\rangle = \sqrt{1-p}\sum_{n=0}^{\infty} p^{1/2}|nn\rangle$, where p is the probability of producing a photon pair, a heralded $g^{(2)}(0)$ measurement takes the form $2p(2+p)/(1+p)^2$. As the pump power increases so does p, and higher-order terms in the downconverted state contribute more to $g^{(2)}(0)$. At the pump power used in the memory experiments, we measure $g^{(2)}(0) = 0.04$ out of the source, heralded by the

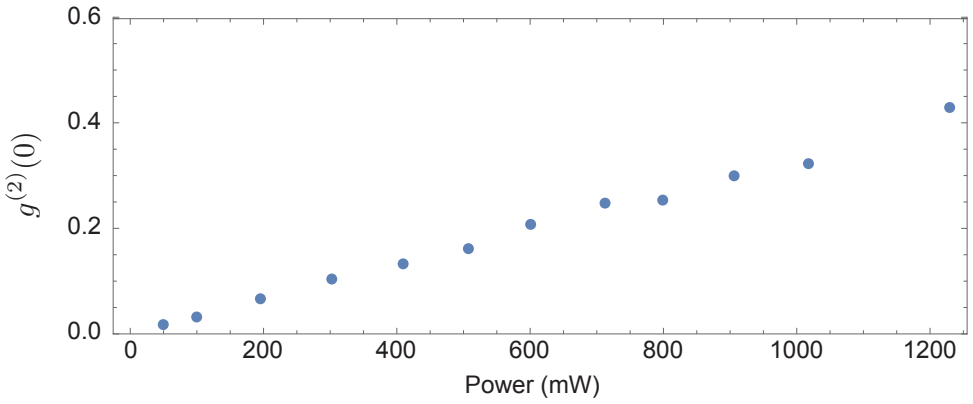

Figure 2.14: The $g^{(2)}(0)$ of the signal photon, triggered by the detection of the idler photon. As the pump power is increased the amplitude of the next-order term in the downconversion state grows, thereby increasing $g^{(2)}(0)$. For a downconverted state of the form $|\psi\rangle = \sqrt{1-p}\sum_{n=0}^{\infty} p^{1/2}|nn\rangle$, the heralded $g^{(2)}(0) = 2p(2+p)/(1+p)^2$.

detection of the 895 nm photon.

If we plug each fibre into a spectrometer (Princeton Instruments [52]) we can measure the spectrum of each photon. The signal and idler photon spectra are shown in Fig. 2.15 as well as the pump spectrum.

2.6.6 Temporal compensation for polarization entanglement

Downconversion sources have been the workhorses for studying entanglement in quantum optics experiments. Since the first bright SPDC sources of entangled photons [45] their use has become ubiquitous. Our source produces entangled photon pairs by making the two possible paths in which downconversion can occur indistinguishable: a vertically-polarized pump downconverts to two horizontally-polarized photons in the first crystal, or a horizontally-polarized pump downconverts to two vertically-polarized photons in the second crystal. However, due to different group velocities for the two polarizations these two processes can occur at very different times. The group velocity $v_g^{(i)}$ for polarization i

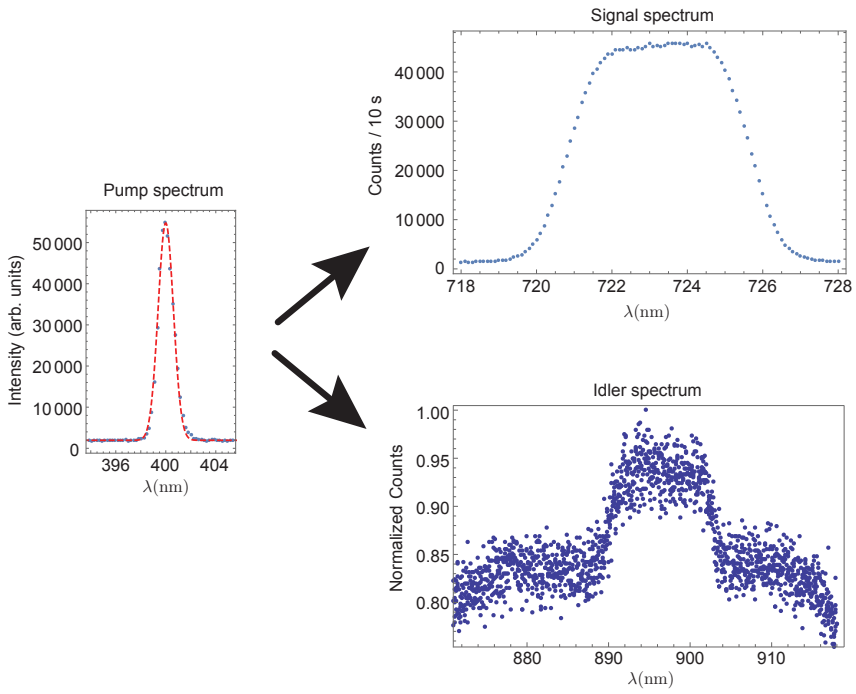

Figure 2.15: A 400 nm, 1.3 full width at half maximum, pump beam downconverts to broadband signal and idler photons at 723 nm and 895 nm wavelengths. The signal and idler are both spectrally filtered resulting in wavelength spreads of approximately ≈ 5 nm and ≈ 12 nm respectively.

400 nm pump power	300 mW
Coincidence rates (Hz)	31000
$g^{(2)}(0)$ of signal photon	0.04
Entangled state rates in HH basis (Hz)	8000
Fidelity of entangled state with $\|\Phi^+\rangle$	0.939
Concurrence	0.912

Table 2.3: Photon source statistics. Each of these numbers was measured while the source was integrated in the memory experiment. As such the signal photon was first spatially filtered in a 7 cm fibre, traversed the diamond memory setup, collected again into single-mode fibre and then detected. This decreased rates significantly. Also important to note here is that all of the laser power is used to pump the photon source, where as in the memory experiments 1.4 W of laser power is used for control beams.

can be calculated as

$$v_g^{(i)}(\lambda) = \frac{c}{n_i(\lambda) - \lambda\frac{\partial}{\partial\lambda}n_i(\lambda)}. \tag{2.135}$$

The group velocity mismatch (GVM) is then the difference between group velocities for ordinary and extraordinary polarizations, $1/v_g^{(o)} - 1/v_g^{(e)}$, which has units fs of walkoff per mm of material. Using the Sellemeier equations for BBO (Eq. 2.128 and coefficients from Table 2.6.3) we find the GVM for 723 nm light to be 105 fs/mm. If we assume that both of the downconversions occur in the centre of each crystal then we can find the timing difference between the two processes, and therefore how much temporal compensation is needed.

In the first crystal a vertically (extraordinarily) polarized 400 nm pump travels 1/2 mm (on average) before splitting into horizontally (ordinarily) polarized 723 nm and 895 nm photons. The downconverted photons travel the remaining 1/2 mm with the ordinary polarization, but are extraordinarily polarized in the second crystal. The other case is that a horizontally polarized pump, ordinary in the first crystal, travels 1/2 mm into the second crystal before downconverting to two ordinarily polarized 723 nm and 895 nm photons. The timing difference between these two processes is not the same for 723 nm and 895 nm. For

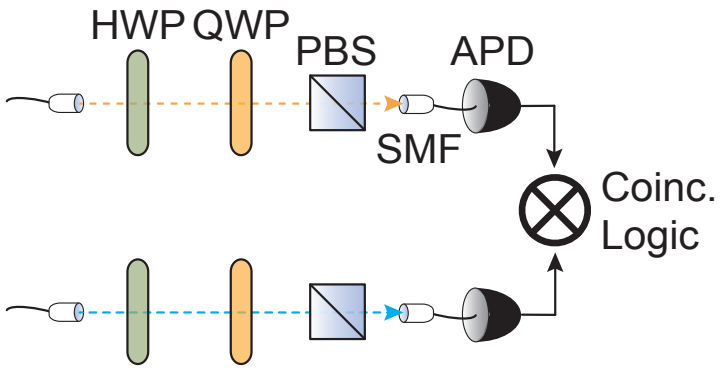

Figure 2.16: Tomographic measurements can be made on a two-photon polarization state, using half- and quarter-waveplates (HWP and QWP) followed by a projective measurement by a polarizing beamsplitter (PBS). Photons are then collected in single-mode fibre and detected in coincidence.

723 nm we find the difference to be $1/v_g^{(o)}(400\,\text{nm}) - 1/v_g^{(e)}(723\,\text{nm})) = 412\,\text{fs}$. For 895 nm the difference is $1/v_g^{(o)}(400\,\text{nm}) - 1/v_g^{(e)}(895\,\text{nm}) = 445\,\text{fs}$. This means we cannot entirely compensate for the temporal walkoff beforehand, but an additional correction is required after the 723 nm and 895 nm photons are separated. We place 1 mm of αBBO and 2 mm of quartz in the 400 nm beam, which have GVM of 522 fs and 76 fs of birefringent walkoff respectively (see Ref. [46] for Sellemeier coefficients). This compensates very nicely for the 895 nm light, but we have an additional 33 fs to deal with for the 723 nm light. This is very nicely accomplished with a 1 mm quartz crystal.

We have successfully compensated for the temporal walkoff in the entangled photon source. (Strictly speaking there is also spatial walkoff in the crystals but it is small enough that we can neglect it.) With balanced coupling efficiencies, i.e., the downconversions from each crystal are detected with equal rates, we have a polarization entangled state of the form $(|HH\rangle + e^{i\phi}|VV\rangle)/\sqrt{2}$. We can set the phase ϕ to zero by placing a waveplate at 0° in one arm and tilting it to adjust the delay between horizontal and vertical polarizations.

We can perform tomographic measurements using a combination of half- and quarter-waveplates and a polarizing beamsplitter before detecting them on APDs (see Fig. 2.16). By reconstructing the two-qubit density matrix using the maximum likelihood techniques

discussed in Chapter 1, we find a state that has 0.939 fidelity with the maximally entangled state, and has a concurrence of 0.912. The real part of the density matrix for this state is shown in Fig. 6.5(a).

Chapter 3

Quantum memories

In order to realize quantum technologies using photons there are a number of practical devices that will be required. We have already discussed photon sources and detectors in Chapter 2. Another essential component is the frequency converter; many photonic components (e.g., fibre optics, waveplates, detectors) are optimized for different optical frequencies which the same qubit must travel through. Finally, we will require a *quantum memory*, a buffer for a single photons. A quantum memory stores a photon and releases it on demand, preserving its encoded quantum information. By reversibly mapping between propagating and stationary qubits, a quantum memory allows for the synchronization of distant or spontaneous events. Quantum memories are key enablers for deterministic photon sources, long-distance quantum communication [53, 54], and much more.

In this chapter we will first give an introduction to quantum repeaters, the traditional use for a quantum memory. We will then overview some of the myriad of methods to implement quantum memories in different physical systems. Lastly, we will discuss some additional applications that quantum memories can be useful for.

3.1 Quantum repeaters

The chief goal of quantum communication [55] is to distribute unknown quantum states between distant or disparate parties. The successful sharing of quantum information across a widespread network enables disruptive quantum technologies such as quantum cryptography [56, 57]. However, imperfect transmission across quantum channels prevents the faithful communication of fragile quantum states. Just as for the transmission of classical data, there are physical limits on the distance quantum information can be sent before it degrades beyond recovery. Long-distance classical transmissions, either radio or optical, use devices called repeaters to amplify signals that have grown weak. Unfortunately, a simple analogue for quantum transmissions does not exist. While strategies such as heralded quantum amplifiers [58] and qubit certification [59] are active fields of research, here we will discuss quantum repeaters based on entanglement swapping [53, 60].

The goal of quantum repeaters is to establish a long-distance entanglement link by connecting many shorter links together. A quantum memory is crucial component to the quantum repeater, storing entangled qubits to be synchronized with those arriving at different times from other locations. With a shared entangled state, quantum states can be transferred using quantum teleportation [61, 62] outlined below.

3.1.1 Quantum teleportation

The simplest version of the teleportation protocol goes as follows: Alice wishes to send a qubit $|\psi\rangle_A = \alpha|0\rangle_A + \beta|1\rangle_A$ to Bob. They share the maximally entangled state, $|\Phi^+\rangle_{A'B} = (|00\rangle_{A'B} + |11\rangle_{A'B})/\sqrt{2}$. Here the subscripts A and A' refer to Alice's subsystems and B refers to Bob's.

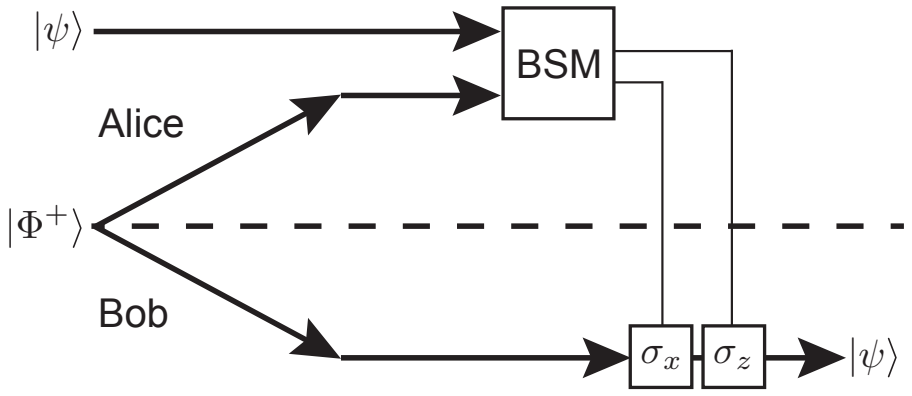

Figure 3.1: If Alice and Bob share the entangled state $|\Phi^+\rangle$, Alice can teleport her qubit $|\psi\rangle$ to Bob by performing a Bell state measurment (BSM) with her qubit and half of the entangled pair, communicating the result to Bob. Bob then performs a simple correction to recover the qubit $|\psi\rangle$.

Writing out the whole system and rearranging term, we get:

$$\begin{aligned}
|\psi\rangle_A|\Phi^+\rangle_{A'B} &= (\alpha|0\rangle_A + \beta|1\rangle_A)(|00\rangle_{A'B} + |11\rangle_{A'B})/\sqrt{2} \qquad (3.1)\\
&= \frac{1}{\sqrt{2}}(\alpha|0\rangle_A|00\rangle_{A'B} + \alpha|0\rangle_A|11\rangle_{A'B} + \beta|1\rangle_A|00\rangle_{A'B} + \beta|1\rangle_A|11\rangle_{A'B})\\
&= \frac{1}{2}[(|\Phi^+\rangle_{AA'} + |\Phi^-\rangle_{AA'})\alpha|0\rangle_B + (|\Psi^+\rangle_{AA'} + |\Psi^-\rangle_{AA'})\alpha|1\rangle_B\\
&\quad +(|\Psi^+\rangle_{AA'} - |\Psi^-\rangle_{AA'})\beta|0\rangle_B + (|\Phi^+\rangle_{AA'} - |\Phi^-\rangle_{AA'})\beta|1\rangle_B]\\
&= \frac{1}{2}[|\Phi^+\rangle_{AA'}(\alpha|0\rangle_B + \beta|1\rangle_B) + |\Phi^-\rangle_{AA'}(\alpha|0\rangle_B - \beta|1\rangle_B)\\
&\quad +|\Psi^+\rangle_{AA'}(\alpha|1\rangle_B + \beta|0\rangle_B) + |\Psi^-\rangle_{AA'}(\alpha|1\rangle_B - \beta|0\rangle_B)]\\
&= \frac{1}{2}[|\Phi^+\rangle_{AA'}|\psi\rangle_B + |\Phi^-\rangle_{AA'}\sigma_z|\psi\rangle_B + |\Psi^+\rangle_{AA'}\sigma_x|\psi\rangle_B + |\Psi^-\rangle_{AA'}\sigma_x\sigma_z|\psi\rangle_B]
\end{aligned}$$

What we see here is that when Alice looks at her two-qubit state in the Bell basis, Bob's state looks like Alice's original state $|\psi\rangle$ (up to a unitary correction). Alice can then perform a Bell measurement on her two-qubit state and communicate her result to Bob with two classical bits a and b. (She would label the measurement outcomes as follows: $|\Phi^+\rangle \to a = 0, b = 0$; $|\Phi^-\rangle \to a = 0, b = 1$; $|\Psi^+\rangle \to a = 1, b = 0$; $|\Psi^-\rangle \to a = 1, b = 1$).

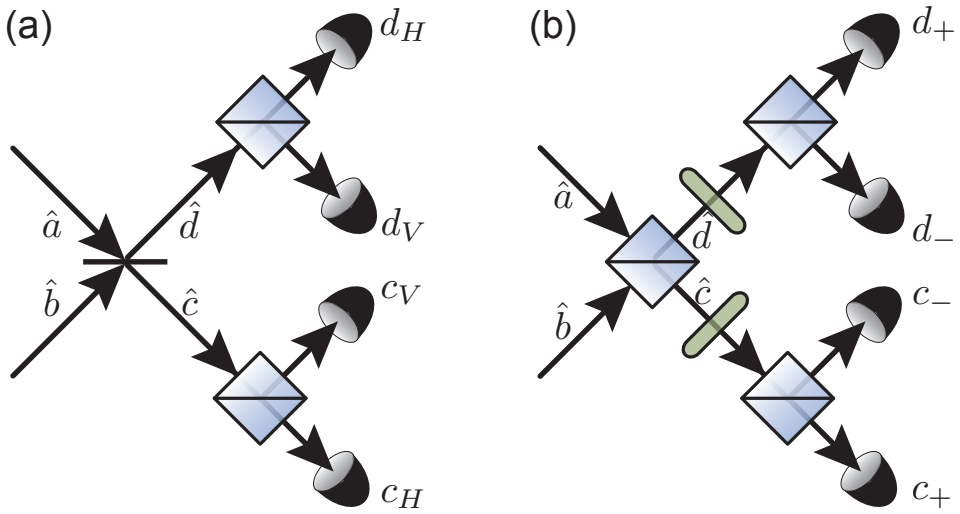

Figure 3.2: Two possible Bell state analyzer setups using linear optics. Using a 50-50 beamsplitter, setup (a) can distinguish $|\Psi^+\rangle$ and $|\Psi\rangle$ from one another and from the other two Bell states. Setup (b) can distinguish $|\Phi^+\rangle$ and $|\Phi\rangle$ from each other and from the other two.

Bob then performs the correction $\sigma_x^a \sigma_z^b$ on his qubit to map it back to the intended $|\psi\rangle$. Then, with shared entanglement and just a classical communication, Alice can "teleport" her qubit to Bob.

Bell state measurements

In order to enact the teleportation protocol we require a Bell state measurement, i.e., a two-qubit measurement which projects onto the Bell state basis $\{|\Phi^+\rangle, |\Phi^-\rangle, |\Psi^+\rangle, |\Psi^-\rangle\}$. This could be done using a controlled-NOT gate ($|i,j\rangle \to |i, i \oplus j\rangle$, for $i,j \in \{0,1\}$). However, in the absence of a deterministic controlled-NOT gate using linear optics, we typically use Bell state analyzers which can only distinguish two out of the four Bell states at a time.

The first Bell analyzer, shown in Fig. 3.2(a), can distinguish $|\Psi^-\rangle$ and $|\Psi^+\rangle$, but cannot distinguish between $|\Phi^+\rangle$ and $|\Phi^-\rangle$. The two polarization qubits being measured, in modes a and b, are incident on a 50-50 beamsplitter at the same time. If they are spectrally

indistinguishable, so that they undergo HOM interference, the $|\Psi^-\rangle$, $|\Psi^+\rangle$ and $|\Phi^\pm\rangle$ Bell states behave differently,

$$
\begin{aligned}
|\Psi^-\rangle_{a,b} &= \frac{1}{\sqrt{2}}\left(|HV\rangle_{a,b} - |VH\rangle_{a,b}\right) && (3.2)\\
&= \frac{1}{\sqrt{2}}\left(\hat{a}_H^\dagger \hat{b}_V^\dagger - \hat{a}_V^\dagger \hat{b}_H^\dagger\right)|00\rangle && (3.3)\\
&\rightarrow \frac{1}{\sqrt{2}}\left[\frac{\left(\hat{c}_H^\dagger + \hat{d}_H^\dagger\right)}{\sqrt{2}}\frac{\left(\hat{d}_V^\dagger - \hat{c}_V^\dagger\right)}{\sqrt{2}} - \frac{\left(\hat{c}_V^\dagger + \hat{d}_V^\dagger\right)}{\sqrt{2}}\frac{\left(\hat{d}_H^\dagger - \hat{c}_H^\dagger\right)}{\sqrt{2}}\right]|00\rangle && (3.4)\\
&= \frac{1}{\sqrt{2}}\left(\hat{c}_H^\dagger \hat{d}_V^\dagger - \hat{c}_V^\dagger \hat{d}_H^\dagger\right)|00\rangle && (3.5)\\
|\Psi^+\rangle_{a,b} &= \frac{1}{\sqrt{2}}\left(|HV\rangle_{a,b} + |VH\rangle_{a,b}\right) && (3.6)\\
&\rightarrow \frac{1}{\sqrt{2}}\left(\hat{d}_H^\dagger \hat{d}_V^\dagger - \hat{c}_H^\dagger \hat{c}_V^\dagger\right)|00\rangle && (3.7)\\
|\Phi^\pm\rangle_{a,b} &= \frac{1}{\sqrt{2}}\left(|HH\rangle_{a,b} \pm |VV\rangle_{a,b}\right) && (3.8)\\
&\rightarrow \frac{1}{2\sqrt{2}}\left[\pm(\hat{c}_H^\dagger)^2 \mp (\hat{c}_V^\dagger)^2 \mp (\hat{d}_H^\dagger)^2 \pm (\hat{d}_V^\dagger)^2\right]|00\rangle && (3.9)
\end{aligned}
$$

The $|\Psi^-\rangle$ state anti-bunches at the beamsplitter, whereas the other three states bunch. Notice from above that with polarizing beamsplitters in modes c and d, followed by detection in each port, we can distinguish between $|\Psi^-\rangle$ and $|\Psi^+\rangle$. The $|\Psi^-\rangle$ state will produce coincidence detections between c and d whereas the $|\Psi^+\rangle$ state will give coincidence detections between the two polarization ports within c and d. Also notice that both the $|\Phi^+\rangle$ and $|\Phi^-\rangle$ states do not produce coincidences and so we cannot tell them apart.

To distinguish between $|\Phi^+\rangle$ and $|\Phi^-\rangle$ we can use a different setup, shown in Fig. 3.2(b). The initial beamsplitter is now polarizing $\left(\hat{a}_H \rightarrow \hat{c}_H, \hat{a}_V \rightarrow \hat{d}_V, \hat{b}_H \rightarrow \hat{d}_H, \hat{b}_V \rightarrow -\hat{c}_V\right)$, and we add half-waveplates at 22.5° to perform the polarization measurement in the diagonal basis. It can be shown, similar to above, that $|\Phi^+\rangle$ will result in coincidence detection between c and d modes, $|\Phi^-\rangle$ will result in coincidence detection in the two polarization ports c or d, and that the $|\Psi^\pm\rangle$ states will not produce coincidences.

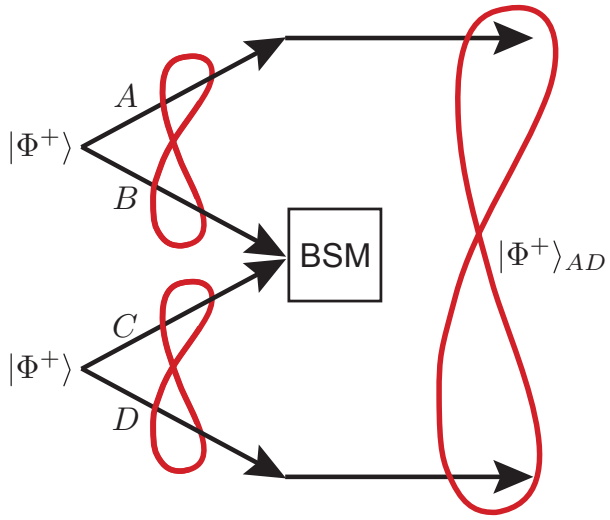

Figure 3.3: With two entangled states, one entangling modes A and B and the other entangling modes C and D, we can "swap" the entanglement to modes A and D by performing a Bell state measurement on modes B and C. Entanglement swapping is identical to the teleportation protocol where the state to be transmitted is one photon of an entangled pair.

3.1.2 Entanglement swapping

Fig. 3.3 shows the basic concept of entanglement swapping. Suppose we have two separate sources of entangled photon pairs, each producing the state $|\Phi^+\rangle$ in modes A, B and C, D. We send one photon from each pair, say modes B and C, to a midpoint between the source where they are jointly measured in the Bell basis. By rewriting the 4-qubit state as a collection of A, D and B, C modes we can see the effect,

$$|\Phi^+\rangle_{AB}|\Phi^+\rangle_{CD} = \frac{1}{2}\left(|HH\rangle_{AB} + |VV\rangle_{AB}\right)\left(|HH\rangle_{CD} + |VV\rangle_{CD}\right) \tag{3.10}$$

$$= \frac{1}{2}(|\Phi^+\rangle_{AD}|\Phi^+\rangle_{BC} + |\Phi^-\rangle_{AD}|\Phi^-\rangle_{BC} + |\Psi^+\rangle_{AD}|\Psi^+\rangle_{BC} + |\Psi^-\rangle_{AD}|\Psi^-\rangle_{BC}). \tag{3.11}$$

By performing a Bell state measurement on modes B and C, entanglement is swapped to be between modes A and D. The result of the Bell state measurement tells us which

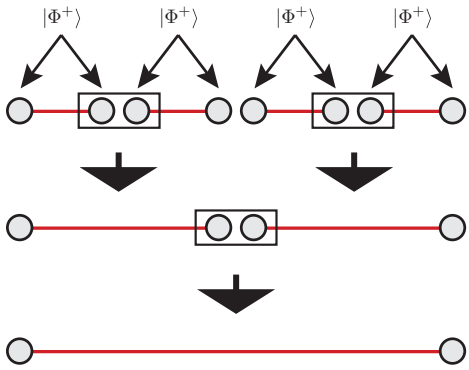

Figure 3.4: The quantum repeater architecture. Entanglement swapping steps generate long distance entanglement between photons that never interacted. Spatially separated entangled photon sources send each of their photons to entanglement swapping stations. In order to synchronize photons coming from separate source each node (grey circles) have a quantum memory. Before entanglement swapping (steps implied by black arrows) an entanglement purification step is required between existing entangled links.

entangled state A and D share. In this way, two photons that have never interacted become entangled and two distant parties now share an entangled state. The concept of entanglement swapping is identical to teleportation where the qubit to be teleported is one half of an entangled pair. In principle this process can be extended to arbitrary distance, and, along with intermediary steps of entanglement purification [8, 63, 64], help constitute a quantum repeater, see Fig. 3.4.

Due to the practical limitations of entangled photon sources, e.g., spontaneous emission and loss, photons from separate sources will in general not arrive at entanglement swapping nodes at the same time. This matters a great deal since entanglement swapping requires that the interfering photons be temporally and spectrally indistinguishable. In order synchronize incoming photons we need to be able to reversibly map between stationary and "flying" qubits. This is the role of a quantum memory. Quantum memories map photonic qubits onto a material or atomic excitation which can be re-addressed when needed, e.g., for the entanglement swapping step. Before discussing various ways to implement a quantum memory, we will overview another example of how they can be used in quantum

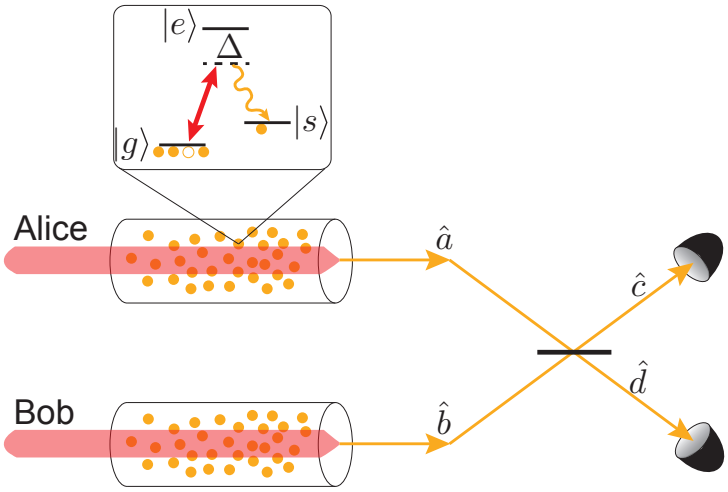

Figure 3.5: The DLCZ scheme. Alice and Bob both have atomic ensembles. An incident laser on each ensemble stimulates the emission of a single photon and creates an atomic spin wave. When Alice and Bob's generated photons interfere on a 50-50 beamsplitter a photon detection heralds entanglement between their atomic spin waves.

communication.

3.1.3 DLCZ scheme

Duan, Lukin, Cirac and Zoeller (DLCZ) [54] introduced a scheme to establish an entangled link between two parties, Alice and Bob, which realizes a quantum repeater. Suppose Alice and Bob each have an atomic ensemble which when stimulated with a laser, generate long-lived excitations and forward propagating single photons (see Fig. 3.5). This process is governed by an interaction Hamiltonian

$$\mathcal{H}_{\text{dlcz}} = \hbar \frac{\sqrt{N_a}\Omega g_c}{\Delta} \hat{S}^\dagger \hat{a}^\dagger + \text{h.c} \tag{3.12}$$

where N_a is the number of atoms in the ensemble, Ω is the Rabi frequency of the laser, g_c is a light-atom coupling constant, Δ is the frequency detuning from resonance (see the inset in Fig. 3.5), and $\hat{S}^\dagger$ is the creation operator for the atomic spin wave. This Hamiltonian

is of similar form to that in Section 2.6 in that a squeezed state is generated between two modes. If both Alice and Bob's atomic clouds undergo this interaction Hamiltonian their joint quantum state, initially the atomic ground state and vacuum $|g,0\rangle$, evolves to

$$|\psi\rangle_{AB} = e^{-\frac{i}{\hbar}\mathcal{H}^A_{\text{dlcz}}}|g,0\rangle_A \otimes e^{-\frac{i}{\hbar}\mathcal{H}^B_{\text{dlcz}}}|g,0\rangle_B \tag{3.13}$$

$$= \left(\mathbb{1} - i\kappa\hat{S}^\dagger_A\hat{a}^\dagger + ...\right)|g,0\rangle_A \otimes \left(\mathbb{1} - i\kappa\hat{S}^\dagger_B b^\dagger + ...\right)|g,0\rangle_B \tag{3.14}$$

$$= |g,0\rangle_A|g,0\rangle_B - i\kappa\left(|s,1\rangle_A|g,0\rangle_B + e^{i\phi}|g,0\rangle_A|s,1\rangle_B\right) \tag{3.15}$$

where $\kappa = \sqrt{N_a}\Omega g_c/\Delta$, and we have assumed Alice and Bob have identical ensembles for simplicity. We have also neglected terms of higher order than κ^2. Notice that we used $\hat{b}^\dagger$ for Bob's photon creation operator. Now suppose that Alice and Bob both direct their generated photons, in modes a and b respectively, to a 50-50 beamsplitter. After the beamsplitter the state in Eq. 3.15 becomes, where we have post-selected out the lowest-order term,

$$\kappa\left(\hat{S}^\dagger_A\hat{a}^\dagger + \hat{S}^\dagger_B\hat{b}^\dagger\right)|g,0\rangle_A|g,0\rangle_B \rightarrow \frac{\kappa}{\sqrt{2}}\left[\hat{S}^\dagger_A\left(\hat{c}^\dagger + \hat{d}^\dagger\right) + e^{i\phi}\hat{S}^\dagger_B\left(\hat{d}^\dagger - \hat{c}^\dagger\right)\right]|g\rangle_A|g\rangle_B|00\rangle_{cd} \tag{3.16}$$

$$= \frac{\kappa}{\sqrt{2}}[\left(|s\rangle_A|g\rangle_B - e^{i\phi}|g\rangle_A|s\rangle_B\right)|10\rangle_{cd} + \left(|s\rangle_A|g\rangle_B + e^{i\phi}|g\rangle_A|s\rangle_B\right)|01\rangle_{cd}]. \tag{3.17}$$

A detection in either the c or d mode then entangles Alice and Bob's atomic ensembles in one of two possible states. This protocol has been realized experimentally in many physical systems [65, 38, 66, 67, 68]. We can imagine that, when ready, each atomic ensemble can be transitioned back to its ground state with a second laser beam, emitting an anti-Stokes photon which can be furthered manipulated or distributed. What we have then is a method, using a quantum memory, to generate long-distance entanglement between two parties. We now turn to a discussion of some specific examples of quantum memories.

3.2 Implementations of quantum memories

In this section we overview various implementations of quantum memories. For the context of this thesis we will be interested in evaluating quantum memories with a few specific

figures of merit. The first is the efficiency of the memory, i.e., the probability that a photon incident on the memory is stored and retrieved at a later time. Next we look at the storage time of the memory. We also look at the bandwidth of the stored light. The multiplication of these two figures, the time-bandwidth product, tells us how many coherence times a photon is stored for, or to put it another way, how many operational time-bins a photon can be mapped between. Lastly, we'll look at the state fidelity of qubits retrieved from the memory. We require that this fidelity be above 2/3 [69] to ensure that the quantum memory outperforms a classical measurement-and-resend strategy (see Appendix D).

As we will soon see, certain quantum memory implementations will be better-suited to long-distance communication than others. In Section 3.3 we will discuss other potential applications for quantum memories besides quantum repeaters. Refs. [70, 71, 72] give excellent overviews of the broad field of quantum memories. In what follows we discuss various implementations of quantum memories giving a brief cross section of their current state of development.

3.2.1 Electromagnetically-induced transparency

Electromagnetically-induced transparency [43, 73] (EIT) is the quantum effect where the presence of a strong laser field in a medium can drastically change the absorption profile of that medium. A signal field in resonance with an absorption line can, when the control field is present, fly through the medium unabsorbed. Instead the signal will experience a large reduction in group velocity, leading to the slow light phenomenon. When the control field is slowly turned off the signal field remains in the medium, storing the light. It can be retrieved by ramping up the control field again to induce transparency. The interaction Hamiltonian for the Λ-level system shown in Fig. 3.6(a) is given by the electric dipole coupling $-\vec{d}\cdot\vec{E}$,

$$\mathcal{H}_{\text{EIT}} = -\frac{\hbar}{2}\begin{pmatrix} 0 & 0 & \Omega_s \\ 0 & 0 & \Omega_c \\ \Omega_s^* & \Omega_c^* & -2\Delta \end{pmatrix} \tag{3.18}$$

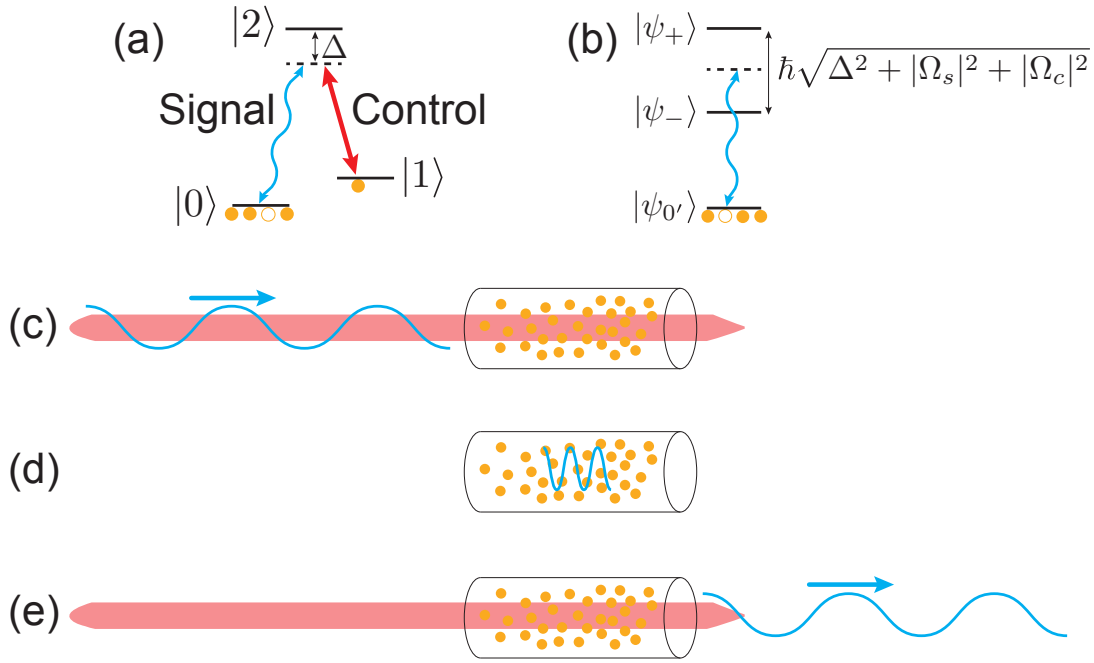

Figure 3.6: The EIT quantum memory scheme. (a) The Λ-level diagram for the storage medium. A signal field and strong control field are in near-resonance (detuning Δ) with the energy level $|2\rangle$. (b) The eigenstates of the interaction Hamiltonian. With the control field present, $|2\rangle$ splits into two levels $|+\rangle$ and $|-\rangle$, with a splitting related to the Rabi frequencies Ω_s and Ω_c. (c) The signal pulse to be stored is long in duration but, (d), is compressed by the EIT effect in the medium. With the signal pulse inside the medium the control field is turned off, stopping the signal. (e) When the control field is turned back on the signal pulse continues to propagate.

in the basis $\{|0\rangle, |1\rangle, |2\rangle\}$, where $|0\rangle = (1,0,0)^{\mathrm{T}}$ (here T is the transpose), Δ is the detuning of the signal and control fields from resonance with $|2\rangle$. The Rabi frequencies, Ω_s and Ω_c, the signal and control fields are defined as $\Omega_j = \vec{d} \cdot E_j/\hbar$, where $\vec{d}$ is the dipole moment for the corresponding transition. The eigenvalues (E_0, E_+, E_-), and respective eigenvectors $(|\psi_{0'}\rangle, |\psi_+\rangle, |\psi_-\rangle)$, of the interaction Hamiltonian are

$$\begin{aligned} E_0 &= 0, & |\psi_{0'}\rangle &= -\sin\theta|0\rangle + \cos\theta|1\rangle \\ E_+ &= \frac{\hbar}{2}\left(\Delta_s + \sqrt{\Delta^2 + |\Omega_s|^2 + |\Omega_c|^2}\right), & |\psi_+\rangle &= \sin\theta\sin\phi|0\rangle + \cos\theta\sin\phi|1\rangle + \cos\phi|2\rangle \\ E_- &= \frac{\hbar}{2}\left(\Delta_s - \sqrt{\Delta_s^2 + |\Omega_s|^2 + |\Omega_c|^2}\right), & |\psi_-\rangle &= \sin\theta\cos\phi|0\rangle + \cos\theta\cos\phi|1\rangle - \sin\phi|2\rangle \end{aligned} \tag{3.19}$$

where $\tan\theta = \Omega_c/\Omega_s$ and $\tan\phi = \sqrt{\Omega_s^2 + \Omega_c^2}/(\Delta + \sqrt{\Delta^2 + |\Omega_s|^2 + |\Omega_c|^2})$. We can see here that due to the presence of the control field the energy level $|2\rangle$ splits into two energy levels $|+\rangle$ and $|-\rangle$; the levels are split by energy $\hbar\sqrt{\Delta^2 + |\Omega_s|^2 + |\Omega_c|^2}$. We assume that $\Delta \approx 0$ so that the signal field is resonant with $|2\rangle$ and absorbed when no control field is present. However, the effect of the control field is a splitting of $|2\rangle$ into two separate levels so that the signal field is no longer in resonance with an absorption line. The medium is now transparent to the signal field provided a large enough splitting, which is determined by the control field Rabi frequency.

The absorption profile then changes from a peak centred on E_2 (energy eigenvalue of $|2\rangle$) to having two sharp peaks at energies E_+ and E_- with zero absorption at E_2. By the Kramers-Kronig relation any features in the absorption profile produces features in the dispersion relation. Hence there will be a steep positive slope through E_2 indicating a very low group velocity. The consequences of this are as follows. As the signal propagates into the medium its pulse contracts such that, though the pulse was initially much longer than the medium to ensure coupling to the atomic line $|2\rangle$, it can now entirely fit within the medium. Once it has fully entered the medium we can ramp down the control field, returning the energy spectrum and absorption profile to its original configuration. This traps the signal pulse inside the medium. To retrieve the pulse the control field is ramped up, inducing transparency, and freeing the signal.

Quantum memory experiments based on EIT have been performed using cold atomic ensembles [38, 67, 74], warm vapours [27, 75] and solid state media [76]. Experimenters

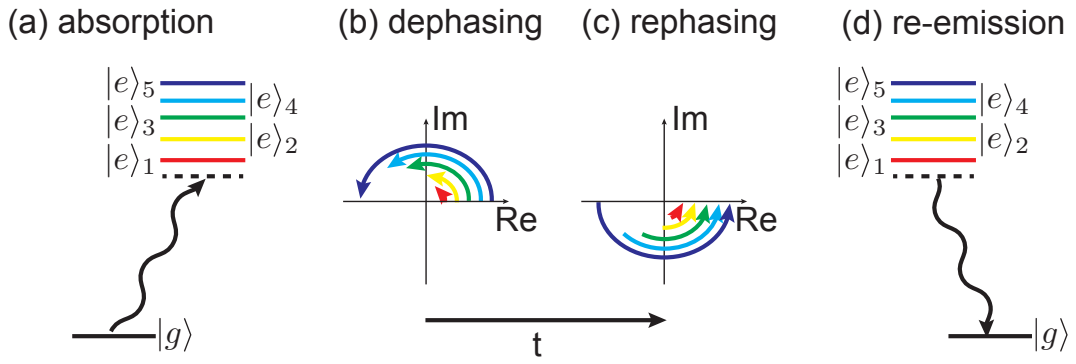

Figure 3.7: The photon echo phenomenon. (a) A photon is absorbed into an ensemble of two-level atoms with ground states $|g\rangle$ and excited states $|e\rangle_j$. The photon has a different different detuning δ_j from each atom's transition. (b) Once the photon is absorbed the different excitation frequencies each dephase at a different rate, but (c) after a time t the frequencies rephase causing (d) the re-emission, or echo, of the photon.

have demonstrated non-classical light storage [38, 75], as well as the storage of entangled photons [67, 74]. The bandwidth of the stored signal field is typically limited to MHz, though slowed light with ultra-broadband pulses has recently been demonstrated [77]. Single-photon demonstrations have shown storage times up to 0.5μs [38] with efficiencies as high as 10% [75]. Demonstrations where one photon of an entangled pair is stored have shown efficiencies up to 17% [67] and have shown violations of Bell's inequality for up to 200 ns of storage time, keeping an average state fidelity of approximately 0.92 [74]. With a photon spectrum 5 MHz wide this results in a time-bandwidth product of 1.

3.2.2 Photon echo memories

The photon echo phenomenon [78] has produced a few strategies for photon storage. The typical context for photon echoes is an ensemble of two-level atoms. Suppose the N-atom ensemble is initially prepared in its ground state $|\psi_0\rangle = |g_1...g_N\rangle$. After the absorption of a photon, travelling through the ensemble along the z direction, the state of the ensemble

becomes

$$|\psi_1\rangle = \sum_j c_j e^{i(kz_j - \delta_j t)} |g_1 ... e_j ... g_N\rangle, \tag{3.20}$$

where z_j is the position of the j^{th} atom which has transitioned to the excited state $|e\rangle$, and δ_j is its detuning from the photon frequency. Though the ensemble phase is initially aligned with the photon wavevector k, this quickly changes since δ_j is different for each atom. A photon echo occurs when these phases re-collect at a later time producing a re-emission of the photon, see Fig. 3.7. There are two primary strategies by which the initial distributions of detunings in the ensemble are engineered: continuous reversible inhomogeneous broadening (CRIB); and atomic frequency combs (AFC).

First, let's touch briefly on CRIB. Photon echo memories are typically implemented with rare-earth doped crystals cooled to below 10K. The atomic line of interest has some inhomogeneous broadening which can be removed by optically pumping atomic population into an auxiliary level. This leaves a single absorption line which is then controllably broadened using an electric (or in some cases magnetic) field applied across the medium which prepares the initial distribution of spectral detunings. An incident resonant photon whose bandwidth matches the broadening is then absorbed into the ensemble.

Next we need to perform some action to recall the photon from the ensemble. We need to map the frequency detuning $\delta_{j,1} \rightarrow \delta_{j,2}$ such that between times t_1 and t_2 the phase $\delta_{j1} t_1 + \delta_{j2}(t_2 - t_1)$ is constant across all atoms. One way to do this is by reversing the direction of the electric field applied across the medium, mapping each detuning to its negative. The detunings then rephase and the photon is emitted. Proof-of-principle implementations of the CRIB memory have been performed [79]. In Ref. [29] a laser field, attenuated to single-photon level, was stored for 2.6μs, and a memory efficiency of 69% was demonstrated. With a 1.6 MHz bandwidth, this a gives time-bandwidth product of 4. Experiments using a gradient echo memory (GEM) [80] have used a Raman transition between the excited state and a long-lived state to enable on-demand readout.

We now turn to atomic frequency comb memories [81]. A frequency comb is a set of discrete, evenly spaced frequency elements (see Fig. 3.8). Starting with a naturally inhomogeneously broadened ground state $|g\rangle$, the frequency comb is prepared with optical

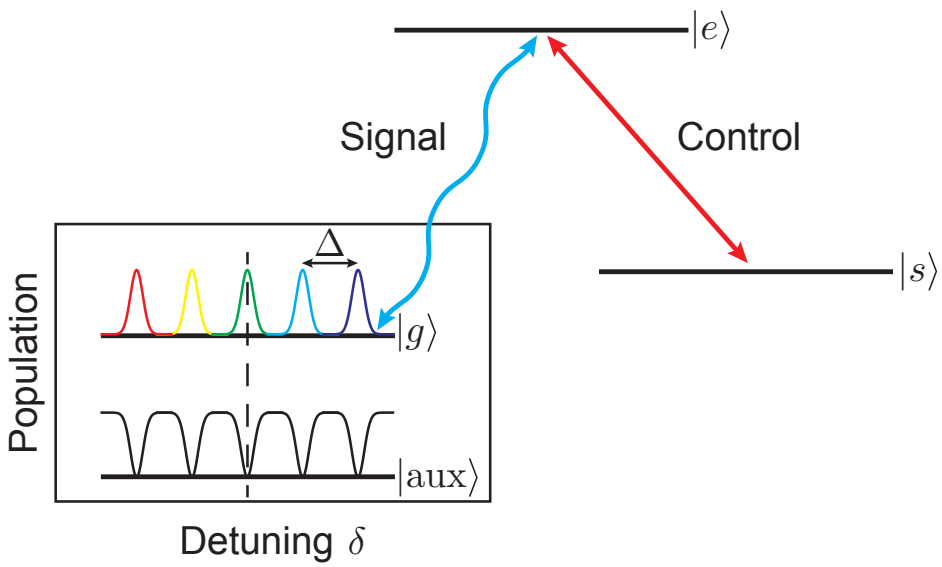

Figure 3.8: The AFC quantum memory scheme. A frequency comb with spacing Δ is prepared in the ground state $|g\rangle$ by removing atoms to an auxiliary state $|\text{aux}\rangle$ by optical pumping. A photon impinging on the medium is absorbed, exciting one of the atoms in the ensemble. A photon echo naturally occurs, and the photon re-released, after a storage time of $2\pi/\Delta$. To increase, and control, the storage time a control field transitions the atom to a long-lived state $|s\rangle$, freezing the dephasing process until the reverse transition is performed.

pumping to an auxiliary state $|\text{aux}\rangle$. Notice that here the comb is prepared by removing atoms from an already broad absorption line, instead of by broadening a thin absorption line, which was the case for CRIB. This means that the optical depth of each element in the comb remains high, whereas the efficiency of CRIB suffers from spreading out the remaining atoms. With a spacing of Δ between each frequency comb element, an absorbed photon will naturally echo after a time $2\pi/\Delta$. This is due to the discrete nature of the frequency comb.

Both CRIB and AFC memories have the capability of storing high-dimensional time-bin states [28], which makes them well-suited for quantum repeaters. The storage of entangled time-bin qubits in an AFC memory has been demonstrated in recent years. One demonstration [82] showed 21% memory efficiency over 200 ns of storage time with 120 MHz bandwidth photons (time-bandwidth product of 24) and violating Bell's inequality. Other demonstrations [83, 84] showed 0.2% efficient storage with light of over 5 GHz bandwidth. After a storage time was 7 ns (time-bandwidth product of 35), the retrieved state had a fidelity of 0.954 with the entangled input state.

Since the photon echo automatically re-emits the photon after a predetermined time, an additional action is required to have on-demand retrieval from an AFC memory. Some of the doped crystals used have an additional, long-lived, storage state $|s\rangle$ addressable with extra optical control fields. After absorption of the photon an applied π-pulse drives the transition $|e\rangle \rightarrow |s\rangle$, effectively freezing the evolution of the phase and preventing the photon echo. By applying a second π-pulse to drive the reverse transition, the re-phasing continues from where it left off and the photon is re-emitted by the echo. This complete version of the AFC storage protocol was recently demonstrated using heralded single photons [85]. With 11% memory efficiency, a storage time of 4.5μs was observed for 2.3 MHz bandwidth photons giving a time-bandwidth product of 10.

3.2.3 Single atom in a cavity

Single Rubidium atoms are also a promising platform for quantum information processing. (Ensembles of Rubidium atoms have also been shown, demonstrating single photon storage up to $\sim$1 ms [39].) By trapping single atoms and exploiting their strong coupling

with light fields, realizations of entangling quantum gates [86], non-destructive detection of photons [87] and non-linear phase gates [88] have been shown. Additionally multiple demonstrations of quantum memories have been shown. We will discuss two such implementations, which both use a single ^{87}Rb atom trapped in a cavity, though in slightly different fashions. Because these demonstrations couple light to hyperfine atomic lines the photon bandwidths are necessarily narrow. The experiments discussed in this section all use photon bandwidths $< 1\,\mathrm{MHz}$.

A first scheme

The first demonstration we discuss is that of Ref. [89], see Fig. 3.9. A single ^{87}Rb atom trapped in a cavity is prepared in the $|F = 1, m_F = 0\rangle$ hyperfine level. An incoming signal photon, which is resonant with the cavity frequency, has an arbitrary polarization state $|\psi\rangle = \alpha|L\rangle + \beta|R\rangle$. The left- and right-circular polarizations have spins along the propagation direction z, which we label as follows: $|L\rangle = |\uparrow_z\rangle$ and $|R\rangle = |\downarrow_z\rangle$. Because of this, they each couple to a different hyperfine level in the Rubidium energy structure. The left-circular component couples to the Stark-shifted state $|F' = 1, m_F = +1\rangle$, whereas the right-circular state couples to $|F' = 1, m_F = -1\rangle$. A π-pulse from a control field, geometrically perpendicular to the signal beam, stimulates a transition from the $|F' = 1, m_F = \pm 1\rangle$ states to the long-lived states $|F = 2, m_F = \pm 1\rangle$ for storage. The polarization state of the photon is mapped to the spin polarization of the atom. For retrieval, another π-pulse is used to drive the reverse transition where either $|F' = 1, m_F = +1\rangle$ or $|F' = 1, m_F = -1\rangle$ decays back to the ground state accompanied by the re-emission of the photon with either left- or right-circular polarization, respectively. Experimental demonstrations [89, 90] have confirmed that re-emitted light is quantum in nature (i.e., $g^{(2)}(0) < 1$), and have also shown average qubit state fidelities 93%. A memory efficiency of 9.3% was reported with a storage time of $184\,\mu\mathrm{s}$. With a bandwidth of $\sim 630\,\mathrm{KHz}$, the time-bandwidth product is 116.

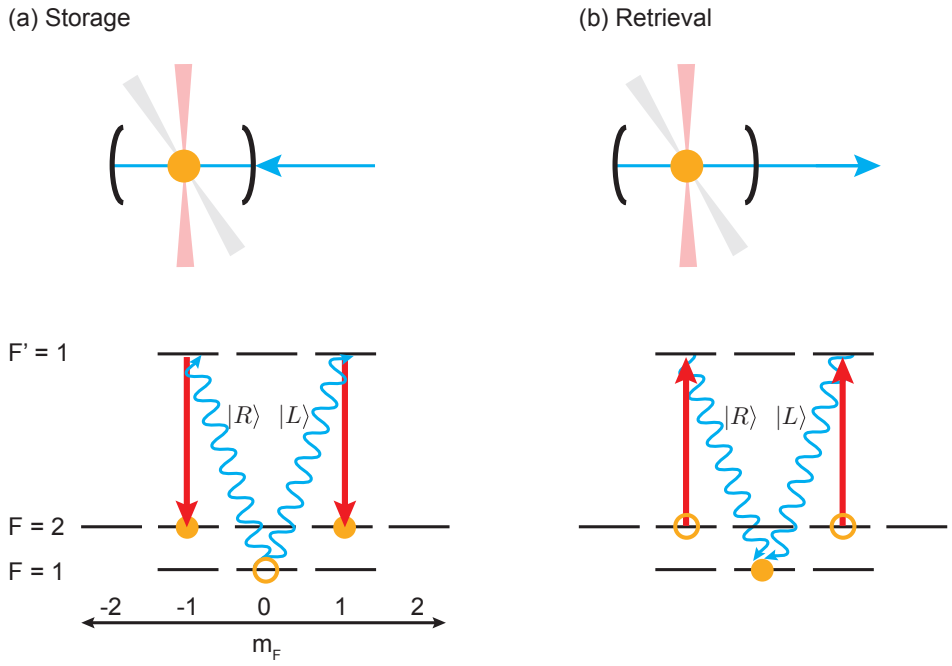

Figure 3.9: Storage and retrieval scheme for a single ^{87}Rb atom in a cavity (trapping laser in grey) from Ref. [89]. (a) The atom is prepared in the $|F = 1, m_F = 0\rangle$ state. An incoming photon (blue) has a polarization state $|\psi\rangle = \alpha|L\rangle + \beta|R\rangle$ that, when incident on the atom-cavity system, transfers the populations of its right- and left-circular polarizations to the $|F' = 1, m_F = 1\rangle$ and $|F' = 1, m_F = -1\rangle$ levels of the atom, respectively. A control field (red) stimulates a Raman transition from the $|F' = 1, m_F = \pm 1\rangle$ states to the long-lived $|F = 2, m_F = \pm 1\rangle$. (b) For retrieval, the control fields drive the reverse process, and a photon is emitted from the cavity with the populations of its two polarizations preserved by the memory.

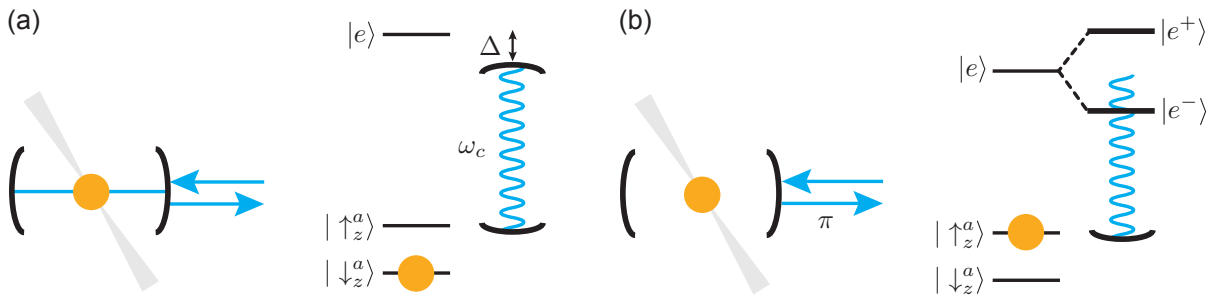

Figure 3.10: A second memory using a single atom in a cavity. (a) When preparing the atom in the state $|\downarrow_z^a\rangle$ it is not coupled to the cavity. A photon of any polarization enters and exits the cavity without incident. (b) When the atom is prepared in $|\uparrow_z^a\rangle$ and strong coupling with the cavity mode occurs, the excited state $|e\rangle$ splits into two levels $|e^+\rangle$ and $|e^-\rangle$. An incident photon with polarization $|L\rangle$ does not enter the cavity, but reflects off of the first mirror, picking up a π phase difference than the case in (a).

A second scheme

The second demonstration [91] exploits an energy level splitting given by the strong coupling with the cavity to map the polarization state of a photon onto the atom. Uniquely, the photon is not absorbed in this technique and is subsequently detected to herald the quantum transfer to the atom. The three relevant energy levels in this scheme are the hyperfine states $|F = 1, m_F = 1\rangle$, $|F = 2, m_F = 2\rangle$ and $|F' = 3, m_F = 3\rangle$ which we label $|\downarrow_z^a\rangle$, $|\uparrow_z^a\rangle$ and $|e\rangle$, respectively.

The cavity frequency is in resonance with the $|\uparrow_z^a\rangle \rightarrow |e\rangle$ transition, up to a detuning Δ. The transition between $|\downarrow_z^a\rangle$ and $|\uparrow_z^a\rangle$ is accessible using additional control fields but is uncoupled from the cavity. The simplified Hamiltonian for the coupled atom-cavity system follows a Jaynes-Cummings form

$$\begin{aligned} \mathcal{H}_{\text{JC}} &= \mathcal{H}_{\text{atom}} + \mathcal{H}_{\text{cavity}} + \mathcal{H}_{\text{int}} && (3.21) \\ &= \hbar(\omega_c + \Delta)|e\rangle\langle e| + \hbar\omega_c \hat{a}^\dagger \hat{a} + \hbar g \left(|e\rangle\langle\uparrow_z^a| \hat{a} + |\uparrow_z^a\rangle\langle e| \hat{a}^\dagger\right) && (3.22) \end{aligned}$$

where $\hbar\omega_c$ is the energies of the cavity, and g is the coupling strength between the atom and

cavity. The coupling strength g is proportional to the dipole moment of the atom, which is very high for Rubidium. The coupling of the atom and cavity results a splitting of the level $|e\rangle$ in to the dressed eigenstates $|e^+\rangle$ and $|e^-\rangle$ with an energy splitting $\hbar\sqrt{(2g)^2+\Delta^2}$. By incorporating the cavity loss rate κ and atomic decay rate γ into the Lindblad master equation, it can be shown [92] that the cavity lowering operator $\hat{a}$ is

$$\frac{\partial}{\partial t}\hat{a}(t) = -i[\hat{a},\mathcal{H}_{\rm JC}] - \left(i\Delta+\frac{\kappa}{2}\right)\hat{a} - \sqrt{\kappa}\hat{a}_{\rm in}(t) \tag{3.23}$$

$$\hat{a}_{\rm out}(t) \approx \frac{i\Delta-\kappa/2}{i\Delta+\kappa/2}\hat{a}_{\rm in}(t) \tag{3.24}$$

where $\hat{a}_{\rm in}$ and $\hat{a}_{\rm out}$ mark the input and output photon modes respectively. There are now a few cases to work through. First, when the atom is prepared in the uncoupled state $|\downarrow_z^a\rangle$ the Hamiltonian in Eq. 3.23 is irrelevant. If the detuning $\Delta \approx 0$, Eq. 3.24 gives $\hat{a}_{\rm out} \approx -\hat{a}_{\rm in}$. The same is true when the atom is initially in $|\uparrow_z^a\rangle$ but the polarization of the incoming photon is orthogonal, $|\downarrow_z^p\rangle = |R\rangle$. In these cases the output light has a π phase shift from the associated input.

The last case to look at is where the atom is prepared in $|\uparrow_z^a\rangle$ and the incoming photon is left-circularly polarized, $|\uparrow_z^p\rangle = |L\rangle$. Here the level $|e\rangle$ splits into $|e^+\rangle$ and $|e^-\rangle$ separated by $\sim 2g$. The relevant detuning Δ is then close to the coupling strength g. The strong coupling regime is defined as where $g \gg \kappa$, in which case we get from Eq. 3.24 that $\hat{a}_{\rm out} \approx \hat{a}_{\rm in}$. Effectively, the photon never enters the cavity but reflects off of the first mirror. Importantly, the output light does not pick up the π phase shift here, distinguishing it from the other cases. This effect is the basis for building a controlled-phase gate in Ref. [86].

To use this as quantum memory we can initialize the atom in the superposition $|\downarrow_x^a\rangle = (|\uparrow_z^a\rangle - |\downarrow_z^a\rangle)/\sqrt{2}$. An incident photon with arbitrary polarization $|\psi^p\rangle = \alpha|H\rangle + \beta|V\rangle$,

undergoes the transformation

$$
\begin{aligned}
|\psi^p\rangle|\downarrow_x^a\rangle &= \alpha\frac{(|L\rangle+|R\rangle)}{\sqrt{2}}\frac{(|\uparrow_z^a\rangle-|\downarrow_z^a\rangle)}{\sqrt{2}}+\beta\frac{(|L\rangle-|R\rangle)}{\sqrt{2}}\frac{(|\uparrow_z^a\rangle-|\downarrow_z^a\rangle)}{\sqrt{2}} && (3.25)\\
&\rightarrow \frac{\alpha}{2}\left(|L\rangle|\uparrow_z^a\rangle+|L\rangle|\downarrow_z^a\rangle-|R\rangle|\uparrow_z^a\rangle+|R\rangle|\downarrow_z^a\rangle\right)\\
&\qquad +\frac{\beta}{2}\left(|L\rangle|\uparrow_z^a\rangle+|L\rangle|\downarrow_z^a\rangle+|R\rangle|\uparrow_z^a\rangle-|R\rangle|\downarrow_z^a\rangle\right) && (3.26)\\
&= \frac{\alpha}{\sqrt{2}}\left(i|V\rangle|\uparrow_z^a\rangle+|H\rangle|\downarrow_z^a\rangle\right)+\frac{\beta}{\sqrt{2}}\left(|H\rangle|\uparrow_z^a\rangle+i|V\rangle|\downarrow_z^a\rangle\right) && (3.27)\\
&= \frac{1}{\sqrt{2}}\left(|H\rangle\sigma_x|\psi^a\rangle+|V\rangle|\psi^a\rangle\right) && (3.28)
\end{aligned}
$$

where the atomic qubit is $|\psi^a\rangle=\alpha|\uparrow_z^a\rangle+\beta|\downarrow_z^a\rangle$. The photon can then be measured in the computational basis, transferring the qubit on the atomic spins. The σ_x correction for the atomic can be applied with optical control pulses.

This memory, of all the examples we look at in this chapter, is unique in that the photon itself is not absorbed by the medium but simply transfers its quantum information. Therefore, in order to retrieve the qubit from the memory we need another photon to be incident on the memory. By a similar protocol, an incoming photon prepared as $(|H\rangle+|V\rangle)/\sqrt{2}$, together with the atom in the state $|\psi^a\rangle$ will be transformed to

$$
\frac{(|H\rangle+|V\rangle)}{\sqrt{2}}\rightarrow\frac{1}{\sqrt{2}}\left(|\psi^p\rangle|\uparrow_x^a\rangle+\sigma_x|\psi^p\rangle|\downarrow_x^a\rangle\right) \qquad (3.29)
$$

A measurement of the atom, using fluorescence, transfers the qubit back on to a photon. The photon-to-atom state mapping was demonstrated with 39% efficiency and 0.86 state fidelity. The reverse process, atom-to-photon, was 69% efficient with fidelity of 0.88, giving a projected overall efficiency of 27%. These were performed as separate experiments and so the storage time was not studied.

3.2.4 Off-resonant Raman memories

The off-resonant Raman memory scheme uses an atomic ensemble, or solid-state medium, with a Λ-level energy structure. Since the diamond quantum memory is in this category

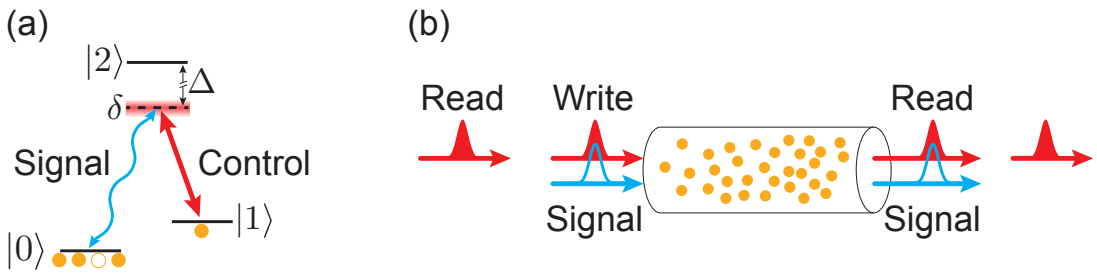

Figure 3.11: The off-resonant Raman quantum memory. (a) The energy structure of a Raman memory. The signal and control fields are in two-photon resonance with the storage state $|1\rangle$. Large detuning Δ from the intermediate state $|2\rangle$, in conjunction with large energy splitting between $|0\rangle$ and $|1\rangle$, allow for the storage of broadband signal photons. (b) A *write* control pulse absorbs a signal photon in the medium via the Raman transition. A *read* pulse later retrieves the photon from the medium by the reverse transition.

we will discuss this system in depth in Chapter 4. As we will see (also refer to Appendix E) the dynamics of this system [93] are similar to those for the EIT memory. The essence of the scheme goes as follows (see Fig. 3.11). The memory ensemble of N atoms is initially prepared with each atom in its ground state $|0_1...0_N\rangle$. An incoming signal photon which, along with a strong control field, is in two-photon resonance with the storage state $|1\rangle$. The ensemble is then transitioned to the superposition over all atoms

$$|\psi_1\rangle = \sum_j c_j e^{ik_j z} |0_1...1_j...0_N\rangle, \tag{3.30}$$

where the j^{th} atom is at position z. Notably in this scheme the signal photon and control field are far-detuned from the excited intermediate state $|2\rangle$. This large detuning, Δ, together with a large energy splitting the ground and storage states, allows for large signal bandwidths to be stored. The Raman coupling of the light, which is a function of the dipole moment of the medium and the strength of the control field, must then be large to overcome decreased efficiency with large Δ. A strong control pulse, called the *write* pulse, stimulates the Raman transition which absorbs the signal photon. After an on-demand storage time the reverse transition is driven by a *read* pulse, retrieving the photon. The input and output photons are often in the same spatial mode, in which case they can be

distinguished with either detection timing or polarization. It is also possible to retrieve the photon in the reverse propagation direction.

The first demonstration of a Raman quantum memory used room-temperature Cesium atomic vapour [30]. An initial experiment [94] showed single-photon-level storage of 1.5 GHz bandwidth light for 4 μs with a memory efficiency of 30%. This gives a time-bandwidth product of 6000. Polarization states using single-photon level pulses were stored with 8% efficiency and a process fidelity of 0.86 for 1.5 μs of storage. More recent experiments [95] have used Cesium vapour trapped in a hollow-core fibre to increase coupling strength, with efficiencies as high as 27% at the single-photon level. Strategies to characterize [96] and reduce [97] noise in the memory have also been investigated.

A Raman memory using the vibrational states of hydrogen molecules was also recently demonstrated [31]. The memory stored attenuated laser pulses, with bandwidth exceeding over 4 THz, for up to 1 ns with an efficiency of 18%. This gave a time-bandwidth product of $\sim$4000.

Another demonstration of a Raman quantum memory [98] has shown storage of single photons as well as polarization-entangled photons in an ensemble of trapped Rubidium atoms. A Bell inequality was violated with retrieved light and a fidelity of 0.85 with the input state was measured. An efficiency of $\sim$21% was reported for 140 MHz bandwidth light with a storage time of 1.4 μs, giving a time-bandwidth product of 196.

3.3 Beyond long distance applications

In this section we explore applications of quantum memories beyond the traditional use for synchronization of entanglement swapping in quantum repeaters. Specifically we will look at their use in controlling the spectral-temporal modes of single photons, and their use in recent quantum information processing protocols. A helpful review for this subject is Ref. [72].

3.3.1 Optical signal processing

Quantum frequency conversion [99] is the act of changing the centre frequency of a photon while preserving its quantum nature; this also implies preserving the state of any quantum information encoded in the photon. Large frequency shifts are desirable for coupling components that function optimally at disparate optical frequencies, e.g., fibre optic cables and coupling to atomic systems. Meanwhile, small frequency shifts can be useful for wavelength-division multiplexing. Both small [100, 101] and large [102, 103, 104, 105, 106] frequency shifts, as well as bandwidth manipulation [107], have been demonstrated with second- and third-order nonlinear optical materials. However, for full control over spectral and temporal modes a single photon buffer is required, i.e., a quantum memory.

Some implementations of quantum memories have shown the dual functions of storage and spectral conversion, providing an avenue towards full spectral-temporal control. Memories based off of photon echo techniques have capability for manipulation of the frequency and bandwidth of a stored photon [108, 109]. In Ref. [108] a weak coherent signal field was frequency converted over a $\sim$1 MHz range. In Ref. [109] a stored input photon pulse could be compressed or stretched for arbitrary re-shaping. Raman memories have also been proposed as means to convert the centre frequency and bandwidth of the stored photon [93]. This is the main result of Chapter 7. As we will see, by changing the spectrum of the read pulse, the spectrum of the retrieved photon follows correspondingly, to within phase matching conditions.

Mapping between temporal modes

By reversibly mapping between stationary and flying qubits, quantum memories naturally act as a means to re-arrange temporally, or time-bin, encoded quantum states. Some quantum memories have shown the capability to perform arbitrary sorting of temporal modes as a built in function [80]. Through directional flips of the external magnetic field, which controls the photon echo, the retrieval times of each input time-mode can be controlled.

For Raman memories, the failure mode of the write process is simply the transmission

of the signal photon through the medium. Similarly once stored, if the read process fails the material excitation remains and a photon is not re-emitted. We can then think of the storage and retrieval operations in a quantum memory as beamsplitters between the optical and storage modes. With multiple read pulses we can then distribute a stored photon over multiple time-bins. Ref. [110] demonstrated this concept with the use of the Cesium vapour memory as a beamsplitter network between time-bins. In Chapter 8 we demonstrate the use of a quantum memory as the beamsplitter between photons in separate temporal modes.

3.3.2 Quantum information processing

Linear-optical quantum computing requires a two-photon entangling gate that is inherently probabilistic [41]. In order to synchronize these gates with parallel processes storage of the photons in a quantum memory is necessary. Also, by storing the successful output of probabilistic gates quantum memories allow repeat-until-success strategies to be used, enhancing the success rate of the computation. In a similar fashion quantum memories can store the output of inherently spontaneous photon sources, such as those based on spontaneous parametric downconversion, for later use. This counteracts the probabilistic nature of photon sources and allows parallel sources to be synchronized providing a more efficient avenue to building high photon number states [111]. Controllable, high-fidelity light-matter interactions, which quantum memories fall under the umbrella of, are highly useful for the development of quantum information processors. We have already discussed one quantum memory, a single Rubidium atom in a cavity, that doubles as both an entangling gate and a non-destructive photon detector.

In recent years there have been proposals for quantum information processing that require the use of quantum memories [112, 113, 114]. A protocol introduced in Ref. [112] gives a technique for performing a universal set of quantum gates on optical time-bin qubits propagating in a single spatial mode. The technique requires arbitrary control of time-bin ordering, which has been demonstrated with quantum memories [80]. By appropriately shuffling time-bins they can be coupled, using the polarization degree of freedom, by a waveplate. Single-qubit operations can be implemented with some ease, and an entangling

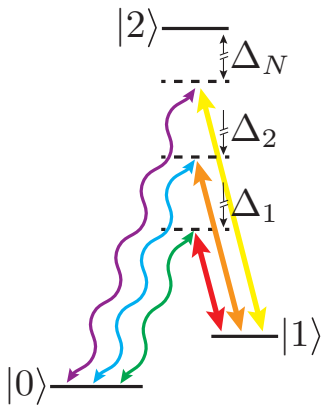

Figure 3.12: N signal frequencies, each having detuning Δ_i from the excited state $|2\rangle$ are each mapped to the storage mode $|1\rangle$ by complementary controls fields. Information carried between the signal frequency modes can mapped to the coherences between levels $|0\rangle$ and $|1\rangle$ in a series of quantum memories. By tuning the control fields for each mode, an arbitrary quantum logic gate can be performed on the frequency-multiplexed information.

gate can be implemented using ancilla photons, mode couplings and post-selection [41].

Arbitrary quantum logic gates on frequency-multiplexed qubits using quantum memories have also been proposed [114]. Using a series of frequency selective quantum memories, such as Raman memories, we could encode and manipulate information in the frequency degree of freedom, see Fig. 3.12. With multiple frequency bins, each far-detuned from the memory's excited state $|2\rangle$, appropriately chosen control pulses frequencies will coherently map the frequency-bin quantum information into the series of quantum memories, performing a logic gate in the process. A second logic gate can be performed upon retrieval from the memories. The authors in Ref. [114] give an explicit scheme for performing a controlled Z-gate between frequency-bin qubits which, similar to that of KLM [41], requires ancilla qubits and postselection.

Building time-frequency encoded cluster states

Another approach to quantum computing is measurement-based quantum computing [6, 7]. Here the idea is to construct cluster states, large entangled states, to use as a resource.

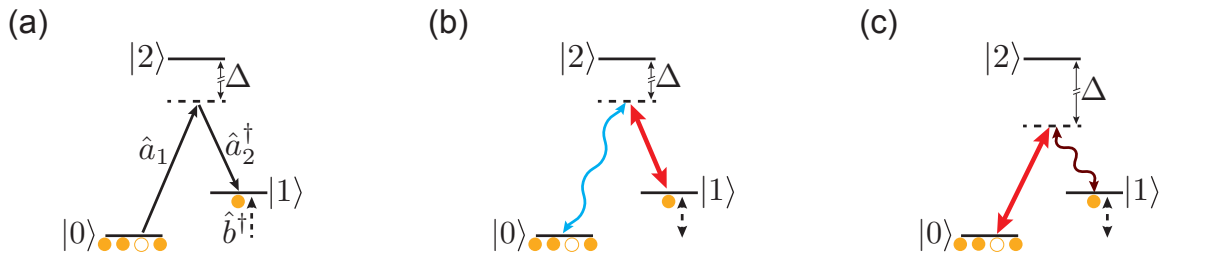

Figure 3.13: (a) The Hamiltonian for an off-resonant Raman process with coupling constant κ. For a photon annihilated in the $\hat{a}_1$ mode, one is created in the $\hat{a}_2$ mode along with a material excitation in the $\hat{b}$ mode. (b) A strong field of amplitude γ in the $\hat{a}_2$ mode turns the process into one analogous to a beamsplitter (BS) between $\hat{a}_1$ and $\hat{b}$ modes. (c) A strong field of amplitude γ in the $\hat{a}_2$ mode gives two-mode squeezing (Sq) between the $\hat{a}_2$ and $\hat{b}$ modes.

Then, universal quantum computations can be performed solely with measurement and feed-forward techniques. The challenge of implementation is shifted from realizing entangling gates to generating large initial entangled states. For optics, this is a good trade-off since generating entangled states with spontaneous parametric downconversion is generally easier than making photons interact with one another in entangling gates. That being said, the current record for a photonic cluster state is 8 qubits [115]; building larger states remains a challenge.

Recently a scheme [113] based on Raman quantum memories presented a method to construct large cluster states in the frequency-time degrees of freedom of photons. A simplified Hamiltonian for the Raman memory has the form

$$\mathcal{H}_{\text{Raman}} = \kappa\hat{a}_1\hat{a}_2^\dagger\hat{b}^\dagger + \kappa^*\hat{b}\hat{a}_2\hat{a}_1^\dagger \tag{3.31}$$

Where optical modes $\hat{a}_1$ and $\hat{a}_2$ are in two-photon resonance with energy level $|1\rangle$, producing a material excitation in mode $\hat{b}$ with coupling strength κ. By using a strong classical pulse in either the $\hat{a}_1$ or $\hat{a}_2$ modes can give either a squeezing (Sq.) or beamsplitter (BS) interaction

between photon and memory modes, see Fig. 3.13. Replacing $\hat{a}_1$ or $\hat{a}_2$ with the classical field amplitude γ we find

$$\mathcal{H}_{\mathrm{Sq}} = \kappa\gamma\hat{a}_2^\dagger\hat{b}^\dagger + \kappa^*\gamma^*\hat{b}\hat{a}_2 \tag{3.32}$$

$$\mathcal{H}_{\mathrm{BS}} = \kappa\gamma^*\hat{a}_1\hat{b}^\dagger + \kappa^*\gamma\hat{b}\hat{a}_1^\dagger \tag{3.33}$$

Using a combination of the beamsplitter and two-mode squeezing interactions we can construct a series of two-mode entangled time-bin states. Then with another combination of beamsplitters and squeezers, time-bin states with different central frequencies can be entangled to construct a large two-dimensional cluster. It has been shown that to build a cluster state across d frequency modes we would require $7d - 3$ quantum memories. We could perform the necessary measurements and feed-forward can be performed with additional quantum memory interactions.

Though we have given only a brief overview it is clear that there is a growing bounty of applications for quantum memories, particularly those which have control over spectral degrees of freedom.

Chapter 4

Diamond as a quantum memory

Diamond has been identified as a promising material for quantum information applications [116]. Defect centres in the diamond lattice have been used for processing, single-photon sources, and to demonstrate a loophole-free Bell test [4]. However, our work in this thesis is not concerned with defect centres, but with the vibrational properties of the bulk diamond crystal. Diamond is a well-understood material; its electronic and vibrational band structure have been thoroughly studied. High purity, low-birefringence diamond crystals can be grown by chemical vapour deposition.

In recent years, the optical phonon mode in diamond has been demonstrated to be promising for quantum information processing by two initial experiments [68, 40]. A Raman interaction makes the optical phonon mode addressable with light fields, with very high bandwidths. This allows ultrafast laser pulses to be used to drive the interaction. In Ref. [40] the authors reported the generation of non-classical light, i.e., photon pairs. A strong laser pulse, with 800 nm centre wavelength, pumped the Raman transition producing a spontaneous Stokes photon, with 895 nm centre wavelength, and exciting an optical phonon. A second 800 nm laser pulse, arriving before the phonon decays, probes the phonon level producing a spontaneous anti-Stokes photon at 723 nm. Detecting the forward-propagating Stoke and anti-Stokes photons in coincidence showed $g^{(2)}_{s,as} > 2$, where the second-order coherence cross-correlation function is as defined in Eq. 2.66.

In Ref. [68] this process was used in two separate diamond crystals simultaneously to

enact the DLCZ protocol (see Section 3.1.3). The spontaneous Stokes photons from each diamond were interfered on a beamsplitter. A detection upon output from the beamsplitter entangled the optical phonon modes between the two diamonds. Probing each diamond to produce the anti-Stokes photons "read-out" the entanglement to light modes where it could be verified.

These two experiments sparked interest in the light-matter interaction in the diamond vibration modes, particularly for use as a quantum memory. An initial experiment [32] demonstrated the reversible mapping between a single-photon level laser pulse and the optical phonon, constituting an optical memory. In this thesis we extend this work for the storage of single photons.

The remainder of this chapter is laid out as follows. We will first discuss the structure of the diamond crystal lattice and review the concept of optical phonons. We will discuss the Raman transition to the optical phonon mode, and the requirements on the light fields involved. We then shift to how our quantum memory functions with some experimental discussion. We will discuss noise processes that arise in the diamond. We conclude with some theoretical background for how diamond can be used as a frequency converter.

4.1 The diamond crystal

The diamond crystal is two interlaced face-centred cubic (FCC) lattices of ^{12}C atoms. The size of the unit cell, see Fig. 4.1, is $a = 3.57\,\text{Å}$ [117]. We can picture the lattice as a single FCC lattice where each point is comprised of two ^{12}C atoms offset by a vector $\vec{r} = a/4(\hat{x}+\hat{y}+\hat{z})$. The electronic band structure of diamond is well studied [118, 119]; the bandgap between its valence and conduction bands, 5.4 eV (∼1300 THz), is large compared to the energies of the optical fields we use in our experiment (∼450 THz).

The conduction band acts as the intermediate state in a Raman transition to a vibrational mode in the lattice, which is what we are interested in here. The vibrational band structure of diamond is also well studied. Early experiments on the vibrational energy spectrum of diamond were performed by Raman [120, 121]. Ref. [122] gives a nice review

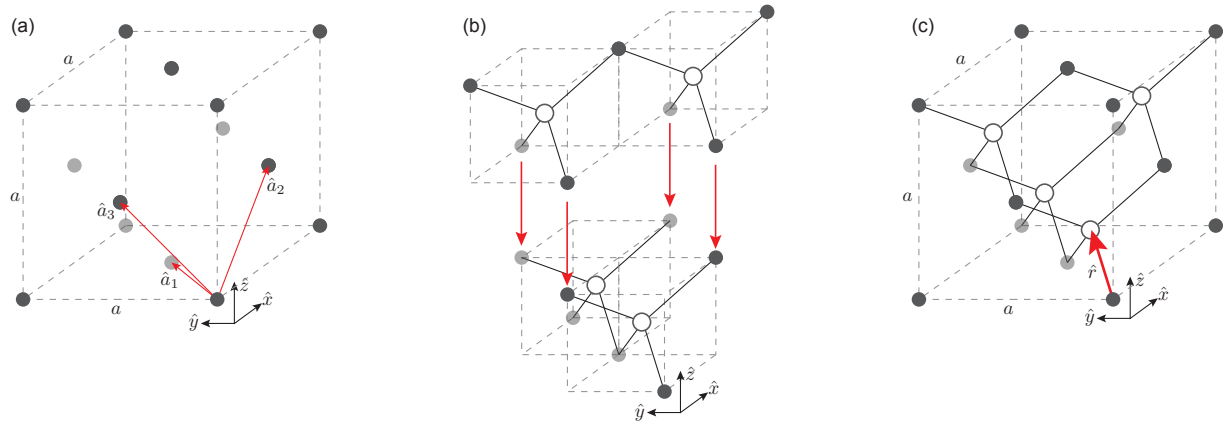

Figure 4.1: (a) A face-centred cubic lattice is defined by primitive vectors, $\hat{a}_1 = a/\sqrt{2}(\hat{x} + \hat{y}), \hat{a}_2 = a/\sqrt{2}(\hat{x} + \hat{z}), \hat{a}_3 = a/\sqrt{2}(\hat{y} + \hat{z})$. For diamond $a = 3.57\,\text{Å}$. Translation by a vector $\vec{R}_n = n_1\hat{a}_1 + n_2\hat{a}_2 + n_3\hat{a}_3$ will land on another atom in the lattice for any integers $n_{1,2,3}$. (b) The diamond crystal structure can visualized as the joining of tetrahedral arrangements of Carbon atoms (white and black dots are both Carbon, semi-transparent black dots are to visualize depth). (c) Diamond is two inter-lacing face-centred cubic (FCC) lattices (one sub-lattice is shown with black dots, the other with white dots) offset by basis vector $\vec{r} = a/4(\hat{x} + \hat{y} + \hat{z})$.

on the subject. Specifically, we are interested in a vibrational excited state of the diamond, the *optical phonon* level.

4.2 Vibrational modes and phonons

There are various vibrational modes that can arise in diamond. Vibrational properties of highly symmetric systems, like crystal lattices, can be solved with group theory [123, 124, 125, 126] (see Appendix F). However, here we will introduce the conceptual differences between different vibrational modes using Newton's second law. We will explicitly work through the case for a one-dimensional chain of atoms, the results of which are very analogous to the three-dimensional case. Ref. [117] is an excellent resource for this discussion.

4.2.1 One-dimensional lattice

First, we will consider a linear chain of N atoms, each of mass M, separated by spacing a and connected by springs with constant K, shown in Fig. 4.2(a). When the system is in equilibrium, i.e., no vibrations, the n^{th} atom in the chain is in the position na. When perturbed from equilibrium, the atom is displaced by an amount $u(na)$. For this discussion we assume the displacements are small relative to the atom spacing a. This is referred to as the harmonic approximation. The total potential of the chain is

$$\mathcal{U} = \frac{1}{2}\sum_{n,m} \xi\left\{u(na) - u[(n+m)a]\right\} \tag{4.1}$$

where here $\xi\{u(na) - u[(n+m)a]\}$ is the potential between the n^{th} and $(n+m)^{\text{th}}$ atoms. Under the harmonic approximation the displacements $u(na)$ are small enough that we can Taylor expand the potential about equilibrium positions and only consider the first few terms. (In practice this approximation works well, however the lifetime of the vibrational level we are interested in for diamond is largely limited by the breakdown of this

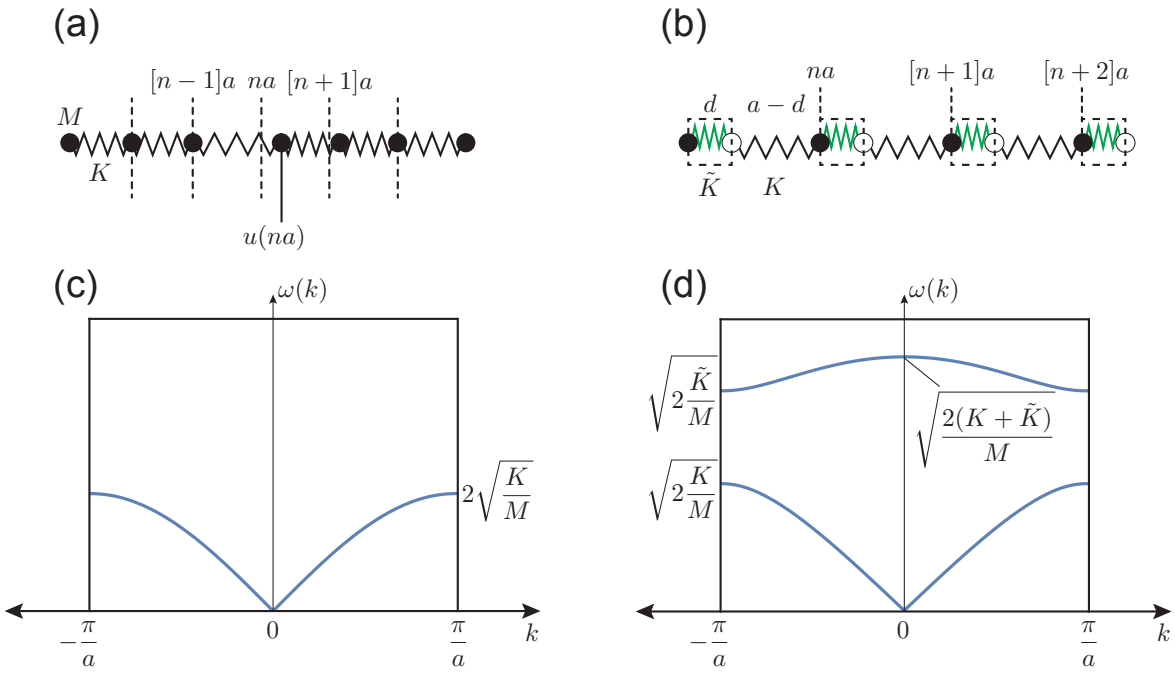

Figure 4.2: (a) A linear chain of atoms of mass M spaced a distance a apart and connected by springs with constant K. The n^{th} atom has an equilibrium position na, and a small displacement from equilibrium given by $u(na)$. (b) A linear chain of atoms with a basis. The atoms all have mass M but now each basis, marked by dashed boxes, has two atoms connected by a spring of constant $\tilde{K}$, whereas each group of two is connected with a spring of constant K. At equilibrium black dots are separated by distance a and the separation in each basis is d. (c)-(d) The respective dispersion relations for the cases in (a) and (b). (d) The addition of a basis adds a second vibrational mode, with energy splitting given by the spring constants. The original mode is the *acoustic phonon* branch; the new mode is the *optical phonon* branch. If $K = \tilde{K}$ the two branches meet at the zone boundary, $k = \pm\pi/a$.

approximation.) The potential expands to

$$\begin{aligned}\mathcal{U} &\approx \frac{N}{2}\sum_n \xi\left(na-ma\right)+\frac{1}{2}\sum_{n,m}[u(na)-u(ma)]\frac{\partial}{\partial x}\xi\left(na-ma\right)\\ &\quad+\frac{1}{4}\sum_{n,m}[u(na)-u(ma)]^2\frac{\partial^2}{\partial^2 x}\xi\left(na-ma\right)+...\end{aligned} \tag{4.2}$$

The zero-order term is the potential when the chain is in equilibrium which we label $\mathcal{U}_{\text{eq}}$. The first-order term gives the first derivative of the potential between two atoms at equilibrium, which equals the negative of the force between them. This is summed over the whole chain giving the net force on one atom due to every other. However, with the chain in equilibrium there is no net force between any atoms, and so the first-order term must be equal to zero. The second-order term we will refer to as $\mathcal{U}_{\text{harm}}$ and drives the dynamics we want to look at.

To simplify matters we only consider nearest-neighbour interactions in the chain. We can then label the second derivative of ξ by its more frequently known form, the spring constant K. We have

$$\mathcal{U}_{\text{harm}} = \frac{K}{2}\sum_n\{u(na)-u[(n+1)a]\}^2 \tag{4.3}$$

We now solve the dynamics for the n^{th} atom using Newton's second law.

$$M\ddot{u}(na) = -\frac{\partial\mathcal{U}_{\text{harm}}}{\partial u(na)} \tag{4.4}$$

$$= -\frac{K}{2}\left\{2u(na)-u[(n-1)a]-u[(n+1)a]\right\} \tag{4.5}$$

We guess a plane wave solution $u(na)=c_1e^{i(kna-\omega t)}$ with wavevector k and frequency ω, and where c_1 is constant with units of position. Since we care about the dynamics in the bulk of the material and not near the edges, we take the boundary solutions to be periodic, $e^{ikNa}=1$. The effect of this is that $kn=2\pi n/aN$ which sets the boundaries $-\pi/a<k<\pi/a$ for $-N/2<n<N/2$. Substituting our solution into Eq. 4.5 we get

$$-M\omega^2 = -\frac{K}{2}\left\{2-e^{-ika}-e^{ika}\right\} \tag{4.6}$$

$$\omega(k) = 2\sqrt{\frac{K}{M}}\left|\sin\frac{ka}{2}\right| \tag{4.7}$$

Equation 4.7 is known as a dispersion relation. It gives the energy of a vibration for a wavevector k. We can see that for small k the dispersion increases linearly from 0, and tapers off to a maximum of $2\sqrt{K/M}$ at the boundaries. This relation is plotted in Fig. 4.2(c).

4.2.2 One-dimensional lattice with a basis

Next we consider a scenario much closer to that of the diamond, though still one-dimensional. Suppose each atom in the linear chain above was really compromised of two smaller constituents separated by a distance d and themselves connected by a spring with constant $\tilde{K}$. A schematic of this is shown in Fig. 4.2(b). This scenario is referred to as a lattice with a basis. We can think of each two-atom unit as we did above, and recover the same dispersion relation. However by considering vibrations within the basis, e.g., the two atoms beating out of phase from one another, we can see some additional physics (see Fig. 4.2(d)).

To solve the dynamics of this system we consider again only nearest neighbour interactions. The displacement of the first atom in the basis, shown as the black dot in Fig. 4.2(b), is given by $u_1(na)$. The displacement of the second atom, white dot, is $u_2(na)$. The harmonic potential is then given by

$$\mathcal{U}_{\text{harm}} = \frac{\tilde{K}}{2}\sum_n [u_1(na) - u_2(na)]^2 + \frac{K}{2}\sum_n [u_2(na) - u_1([n+1]a)]^2 \tag{4.8}$$

where the first term describes the potential within a basis and the second is between neighbouring bases. We can substitute this into Newton's second law for each of the two atoms,

$$\begin{aligned} M\ddot{u}_1(na) &= -\frac{\partial \mathcal{U}_{\text{harm}}}{\partial u(na)} \\ &= -\tilde{K}\left\{u_1(na) - u_2(na)\right\} - K\left\{u_1(na) - u_2([n-1]a)\right\} \qquad (4.9) \\ M\ddot{u}_2(na) &= -\frac{\partial \mathcal{U}_{\text{harm}}}{\partial u(na)} \\ &= -\tilde{K}\left\{u_2(na) - u_1(na)\right\} - K\left\{u_2(na) - u_1([n+1]a)\right\} \qquad (4.10) \end{aligned}$$

We guess the plane wave solution again,

$$u_1(na) \;=\; c_1 e^{i(kna-\omega t)}, \quad u_2(na) = c_2 e^{i(kna-\omega t)} \tag{4.11}$$

where c_1 and c_2 are constants with units of position. Solving the system of equations we find the dispersion relation

$$\omega(k) = \left[\frac{K+\tilde{K}}{M} \pm \frac{1}{M}\sqrt{K^2+\tilde{K}^2+2K\tilde{K}\cos ka}\right]^{\frac{1}{2}} \tag{4.12}$$

requiring that $c_2/c_1 = \pm(Ke^{ika}+\tilde{K})/|(Ke^{ika}+\tilde{K})|$. The dispersion relation is plotted in Fig. 4.2(d). We can see that there are two distinct values of ω for each k. We have the same values as in the simple linear chain, increasing linearly from 0 and reaching a value of $\sqrt{2K/M}$ at the boundary. This is called the *acoustic phonon band*, since it refers to travelling vibrational waves, sound waves. But we also have a second band of values, starting from $\sqrt{2(K+\tilde{K})/M}$ and decreasing as $1-\cos(ka)$. The band decreases to $\sqrt{2\tilde{K}/M}$ at the boundary, giving a bandgap when $K \neq \tilde{K}$. The vibrations giving rise to this band are standing waves within a basis, the beating of the white and black dots against one another in Fig. 4.2(b). This is called the *optical phonon mode* since their energies are often close to those of optical frequencies.

4.2.3 Phonon: the quantum of vibration

We have used the term *phonon* a few times without giving a definition. By treating the harmonic potential quantum mechanically we add together many single-mode harmonic oscillators to form a crystal Hamiltonian

$$\mathcal{H}_{\text{crystal}} = \frac{P^2}{2M} + \mathcal{U}_{\text{harm}} \tag{4.13}$$

where $P^2/2M$ represents the sum of the kinetic energy terms over all single-mode harmonic oscillators in the crystal. As with the single-mode harmonic oscillator we can write $\mathcal{H}_{\text{crystal}} = \sum_k \hbar\omega_k(\hat{b}_k^\dagger \hat{b}_k + 1/2)$, where the sum is over all vibrational modes k. We then

have energy eigenvalues of $E_{n,k} = \hbar\omega_k(n_k + 1/2)$ where there are n excitations in the k^{th} normal mode. The operator $\hat{b}_k$ is the lowering operator for a single vibrational excitation in mode k, and has all the same properties as the lowering operator for photons. Due to this similarity with photons, and since the vibrational modes are related to sound, the term *phonons* was adopted. One phonon is then a single excitation of a vibrational mode in the crystal.

4.2.4 Vibrational modes in diamond

The vibrational modes in diamond follow the same general pattern as what we have just look at in the one-dimensional case. The two inter-lacing face-centred cubic lattices in the diamond structure can be thought of as a single FCC lattice with a basis. Because of the two-atom basis, we expect two types of vibrations to occur: acoustic and optical. Since the crystal is three-dimensional we also expect that there will be three branches of each type, one for each direction. It is also important to note that the wavevector $\vec{k}$ is three-dimensional and so the phonon dispersion relation $\omega(\vec{k})$ will look different along the various axes (see Fig. 4.4). The energies of all three optical phonon branches at the zone centre, i.e., $k = 0$, are equal to $2\pi\hbar \times 40\,\text{THz}$ [122]. Away from $k = 0$ the optical branch splits into longitudinal and transverse branches with different energies. We are concerned with the longitudinal phonon branch, which we can address with the appropriate polarizations of incident light (discussed in Section 4.3). We are also concerned with the $k = 0$ phonon mode; the difference in energies of phonons at $k = 0$ and the zone boundary is approximately $2\pi\hbar \times 4\,\text{THz}$.

We are now in a position introduce the relevant three-level system for our quantum memory (see Fig. 4.4). The ground of the state crystal, $|0\rangle$, has no vibrations. The storage state, $|1\rangle$, is the optical phonon level. Strictly speaking the optical phonon branch is a continuum, however near the zone centre ($k = 0$) its energy is well defined as 40 THz above the ground state, with a linewidth of $\sim 0.3\,\text{THz}$. While the crystal will not be free of acoustic vibrations at room temperature, the large energy splitting ensures a low population ($\sim 1.6 \times 10^{-3}$) of optical phonons at room temperature. This means that to a good approximation the memory is initialized in the ground state, and as we will discuss later,

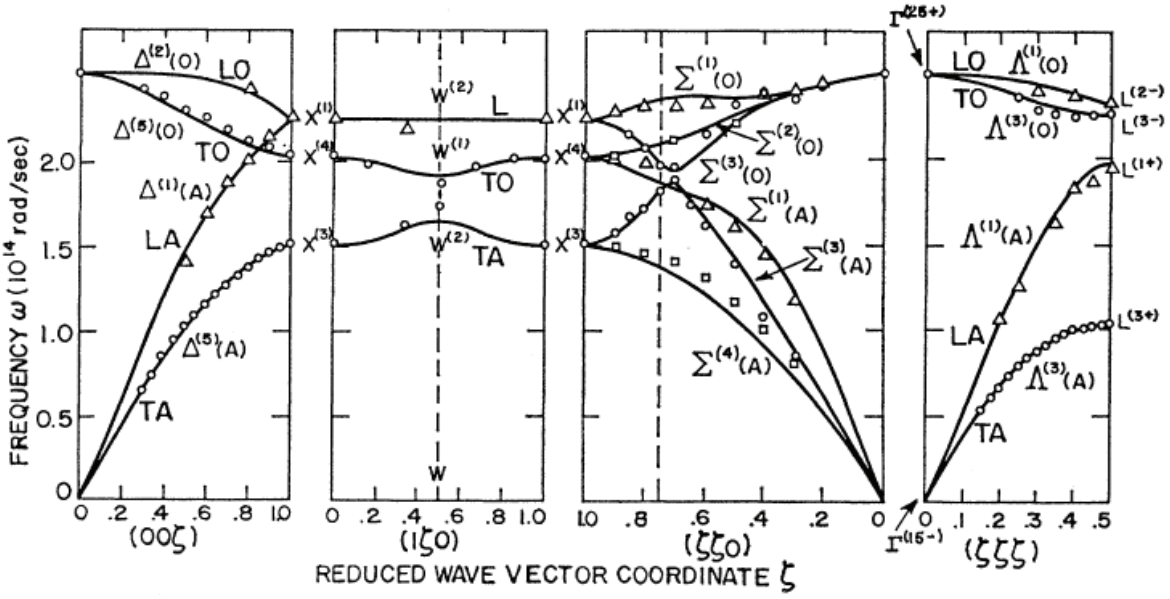

Figure 4.3: Reproduced from *Solin & Ramdas*, Physical Review B, **1** 1670 (1970) with permission from the American Physical Society (License Number 3895380446931). Measured phonon dispersion curve in diamond across important wavevector directions. In the first pane, there is a 40 THz (2.51×10^{14} rad/s) splitting between acoustic and optical branches at the zone centre (000). Away from the zone centre each branch splits into longitudinal and transverse modes: longitudinal optical (LO); transverse optical (TO); longitudinal acoustic (LA); transverse acoustic (TA). At the zone boundary (001) the longitudinal optical and acoustic branches are equal, which is equivalent to the one-dimensional case where the two spring constants are equal. Greek letters label the symmetry that each branch has.

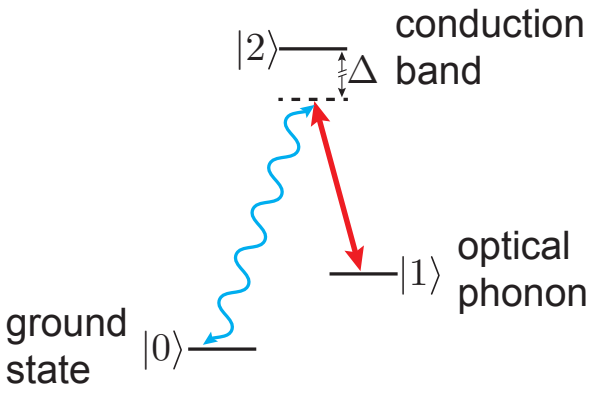

Figure 4.4: The relevant energy levels for the diamond quantum memory. The optical phonon $|1\rangle$ is the storage state, which has a 40 THz splitting from the ground state, where there are no vibrations in the crystal. The light fields used to address $|1\rangle$ are detuned by ~ 950 THz from the conduction band, $|2\rangle$, which acts as an intermediate state.

suppresses the generation of noisy photons that can degrade our memory functionality. Lastly, we will need an intermediate state for the Raman transition. The electron conduction band, $|2\rangle$, plays this role, which is far above the ground state, ~1300 THz. This means that the incident optical fields, 800 nm and 723 nm wavelengths, are detuned by ~950 THz from $|2\rangle$. This large detuning, in tandem with the 40 THz splitting between ground and storage states, is the basis for the large acceptance bandwidth of the memory.

4.2.5 Decay of optical phonon

So far we have assumed that the crystal vibrations are perfect harmonic oscillations. We also assumed that atoms only interact with their nearest neighbours. However, this is not the reality. Deviations from the harmonic approximation, *anharmonicity*, will cause more complex lattice vibrations. Both these effects will produce a coupling between the optical phonon vibrations and lower-energy acoustic vibrations. By treating the deviation from harmonic oscillation as a first-order perturbation, it has been shown [127] that the dominant mechanism for the decay of the optical phonon produces two acoustic phonons

with equal and opposite $\vec{k} \neq 0$. In other words, the standing wave formed by the two sub-lattices beating out of phase against one another decays into two travelling waves in opposite directions. Conservation of energy requires that the two acoustic phonon energies add to $2\pi\hbar \times 40\,\mathrm{THz}$.

The $1/e$ decay time of the optical phonon mode in diamond is 3.5 ps which defines the lifetime of our quantum memory. Unfortunately, this effect decay time doesn't significantly decrease at lower temperatures, and will still occur at absolute zero. However, we will see in the next few chapters that though this lifetime is very short, we can use ultrafast laser pulses to perform all of our operations before the phonon decay.

4.3 Raman transition in diamond

Raman spectroscopy is a rich field which has enabled the exploration of atomic, molecular and crystal energy levels which are inaccessible through one-photon transitions. The reason for this is due to the parities of the initial and final states of the transition, $|\psi_i\rangle$ and $|\psi_f\rangle$. A dipole transition between these state involves the Hamiltonian $\vec{E} \cdot \vec{d}$, where $\vec{d} = -e\vec{r}$ is the dipole moment operator. The probability of mapping between these states with an incident electric $\vec{E}$ depends on the matrix element, $\langle\psi_f|\vec{r}|\psi_i\rangle$. Since the dipole operator is negative under inversion about the origin, the transition probability

$$P_{if} \propto \int_V d^3\vec{r}\psi_f^*(\vec{r}) \times \vec{r} \times \psi_i(\vec{r}) \tag{4.14}$$

is only non-zero if $|\psi_f\rangle$ and $|\psi_i\rangle$ have different parity, under the dipole approximation. For example, if $\psi_i(\vec{r})$ is an even function then for P_{if} to be non-zero $\psi_f^*(\vec{r})$ must be odd, since $\vec{r}$ is odd. Using a single electric field we can only dipole transition between states of different parity. Raman spectroscopy explores two-photon transitions. With two electric fields and two dipole moments present, states can be accessed that have the same parity as the initial state. Beyond spectroscopy, it is a relatively recent notion that Raman transitions can be exploited for photon storage in vibrational and/or rotational excitations of various media [128].

The Hamiltonian of the Raman process is

$$\mathcal{H} = \mathcal{H}_{\text{crystal}} + \mathcal{H}_{\text{light}} + \mathcal{H}_{\text{dip}} \tag{4.15}$$

While the microscopic Hamiltonian for the diamond crystal is quite complex (see Chapter 9 of Ref. [129] for an in-depth discussion) we will use the simplified model of the three-level system introduced above (see Fig. 4.4), expressed as $\mathcal{H}_{\text{crystal}} = \hbar \sum_i \omega_i |i\rangle\langle i|$. We write the projection on the optical phonon level as $|1\rangle\langle 1| = b^\dagger(t)b(t)$. Here, we define a phonon ladder operator in the same manner as for the photon, $b(t) = \int d\omega_b \delta(\omega_b - \omega_{ph}) e^{-i\omega_b t}$, where we take $\omega_{ph} = 2\pi \times 40\,\text{THz}$ and the width of the phonon line to be negligibly narrow ($\sim 0.3\,\text{THz}$). Applying the lowering operator $\hat{b}(t)$ annihilates an optical phonon until the lowest rung on the ladder is reached, which here is the ground state of the crystal ($|0\rangle$).

The Hamiltonian for freely propagating light has the same form as outlined at the beginning of Chapter 2,

$$\mathcal{H}_{\text{light}} = \int d\omega \hbar\omega \left[\hat{a}^\dagger(\omega)\hat{a}(\omega) + \frac{1}{2}\right]. \tag{4.16}$$

The dipole Hamiltonian, $\mathcal{H}_{\text{dip}} = -\vec{E} \cdot \vec{d}$, where the electric field is the sum of two parts: the signal $\vec{E}_s$ and the control $\vec{E}_c$. The signal field is our single photon to be stored, so we treat it quantum mechanically

$$\vec{E}_s \;=\; i\mathcal{A}_s \hat{a}_s(\omega_s) e^{i(k_s z - \omega_s t)} \vec{\varepsilon}_s + \text{h.c.} \tag{4.17}$$

where we express only a single spatial mode k, frequency mode ω_s and collinear propagation along the z-axis. The slowly-varying envelope term is $\mathcal{A}_s = \sqrt{\hbar\omega_s/2\epsilon_0}$. The control field is a strong laser pulse which we treat classically,

$$\vec{E}_c \;=\; \tilde{\alpha}(t) e^{i(k_c z - \omega_c t)} \vec{\varepsilon}_c + \text{c.c.} \tag{4.18}$$

where $\tilde{\alpha}(t)$ is the pulse shape in time, which will be Gaussian. With expressions for all the terms in the Hamiltonian we wish to find the Maxwell-Bloch equations that describe the coupling between photon and phonon fields as a function of propagation through the

diamond. This treatment begins with Heisenberg's equation of motion, $i\hbar\partial_t\hat{A} = [\hat{A}, \mathcal{H}]$, choosing $\hat{A}$ to be each of the coherences between energy levels in the diamond crystal, $|0\rangle\langle 1|$, $|0\rangle\langle 2|$, etc. This is described in detail in Appendix E, and does not include decoherence and decay. Here we write the resulting coupled equations

$$\left[\frac{\partial}{\partial z} + \frac{1}{c}\frac{\partial}{\partial t}\right]\hat{a}_s = -\kappa^*\hat{P}, \tag{4.19}$$

$$\frac{\partial\hat{P}}{\partial t} = i\Delta\hat{P} - \kappa\hat{a}_s + i\Omega_c\hat{b}, \tag{4.20}$$

$$\frac{\partial\hat{b}}{\partial t} = i\Omega_c^*\hat{P}, \tag{4.21}$$

where $\hat{P}$ is the amplitude of the material polarization, which expresses the coherence between levels $|0\rangle$ and $|2\rangle$. Here we express the phonon ladder operator $b(t)$ as the coherence between levels $|0\rangle$ and $|1\rangle$. The Rabi frequency of the control field is $\Omega_c = \vec{d}_{12}\cdot\vec{\varepsilon}_c\tilde{\alpha}/\hbar$, where $\vec{d}_{12}$ is the dipole moment between levels $|1\rangle$ and $|2\rangle$. The term Δ is the frequency detuning between level $|1\rangle$ and the electric fields. Lastly, there is a coupling term $\kappa = \vec{d}_{02}^*\cdot\vec{\varepsilon}_s\mathcal{A}_s/\hbar$, which depends on the dipole moment between levels $|0\rangle$ and $|2\rangle$.

We notice above that the polarizations of the signal and control field must be parallel to the dipole moments $\vec{d}_{02}$ and $\vec{d}_{12}$, respectively. Using a group theory approach (see Appendix F) we can also learn that given the specific symmetries of the diamond lattice these two dipole moments must be orthogonal to one another. This can be written in the form of a Raman tensor $\mathcal{R}$ which, to excite the optical phonon vibrating in the x, y or z direction, has matrix components

$$\mathcal{R}_x = \begin{pmatrix} 0 & 0 & 0 \\ 0 & 0 & 1 \\ 0 & 1 & 0 \end{pmatrix}, \quad \mathcal{R}_y = \begin{pmatrix} 0 & 0 & 1 \\ 0 & 0 & 0 \\ 1 & 0 & 0 \end{pmatrix}, \quad \mathcal{R}_z = \begin{pmatrix} 0 & 1 & 0 \\ 1 & 0 & 0 \\ 0 & 0 & 0 \end{pmatrix}, \tag{4.22}$$

where the matrices act on the three-dimensional polarization vectors. For an optical phonon vibrating in the z-direction we then require that the control polarization relates to the signal polarization by $\vec{\varepsilon}_c = \mathcal{R}_z\vec{\varepsilon}_s$, from which we get the rule that the two must be orthogonal. In other words, to store a horizontally-polarized signal field we require a vertically-polarized control field, and vice versa.

We can use an adiabatic approximation for the transition between levels $|0\rangle$ and $|1\rangle$, meaning that we assume any change in the amplitude $\hat{P}$ is negligibly small. The conditions to make this approximation are that the Rabi frequency $\Omega \ll \Delta$, and the bandwidth of the control field $\delta_c \ll \Delta$. Both these conditions are well satisfied in diamond since the detuning (Δ) from the conduction band is so large. We then take $\partial\hat{P}/\partial t = 0$, meaning that we have $i\Delta\hat{P} = \kappa\hat{a}_s - i\Omega_c\hat{b}$. The coupled equations become

$$\left[\frac{\partial}{\partial z} + \frac{1}{c}\frac{\partial}{\partial t} - i\frac{|\kappa|^2}{\Delta}\right]\hat{a}_s = \frac{\kappa^*\Omega_c}{\Delta}\hat{b}, \tag{4.23}$$

$$\left[\frac{\partial}{\partial t} + i\frac{|\Omega_c|^2}{\Delta}\right]\hat{b} = \frac{\kappa\Omega_c^*}{\Delta}\hat{a}_s, \tag{4.24}$$

Ref. [93] solves these equations for a general Raman memory with large detuning Δ, and shows that high efficiencies can be achieved in the transition $|0\rangle \leftrightarrow |1\rangle$. We note here that after the adiabatic approximation the system takes the form of a two-level system where $|1\rangle$ has been dressed with the control field. Importantly, the spectral width of the dressed state is then the same as that of the control field, in our experiment on the order of 1 THz, allowing the signal photon to have the same bandwidth. The two-level effective Hamiltonian has the form

$$\mathcal{H}_{\text{eff.}} = \zeta\int_0^L dz E_c^{(-)}E_s^{(+)}\hat{b}^\dagger e^{i\omega_{\text{ph}}t} + \zeta^*\int_0^L dz E_c^{(+)}E_s^{(-)}\hat{b}e^{-i\omega_{\text{ph}}t} \tag{4.25}$$

where the coupling term ζ will be a function of the signal coupling κ and the detuning Δ. However, we keep the control electric field separate to show how the state of the stored and retrieved photon can change as a function of the control field frequency. This looks like a three-wave mixing Hamiltonian where one of the waves is the vibrational excitation. If we transition the crystal into and out of the phonon level all in one step, such that we ignore the phonon operators, then the process takes on the form of four-wave mixing.

4.4 State of the retrieved photon

Using the effective Hamiltonian in Eq. 4.25 we can express the state of the excited phonon, as well as the retrieved photon. We take the input state as a single photon in mode a

with spectral shape $f(\omega_i)$, and no phonon initially in mode b. The input state is $|\psi\rangle_{\text{input}} = \int d\omega_i f(\omega_i)|\omega_i\rangle_a|0\rangle_b$, where here $|0\rangle$ refers to the $n = 0$ Fock state. We will apply the effective Hamiltonian to the input state twice, one for the "write" process, and the second for the "read" process. First we express the write process, which stores the photon in the memory. Following the same logical steps as for the downconverted state in Chapter 2, we find

$$
\begin{aligned}
|\psi\rangle_{\text{ph}} &= \exp\left\{\frac{-i}{\hbar}\int_0^t dt' \mathcal{H}_{\text{eff.}}(t')\right\}|\psi\rangle_{\text{input}} && (4.26)\\
&= \left\{\mathbb{1} - \frac{i}{\hbar}\int_0^t dt'\zeta \int_0^L dz \tilde{\alpha}_w^*(t') e^{-ik_w z}\int d\omega_s \mathcal{A}_s \hat{a}(\omega_s) e^{i(k_s z - \omega_s t)}\hat{b}^\dagger e^{i\omega_{ph} t} + ...\right\} \\
&\qquad \times \int d\omega_i f(\omega_i)|\omega_i\rangle_a|0\rangle_b && (4.27)\\
&\approx -\frac{i}{\hbar}\zeta\mathcal{A}_i \int_0^t dt' \iint d\omega_w d\omega_i \alpha_w^*(\omega_w) f(\omega_i) e^{-i(\omega_i - \omega_w - \omega_{\text{ph}})t}\int_0^L dz e^{i(k_s - k_w)z}|0\rangle_a|1\rangle_b && (4.28)\\
&\approx -\frac{2\pi i}{\hbar}\zeta\mathcal{A}_i \int d\omega_i \alpha_w^*(\omega_i - \omega_{\text{ph}}) f(\omega_i)\int_0^L dz e^{i(k_s - k_w)z}|0\rangle_a|1\rangle_b && (4.29)
\end{aligned}
$$

where we have ignored the zero-order process, $\mathbb{1}$, since we are going to post-select on detecting a photon in the readout mode. We have labelled the first control pulse (write) using the subscript w. We made the substitution of the write pulse temporal envelope with its spectral shape using a Fourier transform. The spectral shape will be Gaussian, $\alpha(\omega_w) = \exp[-(\omega_w - \omega_w^0)^2/4\sigma_w^2]$, centred around 800 nm wavelength. To match, the input pulse spectrum $f(\omega_i)$ will also be Gaussian with centre wavelength at 723 nm. In the third step above, we acted the lowering operator on the single photon $\hat{a}(\omega_s)|\omega_i\rangle_a$, producing a delta function $\delta(\omega_s - \omega_i)|0\rangle_a$. In the last step we performed the time integral which produced a delta function $2\pi\delta(\omega_i - \omega_w - \omega_{\text{ph}})$ which we then evaluated with the integral over ω_w.

Once the photon has been written into the phonon state, the state will evolve with a phase corresponding to the phonon frequency ω_{ph}. When we apply the read pulse to retrieve the photon after a time τ, the state has accumulated a phase $e^{i\omega_{\text{ph}}\tau}$. To express

the state of the retrieved photon we apply the Hamiltonian to the state in Eq. 4.29,

$$
\begin{aligned}
|\psi(t)\rangle_{\text{ret.}} &\approx -\frac{2\pi i}{\hbar} e^{i\omega_{\text{ph}}\tau}\zeta^{*}\mathcal{A}_o \iint d\omega_r d\omega_o \alpha_r(\omega_r)\delta(\omega_o-\omega_r-\omega_{\text{ph}}) \\
&\qquad \times \int_0^L dz' e^{-i(k_o-k_r)z'}\hat{a}^{\dagger}(\omega_o)\hat{b}|\psi\rangle_{\text{ph}} \qquad (4.30) \\
&\approx -\left(\frac{2\pi}{\hbar}\right)^2 |\zeta|^2 \mathcal{A}_o\mathcal{A}_i e^{i\omega_{\text{ph}}\tau} \iint d\omega_o d\omega_i \alpha_w^{*}(\omega_i-\omega_{\text{ph}})\alpha_r(\omega_o-\omega_{\text{ph}})f(\omega_i) \\
&\qquad \times \int_0^L dz e^{i(k_i-k_w)z}\int_0^L dz' e^{-i(k_o-k_r)z'}|\omega_o\rangle_a|0\rangle_b \qquad (4.31)
\end{aligned}
$$

where we have used the subscript r to refer to the read pulse, and the subscript o to refer to the output photon. The spectral shape of read pulse will be of interest to us in a discussion coming shortly. The integrals over z and z' each produce a $\text{sinc}((k_1-k_2)L/2)$ function. However, if we think of the whole memory process as a four-wave mixing, i.e., write and read occurring all in one time step, then we would have a single phase matching function $\text{sinc}(\Delta kL/2)$ with $\Delta k = k_i - k_w + k_r - k_o$. Our state would then be expressed as

$$
\begin{aligned}
|\psi(t)\rangle_{\text{ret.}} &\approx -\left(\frac{2\pi}{\hbar}\right)^2 |\zeta|^2 \mathcal{A}_o\mathcal{A}_i L e^{i(\omega_{\text{ph}}\tau+\Delta kL/2)} \iint d\omega_o d\omega_i \alpha_r(\omega_o-\omega_{\text{ph}})\alpha_w^{*}(\omega_i-\omega_{\text{ph}})f(\omega_i) \\
&\qquad \times \text{sinc}\left(\frac{\Delta kL}{2}\right)|\omega_s\rangle_a|0\rangle_b \qquad (4.32)
\end{aligned}
$$

We can learn a few important lessons by looking at the output state in Eq. 4.32. First, the amplitude of our state, and thus the efficiency of the process, depends on how well the spectrum of the input photon matches that of the write field. We take the input photon spectrum to be Gaussian in shape, $f(\omega_i) = \exp\{-(\omega_i-\omega_i^0)^2/2\sigma_i\}$. If the centre frequency of the input photon ω_i^0 does not equal $\omega_w^0 + \omega_{\text{ph}}$ then the storage efficiency will suffer. Similarly the spectral shape of the photon and write fields should be appropriately matched in order to maximize the storage efficiency, which is proportional to the integral $\int d\omega_i \alpha_w^{*}(\omega_i-\omega_{\text{ph}})f(\omega_i)$. For example, if the photon bandwidth $\sigma_i > \sigma_w$ then some of the photon spectrum cannot be stored in the memory.

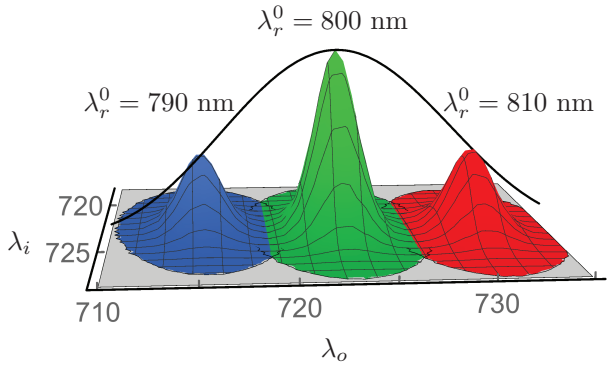

Figure 4.5: The normalized intensity of the output state as a function of the input and output photon wavelengths, λ_i and λ_o. We take the write wavelength to be centred at 800 nm, meaning that efficiency is maximized when the input photon is centred at $\lambda_i^0 = 723$ nm. The intensity is maximized when the input wavelength is such that the condition $\omega_i = \omega_w + \omega_{\text{ph}}$ is met. By changing the centre frequency of the read field, λ_r^0, the centre wavelength of the output photon spectrum can be tuned to both red and blue wavelengths. The different spectral peaks are traced out by $\text{sinc}^2(\Delta kL/2)$, meaning that the range for frequency conversion is set by phase matching.

4.4.1 Frequency conversion in the diamond memory

The second thing we can see in Eq. 4.32 is that the spectrum of the output photon is directly influenced by the envelope of the read field, $\alpha_r(\omega_o - \omega_{\text{ph}})$. This implies that changing the centre frequency of the read field, ω_r^0, will also change the centre frequency of the output photon spectrum. The consequence of this is that we can store a photon in the memory at one frequency, ω_i^0, and read it out with a new frequency $\omega_o^0 = \omega_r^0 + \omega_{\text{ph}}$. We can also see that the range over which we can frequency shift is limited by the phase matching term $\text{sinc}(\Delta kL/2)$. The range over which we can shift the frequency of the input beam is plotted in Fig. 4.5. We explore this concept experimentally in Chapter 7.

Finally, the control over the output photon spectrum extends beyond frequency shifting. We have not yet committed to a specific shape for the read pulse envelope, α_r. Eq. 4.32 implies that regardless of the shape of the read spectrum that the output photon spectrum will follow it. In Chapter 7 we explore this experimentally, and though we keep the shape

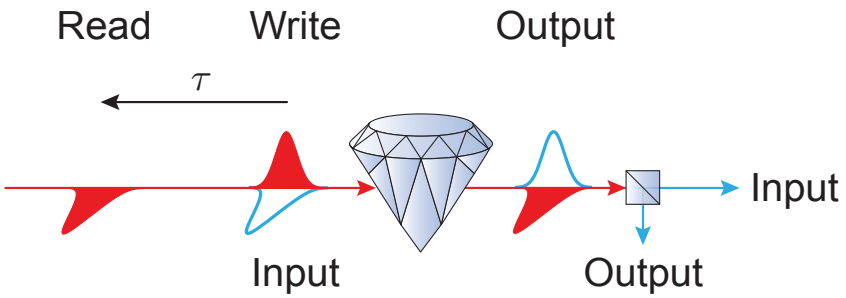

Figure 4.6: A horizontally-polarized *input* photon (blue outline) is absorbed into the optical phonon level of diamond via a Raman transition stimulated by a strong vertically-polarized laser pulse (*write*). After a time delay τ, a horizontally-polarized *read* laser pulse stimulates the reverse Raman transition resulting in the emission of a vertically-polarized *output* photon. The output can be distinguished from an un-stored input photon by polarization.

of the read envelope a Gaussian, we show that the output photon spectrum can be both narrowed or broadened from the input spectrum, by controlling the bandwidth of the read field, σ_r.

4.5 Experimental quantum storage

We now transition to discussing how to demonstrate quantum storage in diamond with an experiment. We will leave most of the details for each of the following chapters which each present a different experiment. The scheme is laid out in Fig. 4.6. An input photon, which is horizontally-polarized, is stored in the memory via the Raman transition discussed above. A vertically-polarized strong laser pulse, labelled *write*, stimulates the absorption of the photon into the optical phonon level in diamond.

4.5.1 Absorption

In Ref. [32] the memory protocol was demonstrated using single photon-level laser pulses as the input. These pulses, with centre wavelength 723 nm, were generated using an optical parametric oscillator (OPO). Results showed a nearly linear trend of absorption efficiency, η_w, as a function of energy in the write pulse. As much as 30% of the input light could be absorbed using all available laser power – for this efficiency there was ~ 20 nJ of energy in each write pulse which translates to 1.6 W given the 80 MHz repetition rate of the laser.

Other than the orthogonal polarization rule it is important that the write pulse and photon spectra be appropriately matched, and that the timing delay between the two pulses is set so that they arrive at the diamond simultaneously. In practice, we scan the delay of the write pulse using a motorized stage to find the proper delay. If we measure detection of the input light after the diamond we expect to observe a reduced detection rate when this delay is matched, resulting in a Gaussian-shaped dip. The width of the absorption dip will depend on the pulse lengths of both the input photon and write pulse.

Absorption of single photons

For the work in this thesis we generated single photons for the input signal using the source described in Section 2.6. The single photon is filtered to a spectral bandwidth of 4.1 nm FWHM and then passes through a 7 cm-long single-mode fibre optic cable (Thorlabs custom order). We find that the length of the single photon pulse, affected by group velocity mismatch in the nonlinear crystals for SHG and SPDC, affects the efficiency of its absorption in the diamond.

As outlined in Section 2.6.5, we used 1 mm Barium Borate (BBO) crystals for both SHG and SPDC. This combination of crystals was chosen to optimize the absorption efficiency of single photons. The group velocity mismatch (GVM) of BBO for SHG from 800 nm to 400 nm is 187 fs/mm, and for SPDC from 800 nm to 723 nm is 176 fs/mm. For comparison, Bismuth Borate (BiBO) has a GVM of 430 fs/mm for SHG from 800 nm to 400 nm.

A large GVM in the SHG step results in a 400 nm pump pulse with a smeared temporal envelope. In turn, this affects the single photon wave packet as well. If the photon is more

SHG crystal	SPDC crystal	Measured FWHM of dip
3 mm BiBO	1 mm BBO	453 fs
3 mm BiBO	2 mm BBO	461 fs
3 mm BiBO	3 mm BBO	442 fs
1 mm BBO	1 mm BBO	325 fs
1 mm BBO	3 mm BBO	441 fs

Table 4.1: Absorption dip widths for different nonlinear crystals in the photon source. The combination of 1 mm BBO crystals for both second harmonic generation and downconversion produced single photons with shorter durations, more closely matched to the temporal envelope of the write pulse.

dispersed than the write pulse at the diamond then the resulting absorption dip will be wide and shallow, i.e., a less efficient write process. One strategy to compensate for this is to match this dispersion with the write laser. However, we found that the choice of nonlinear crystals in the source had the largest impact, see Table 4.1.

We can estimate the length of the 723 nm photon as the sum in quadrature of the initial laser pulse length, the GVM in the SHG crystal, and the GVM in the SPDC crystal. Using a 1 mm BBO crystal for SHG and a 1 mm BBO crystal for SPDC, we calculate a photon pulse length of 319 fs. Calculating the expected absorption dip width as the sum in quadrature of the photon pulse length and the write pulse length, we get 372 fs, which is comparable with the observed absorption dip width. Using all control field power for the write process, we measured a typical photon absorption efficiency of 20%. Using 723 nm pulses generated in an OPO for the signal field, we measured a 29% absorption dip with a width of 272 fs.

4.5.2 Readout

Once the photon is absorbed, we wait a time delay τ before applying a second strong laser pulse, *read*, to retrieve the photon. In the proof-of-concept experiment of Ref. [32] the read pulse, derived from the same laser as the write pulse using a Michelson interferometer, was scanned in energy producing a linear trend in efficiency, η_r. The total memory efficiency

$\eta_m = \eta_w \eta_r$ then increases quadratically as a function of energy in the read and write pulses. When both the read and write pulses had energies of 10 nJ (0.8W) a total memory efficiency of $\sim 4\%$ was reported. Of course, the quadratic trend in efficiency does not continue forever — eventually the efficiency is saturated as seen in the Raman memory based on hydrogen molecules [31].

In our demonstrations of the storage and retrieval of single photons, Chapters 5 and 6, the read pulse is derived from the same laser as the write pulse in the same manner as Ref. [32]. However, to demonstrate frequency and bandwidth conversion upon retrieval, we use a separate laser for the read pulse in Chapter 7. These results are reported in the following chapters.

4.6 Sources of noise

As a final note, we discuss the two main sources of noise on our experiment: spontaneous Stokes and anti-Stokes emission through four-wave mixing (4WM), and spontaneous anti-Stokes scattering off of thermally-populated phonons. Both these processes produce 723 nm light, and contribute detections in the retrieved signal mode even when no input single photon was present.

4.6.1 Four-wave mixing

The Stokes and anti-Stokes noise production is described by the Hamiltonian

$$\mathcal{H} = \zeta \int_0^L dz E_1^{(+)} E_S^{(-)} \hat{b}^\dagger e^{i\omega_{\mathrm{ph}} t} + \zeta^* \int_0^L dz E_2^{(+)} E_{aS}^{(-)} \hat{b} e^{-i\omega_{\mathrm{ph}} t} \tag{4.33}$$

where the subscripts 1 and 2 refer to either read or write fields at 800 nm (often called pump (1) and probe (2) in Raman spectroscopy), S refers to the Stokes photon at 895 nm, and aS to the anti-Stokes at 723 nm. By evaluating the state of the anti-Stokes photon, we find the efficiency of this process depends on $\mathrm{sinc}^2(\Delta k L/2)$, where $\Delta k = k_1 - k_S + k_2 - k_{aS}$. Since $\Delta k \neq 0$ for collinear propagation we can use a longer diamond crystal to suppress the four-wave mixing noise.

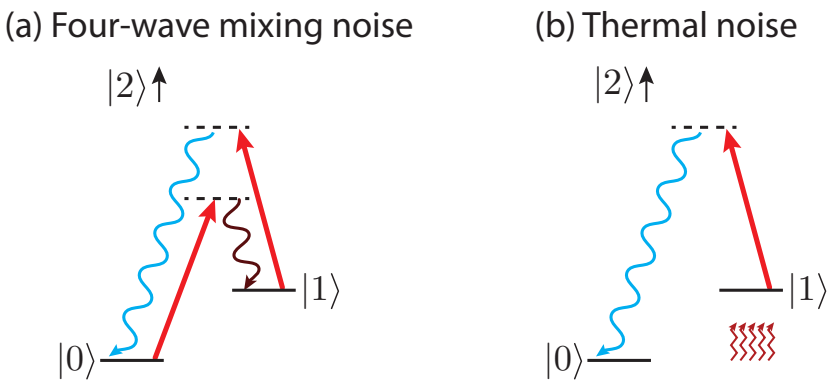

Figure 4.7: The two primary types of noise in the memory. (a) Four-wave mixing noise occurs when an incident control pulse (read or write) pumps spontaneous Stokes scattering. This produces a Stokes photon at 895 nm and populates the optical phonon level. The reverse transition, probed by either the same pulse or the read pulse, emits a spontaneous anti-Stokes photon of the same wavelength and polarization as a retrieved signal photon. (b) At any time, and at room temperature, there is a 0.0016 probability per pulse that there is an optical phonon present. An incident control pulse can scatter off of the phonon producing a spontaneous anti-Stokes emission of a 723 nm photon.

The four combinations of the read and write (pump-probe) fields that will produce an anti-Stokes photon are: (1) write-write; (2) write-read; (3) read-write; (4) read-read. When the vertically-polarized write pulse is the probe, the anti-Stokes photon will be horizontally polarized according to the memory selection rules. We will then only see two 4WM noise combinations: write-read, and read-read.

When the write field excites the optical phonon and the read pulse produces the anti-Stokes photon, the noise rate will decay with the phonon lifetime $e^{-\tau/\tau_{\rm ph}}$ for $\tau \geq 0$, and 0 for $\tau < 0$. Here $\tau_{\rm ph} = 3.5\,{\rm ps}$ is the $1/e$ lifetime of the phonon level. When the Stokes and anti-Stokes are both produced by the same read pulse there will be no time dependence. If the write and read pulses have the same energy we expect that the four-wave mixing noise will have a constant rate $\mathcal{N}$ which doubles at $\tau = 0$ and exponentially decays,

$$N_{\rm 4WM} = \mathcal{N}(1 + e^{-\tau/\tau_{\rm ph}}). \tag{4.34}$$

4.6.2 Thermally-populated phonons

Though the 40 THz frequency splitting between the ground and optical phonon states allows for low-noise room-temperature operation, we still find a non-negligible contribution of initial excitations in the phonon level. We can calculate the probability of having an excitation in the optical phonon level, $P_{\rm ph}$, using Bose-Einstein statistics for bosons,

$$P_{\rm ph}(E) = \frac{1}{e^{E/k_B T} - 1} \tag{4.35}$$

where $E = 2\pi\hbar \times 40\,{\rm THz}$ for the optical phonon, k_B is Boltzmann's constant, and $T = 298\,{\rm K}$ at room temperature. We find the probability that an optical phonon is present in the relevant mode to be $P_{\rm ph} = 0.0016$ per laser pulse. Though this seems negligible, recall that we probe the memory with a laser repetition rate of 80 MHz. Since these phonons have random phases they will be scattered into a solid angle of 4π. With a typical readout efficiency of ~ 0.1, and herald photon detection rate of $\sim 100\,{\rm KHz}$, the expected coincidence detection rate due to thermal noise is $\sim 1\,{\rm Hz}$. This will be compared to a retrieved photon coincidence rate on the order of 10 Hz, and so is not negligible. In the next Chapter we discuss a strategy for suppressing this noise with cooling.

Chapter 5

Experimental storage and retrieval of single photons from the diamond quantum memory

5.1 Notes and acknowledgements

The contents of this chapter have been published as: D.G. England, K.A.G. Fisher, J.-P. Maclean, P.J. Bustard, R. Lausten, K.J. Resch, B.J. Sussman, Storage and retrieval of THz-bandwidth single photons from a room-temperature diamond quantum memory, *Physical Review Letters* **114**, 053602 (2015).

This project was a collaboration with the Quantum Technologies group at the National Research Council of Canada. The experiment was conceived by **K.J. Resch** and **B.J. Sussman**. **D.G. England** constructed the diamond memory setup. **K.A.G. Fisher** and **J.-P. Maclean** constructed the photon source. **D.G. England**, **K.A.G. Fisher** and **J.-P. Maclean** performed the experiment and analyzed the data. **D.G. England** wrote the initial manuscript, and all authors contributed the final manuscript.

5.2 Abstract

We report the storage and retrieval of single photons, via a quantum memory, in the optical phonons of room-temperature bulk diamond. The THz-bandwidth heralded photons are generated by spontaneous parametric downconversion and mapped to phonons via a Raman transition, stored for a variable delay, and released on demand. The second-order correlation of the memory output is $g^{(2)}(0) = 0.65 \pm 0.07$, demonstrating preservation of non-classical photon statistics throughout storage and retrieval. The memory is low-noise, high-speed and broadly tunable; it therefore promises to be a versatile light-matter interface for local quantum processing applications.

5.3 Introduction

Single photons are challenging to create, manipulate and measure, yet are essential for a diverse range of quantum technologies, including cryptography [56], enhanced measurement [130], and information processing [41]. Quantum memories, which act as buffers for photonic states, are a key enabling component for these future technologies [131]. They allow repeat-until-success strategies to counteract the intrinsically probabilistic nature of quantum mechanics, thereby providing scalable quantum technologies. An ideal quantum memory would store a single photon, maintain the quantum state encoded in the photon, and release it, on-demand, as a faithful recreation of the input. Efforts to implement optical quantum memories have used a number of platforms including single atoms in a cavity [89], ultracold atoms [67], atomic vapours [30], molecular gases [31] and rare-earth doped crystals [29].

The potential for quantum storage in optical memories is often investigated using laser pulses attenuated to the single-photon level [28]. However, the transition between storing weak coherent states and true single photons produces two significant obstacles. Firstly, to achieve high efficiency, most memories must operate near resonance with a dipole transition, typically limiting storage bandwidths to ∼GHz or below [30, 83]. Single photon sources compatible with such devices require careful engineering to match the frequency

and bandwidth of the photons to that of the memory [67, 83, 109, 38, 74, 82, 85]. Secondly, the intense read and write beams used to mediate storage and retrieval may introduce noise which obscures the quantum properties of the signal [96]. Where non-classical memory operation has been demonstrated, laser-cooled [67, 38, 74] or cryogenic [83, 109, 82, 85] substrates are often required to reduce noise.

In this letter, we demonstrate the storage and retrieval of broadband single photons using a room-temperature solid-state quantum memory. The THz-bandwidth heralded single photons are created by spontaneous parametric downconversion (SPDC) and are stored, via an off-resonant Raman transition, in the optical phonon modes of a room-temperature bulk diamond. As the Raman interaction occurs far from any optical resonances, the memory can operate at a range of visible and near-infrared wavelengths. The bandwidth of the memory is limited only by the 40 THz splitting between the ground and storage states [122]. This broad bandwidth and large tuning range makes the memory compatible with ultrafast SPDC photon sources [132]. Furthermore, the memory exhibits a quantum-level noise floor, even at room temperature [32].

The memory utilized a high-purity, low-birefringence synthetic diamond manufactured by Element Six Ltd. The diamond, which is 2.3 mm thick, was grown by chemical vapour deposition and is cut along the $\langle 100 \rangle$ face of the diamond lattice. The relevant energy levels can be described by a Λ-level system consisting of the crystal ground state $|0\rangle$, an optical phonon acting as the storage state $|1\rangle$ and an off-resonant intermediate state $|2\rangle$ representing the conduction band. Single photons are stored to, and retrieved from, the optical phonon by strong *write* and *read* pulses via an off-resonant Raman interaction [93, 30]. The photons and read/write pulses are in two-photon resonance with the optical phonon energy (see Fig. 5.1(b)). In the $\langle 100 \rangle$ configuration, the Raman interaction couples fields of orthogonal polarization [126] such that the H-polarized input photons are stored by a V-polarized write pulse and V-polarized output photons are retrieved using a H-polarized read pulse.

The high carrier frequency of the optical phonon (40 THz [122]) and a large detuning from the conduction band ($\sim$ 950 THz) are the key features allowing storage of THz-bandwidth photons. These features also provide an intrinsically low noise floor: the large detuning from optical resonance eliminates fluorescence noise, and the high energy of the

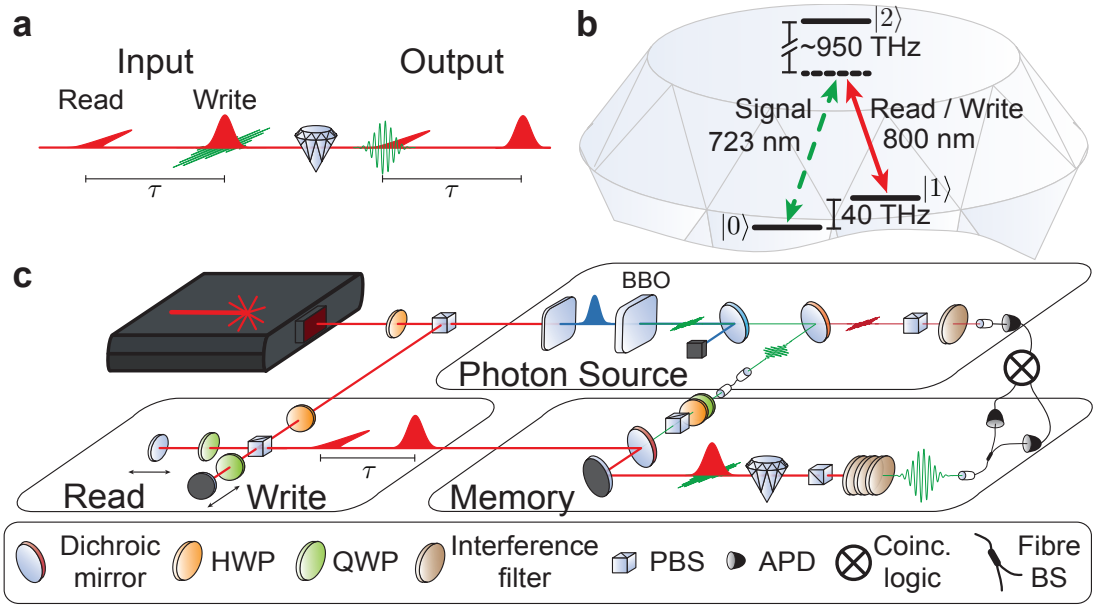

Figure 5.1: Experimental concept, energy level diagram, and setup. (a) The memory protocol. A horizontally (H) polarized single photon (green, 723 nm) is written into the quantum memory with a vertically (V) polarized *write* pulse (red, 800 nm). After a delay τ an H-polarized *read* pulse recalls a V-polarized photon. (b) Energy levels in the memory. The ground state $|0\rangle$ and storage state $|1\rangle$ correspond to the crystal ground state and an optical phonon respectively. The signal photon and the read/write pulses are in two-photon resonance with the optical phonon (40 THz) and are far detuned from the conduction band $|2\rangle$. (c) The experimental setup. The laser output is split to pump the photon source and to produce the orthogonally-polarized read and write beams. The photons are produced in pairs with one (signal) at 723 nm and the other (herald) at 895 nm. The signal photon is stored in, and recalled from, the quantum memory. The herald and signal photons are detected using APDs and correlations between them are measured using a coincidence logic unit.

optical phonon results in low thermal phonon population at room temperature. Four-wave mixing noise, which is a pervasive problem in many Λ-level systems [133, 96], is suppressed in diamond due to the large splitting and high optical dispersion [32]. Following excitation, the optical phonons decay into a pair of acoustic phonons with a characteristic timescale of 3.5 ps [40], which sets the storage lifetime of the memory. The advantage of the rapid acoustic decay is that it returns the crystal lattice to the ground state, resetting the memory such that it is ready to store the next photon. This sub-nanosecond reset time permits GHz repetition rates in the diamond phonon system.

The high bandwidth and rapid reset time of our memory may benefit local quantum processing applications such as quantum frequency conversion [101], memory-enhanced optical non-linearities [134], or programmable linear-optical components [110]. However, the lifetime is too short for quantum communication protocols [135]. The diamond memory is complementary to existing atomic [67] or rare-earth-doped [29] quantum memories: the long storage times of the latter benefiting long-distance quantum communication and the high bandwidth of the former providing advantages for small-scale quantum processing. To leverage the full bandwidth of this memory, we require multiple operational time bins during storage. This could be achieved by creating multiple time-delayed replicas of an 80 MHz laser pulse train to generate bursts of pulses separated by $\ll$1 ps [136]; these bursts could be used to pump an SPDC source.

5.4 Experiment

The master laser for the experiment is a mode-locked Ti:sapphire laser producing pulses of 190 fs duration at a repetition rate of 80 MHz, central wavelength of 800 nm and a pulse energy of 28 nJ. The laser beam is split between the photon source and the memory with 12.5 nJ used to generate the orthogonally-polarized read and write pulses (read/write panel, Fig. 5.1(c)). The remaining energy for the photon source is frequency-doubled in a 1 mm β-barium borate (BBO) crystal to produce pulses at 400 nm (pulse energy 2.4 nJ). In a second 1 mm BBO crystal, angle tuned to phase-match type-I non-degenerate SPDC, the pump field at 400 nm produces horizontally-polarized photon pairs at 723 nm (signal) and 895 nm

(herald). The photon pairs are emitted collinearly from the BBO and, after the remaining 400 nm pump light has been removed by interference filters, the signal and herald photons are spatially separated by an 801 nm long-pass dichroic mirror. The herald photons pass through a polarizing beam splitter (PBS) and a 5 nm bandwidth interference filter before being coupled into a single-mode fiber and detected on an avalanche photodiode (APD). The signal photons are coupled into a 7 cm long single-mode fiber for spatial filtering before being directed to the memory.

The horizontally-polarized signal photon is spatially and temporally overlapped on a dichroic mirror with the vertically-polarized write pulse and focused into the diamond for storage by a 6 cm focal length achromatic lens. After a time delay τ the horizontally-polarized read pulse arrives at the memory and the photon is re-emitted, this time with vertical polarization. We can thus distinguish between the input and the output states of the memory by their polarization (Fig. 5.1(a)). Following the memory, the signal photons are spectrally filtered from the read/write pulses using interference filters[1] and coupled into a single-mode fiber. By rotating the polarization basis we collect either the memory output or the unabsorbed memory input (memory panel, Fig. 5.1(c)). The photons are detected by an APD and correlations in photon detection events are measured using coincidence counting logic.

Storage of the signal photons is demonstrated by scanning the delay of the write pulse with respect to the signal photon. With 12.5 nJ in the write pulse, a 20% reduction in signal-herald coincidences at zero delay indicates that signal photons are being written to the memory (inset, Fig. 5.2). The full width at half maximum of the absorption profile is $w_{\mathrm{a}} = 326$ fs. Deconvolving this width with that of the write pulse ($w_{\mathrm{w}} = 190$ fs) using the expression $w_{\mathrm{a}}^2 = w_{\mathrm{w}}^2 + w_{\gamma}^2$ returns an estimated photon duration of $w_{\gamma} = 260$ fs, assuming transform limited pulses with Gaussian spectra.

Readout of the signal photons is observed by rotating the polarization filter to measure the vertically-polarized output of the memory. With 6.25 nJ in each pulse, we scan the delay between the write and read pulses; the sharp step in signal-herald coincidences at

[1] The read/write pulses were removed using 4 angle-tuned notch filters (Semrock NF03-808E-25). The single photons were spectrally-isolated from other noise photons using a 723 nm bandpass filter (Foreal Inc., 5 nm bandwidth).

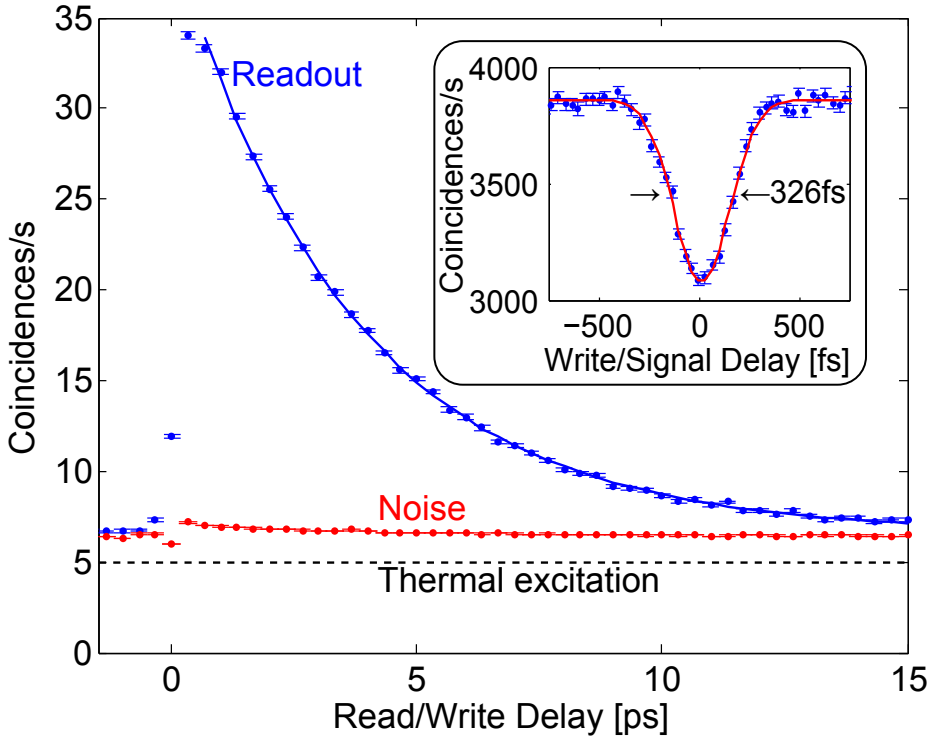

Figure 5.2: Measured coincidences between the signal and herald photons as a function of read-write delay (blue bars). An exponential decay of half-life 3.5 ps (solid blue fit) is characteristic of the optical phonon lifetime. The background noise (red bars) shows a SNR of 3.8:1 for single photon retrieval. The estimated noise due to thermal phonon population is shown by the dotted line. **Inset:** Transmission through the diamond in the presence of the write pulse, showing memory absorption. The profile width of 326 fs (solid red fit) indicates the large bandwidth of the photons stored in the memory. All error bars are from poissonian counting statistics. Signal and herald detection events are defined as coincident if the time delay between them falls within a 1 ns window.

zero delay indicates that signal photons are being retrieved from the memory (Fig. 5.2). The exponential decay in read efficiency has a half-life of 3.5 ps which is characteristic of the optical phonon lifetime [40]. We have therefore demonstrated that the memory stores a single photon for over 13 times its duration. The maximum total memory efficiency is $\eta_{\mathrm{t}} = 0.9\%$ and the write efficiency is $\eta_{\mathrm{w}} = 9\%$ from which we extract a read efficiency of $\eta_{\mathrm{r}} = \eta_{\mathrm{w}}/\eta_{\mathrm{t}} = 10\%$. The memory efficiency was limited by available laser power, but could be improved using high-energy read/write pulses as has been demonstrated in other Raman memories [31], or by exploiting enhanced coupling in a waveguide structure [137].

5.5 Results and Discussion

By blocking the input signal photons we can measure the background noise of the memory (see Fig. 5.2), the maximum signal-to-noise ratio (SNR) is 3.8:1; it is important to note that this is a raw measurement and no background subtraction has been performed. This noise has two origins: spontaneous anti-Stokes scattering from thermally-excited phonons and spontaneous four-wave mixing (FWM). The FWM noise process is intrinsic to the memory and cannot be completely eliminated, however in a dispersive material such as diamond it is strongly suppressed due to phase-matching conditions [32]. From Boltzmann statistics we calculate that around 5 coincidence counts per second can be attributed to thermal noise (dashed line in Fig. 5.2), we note that the thermal noise could be reduced by an order of magnitude by cooling the diamond to -60°C. The photon heralding efficiency at the memory is 16% meaning that a single photon is present at the memory in only 16% of the heralded experiments; despite this, we still observe a high contrast between signal and noise. At -60°C, with an ideal heralding efficiency, the SNR in this memory could be 70:1.

Correlations between the memory output and the herald photon can be seen in their coincidence statistics, as shown in Fig. 5.3. The coincidence rate as a function of the electronic delay between the memory output and the herald photon shows periodic peaks due to accidental coincidences between the memory noise and the herald photon; the time period of these peaks is 12.5 ns corresponding to the repetition period of the laser

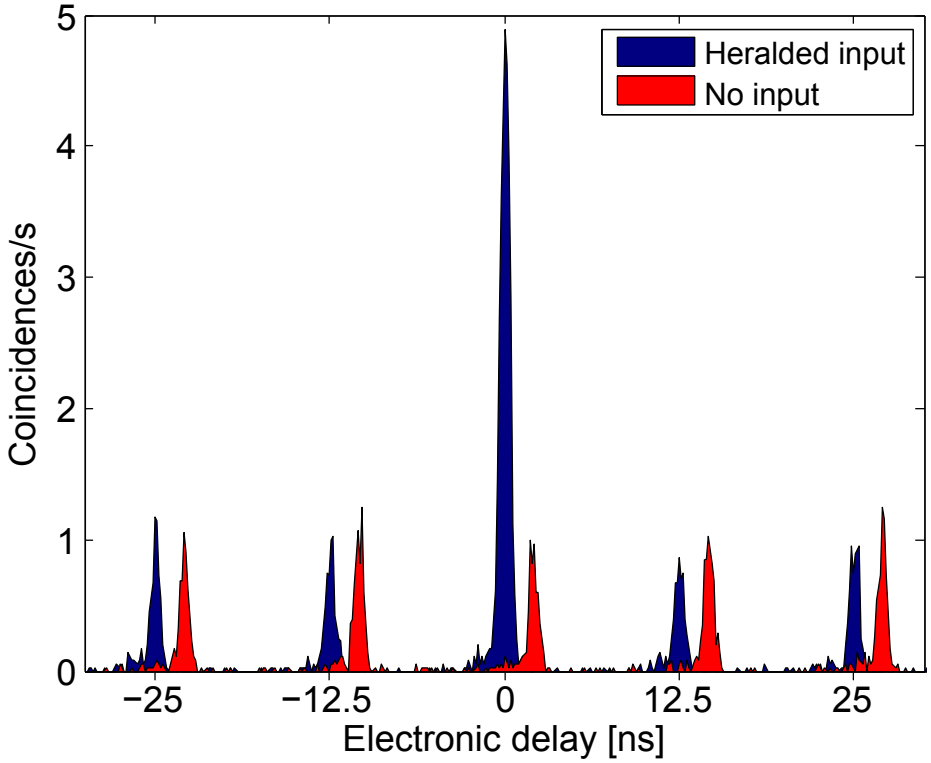

Figure 5.3: Detection coincidences between the herald photon and the signal photon retrieved from the memory as a function of electronic delay (blue). A peak of five times the accidental rate at zero delay demonstrates strong correlations between the herald and signal photons after readout from the memory. The memory noise (red, offset by 2 ns for clarity) shows no increase at zero delay. Signal and herald detection events are defined as coincident if the time delay between them falls within a 156 ps window. The width of the peaks is due to the timing jitter (∼500 ps) of the APDs.

oscillator. The largest peak, at zero delay, indicates retrieval of signal photons which have been written to the memory. These coincidence rates exceed the accidental rate by a factor of five, a clear indication that the non-classical correlations between herald and signal are maintained during storage and retrieval from the quantum memory.

A stringent test for non-classical photon statistics is to measure the second-order correlation function $g^{(2)}(0)$ [138]. Using the Hanbury Brown and Twiss configuration [36], the input light field is partitioned between two detectors using a 50:50 fiber beamsplitter, as shown in Fig. 5.1(c). The triggered $g^{(2)}(0)$ function of the heralded SPDC source is calculated as [139]:

$$g^{(2)}(0) = \frac{N_{\mathrm{h},1,2} N_{\mathrm{h}}}{N_{\mathrm{h},1} N_{\mathrm{h},2}}, \tag{5.1}$$

where N_{h} is the number of herald photons detected in a given time window, $N_{\mathrm{h},1}$ ($N_{\mathrm{h},2}$) is the number of two-fold coincident detections between the herald and output port 1 (2) of the beam splitter and $N_{\mathrm{h},1,2}$ is the number of three-fold coincidences between the herald and both ports of the beamsplitter. A correlation function of $g^{(2)}(0) < 1$ is a direct measure of sub-poissonian statistics which cannot be explained classically, and is evidence of single photons.

At the memory input, we measure $g^{(2)}_{\mathrm{in}}(0) = 0.04 \pm 0.01$; after the memory the correlation function $g^{(2)}_{\mathrm{out}}(0)$ depends on the storage time, as shown in Fig. 5.4. When the storage time is 0.5 ps, we measure $g^{(2)}_{\mathrm{out}}(0) = 0.65 \pm 0.07$, five standard deviations below the classical limit of 1. The measured $g^{(2)}_{\mathrm{out}}(0)$ function increases with increasing storage time as the noise comprises a larger fraction of the measured counts, however the memory output maintains non-classical statistics for >2.5 ps. A $g^{(2)}_{\mathrm{out}}(0)$ correlation of 0.65 confirms non-classicality, but the storage and readout has introduced noise thereby degrading the correlation measured directly from the source, $g^{(2)}_{\mathrm{in}}(0)$. For completeness, we point out that a $g^{(2)}_{\mathrm{out}}(0) > 0.5$ cannot distinguish between a state comprised of single photons mixed with thermal noise, and a different non-classical state comprised entirely of $n = 2$ and larger Fock states. However the latter state is unlikely given the physics of the system.

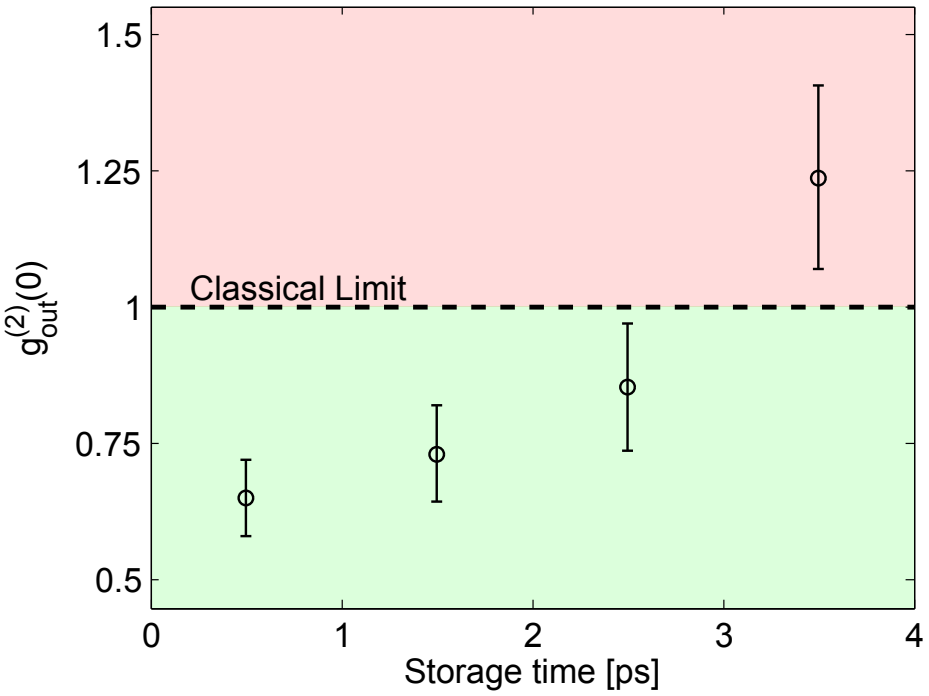

Figure 5.4: The heralded second-order correlation function of the memory output as a function of storage time. Values below the classical limit of $g^{(2)}_{\mathrm{out}}(0) = 1$ demonstrate the quantum characteristics of the output field. Non-classical statistics are observed for storage times up to $\sim$3 ps. Error bars are from Poissonian counting statistics.

5.6 Conclusion

In conclusion, we have demonstrated a THz-bandwidth quantum memory for light using the optical phonon modes of a room-temperature diamond. The unique features of the memory enable storage of single photons produced by ultrafast spontaneous parametric downconversion — the most widespread source of single and entangled photons. The heralded second-order correlation function of the memory output was $g^{(2)}_{\text{out}}(0) = 0.65 \pm 0.07$ which is five standard deviations below the classical limit. This result confirms the quantum nature of our memory by mapping a single photon to and from a single phonon maintaining non-classical photon statistics. Future work will focus on developing a multi-mode memory capable of storing dual-rail or polarization qubits and entangled photons. The device requires no cooling or optical preparation before storage and is a few millimetres in size; diamond is therefore a robust, convenient and high-speed testbed system in which to evaluate operational memory parameters, study the effects of noise, and develop quantum protocols.

Chapter 6

Storage and retrieval of entangled qubits from the diamond quantum memory

6.1 Notes and acknowledgements

The contents of this chapter have been prepared as a manuscript to be submitted for publication K.A.G. Fisher, D.G. England, J.-P. Maclean, P.J. Bustard, K. Heshami, K.J. Resch, B.J. Sussman, Storage of polarization-entangled photons with THz-bandwidths in a diamond quantum memory, *To be submitted* (2016).

This project was a collaboration with the Quantum Technologies group at the National Research Council of Canada. The experiment was conceived by **K.A.G. Fisher**, **D.G. England** and **B.J. Sussman**. **D.G. England** constructed the initial diamond memory setup. **K.A.G. Fisher** and **J.-P. Maclean** constructed the photon source. **D.G. England** and **K.A.G. Fisher** performed the experiment and analyzed the data. **K.A.G. Fisher** wrote the initial manuscript, and all authors contributed the final manuscript.

6.2 Abstract

A quantum memory, which stores and releases a photonic qubit on demand, is a key enabling component for emerging quantum technologies. However many implementations of quantum memories place strict bandwidth limitations on the photons to be stored. Here we store and retrieve THz-bandwidth photons in a room-temperature diamond quantum memory, preserving their polarization states. Performing a quantum process tomography we observe qubit storage above the classical bound for 3 ps, over 11 times longer than the input photon coherence time. We also store one photon from an entangled photon pair and show that the quantum memory preserves entanglement for over 7 times the input coherence time. We expect the diamond quantum memory to find use in many ultrafast applications where long storage times are not necessary.

6.3 Introduction

Photons are the natural choice to transmit quantum information. They play a vital role in many emerging quantum technologies such as quantum computing [41], communication [53, 54, 140], and cryptography [56]. The full realization of these technologies necessitates the development of quantum memories [70, 131]. For example, by acting as a buffer for photonic qubits, quantum memories can synchronize random events, counteracting the probabilistic nature of many quantum light sources.

An ideal quantum memory stores and releases a single photon on demand while faithfully preserving its quantum information. Quantum storage has been demonstrated in various physical systems using heralded [85, 96] and entangled [67, 74, 83, 82, 98] single photons, as well as attenuated laser pulses [89, 13, 141]. Quantum storage times have been demonstrated as long as hours [142], however achieving long storage times for photons often limits their acceptance bandwidth to GHz or below [30, 83].

Demonstrations of THz-bandwidth [31, 32, 143] storage have been achieved using Raman transitions [93], increasing the operational speeds of quantum memories by several orders of magnitude. Raman memories have also demonstrated additional features such as

constructing tunable beamsplitter networks [110] and spectral manipulation [144]. These aspects of quantum memories enable applications such as rapidly reconfigurable quantum logic gates [114], and generating time-frequency domain entangled states for cluster-state quantum computing [113]. Room-temperature diamond is a candidate for such applications: it is a robust system for the generation of non-classical states [68] and macroscopic entanglement [68], as well as the storage [143] and manipulation [144] of single photon wave-packets.

In this work we store ultrafast photonic qubits in the vibrational excitations of room-temperature diamond using the Raman memory protocol. Recently we demonstrated the storage of single photon in diamond [143], however, since the Raman process in diamond precludes multi-mode storage, the transition to storing qubits is non-trivial. Here we achieve qubit storage by employing a second memory — we use two spots at separate times in the same diamond crystal to provide multimode storage. The two modes forming the qubit are then coherently recombined after retrieval from the memory. We characterize the performance of the memory with a quantum process tomography. We observe faithful storage above a classical bound for many times longer than the input photon coherence time. Additionally, we store one photon from a polarization-entangled photon pair and observe that the entanglement between the stored photon and a herald persists for multiple durations of the photon.

6.4 Experiment

The memory functions as follows. A *signal* photon is stored in the optical phonon modes of the diamond lattice ($|\mathrm{s}\rangle$ in Figure 6.1(c)) via a Raman transition stimulated by a strong *write* pulse. The 40 THz splitting between the ground ($|g\rangle$) and optical phonon states produces a quantum-level noise floor when operating at room temperature [32]. The storage of THz-bandwidth photons is made possible by the large detunings of the signal and write frequencies from the conduction band ($|\mathrm{c}\rangle$); the signal photons have 2.4 THz bandwidth (4.1 nm at center wavelength 723 nm). (Note that in this chapter we have changed the labelling of the diamond energy levels from $\{|0\rangle, |1\rangle, |2\rangle\}$ to $\{|g\rangle, |s\rangle, |c\rangle\}$ to avoid confusion

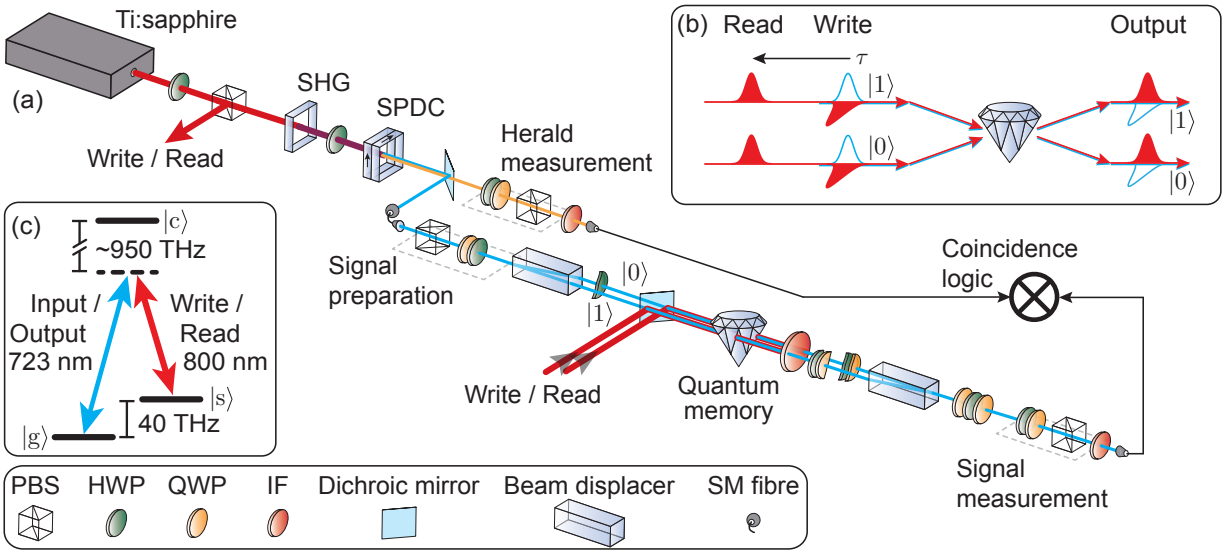

Figure 6.1: (a) Pulses for the read, write and photon source pump are derived from the same laser. A photon pair (signal, herald) is generated via SPDC pumped by the second-harmonic (SHG) of the laser. A polarization qubit is prepared in the signal arm, converted to a dual-rail qubit and sent to the memory. (When generating entangled photon pairs in the source the signal preparation step is removed.) Read and write pulses are prepared in displaced Mach-Zehnder and Michelsen interferometers (not shown), and are overlapped with the qubit modes on a dichroic mirror. After retrieval, the qubit is converted back to polarization. Half- (HWP) and quarter-waveplates (QWP) are used in each mode to correct polarization and phase rotations, and the state is analyzed by a HWP, QWP and polarizing beamsplitter (PBS). After passing through an interference filter (IF), coincident photon detections with the herald are counted. (b) A qubit, $\alpha|0\rangle + \beta|1\rangle$, (hollow blue) is stored in dual-rail modes by two write pulses (solid red). Two read pulses retrieve each mode after time τ. (c) Λ-level diagram for diamond. Input and write fields transition the crystal from its ground state ($|\mathrm{g}\rangle$) to the optical phonon level ($|\mathrm{s}\rangle$); read and output fields drive the reverse the transition. All frequencies are far detuned from the conduction band ($|\mathrm{c}\rangle$).

with the state of the stored qubit defined by $|0\rangle$ and $|1\rangle$.) After a time τ, the photon is retrieved from the memory by a *read* pulse. Propagating along the z-direction in diamond, Raman selection rules require that write and signal pulses have orthogonal polarizations. Similarly, the photon retrieved from the memory has orthogonal polarization to the read pulse. Our memory is intrinsically single mode in polarization; in order to store polarization qubits spatial or temporal multiplexing is required. The two modes for the qubit memory must function independently, each requiring a set of write and read pulses, see Figure 6.1(b).

Figure 6.1(a) shows the experimental setup. A mode-locked Ti:sapphire oscillator operating at 80 MHz outputs 190 fs pulses at 800 nm center wavelength. The laser power is divided between read/write pulses and the pump for the photon source. The source generates photon pairs by pumping type-I spontaneous parametric downconversion (SPDC) in a 1 mm Barium Borate (BBO) crystal with the second harmonic of the pump pulse. The detection of an 895 nm photon *heralds* the presence of a 723 nm photon in the signal mode. With the quantum memory not active — no control pulses are present and input photons are transmitted through the diamond — we measure a coincidence rate of ∼1100 Hz between signal and herald detections, using a coincidence detection window of 1 ns. The polarization state of the signal photon is prepared using a polarizing beamsplitter (PBS), quarter- (QWP) and half-waveplate (HWP) which is then mapped into spatial modes using a calcite beam displacer which separates horizontal ($|\mathrm{H}\rangle$) and vertical ($|\mathrm{V}\rangle$) polarizations by 4 mm in the transverse direction. The two signal modes, $|\mathrm{H}\rangle$ and $|\mathrm{V}\rangle$, are overlapped spatially and temporally with their corresponding write pulses and are incident on the diamond. The 2.3 mm-long, high-purity diamond was grown by chemical vapour deposition. With 4.4 nJ of energy in each write pulse we observe a write efficiency of $\eta_w = 6.2\%$ marked by a dip in signal-herald coincidences in both memory modes due to absorption. We note that though the signal spatial modes are separated by 4 mm, they are focussed to the same point in the diamond crystal. To avoid cross-talk between the two memory modes we separate the two write processes in time by 16.7 ps such that the first signal mode is stored, retrieved, and the memory restored to its ground state before the second signal mode arrives at the diamond.

After time τ, two 4.4 nJ read pulses are incident on the memory. Half- and quarter-waveplates in each spatial mode correct for polarization rotations. Retrieved signal modes

are coherently recombined on a polarizing beam displacer, converting the quantum information back to polarization, and the phase is corrected using a QWP-HWP-QWP combination. Any light that is not stored in the memory is transmitted through the diamond, but has orthogonal polarization to the retrieved light and is removed by the beam displacer. The polarization state of the retrieved photon is analyzed using an HWP-QWP-PBS combination before collection in single-mode fibre and detection by an avalanche photodiode; joint detections of signal and herald photons are recorded by coincidence counting logic.

Figure 6.2(a) shows the coincidence rate of retrieved signal photons as a function of storage time when preparing and measuring the horizontal polarization. At the peak we measure a retrieval coincidence rate of 8.33 Hz. The memory efficiency is then $\eta_{\mathrm{M}} = (0.76 \pm 0.03)\%$, implying a retrieval efficiency of $\eta_r = \eta_{\mathrm{M}}/\eta_w = 12.2\%$. The efficiency of our memory is limited by the amount of available laser power for write and read pulses. An exponential fit $N_c/2 + (S_0 + N_0/2)e^{-\tau/\tau_{\mathrm{M}}}$ yields a memory lifetime of $\tau_{\mathrm{M}} = 3.5\,\mu$s which is limited by acoustic decay of the optical phonon [127]. Spurious noise processes in the memory can trigger counts when no photon is input to the memory. We measure a constant noise rate of $N_c = 3.737 \pm 0.004$ Hz, a time-dependent noise rate $N_0 e^{-\tau/\tau_{\mathrm{M}}}$, where $N_0 = 0.464 \pm 0.008$ Hz, and an initial retrieved signal rate $S_0 = 6.2 \pm 0.3$ Hz. A factor of 2 in the noise rate compensates for the fact that though noise is generated in both memory modes, half is removed by polarization analysis. The probability that a photon detection corresponds to a successful storage and retrieval from the memory is then $p(\tau) = S_0 e^{-\tau/\tau_{\mathrm{M}}}/[N_c + (N_0 + S_0)e^{-\tau/\tau_{\mathrm{M}}}]$.

6.5 Results and Discussion

6.5.1 Quantum state tomography

To characterize the performance of the quantum memory we prepare and store each of the following input states: $|0\rangle = |\mathrm{H}\rangle$, $|1\rangle = |\mathrm{V}\rangle$, $|\pm\rangle = (|\mathrm{H}\rangle \pm |\mathrm{V}\rangle)/\sqrt{2}$, $|\pm_y\rangle = (|\mathrm{H}\rangle \pm i|\mathrm{V}\rangle)/\sqrt{2}$, which is a tomographically overcomplete set. Retrieving the photon from the memory we perform a maximum likelihood quantum state [11] and process tomographies [25]. Figure 6.3 shows the reconstructed density matrices for all six input states after storage in

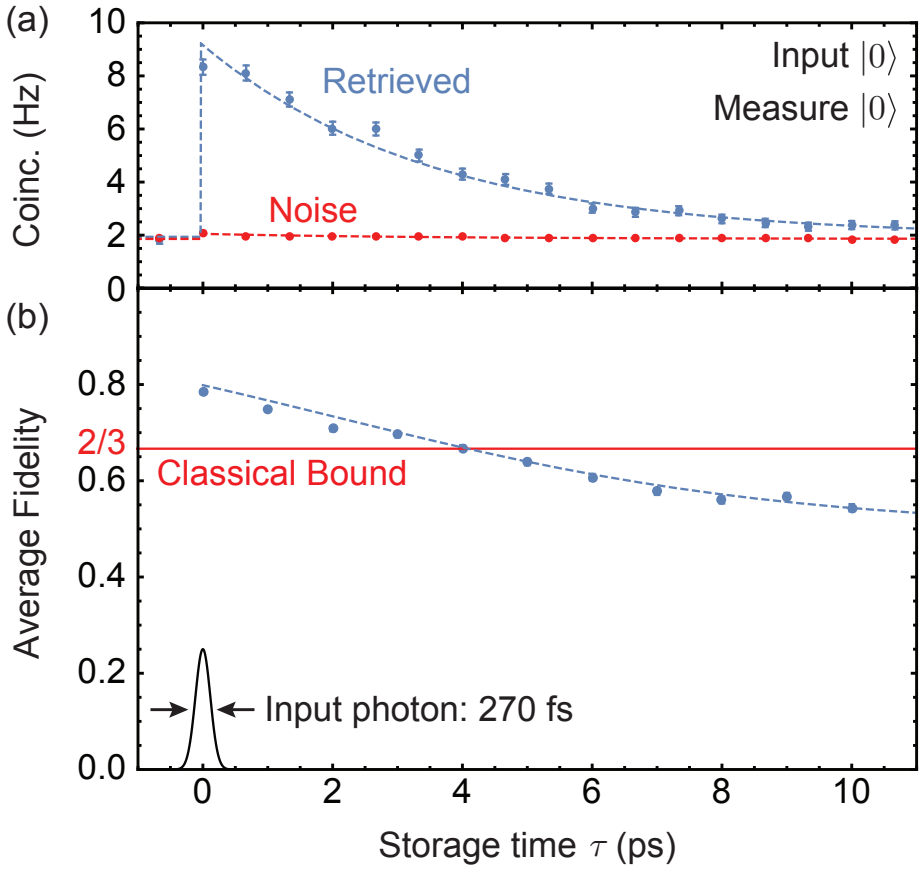

Figure 6.2: (a) Measured herald-signal (blue) coincidences after the memory, where the input state is prepared as $|0\rangle$ and the output is projected onto $|0\rangle$. Error bars show one standard deviation assuming Poissonian noise. Coincidences due to noise photons (red), i.e., when there is no input signal, are also present in the retrieved signal which degrade stored qubits. The function $N_c/2 + (S_0 + N_0/2)e^{-\tau/\tau_M}$ is fit to the data (dashed lines). (b) Average state fidelity of the memory output as a function of storage time. The quantum memory operates above the 2/3 classical bound for 3 ps, over 11 durations of the 270 fs input photon (shown for reference). Modelling the memory with noise as a partially depolarizing channel (Eq. 1) the average fidelity is $[1 + p(\tau)]/2$ (dashed line).

the the quantum memory. The fidelity of the output state ρ_o with an ideal input ρ_i is calculated [16] as $\mathcal{F}(\rho_o, \rho_i) = \left(\mathrm{Tr}\sqrt{\sqrt{\rho_i} \cdot \rho_o \cdot \sqrt{\rho_i}}\right)^2$ (see Section 1.3.2). The fidelity averaged over the six input states is 0.784 ± 0.004, where the uncertainty is calculated using Monte Carlo simulations by adding Poissonian noise to measured counts. By contrast a classical memory, i.e., measuring and re-preparing the qubit, can function with an average state fidelity of 2/3 [69] (see Appendix D). As shown in Figure 6.2(b), our quantum memory beats this bound up to 3 ps of storage, which is over 11 durations of the input photon coherence time. From these measurements we can also reconstruct the process matrix for the memory, χ_{M}, using a maximum likelihood quantum process tomography (see Section 1.4.1), shown in Fig. 6.4. We compare χ_{M} with the process matrix when the memory is inactive, χ_{inactive}, i.e., with no read and write pulses present, and find a process fidelity (see Section 1.4.2) of $\mathcal{F}(\chi_{\mathrm{M}}, \chi_{\mathrm{inactive}}) = 0.761 \pm 0.006$.

The primary limitation on memory fidelity is noise produced by the read and write pulses. Reconstructing the process matrix when no input photon is present we find a process fidelity > 0.999 with the completely depolarizing channel, producing the maximally mixed state $\mathbb{1}_2/2$. This implies the noise is completely unpolarized and so the memory operating in the presence of noise can be modelled as a partially depolarizing channel

$$\mathcal{E}(\rho) = p(\tau)\rho + [1 - p(\tau)]\,\mathbb{1}_2/2, \tag{6.1}$$

where is $p(\tau)$ is as stated above. The average state fidelity of the channel output is $[1 + p(\tau)]/2$ which is plotted alongside the data in Figure 6.2(b). We find the process fidelity between χ_{M}, reconstructed for a storage time τ, and the channel in Eq. 6.1 to be > 0.99 for all measured storage times. This suggests that our simple model describes the memory process well.

6.5.2 Entanglement storage

We now turn to the storage of one photon of an entangled pair. To prepare a two-photon polarization-entangled state we pump type-I SPDC in two orthogonally oriented 1 mm BBO crystals, using a diagonally-polarized pump pulse. With appropriate temporal compensation and phase correction, this ideally generates the state $|\Phi^+\rangle = (|0\rangle_s|0\rangle_h + |1\rangle_s|1\rangle_h)/\sqrt{2}$,

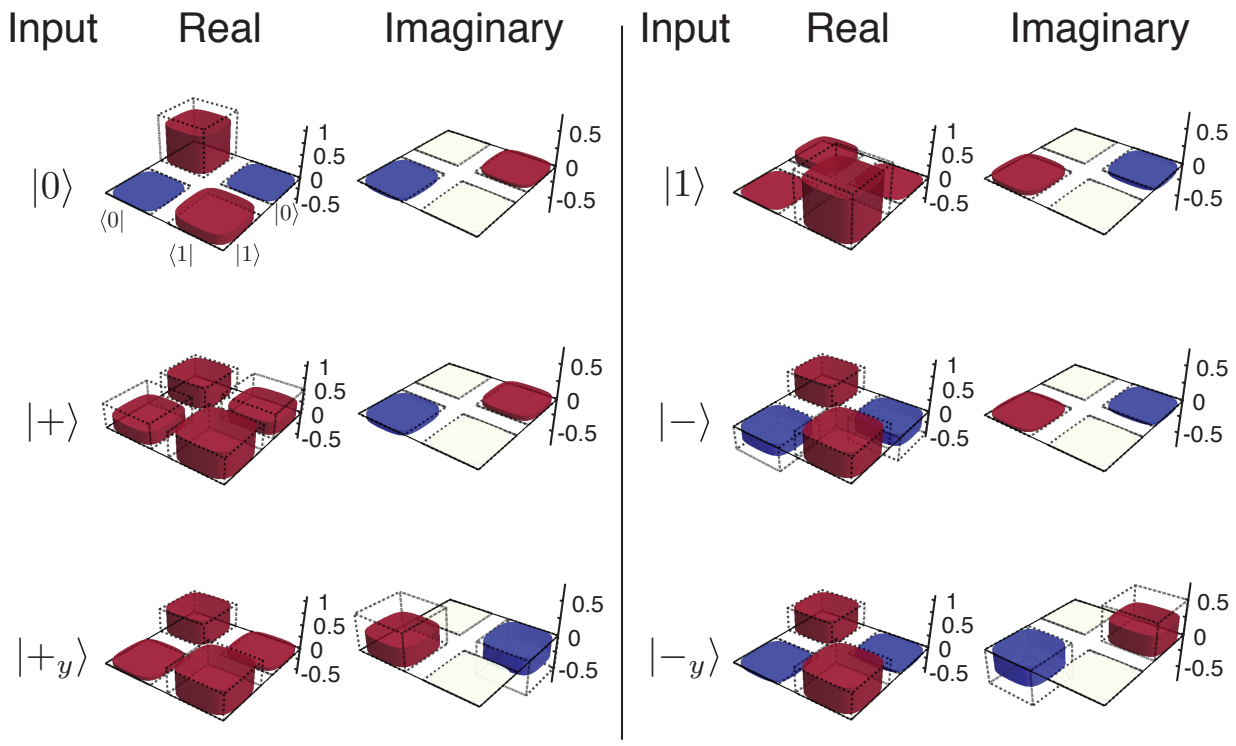

Figure 6.3: Reconstructed density matrices for each of the six input states after storage in the quantum memory. The average of the state fidelities with corresponding ideal inputs (dashed black) is 0.784 ± 0.004.

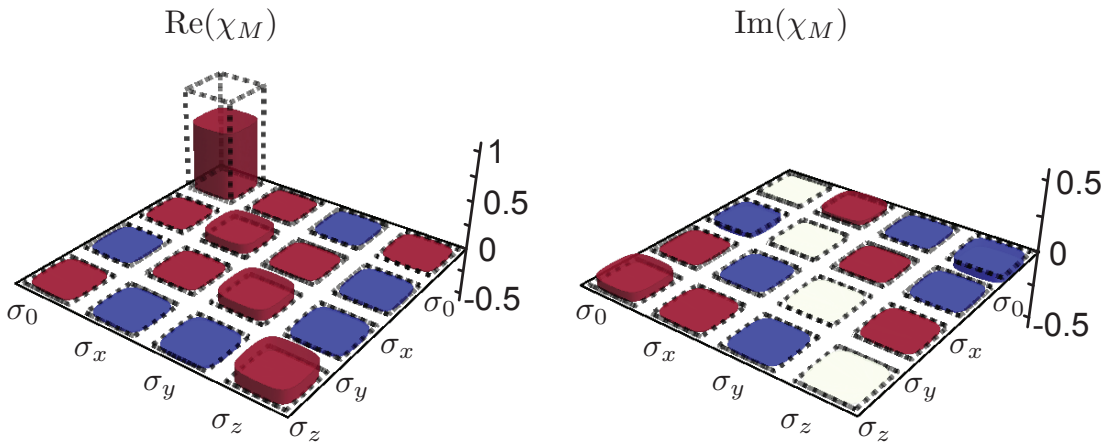

Figure 6.4: The real and imaginary parts of χ_M, the reconstructed process matrix describing the quantum memory. The process matrix is represented in the basis of Pauli operators $\{\sigma_0 = \mathbb{1}, \sigma_x, \sigma_y, \sigma_z\}$. The process fidelity with the ideal memory, i.e., the identity process (dashed black), is 0.677 ± 0.006. The process fidelity with the same optical setup when the memory is not active, i.e., control beams not present, is 0.761 ± 0.004.

where the subscripts s and h refer to signal and herald modes, respectively. In order to store the entangled signal photon we remove the state preparation apparatus from the signal path shown in Figure 6.1(a); otherwise the procedure is identical to above. Using a two-qubit maximum likelihood state tomography we reconstruct the density matrix of the retrieved signal-herald state. We perform quantum state tomography on the initial state, before storage, and find a fidelity of 0.939 ± 0.001 with $|\Phi^+\rangle$ — the real part of the input state density matrix is shown in Figure 6.5(a). We measure an input coincidence rate of 360 Hz in both $|0\rangle_s|0\rangle_h$ and $|1\rangle_s|1\rangle_h$ bases when the memory is inactive, and retrieval rates of 2.32 Hz in each basis. The state after retrieval has 0.562 ± 0.007 fidelity with $|\Phi^+\rangle$, and 0.764 ± 0.005 fidelity with the input state (see Figure 6.5(b)). (The discrepancy between these two fidelities is explained in Section 1.2.1.) The retrieved state fidelities as a function of storage time are shown in Figure 6.5(c).

When the channel in Eq. 6.1 acts one qubit of the maximally entangled state $|\Phi^+\rangle$ the result is a Werner state $\rho_{\mathrm{W}}(\tau) = p(\tau)|\Phi^+\rangle\langle\Phi^+| + [1 - p(\tau)]\mathbb{1}_4/4$ (see Section 1.2.1). The fidelity of ρ_{W} with the maximally entangled state is $\mathcal{F}(\rho_{\mathrm{W}}, |\Phi^+\rangle\langle\Phi^+|) = [1 + 3p(\tau)]/4$,

which is plotted in Figure 6.5(c) (dashed line). Here we found the initial retrieved signal rate to be $S_0 = 1.39 \pm 0.07\,\text{Hz}$, the constant noise rate to be $N_c = 1.41 \pm 0.04\,\text{Hz}$ and the time-dependent noise rate to be initially at $N_0 = 0.46 \pm 0.09\,\text{Hz}$. Over all investigated storage times output states show high overlap with the Werner state $\rho_{\text{W}}(\tau)$, averaging to 0.990 ± 0.001.

We use concurrence [9] (see Section 1.2.1) to quantify the amount of entanglement remaining in the state after storage. The concurrence of a state ρ is $\mathcal{C}(\rho) = (\max\{0, \lambda_1 - \lambda_2 - \lambda_3 - \lambda_4\})$, where λ_i are the eigenvalues, in decreasing order, of the matrix $R = \sqrt{\sqrt{\rho}\tilde{\rho}\sqrt{\rho}}$; here $\tilde{\rho} = (\sigma_y \otimes \sigma_y)\rho^*(\sigma_y \otimes \sigma_y)$. Maximally entangled states have $\mathcal{C} = 1$, whereas separable states have $\mathcal{C} = 0$. The concurrence of the input state is 0.912 ± 0.002. Figure 6.5(d) shows the concurrence of the retrieved signal as a function of storage time. The concurrence for the Werner state is $\mathcal{C}(\rho_W(\tau)) = \max\{0, [3p(\tau) - 1]/2\}$. This is plotted alongside the data in Figure 6.5(d) (dashed line). We can see that though the state is diminished due to noise, entanglement between the stored and herald photons persists for up to 2 ps of storage time.

As a final note, we return to the result in Fig.6.2(a), which shows the retrieved signal and associated noise. Noise photons are generated by one of two processes: four-wave mixing between read, write and Stokes pulses [32]; and read pulses scattering off of thermally populated phonons [143]. While thermal noise will not depend on the delay between read and write pulses, four-wave mixing noise is equal parts constant and time-dependent from read-read scattering and write-read scattering, respectively. We estimate that 80% of the observed noise is thermal. While four-wave mixing noise can be mitigated through phase matching conditions, thermal noise can be reduced with cooling. For instance at $-40°\text{C}$, which is achievable with Peltier cooling, thermal noise should be reduced by a factor of 6. From our model we expect that the peak average state fidelity (Fig.6.2(b)) would increase to 0.91 and would remain above the classical bound for 7.6 ps of storage, over 28 times longer than the input photon. In the entangled state case, the output fidelity of the with $|\Phi^+\rangle$ would increase to 0.787 and the concurrence would remain above zero for 6 ps of storage.

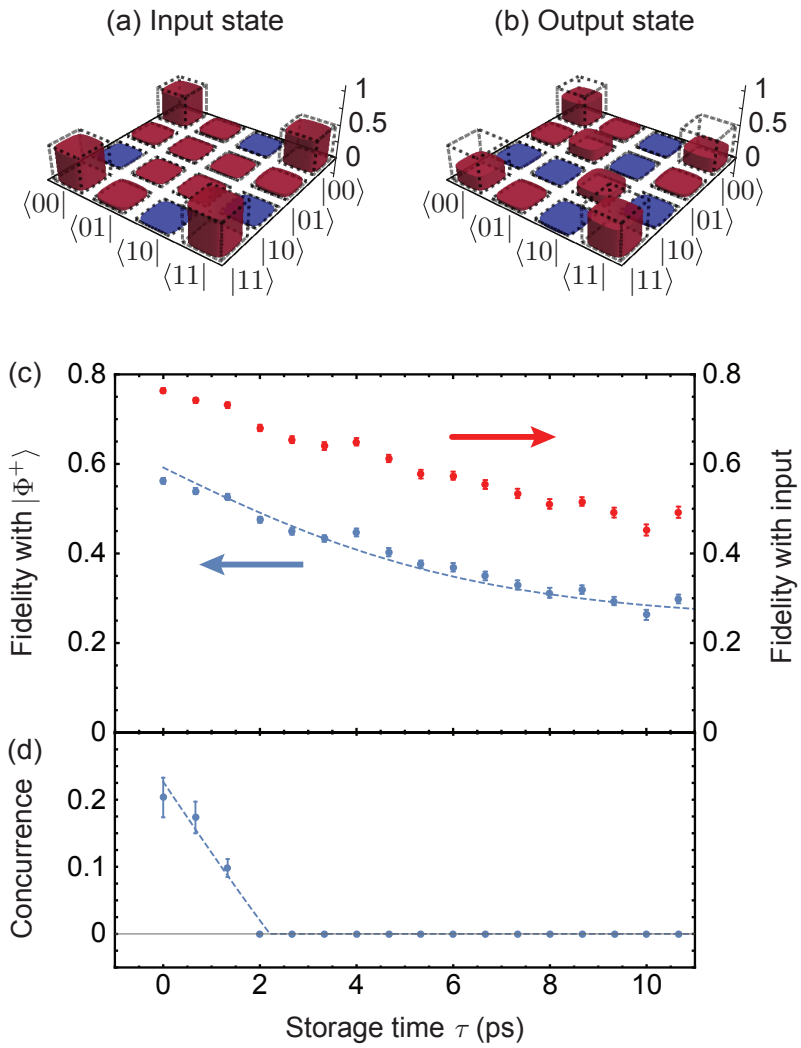

Figure 6.5: The real parts of the reconstructed input (a) and output (b) density matrices show entanglement between signal and herald photons. The input state has 0.939 ± 0.001 fidelity with $|\Phi^+\rangle$, and at the peak the output of the quantum memory has 0.562 ± 0.007 fidelity with $|\Phi^+\rangle$, and 0.764 ± 0.005 with the input state. (c) Fidelity of the joint output-herald state with $|\Phi^+\rangle$ (blue dots, left axis) and fidelity with the input state (red dots, right axis) as a function of storage time. (d) Concurrence of the joint output-herald state (dots) and for the Werner state (dashed) as a function of storage time. Entanglement persists for up to 2 ps of storage.

6.6 Conclusion

We have shown that the diamond memory supports non-classical storage of ultrafast photonic qubits. To our knowledge, this study demonstrates the highest storage bandwidth of an entangled photon to date. While the storage time remains prohibitively short for many long-distance applications, we expect that the diamond memory will find use in communication architectures where long-lived storage is not required. This includes rapidly reconfigurable quantum logic gates [114], and processing spectral properties of photonic qubits [144]. That the diamond memory can also support polarization qubit storage establishes it as an key enabler for future quantum technologies.

Chapter 7

Frequency and bandwidth conversion of single photon in the diamond quantum memory

7.1 Notes and acknowledgements

The contents of this chapter have been published as: K.A.G. Fisher, D.G. England, J.-P. Maclean, P.J. Bustard, K.J. Resch, B.J. Sussman, Frequency and bandwidth conversion of single photons in a room-temperature diamond quantum memory, *Nature Communications*, **7**, 11200 (2016).

This project was a collaboration with the Quantum Technologies group at the National Research Council of Canada. The experiment was conceived by **K.A.G. Fisher**, **D.G. England** and **B.J. Sussman**. **D.G. England** constructed the initial diamond memory setup. **K.A.G. Fisher** and **J.-P. Maclean** constructed the photon source. **K.A.G. Fisher**, **D.G. England** and **J.-P. Maclean** performed the experiment and analyzed the data. **K.A.G. Fisher** wrote the initial manuscript, and all authors contributed the final manuscript.

7.2 Abstract

The spectral manipulation of photons is essential for linking components in a quantum network. Large frequency shifts are needed for conversion between optical and telecommunication frequencies, while smaller shifts are useful for frequency-multiplexing quantum systems, in the same way that wavelength division multiplexing is used in classical communications. Here we demonstrate frequency and bandwidth conversion of single photons in a room-temperature diamond quantum memory. Heralded 723.5 nm photons, with 4.1 nm bandwidth, are stored as optical phonons in the diamond via a Raman transition. Upon retrieval from the diamond memory the spectral shape of the photons is determined by a tunable read pulse through the reverse Raman transition. We report central frequency tunability over 4.2 times the input bandwidth, and bandwidth modulation between 0.5 and 1.9 times the input bandwidth. Our results demonstrate the potential for diamond, and Raman memories in general, as an integrated platform for photon storage and spectral conversion.

7.3 Introduction

The fragility of the quantum state is a challenge facing all quantum technologies. Great efforts have been undertaken to mitigate the deleterious effects of decoherence by isolating quantum systems, for example, by cryogenically cooling and isolating in vacuum. State-of-the-art decoherence times are now measured in hours [142]. An alternative approach is to build quantum technologies that execute on ultrafast time scales – as short as femtoseconds – such that operations can be completed before decoherence overwhelms unitarity. A shining example is the Raman quantum memory [93, 30, 31, 96] which can absorb single photons of femtosecond duration and release them on demand several picoseconds later [143]. While picosecond storage times are not appropriate for conventional quantum memory applications such as long distance communication, it has been suggested [93] that Raman quantum memories can find additional uses such as frequency and bandwidth conversion.

Controlling the spectral properties of single photons is essential for a wide array of emerging optical quantum technologies spanning quantum sensing [130], quantum computing [41], and quantum communications [54]. Essential components for these technologies include single photon sources [145], quantum memories [128], waveguides [146], and detectors [147]. The ideal spectral operating parameters (wavelength and bandwidth) of these components are rarely similar; thus, frequency conversion and spectral control are key enabling steps for component hybridization [148]. Beyond hybridization, frequency conversion is an area of emerging interest in quantum optical processing. The frequency degree of freedom can be used along side conventional encoding in, for example, polarization, or time-bin, to build quantum states of higher dimensionality [113].

Spectral control is a mature field in ultrafast optics where phase- and amplitude-shaping of a THz-bandwidth pulse can be achieved using passive pulse-shaping elements in the Fourier plane [149]. Meanwhile, a range of nonlinear optical techniques [43] such as second harmonic generation, sum- and difference-frequency generation, four-wave mixing, and Raman scattering are routinely employed to shift the frequency of laser pulses. Extending these frequency conversion techniques into the quantum regime is a critical task for many quantum technologies but is made difficult by the low intensity of single photons, and the sensitivity of quantum states to loss and noise. Despite these challenges, quantum frequency conversion [99] has been demonstrated in a number of systems including waveguides in nonlinear crystals [150, 100, 102, 103, 104, 105], photonic crystal fibres [101], and atomic vapour [106]. Similarly, photon bandwidth compression has been shown using chirped pulse upconversion [107]. Full control over the spectral properties of single photons [151] has been proposed using second- [148, 152] and third-order [153] optical nonlinearities.

Large frequency shifts, such as those achieved using sum- and difference-frequency generation, are desirable to convert photons to, and from, the telecommunication band. Meanwhile, smaller shifts can be useful for frequency-multiplexing in several closely spaced bins. This concept is widely used in classical fiber optics where wavelength division multiplexing (WDM) is employed to achieve data rates far beyond that which could be achieved with monochromatic light [154]. However, in quantum optics the utility of frequency multiplexing has only recently been explored [155, 113, 114, 156]. In a frequency-multiplexed

quantum architecture, it will be critical to build components that can add, drop, and manipulate different frequency bins: it has been proposed that frequency-selective quantum memories can perform this task [113, 114]. As with classical WDM, the frequency bins will likely be closely spaced so that small shifts around a central frequency will be required.

In this article, we demonstrate the use of a Raman quantum memory to perform quantum frequency conversion: we manipulate the spectral properties of THz-bandwidth photons using a memory in the optical phonon modes of diamond [143]. Crucially, the quantum properties of the photon must be maintained even while the carrier frequency and bandwidth are modified. In our demonstration, a signal photon is mapped into an optical phonon by the write pulse, and then retrieved with its spectral properties modified according to the properties of the read pulse.

7.4 Results

7.4.1 Experiment

The frequency converter is based on a quantum memory [143] modeled by the Λ-level system shown in Fig. 7.1(b), where an input signal photon (723.5 nm centre wavelength and bandwidth $\delta = 4.1$ nm full width at half maximum (FWHM)) and a strong write pulse (800 nm, 5 nm FWHM) are in Raman resonance with the optical phonon band (frequency 40 THz). The large detuning of both fields from the conduction band (detuning $\Delta \approx 950$ THz) allows for the storage of high-bandwidth photons while the memory exhibits a quantum-level noise floor even at room temperature [143]. The input signal photon is stored in the memory by Raman absorption with the write pulse, creating an optical phonon. After a delay τ, the read pulse annihilates the phonon and creates a modified output photon. By tuning the wavelength and bandwidth of the read pulse, we convert the wavelength of the input signal photon over a range of 17 nm as well as performing bandwidth compression to 2.2 nm and expansion to 7.6 nm (FWHM). The diamond memory is ideally suited to this task, offering low-noise frequency manipulation of THz-bandwidth quantum signals at a range of visible and near-infrared wavelengths in a robust room-temperature device [32].

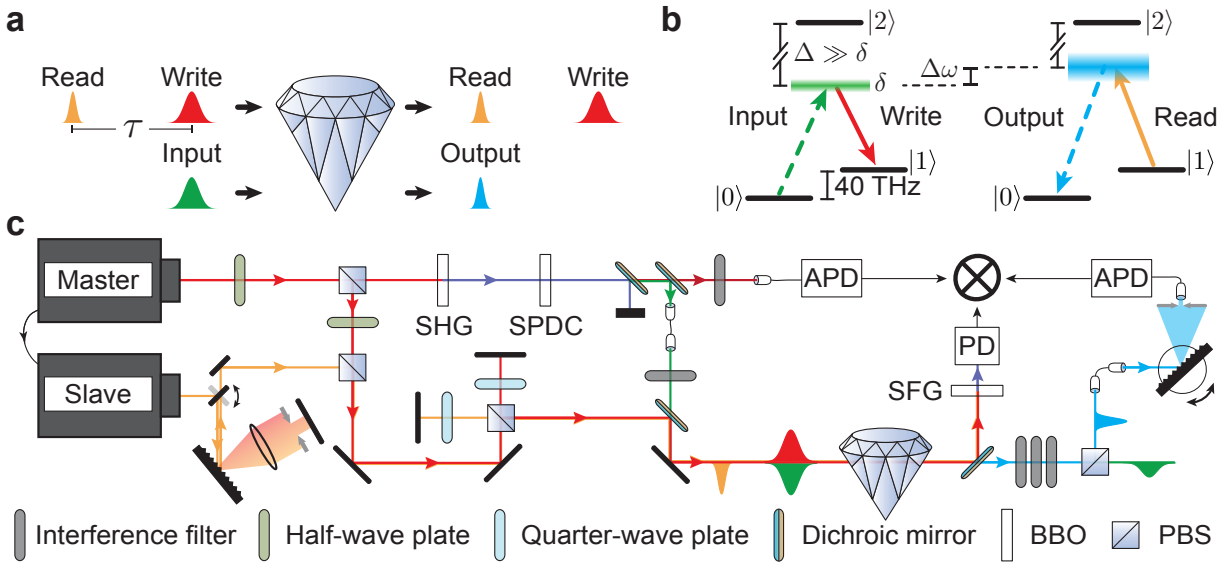

Figure 7.1: Concept and experiment. (a) Input signal photons stored in the diamond by the strong write pulse can be retrieved with modified spectral properties upon the output. The output spectrum is controlled by that of the read pulse. (b) Photons are Raman-absorbed to create optical phonons ($|1\rangle$), 40 THz above the ground state ($|0\rangle$). A read pulse of tunable wavelength and bandwidth retrieves the photon, determining its spectrum. Here, Δ is the detuning from the conduction band ($|2\rangle$), δ is the input photon bandwidth, $\Delta\omega$ is the detuning between input and output frequencies. (c) The master laser (red) is split between the write field and photon source. In the photon source, frequency-doubled laser light pumps spontaneous parametric downconversion and heralded input signal photons (green) are generated. Signal photons are Raman-absorbed into the optical phonon modes in the diamond via the write field. The slave laser (orange) emits the read field which retrieves the photon from the diamond after time τ. The output signal photon (blue) spectrum is measured on a monochromator. The sum-frequency generation (SFG) of read and write pulses triggers the experiment. Coincident detections of output, herald photons and SFG events are measured by a coincidence logic unit.

The experimental setup is shown in Fig. 7.1c. The master laser for the experiment is a Ti:sapphire oscillator producing 44 nJ pulses at a repetition rate of 80 MHz and a central wavelength of 800 nm. This beam is split in two parts: the photon-source pump and the write field. In the photon source, the second harmonic generation (SHG) of the laser light pumps collinear type-I spontaneous parametric downconversion (SPDC) in a β-barium borate (BBO) crystal, generating photons in pairs, with one at 723.5 nm (*input signal*) and the other at 894.6 nm (*herald*). The herald photon is detected on an avalanche photodiode (APD) while the input is spatially and spectrally filtered, and overlapped with the orthogonally polarized write pulse on a dichroic mirror. The input signal photon and write field are incident on the $\langle 100 \rangle$ face of the diamond and the input is Raman-absorbed.

The photon is retrieved from the diamond using a read pulse produced by a second Ti:sapphire laser (*slave*), whose repetition rate is locked to the master, but whose frequency and bandwidth can be independently modified. In this experiment we vary the read field wavelength between 784 nm and 814 nm, and its bandwidth between 2.1 nm and 12.1 nm FWHM. In order to narrow the bandwidth of the read pulse, a folded-grating $4f$-system [149] with a narrow slit is used, while in all other configurations the $4f$ line is removed. The read pulse is then overlapped with the write on a polarizing beamsplitter (PBS), arriving at the diamond a time τ after storage. The horizontally polarized read pulse retrieves a vertically polarized photon (*output*) from the diamond with spectral shape close to that of the read pulse, blue-shifted by the phonon frequency (40 THz).

The read and write pulses are separated from the signal photons after the diamond by a dichroic mirror; sum-frequency generation (SFG) of the pulses is detected on a fast-photodiode (PD) and used to confirm their successful overlap. Frequency-converted output photons are separated from any unstored input photons by a PBS, coupled into a single-mode fibre, and directed to a monochromator. The spectrally filtered output from the monochromator is coupled into a multi-mode fibre and detected on an APD. Coincident detections between output, herald, and read-write SFG events are measured; the experiment is triggered by the joint detection of a herald photon and an SFG signal. (See *Methods* for further details.)

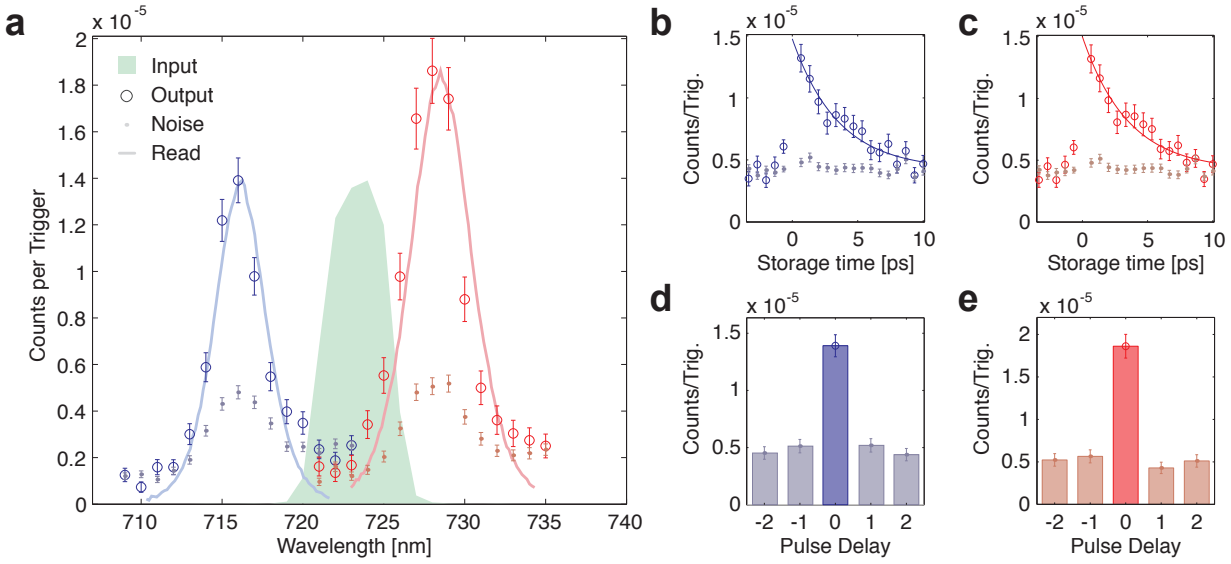

Figure 7.2: Frequency conversion. (a) The measured blue- and red-shifted output photon spectra (hollow circles), and noise (dots), when the read beam is tuned to 792 nm and 808 nm respectively. Corresponding read beam spectra, blue-shifted by the phonon frequency, are shown (solid lines) for reference along with the input photon spectrum (green). (b) Retrieved blue- and (c), Red-shifted signal (hollow circles), and noise (dots), as read-write delay is scanned. An exponential fit gives a phonon lifetime of 3.5 ps. (d) Coincidence detection events between blue- and (e), red-shifted output and herald photons while scanning the electronic delay between them, as measured at the peak of the spectrum. (a)–(e) Error bars show one standard deviation calculated assuming Poissonian noise.

7.4.2 Frequency shifts

Frequency conversion of the signal photon is observed by tuning the slave laser wavelength. We vary this from 784 nm to 812 nm and measure the output photon wavelength using the monochromator, recording three-fold coincidence events. The resulting output spectra, with the read pulse centred at 792 nm and 808 nm, are shown in Fig. 7.2a (hollow circles). The spectrum of each read pulse (solid lines), blue-shifted by the phonon frequency, is plotted alongside the relevant output photon spectrum to show how the photon spectrum is determined by the read pulse. We find the peaks of the output spectra to be 716 nm and 728 nm with bandwidths 3.3 nm and 3.5 nm, FWHM respectively, making the output spectrally distinguishable from the input (green).

Following retrieval, the time-correlations characteristic of SPDC photon-pairs are preserved. This is measured by scanning the electronic delay between the signal and herald detection events in steps of 12.5 ns (the time between adjacent oscillator pulses) and counting coincident detections. Results are shown in Fig. 7.2d-e for blue- and red-shifted cases respectively. We quantify this using the two-mode intensity cross-correlation function between output signal and herald fields given by $g^{(2)}_{\mathrm{s,h}} = P_{\mathrm{s,h}}/(P_{\mathrm{s}}P_{\mathrm{h}})$. Here, $P_{\mathrm{s}}(P_{\mathrm{h}})$ is the probability of detecting a photon in the signal (herald) mode, and $P_{\mathrm{s,h}}$ is the probability of measuring a joint detection. A measurement of $g^{(2)}_{\mathrm{s,h}} > 2$ indicates non-classical correlation [157, 37] (see Methods), whereas uncorrelated photon detections, e.g., from noise, give $g^{(2)}_{\mathrm{s,h}} = 1$. We calculate the values of $g^{(2)}_{\mathrm{s,h}}$ at the peak of the blue- and red-shifted spectra to be 2.7 ± 0.2 and 3.4 ± 0.3, respectively.

Figure 7.2b(c) shows the blue-(red-)shifted photon retrieval rate as a function of the optical delay τ between read and write pulses. An exponential function is fit to the data and we find a memory lifetime of 3.5 ps as expected from the lifetime of the optical phonon [40, 32]. This exceeds 12 times the duration of the input photon (see Methods). Also plotted in Fig. 7.2a-c are the measured coincidences due to noise (dots), which are measured by taking the average of the ± 12.5 and ± 25 ns time-bins as shown in Fig. 7.2d and e. Noise comes from two processes: four-wave mixing [32]; and read pulses scattering from thermally-populated phonons producing anti-Stokes light [143, 32]. The latter can be reduced by an order of magnitude by cooling the diamond to -60° C.

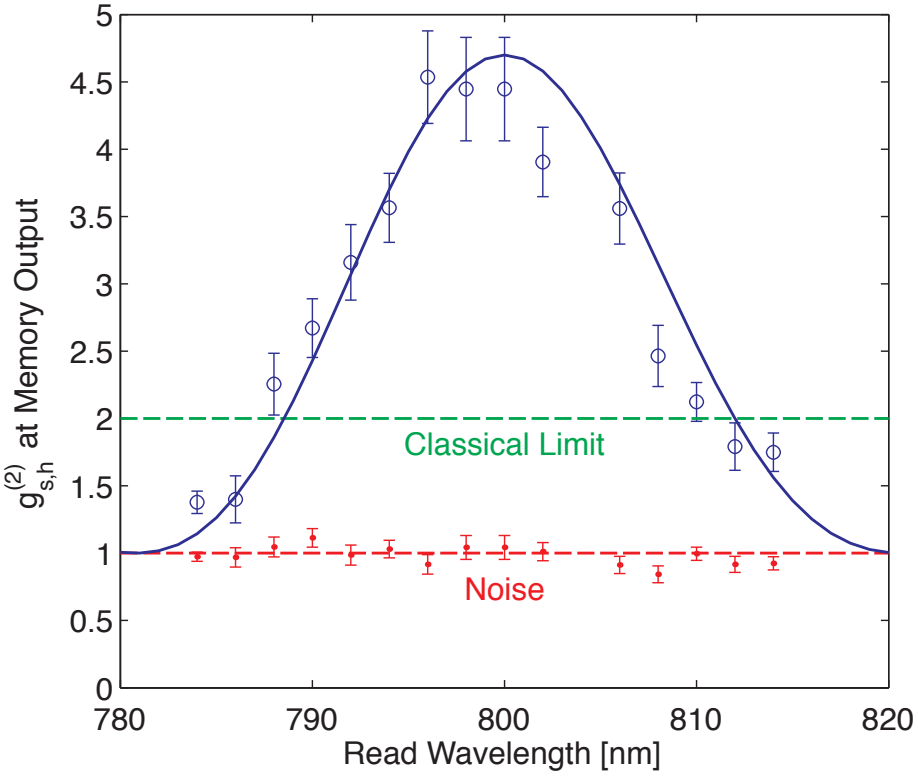

Figure 7.3: Range of frequency conversion. Measured $g^{(2)}_{\mathrm{s,h}}$ of frequency-shifted photons. Frequency conversion, tuning the read beam over a 30 nm range, is observed. Non-classical statistics, i.e., $g^{(2)}_{\mathrm{s,h}} > 2$, are maintained over a 18 nm range. The estimated $g^{(2)}_{\mathrm{s,h}}$ (solid line) which depends on $\mathrm{sinc}^2(\Delta kL/2)$ agrees well with experimental data suggesting that the range of frequency conversion is determined by phase matching conditions. Error bars show one standard deviation calculated assuming Poissonian noise.

Figure 7.3 shows $g^{(2)}_{\mathrm{s,h}}$ measured at the peak of each output signal spectrum as the read wavelength is tuned over a 30 nm range. We find that blue- and red-shifted single photons maintain non-classical correlations over a 17 nm range. Since noise is uncorrelated with herald photons, we expect the noise to have cross-correlation $g^{(2)} = 1$. The $g^{(2)}_{\mathrm{s,h}}$ will increase from 1 in proportion to the signal-to-noise ratio (see Methods for further details),

$$g^{(2)}_{\mathrm{s,h}} \approx 1 + \frac{\eta_{\mathrm{h}}\eta_{\mathrm{fc}}(\Delta\omega)}{P_{\mathrm{n}}}. \tag{7.1}$$

Here $\eta_{\mathrm{h}} = P_{\mathrm{s,h}}/P_{\mathrm{h}} = 0.13\%$ is the photon heralding efficiency in the signal arm including the monochromator, $P_{\mathrm{n}} = 3.8 \times 10^{-6}$ is the probability of detecting a noise photon, and $\eta_{\mathrm{fc}}(\Delta\omega)$ is the conversion efficiency as a function of frequency detuning, $\Delta\omega$, between input and output photons. The conversion efficiency $\eta_{\mathrm{fc}}(\Delta\omega) = \eta_{\mathrm{fc}}(0) \times \mathrm{sinc}^2(\Delta\mathbf{k}L/2)$, where $L = 2.3$ mm is the length of the diamond along the propagation axis, and $\Delta\mathbf{k} = \mathbf{k}_{\mathrm{i}} - \mathbf{k}_{\mathrm{o}} + \mathbf{k}_{\mathrm{r}} - \mathbf{k}_{\mathrm{w}}$ is the phase mismatch between the input signal (i), output signal (o), read (r), and write (w) fields due to material dispersion in diamond [32]. The conversion efficiency was measured to be $\eta_{\mathrm{fc}}(0) = 1.1\%$, inside the diamond at zero detuning. As the diamond is not anti-reflection coated, a 17% reflection loss occurs at each face.

Inserting experimental parameters into Eq. 7.1 returns $g^{(2)}_{\mathrm{s,h}} \approx 1 + 3.7 \times \mathrm{sinc}^2(\Delta\mathbf{k}L/2)$ which is plotted along side data in Fig. 7.3 (solid line). The close agreement with experiment suggests that the limitation on frequency conversion comes primarily from phase-matching conditions. We then expect that the range of frequency conversion in diamond can be extended by modifying the phase-matching conditions. This could be achieved by shortening the diamond crystal, or by employing non-collinear beam geometries [158]. In the current configuration, the maximum conversion efficiency is limited to $\sim 1\%$ due to the efficiency of the quantum memory [143]. However, we note that this could be improved with increased intensity in read and write pulses, or by increasing the Raman coupling, for example by use of a waveguide.

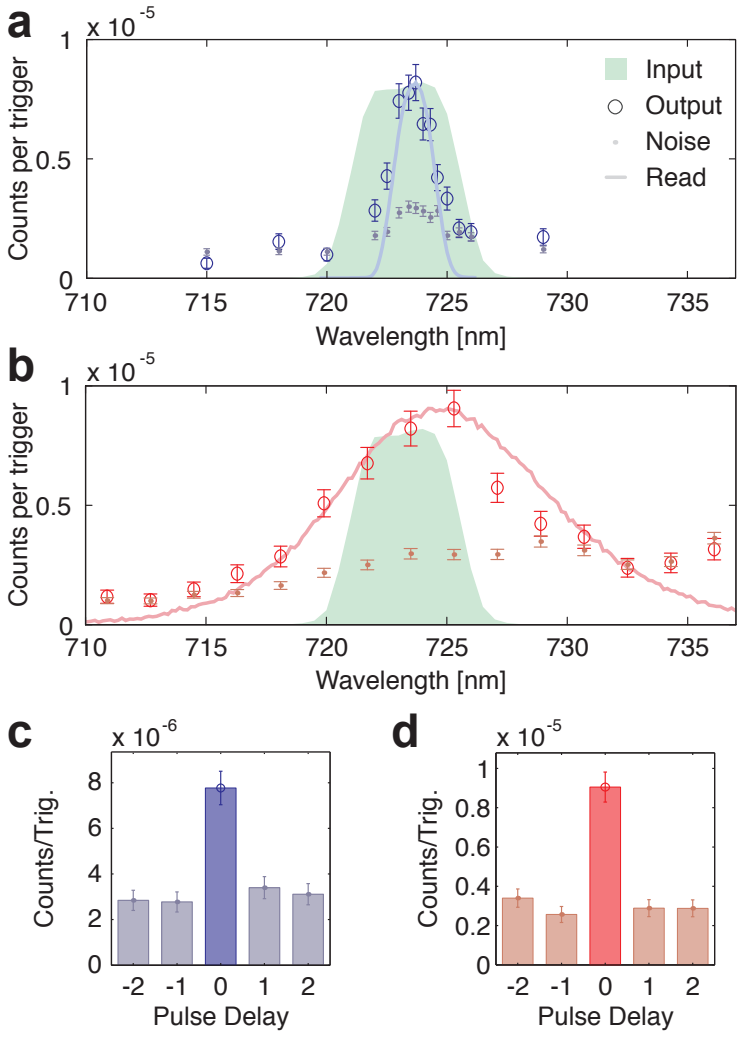

Figure 7.4: Bandwidth conversion. (a) Narrowed output spectrum (hollow circles) and noise (dots) with read beam FWHM at 2.1 nm. (b) Expanded output photon spectrum (hollow circles) and noise (dots) with read beam FWHM at 12.1 nm. (a)–(b) Corresponding read beam spectra, blue-shifted by the phonon frequency, are shown (solid lines) for reference along with the input photon spectrum (green). (c) Coincidence detection events between bandwidth narrowed and (d), expanded output photons and heralds while scanning the electronic delay between them, as measured at the peak of the spectrum. (a)–(d) Error bars show one standard deviation calculated assuming Poissonian noise.

7.4.3 Bandwidth manipulation

Bandwidth conversion is observed by tuning the slave laser bandwidth. With the read pulse wavelength centred at 801 nm, its bandwidth could be tuned from 12.1 nm FWHM to 2.1 nm FWHM using a slit in a grating $4f$ line. Figure 7.4a(b) shows the resulting narrowed (expanded) output photon spectrum with the corresponding read pulse spectrum, blue-shifted by the phonon frequency, and the input signal photon spectrum for reference. The resulting narrowed and expanded photon bandwidths are 2.2 nm and 7.6 nm, FWHM respectively. Figure 7.4c(d) shows the conservation of timing correlations between bandwidth-narrowed (-expanded) photons and herald photons, respectively. We measure $g^{(2)}_{\mathrm{s,h}} = 2.6 \pm 0.2$ in the narrowed bandwidth case, $g^{(2)}_{\mathrm{s,h}} = 2.9 \pm 0.2$ in the expanded bandwidth case, showing that bandwidth-converted output light from the diamond maintains non-classical correlations with herald photons.

7.5 Discussion

We have demonstrated ultrafast quantum frequency manipulation by adjusting the central wavelength and spectrum, of THz-bandwidth heralded single photons. We achieve this spectral control using a modified Raman quantum memory in diamond. The single photons are written to the memory from one spectral mode, and recalled to another. Critically – and unlike frequency conversion based on, e.g., amplification – the non-classical photon statistics in our demonstration were retained after spectral manipulation. Diamond therefore offers low-noise THz-bandwidth storage and frequency control of single photons on a single, robust, room-temperature platform. We have demonstrated frequency conversion of a single polarization; two memories could be used in parallel to convert a polarization qubit. Quantum memories for long-distance quantum communication typically demand long storage times at the expense of high bandwidth; this application leverages a high-bandwidth memory where long storage time is not relevant. We believe that this system could find use in a number of applications, including entangling two photon pair-sources of different colour; reducing the bandwidth of the ubiquitous ultrafast SPDC photon source, without losing photons (as occurs in passive filtering); broadening the bandwidth of an

SPDC photon source to match a chosen material system (not possible with a passive filtering system); and increasing the dimensionality of quantum encoded information [113]. Ultimately, we believe that arbitrary optical function generation [159] – with both classical and quantum light – and associated signal processing capabilities will be a platform for future technology development. We expect that the large-bandwidth nonlinear optical conversion of Raman-based quantum memories will find use in implementations of these generators.

7.6 Methods

7.6.1 Photon source

Laser light is frequency-doubled by type-I SHG in a 1 mm BBO crystal before pumping collinear type-I SPDC in a second 1 mm BBO crystal. Horizontally-polarized photon pairs are generated at 894.6 nm and 723.5 nm. Remaining pump light is filtered out and photon pairs are separated by a 801 nm long-pass dichroic mirror. The 894.6 nm photon passes through a 5 nm interference filter, is coupled into a single-mode fibre, and detected on an APD. A detection heralds the presence of the 723.5 nm photon, which is spatially filtered in a single-mode fibre and spectrally filtered by an interference filter with bandwidth of 5 nm (FWHM). The input and write pulses are overlapped using a 750 nm shortpass dichroic mirror. The input and write pulses are focused into the diamond by an achromatic lens of focal length 6 cm.

7.6.2 Diamond

The diamond is a high-purity, low birefringence crystal grown by chemical vapour deposition by Element Six Ltd. The crystal is 2.3 mm long, cut along the $\langle 100 \rangle$ lattice direction, and polished on two sides.

7.6.3 Storage time

Absorption of the input photon by the diamond lattice is observed by an 18% dip in input-herald coincidences when the input photon and write field arrive at the diamond simultaneously. The duration of the input photon can be deconvolved from the width of the absorption dip, 346 fs. With write pulses 190 fs in duration, the input photon pulse duration time is $\sqrt{346^2 - 190^2} = 289$ fs, assuming transform-limited Gaussian pulses. The characteristic storage time of the diamond memory is 3.5 ps, found from an exponential fit to storage data, over 12-times the duration of the input pulse.

7.6.4 Laser locking

The repetition rate of the slave laser is locked to that of the master using a Spectra Physics Lok-to-Clock device. We send read and write beams through a cross-correlator (type-II sum-frequency generation (SFG) in a 1 mm BBO crystal) and detect the resulting signal on a fast-photodiode (PD) confirming that the time difference between the two pulses is ≤ 200 fs. We measure a typical SFG signal rate of 2.5 MHz; we use this signal to trigger the experiment.

7.6.5 Monochromator

The monochromator (Acton SP2300) is comprised of a 1200 g/mm grating between two 30 cm focal length spherical mirrors. The output is coupled to a multi-mode fibre (105 μm core). The apparatus has a spectral resolution of 1.1 nm and an overall efficiency of 10% at 723 nm.

7.6.6 Cross-correlation function

The cross-correlation function between the herald and frequency-converted light is given by $g^{(2)}_{\mathrm{s,h}} = P_{\mathrm{s,h}}/(P_{\mathrm{s}}P_{\mathrm{h}})$. Classically, $g^{(2)}_{\mathrm{s,h}}$ is upper-bounded by a Cauchy-Schwarz inequality [157, 37] $g^{(2)}_{\mathrm{s,h}} \leq \sqrt{g^{(2)}_{\mathrm{s,s}} g^{(2)}_{\mathrm{h,h}}}$. Here, the terms on the right-hand side are the intensity

auto-correlation functions for the output signal and herald fields, which we assume, being produced by spontaneous parametric downconversion, follow thermal statistics and have $g^{(2)}_{\mathrm{s,s}} = g^{(2)}_{\mathrm{h,h}} = 2$. Adding any uncorrelated noise would strictly lower terms on the right-hand side toward 1. To model the effect of noise on this measurement, we assume that the signal is made up of a mixture of noise photons (detected with probability $P_{\mathrm{n}} = 3.8 \times 10^{-6}$) and frequency-converted photons (probability P_γ), such that

$$P_{\mathrm{s}} = P_\gamma + P_n \approx P_{\mathrm{h}}\eta_{\mathrm{h}}\eta_{\mathrm{fc}}(\Delta\omega) + P_{\mathrm{n}}, \tag{7.2}$$

$$P_{\mathrm{s,h}} = P_{\gamma,\mathrm{h}} + P_{\mathrm{n,h}} \approx P_{\mathrm{h}}\eta_{\mathrm{h}}\eta_{\mathrm{fc}}(\Delta\omega) + P_{\mathrm{n}}P_{\mathrm{h}}, \tag{7.3}$$

where $\eta_{\mathrm{h}} = 1.3 \times 10^{-3}$ is the heralding efficiency which equates to the collection efficiency of the entire signal arm, including the monochromator, and $\eta_{\mathrm{fc}}(\Delta\omega)$ is the efficiency of the quantum frequency conversion. This returns:

$$g^{(2)}_{\mathrm{s,h}} = \frac{\eta_{\mathrm{h}}\eta_{\mathrm{fc}}(\Delta\omega) + P_{\mathrm{n}}}{P_{\mathrm{h}}\eta_{\mathrm{h}}\eta_{\mathrm{fc}}(\Delta\omega) + P_{\mathrm{n}}}, \tag{7.4}$$

from which Eq. 7.1 follows, given that $P_{\mathrm{h}}\eta_{\mathrm{h}}\eta_{\mathrm{fc}}(\Delta\omega) \ll P_{\mathrm{n}}$.

7.6.7 Background subtraction

When measured at the photon source the input and herald photon cross-correlation is $g^{(2)}_{\mathrm{in,h}} = 164$. Due to imperfect polarization extinction the input photon can, with low probability, traverse the monochromator and be detected, thereby artificially inflating the measured $g^{(2)}_{\mathrm{s,h}}$ of the converted output. For this reason we make a measurement with no read/write pulses present and subtract these counts from the output signal when read/write pulses are present to portray an accurate value of $g^{(2)}_{\mathrm{s,h}}$. As an example, in Figure 7.3, the peak count rate is 19×10^{-6} photons per pulse compared to a background of 3×10^{-6} photons per pulse.

Chapter 8

Two-photon interference mediated by the diamond quantum memory

8.1 Notes and acknowledgements

The contents of this chapter have been published as: D.G. England, K.A.G. Fisher, J.-P. Maclean, P.J. Bustard, R. Lausten, K.J. Resch, B.J. Sussman, Phonon-mediated non-classical interference in diamond, *Physical Review Letters*, **117**, 073603 (2016).

This project was a collaboration with the Quantum Technologies group at the National Research Council of Canada. The experiment was conceived by **D.G. England**, **K.A.G. Fisher** and **B.J. Sussman**. **D.G. England** constructed the diamond memory setup. **K.A.G. Fisher** and **J.-P. Maclean** constructed the photon source. **D.G. England** and **K.A.G. Fisher** performed the experiment and analyzed the data. **D.G. England** wrote the initial manuscript, and all authors contributed the final manuscript.

8.2 Abstract

Quantum interference of single photons is a fundamental aspect of many photonic quantum processing and communication protocols. Interference requires that the multiple pathways

through an interferometer be temporally indistinguishable to within the coherence time of the photon. In this Letter, we use a diamond quantum memory to demonstrate interference between quantum pathways, initially temporally separated by many multiples of the optical coherence time. The quantum memory can be viewed as a light-matter beamsplitter, mapping a THz-bandwidth single photon to a variable superposition of the output optical mode and stored phononic mode. Because the memory acts both as a beamsplitter and as a buffer, the relevant coherence time for interference is not that of the photon, but rather that of the memory. We use this mechanism to demonstrate non-classical single-photon and two-photon interference between quantum pathways initially separated by several picoseconds, even though the coherence time of the photons themselves is just $\sim$250 fs.

8.3 Introduction

Single photons are an attractive choice of qubit because they are robust against environmental decoherence and their state can be manipulated using linear optics. However, the interaction between two single photons is weak, making the implementation of deterministic two-photon gates between two photons challenging [160]. One path forward is to exploit the interference of single photons at optical beamsplitters, combined with feed-forward techniques, to build logic gates which operate in a probabilistic fashion [41]. The probabilistic nature of these gates is a barrier to the scalability of linear-optical quantum processors and, thus far, demonstrations have been limited to small numbers of qubits [161]. Quantum memories, devices that can store a quantum state of light and release them on demand, have been proposed as a solution to the scalability problem of linear-optical quantum processing [131, 72]. By acting as a buffer for single photons, a quantum memory allows storage during feed-forward operations [162, 163], and the synchronization of multiple probabilistic quantum events [111].

Beyond acting as a buffer, it has been shown that a quantum memory can behave as a *light-matter beamsplitter* which partitions an excitation between the light mode, a photon, and the matter mode, a material excitation (see Fig. 8.1 (a,b)). In the classical regime, this functionality has previously been exploited to investigate interference between

atomic spin coherences and an optical field [164], and to develop new capabilities such as reconfigurable optical components [110] and a mirror-less optical resonator [165]. At the quantum level, it has been proposed that quantum memories could be used for continuous-variable quantum computing in the time domain [113], or to perform unitary transforms and linear logic gates [114]. In these proposals, the quantum memory both stores the single photons and performs linear operations upon them and therefore offers a promising route toward scalable linear-optical quantum computing.

In this Letter, we investigate using the beamsplitter functionality of a diamond quantum memory [32, 143] to demonstrate quantum interference phenomena with THz-bandwidth single photons. We use the quantum memory to mediate non-classical single- and multi-photon interference effects between quantum pathways which, in the absence of the memory, would otherwise be temporally distinguishable. In the first experiment, a single photon is partitioned between two time-bin modes. The first time-bin mode ($B1$) is written, with efficiency R_1, into the memory; when a read pulse retrieves this excitation while simultaneously writing time-bin mode $B2$ into the memory (with efficiecny R_2) interference is detected in the output optical mode. In the second experiment, a weak coherent state is written into the memory in time-bin $B1$; when a read pulse retrieves this excitation while simultaneously writing a heralded single photon into the memory, non-classical photon bunching is observed in the output optical mode.

The quantum memory dynamics can be modelled as a beamsplitter interaction, where the single photon mode with creation operator $a^\dagger$ is partially mapped to a phonon mode with creation operator $b^\dagger$, thereby creating a superposition:

$$a^\dagger e^{i\omega_a t} \longrightarrow i\sqrt{R_1} b^\dagger e^{i\omega_b t} + \sqrt{1-R_1} a^\dagger e^{i\omega_a t}. \tag{8.1}$$

Here the write efficiency of the memory R_1 is analogous to the reflectivity of the beamsplitter [166], and ω_a, ω_b are the oscillation frequencies of the photon and phonon respectively. Similarly, the retrieval of a photon from the memory can be written as:

$$b^\dagger e^{i\omega_b t} \longrightarrow i\sqrt{R_2} a^\dagger e^{i\omega_a t} + \sqrt{1-R_2} b^\dagger e^{i\omega_b t}, \tag{8.2}$$

where R_2 is the read efficiency of the memory. Between the write and read interactions, the photon is stored in the memory for a storage time τ; during this time the phase of the

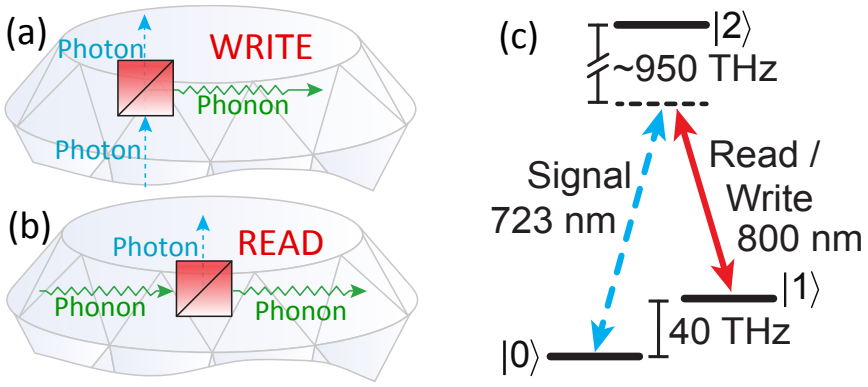

Figure 8.1: (a) The write interaction of the diamond quantum memory is analogous to a beamsplitter partitioning an input photon between the photon and phonon modes. (b) Similarly, the read interaction also behaves as a beamsplitter. (c) Energy level diagram of the diamond memory. The diamond crystal is initially in the ground state $|0\rangle$. The signal photon (723 nm) and the read/write pulses (800 nm) are in two-photon resonance with the optical phonon mode $|1\rangle$, but far detuned from the conduction band $|2\rangle$.

phonon evolves, and its amplitude decays, resulting in loss from the memory. We model the loss as a beamsplitter with time-dependent transmission $T(\tau)$:

$$b^\dagger e^{i\omega_b t} \longrightarrow \sqrt{T(\tau)} b^\dagger e^{i\omega_b (t+\tau)} + \sqrt{1-T(\tau)} d^\dagger, \tag{8.3}$$

where $T(\tau) = e^{-\tau/\tau_0}$, and $\tau_0 = 3.5\,\text{ps}$ [40]. The operator $d^\dagger$ encompasses any form of loss during storage, the predominant mechanism being acoustic decay [127].

8.4 Experiment

The diamond quantum memory is described by the Λ-level system shown in Fig. 8.1 (c) where the initial state $|0\rangle$ corresponds to the ground state of the crystal lattice and the storage state $|1\rangle$ is the optical phonon band. A *signal* photon (wavelength 723 nm) is stored to, and retrieved from, the optical phonon modes by the write and read pulses (wavelength 800 nm). The signal and read/write pulses are in two-photon Raman resonance with the optical phonon frequency (40 THz) and are far-detuned from the conduction

band, $|2\rangle$. The diamond, which is 2.3 mm thick, was grown by chemical vapor deposition and is cut on the $\langle 100 \rangle$ face. In this configuration, the Raman interaction couples fields of orthogonal polarization such that a vertically polarized write pulse is used to store horizontally polarized light and a horizontally polarized read pulse is used to retrieve a vertically polarized output [32].

The master laser for the experiment is a mode-locked titanium:sapphire laser oscillator with a central wavelength of 800 nm, pulse duration of 190 fs, and a pulse repetition rate of 80 MHz. The read and write pulses, each of energy $\sim$6 nJ, are derived from the oscillator. Single photons are produced by a non-degenerate spontaneous parametric downconversion (SPDC) photon pair source where the detection of a *herald* photon (895 nm) implies the presence of the signal photon (723 nm) and triggers the experiment. At the output of the memory, photons are measured on an avalanche photodiode (APD), and timing correlations with the herald are measured using coincidence counting logic.

8.5 Single-photon interference

To demonstrate single-photon interference in this system, the photon from the SPDC source is partitioned into two orthogonally polarized time-bins $B1$ and $B2$ by a polarization-dependent optical delay line (see Fig. 8.2). The 800 nm pulse is also sent through the delay line to generate the read and write pulses. The signal photon is horizontally polarized at $B1$ and vertically polarized at $B2$; in each time-bin the write ($B1$) or read ($B2$) pulse is orthogonally polarized to the signal to enable the necessary Raman coupling. The delay τ between the two time-bins is coarsely tuned by a motorized delay stage, and fine control is achieved using a piezoelectric actuator [1]. After the diamond, the photons are spectrally isolated from the control pulses by interference filters, and a polarizer is used to select the horizontally (vertically) polarized photons in $B1$ ($B2$).

We begin with a horizontally polarized signal photon such that all of the photons arrive in $B1$. When we apply the write pulse at $B1$, a dip of $11.0 \pm 0.8\%$ in the signal-herald

[1] The displacement of the piezoelectric actuator as a function of applied voltage was calibrated using optical interferometry.

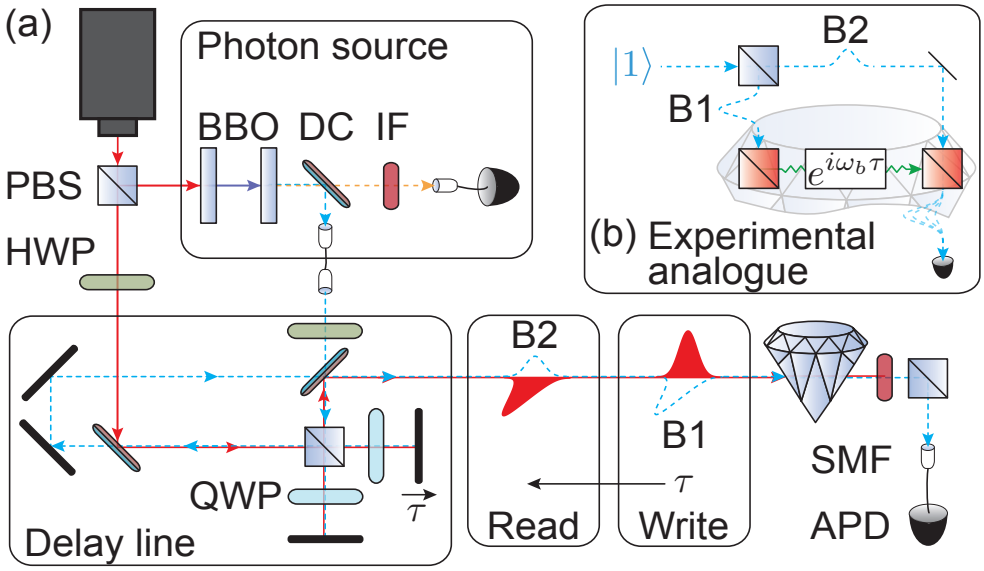

Figure 8.2: (a): Experimental diagram for single photon interference. A single photon from the SPDC photon source (dashed blue) is split into two time-bins, in the first (B1) the photon is horizontally polarized, and in the second (B2) vertically. Each time-bin is overlapped with orthogonally polarized read and write pulses (solid red) resulting in interference in the second time bin. BBO: β-barium borate, HWP/QWP: half/quarter-wave plate, PBS: polarizing beamsplitter, DC: dichroic mirror, IF: interference filter, POL: polarizer, SMF: single-mode fiber, APD: avalanche photodiode.(b) Conceptual setup. The single photon is partitioned into two time-bins by an optical beamsplitter (blue). Each time-bin then impinges upon a memory beamsplitter (red) separated by a time delay τ.

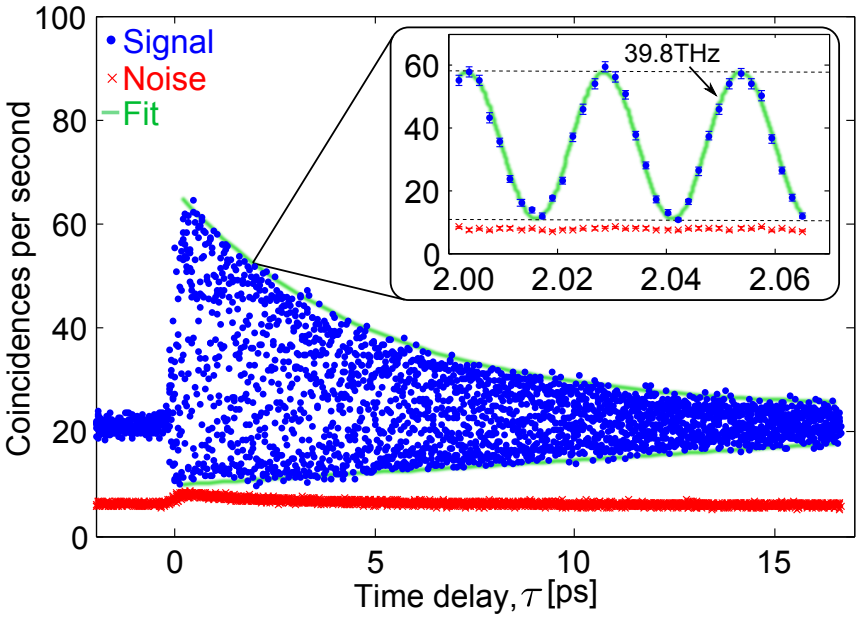

Figure 8.3: Signal-herald coincidences (blue dots) and memory noise (red crosses) as a function of time delay τ between $B1$ and $B2$, with an exponential fit to the envelope (green line). **Inset:** High-resolution scan around delay $\tau = 2\,\text{ps}$ exhibiting interference fringes of frequency $39.8 \pm 0.9\,\text{THz}$, extracted via a sinusoidal fit.

coincidence rate is observed due to Raman absorption of the signal photons. The reflectivity of the first memory beamsplitter is therefore $R_1 = 11\%$. We then set the delay τ between the two time bins to be 1 ps and apply the read pulse in $B2$ to retrieve vertically polarized photons from the memory with overall memory efficiency of $\eta = 1.20 \pm 0.04\%$. We can therefore calculate the reflectivity of the second beamsplitter to be $R_2 = \eta/R_1 = 11 \pm 1\%$. It should be noted that the reflectivity of each memory beamsplitter can be tuned by adjusting the read/write pulse energy [110] and is limited to 11% by the available laser power.

Next, we rotate the polarization of the input signal photon such that a small fraction of the photons arrive at the memory in time-bin $B2$. There are two ways in which a photon can be detected in time-bin $B2$ at the memory output: either the photon originated in $B2$ and was simply transmitted by the memory, or the photon originated in $B1$, was stored,

and then recalled into $B2$ by the read pulse. These two pathways constructively and destructively interfere resulting in a detection probability that oscillates as a function of the time delay τ between the two time-bins, as can be seen in Fig. 8.3. By adjusting the polarization so that $\sim 1\%$ of the photons arrive in $B2$ we balance the amplitudes of the two pathways resulting in maximum interference visibility.

The functional form of the interference pattern in Fig. 8.3 can be derived by considering the action of transformations (8.1-8.3) on initial photon input state $(p_1 a^\dagger_{\mathrm{B1}} + p_2 a^\dagger_{\mathrm{B2}})|0\rangle$. Where p_1 and p_2 are the input population amplitudes in time-bin $B1$ and $B2$ respectively. We apply transformation (8.1), then (8.3), and then (8.2) to $a^\dagger_{\mathrm{B1}}$, and transformation (8.1) to $a^\dagger_{\mathrm{B2}}$ returning:

$$\begin{aligned} a^\dagger_{\mathrm{B1}} e^{i\omega_a t} &\rightarrow -R a^\dagger_{\mathrm{B2}} e^{i\omega_b \tau} e^{i\omega_a t} e^{-\tau/2\tau_0} + \sqrt{1-R}\, a^\dagger_{\mathrm{B1}} e^{i\omega_a t}, \\ a^\dagger_{\mathrm{B2}} e^{i\omega_a t} &\rightarrow i\sqrt{R} b^\dagger e^{i\omega_b t} e^{-t/2\tau_0} + \sqrt{1-R}\, a^\dagger_{\mathrm{B2}} e^{i\omega_a t}. \end{aligned} \tag{8.4}$$

Here, $R = R_1 = R_2 = 11\%$. The expected photon number in $B2$ is therefore:

$$\begin{aligned} \left\langle a^\dagger_{\mathrm{B2}} a_{\mathrm{B2}} \right\rangle &= \left| -p_1 R e^{i\omega_b \tau} e^{-\tau/2\tau_0} + p_2 \sqrt{1-R} \right|^2, \\ &= R^2 p_1^2 e^{-\tau/\tau_0} + (1-R) p_2^2 \\ &\quad -2R\sqrt{1-R} p_1 p_2 e^{-\tau/2\tau_0} \cos(\omega_b \tau). \end{aligned} \tag{8.5}$$

This shows the two key features of the phonon-mediated interference. Firstly, the interference visibility decreases with storage time due to the decay of the optical phonon, as can be seen in Fig. 8.3. Secondly, the interference fringes oscillate at the phonon frequency $\omega_b/2\pi = 40\,\mathrm{THz}$, rather than the optical frequency of the photon ($\omega_a/2\pi = 415\,\mathrm{THz}$) as can be seen in the inset of Fig. 8.3. The read and write steps are phase-preserving processes [128], therefore the only phase difference between the two pathways is due to the evolution of the phonon during storage.

The memory output includes noise photons (shown in red crosses in Fig. 8.3), which are present even when no photon is stored [133, 143]. The noise photons are generated spontaneously so they do not contribute to the interference and simply degrade the visibility. The visibility is extracted by fitting the envelope of the interference pattern in Fig. 8.3 (green line) and reaches a peak of 73%. It is important to note that interference persists for

over 60 times the duration of the photon (264 fs). The longevity of the interference pattern demonstrates that the quantum memory can be used to mediate interference between two temporally distinct quantum pathways traversed by a single photon. In the next experiment, we show that this technique can be extended to multi-photon quantum interference effects.

8.6 Two-photon interference

The archetypal multi-photon interference effect is Hong-Ou-Mandel (HOM) interference, the signature of which is photon bunching, where identical single photons, incident upon the two input ports of a beamsplitter, emerge together from the same output port due to quantum interference. HOM interference is often detected by measuring a 'dip' in coincident detections between the two output modes [167]. Alternatively, when one of the output modes cannot be accessed, interference can be observed by measuring a 'peak' in the number of two-photon events in the accessible output mode [168, 169]. Here we use the beamsplitter functionality of the memory to investigate HOM-type interference, where bunching results in either two photons exiting the memory, or two phonons remaining in storage, in the ideal case. Using an optical beamsplitter, HOM interference can be observed between a single photon and a weak coherent state [42]; we show the same to be true using the memory beamsplitter.

To investigate two-photon interference we use two light sources: the SPDC source and an optical parametric oscillator (OPO) which is synchronously pumped by the master laser oscillator. The OPO output can be modeled by a coherent state [138], $|\alpha_{\mathrm{l}}\rangle$, which is attenuated such that the mean photon number at the diamond is $|\alpha_{\mathrm{l}}|^2 \approx 2.5$ per pulse. The coherent state and single photon are combined on a polarizing beamsplitter (PBS) and coupled into the same single-mode fiber before being sent to the memory (see Fig. 8.4). The horizontally polarized coherent state arrives first at the memory and is stored with efficiency $R_1 = 10\%$. The resulting phonon excitation $|\alpha_{\mathrm{m}}\rangle = \sqrt{R_1}|\alpha_{\mathrm{l}}\rangle$ contains, on average, $|\alpha_{\mathrm{m}}|^2 \approx 0.25$ phonons per laser pulse. The vertically polarized single photon arrives at the memory 1 ps after the coherent state, along with the read pulse. The output from the

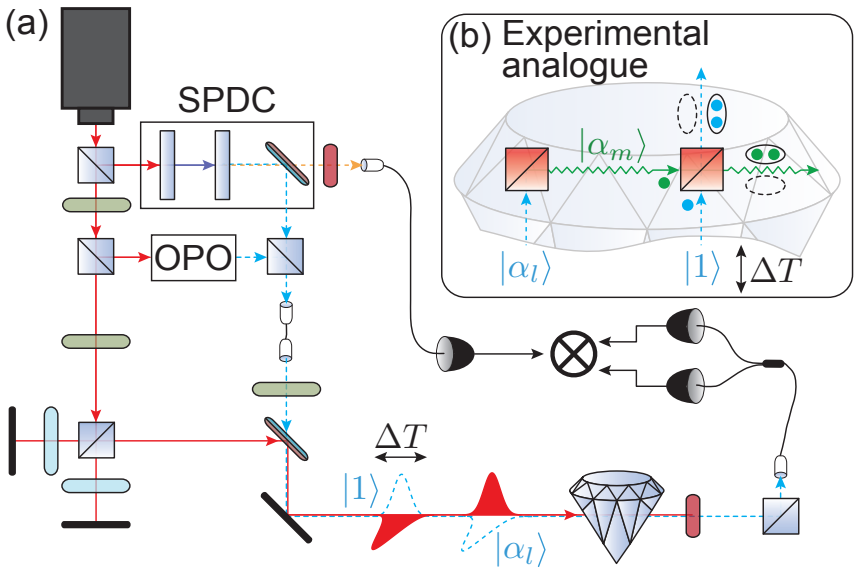

Figure 8.4: (a) Experimental setup figure for two-photon interference. The master laser pumps two independent sources of photons. The SPDC source produces single photons $|1\rangle$, and an optical parametric oscillator (OPO) produces a coherent state of amplitude $|\alpha_{\rm l}|^2 = 2.5$ photons per pulse. The coherent state is stored into the memory by the write pulse creating a phonon excitation. After a delay of $\tau = 1\,$ps, the single photon and the read pulse arrive at the memory and the photon interferes with the phonon excitation resulting in HOM-type bunching. The 2-photon component of the optical output field is detected using a 50:50 fibre beamsplitter and 2 APDs. (b) Conceptual setup. A coherent state of light $|\alpha_{\rm l}\rangle$ is reflected at the first memory beamsplitter creating a phonon excitation $|\alpha_{\rm m}\rangle$. The phonon excitation combines with a single photon on the second memory beamsplitter resulting in bunching.

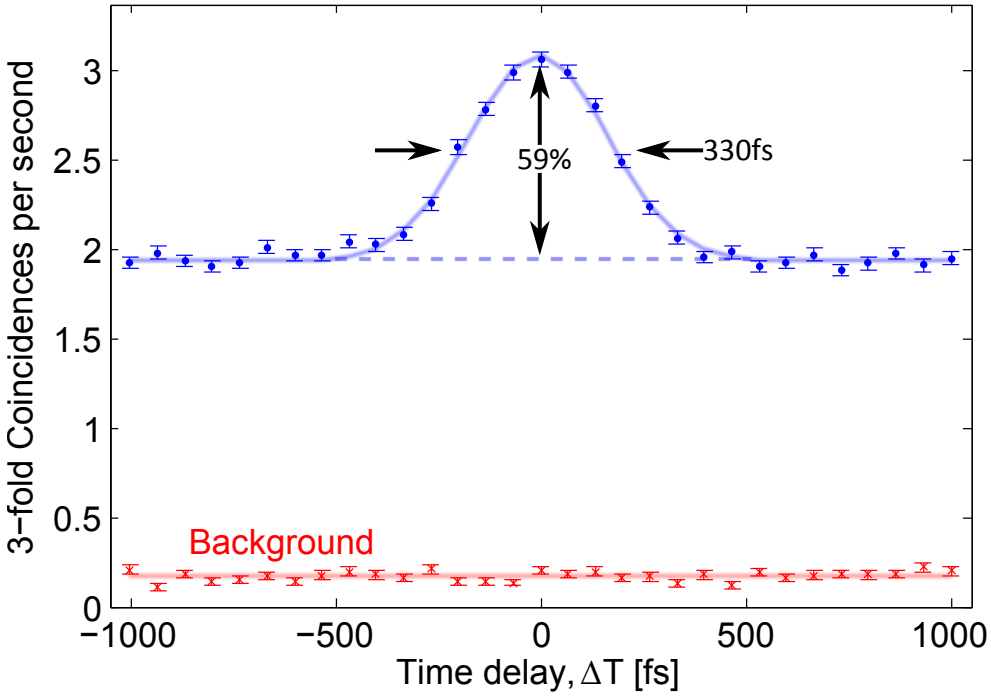

Figure 8.5: Three-fold coincident detections of a herald photon and two photons in the output of the quantum memory as a function of delay ΔT between the single photon and the memory read pulse. A peak at zero delay is evidence of Hong–Ou–Mandel-type bunching.

second time-bin is isolated using interference filters and a polarizer as before; it is then coupled into a single-mode fiber for photon counting.

We measure the peak in two-photon detection in the optical output of the memory as our accessible signature of HOM interference. In the absence of photon-number-resolving detectors [170], we measure two-photon events by splitting the optical mode on a 50:50 fibre beamsplitter and detecting on two separate APDs, as shown in Fig. 8.4. Our metric is therefore the rate of 3-fold coincident detections of a herald photon and a photon in each arm of the fibre beamsplitter. Fig. 8.5 shows three-fold detection rates as a function of delay between the single photon and the read pulse, ΔT; a peak at zero delay demonstrates HOM interference between single photons and the weak coherent state mediated by the

quantum memory. The width of the peak is 330 ± 10 fs, in good agreement with the cross-correlation between the single photon and the read/write pulses as measured by photon absorption (326 fs [143]).

The raw visibility of the HOM peak is $59 \pm 2\%$, whereas the noise-subtracted visibility is $65 \pm 3\%$. The HOM peak visibility is a measure of the indistinguishability of a photon generated by SPDC and one retrieved from the memory or, equivalently, the indistinguishabilty of the phonon in the memory and one created by Raman absorption of the single photon. In this experiment, spatial overlap between the photons and the coherent state was ensured by the use of single-mode fibers, but HOM visibility could be degraded by multi-photon components in $|\alpha_1\rangle$, and by spectral and temporal mismatch between $|1\rangle$ and $|\alpha_1\rangle$.

8.7 Conclusion

In conclusion, we have demonstrated single-photon and two-photon non-classical interference effects via a diamond quantum memory. The quantum memory acts as a buffer, and as a beamsplitter, allowing interference between quantum pathways that would otherwise be temporally distinguishable — a functionality that is not possible using only optical beamsplitters. In the future, quantum memories of this type could be used to build rapidly reconfigurable optical components for linear-optical quantum processing applications [171, 114, 113].

Chapter 9

Conclusions and outlook

We have demonstrated in this thesis that room-temperature diamond can function as a memory for qubits comprised of single photons. The large detuning in the Raman process, along with the large energy splitting between ground and storage states, allows for the storage of THz-bandwidth photons with low noise. After confirming that the retrieved light from the memory was still single photon in nature, we then demonstrated the storage of polarization-entangled qubits. We confirmed that the retrieved qubit was still entangled with a herald, and we showed that the noise processes in diamond are well-understood. Next we explored additional functionalities of the diamond memory. We demonstrated that by tuning the spectral properties of the read pulse the photon retrieved from the memory could be shifted in central frequency and modulated in bandwidth. We found that frequency shifts could be performed within a range set by the phase matching of the four involved fields (write, input, read, output). Lastly, we demonstrated that the quantum memory acts as a beamsplitter between light and matter modes. Using this property we demonstrated both one- and two-photon interference effects, each mediated by the phonon mode in the memory.

The optical phonon level in diamond decays with a characteristic lifetime of just 3.5 ps, decohering any quantum information. In this thesis we have demonstrated that despite this short timescale, the quantum properties of the diamond lattice can still be harnessed using ultrafast optical pulses. It is clear that the diamond will not find use for photon

storage in the traditional quantum repeater architecture. However, there is a growing list of potential uses for quantum memory that range from spectral manipulation to acting as building blocks for quantum computation. In these contexts, the diamond quantum memory has great potential.

The time-bandwidth products displayed in the experiments here were on the order of ∼10, where the bandwidth of the stored light was 2.3 THz. The fundamental limit on storage bandwidth in the optical phonon level in diamond is ∼20 THz. Beyond this the control pulses will begin to excite the phonon level by themselves degrading the memory functionality. We also expect that with reduced noise, and increased storage efficiency, that retrieved photon rates will be detectable above the background noise for storage times well beyond 3.5 ps. Our results in Chapter 8 showed coherence between two time-bins, in the form interference fringes, beyond 15 ps of storage in the diamond. We expect that the time-bandwidth product of the diamond quantum memory could be improved to ∼200.

The experiments in this thesis are also a proof-of-concept for Raman memories in general. Other Raman quantum memories, such as Cesium vapour and molecular Hydrogen, have shown time-bandwidth products orders of magnitude higher than what we have demonstrated here and other memory schemes. Given that the operations of these memories are the same as for diamond we expect that additional functionalities, such as spectral conversion and mediating two-photon interference, will also exist in these systems.

9.1 HOM interference with spectrally distinct photons

In Chapter 8 we demonstrated two-photon interference of photons initially separated in time. This interference was displayed by storing the first photon (from a weak coherent state) in the diamond memory, and performing the readout operation at the same time that the second photon was incident on the memory. Hong-Ou-Mandel (HOM) interference was observed by measuring a increase in two-photon events due to bunching.

Our experiment in Chapter 7, where a stored photon could be frequency converted

upon retrieval from the memory, suggests an immediate extension to the HOM interference experiment. We showed that the frequency of the stored photon could be red- or blue-shifted across a range of 4.1 times the bandwidth of the input. Over this range of frequency tuning, the retrieved photons can be made spectrally distinguishable from the input.

We can then imagine storing a photon in the diamond memory and having a second photon, which is spectrally distinct from the first, interfere with the first via frequency conversion upon retrieval. The read pulse, derived from a second laser as in Chapter 7, would perform the frequency conversion and retrieval of the first photon while simultaneously storing the second photon. Here the spectrum of the second photon would have to match that of the retrieved photon. This could be ensured by spectral filtering and by the spectral envelope of the read pulse.

One difficulty in performing this experiment come from low photon detection rates. Use of the optical parametric oscillator for the experiment in Chapter 8 reduced the amount of laser power available for both the source, and for the memory. This is not a great problem since in the frequency conversion experiment of Chapter 7 we used a second laser for the readout process. However, the laser-locking mechanism used in Chapter 7 would have to be drastically improved. The timing jitter of pulses from the two lasers would need to be significantly reduced in order for the readout control pulse to be overlapped with the second photon wavepacket – jitter on the order of 100 fs would be significant to the experiment.

Nonetheless, these hurdles are not fundamental in nature and can be overcome with minor technological improvements. A demonstration such as this would be a strong step forward for developing an entangling gate between frequency-multiplexed photons, having implications in quantum communications as well as the quantum memory applications discussed in Chapter 3.

9.2 Long term development

For the diamond quantum memory to enable the various quantum technologies we have discussed in this thesis, a few developments are needed. First, and foremost, the coupling strength needs improvement. In this thesis we demonstrated an overall memory efficiency

on the order of 1%, with an average gate fidelity of 0.761. Higher coupling strengths, and therefore efficiencies, could be attained by confining the spatial modes of the signal and control fields was used. This could be realized with a diamond waveguide [137], as demonstrated in Ref. [95] for the Cesium vapour memory. The dimensions of the diamond waveguide would have to be ∼450 nm to restrict propagation of the 723 nm light to a single mode (400 nm to also restrict 800 nm light to a single mode), when the surrounding material is air.

With larger coupling strengths, allowing for a higher memory efficiency using less laser power, we can start to think about realizing protocols which require multiple memories, such as linear optical quantum computing in a single spatial mode. Multiple, tightly packed photon time-bins could be manipulated via an efficient beamsplitter network mediated by the quantum memory.

An additional feature of a waveguide structure is the further suppression of four-wave mixing noise. With mode confinement, the memory can be made longer, exploit the phase mismatch in the four-waving mixing process. It is also possible that if the waveguide supports single-mode propagation at 800 nm, the Stokes field in the four-wave mixing process, wavelength 895 nm, would not be supported by the waveguide and then further suppressed. This could be combined with a Pelletier cooling apparatus to reduce the thermal noise in the memory. As we have mentioned in previous chapters, cooling by as little as 60° C would increase the functionality of the memory immensely. Efforts to manufacture diamond-based waveguides structures are currently underway in research groups around the world.

With these developments, the author of this thesis believes that the future of the diamond quantum memory is promising, and that it will be a play a role in emerging quantum optical networks and computers.

References

[1] Bell, J. On the Einstein-Podolsky-Rosen paradox. *Physics* **1**, 195–200 (1964).

[2] Shalm, L. K. *et al.* Strong loophole-free test of local realism. *Physical Review Letters* **115**, 250402 (2015).

[3] Giustina, M. *et al.* A significant-loophole-free test of Bell's theorem with entangled photons. *Physical Review Letters* **250401**, 1–7 (2015).

[4] Hensen, B. *et al.* Loophole-free Bell inequality violation using electron spins separated by 1.3 kilometres. *Nature* (2015).

[5] Nielsen, M. A. & Chuang, I. L. *Quantum Computation and Quantum Information* (Cambridge University Press, 2000).

[6] Raussendorf, R. & Briegel, H. J. A One-Way Quantum Computer. *Physical Review Letters* (2001).

[7] Walther, P. *et al.* Experimental one-way quantum computing. *Nature* **434**, 169–76 (2005).

[8] Bennett, C. H., DiVincenzo, D. P., Smolin, J. A. & Wootters, W. K. Mixed-state entanglement and quantum error correction. *Physical Review A (Atomic, Molecular, and Optical Physics)* **54**, 3824 (1996).

[9] Wootters, W. Entanglement of formation of an arbitrary state of two qubits. *Physical Review Letters* **80**, 2245–2248 (1998).

[10] Werner, R. F. Quantum states with Einstein-Podolsky-Rosen correlations admitting a hidden-variable model. *Physical Review A* **40**, 4277–4281 (1989).

[11] James, D. F. V., Kwiat, P. G., Munro, W. J. & White, A. G. Measurement of qubits. *Physical Review A* **64**, 052312 (2001).

[12] Langford, N. K. *et al.* Efficient quantum computing using coherent photon conversion. *Nature* **478**, 360–363 (2011).

[13] England, D. G. *et al.* High-fidelity polarization storage in a gigahertz bandwidth quantum memory. *Journal of Physics B: Atomic, Molecular and Optical Physics* **45**, 124008 (2012).

[14] Fedrizzi, A. *et al.* Experimental Distribution of Entanglement with Separable Carriers. *Physical Review Letters* **111**, 230504 (2013).

[15] Hamel, D. R. *et al.* Direct generation of three-photon polarization entanglement. *Nature Photonics* 1–7 (2014).

[16] Jozsa, R. Fidelity for Mixed Quantum States. *Journal of Modern Optics* **41**, 2315–2323 (1994).

[17] Uhlmann, A. The "transition probability" in the state space of a *-algebra. *Reports on Mathematical Physics* **9**, 273–279 (1976).

[18] Kraus, K., Böhm, A., Dollard, J. & Wootters, W. *States, Effects, and Operations Fundamental Notions of Quantum Theory.* Lectures in Mathematical Physics at the University of Texas at Austin (Springer, 1983).

[19] Choi, M.-D. Completely positive linear maps on complex matrices. *Linear Algebra and its Applications* **10**, 285 – 290 (1975).

[20] kowski, A. J. Linear transformations which preserve trace and positive semidefiniteness of operators. *Reports on Mathematical Physics* **3**, 275 – 278 (1972).

[21] Stinespring, W. F. Positive Functions on C^*-Algebras. *Proceedings of the American Mathematical Society* **6**, 211–216 (1955).

[22] Watrous, J. Theory of Quantum Information. URL https://cs.uwaterloo.ca/~watrous/TQI/.

[23] Altepeter, J. B. *et al.* Ancilla-assisted quantum process tomography. *Physical Review Letters* **90**, 193601 (2003).

[24] Fisher, K. A. G., Prevedel, R., Kaltenbaek, R. & Resch, K. J. Optimal linear optical implementation of a single-qubit damping channel. *New Journal of Physics* **14**, 033016 (2012).

[25] Chow, J. M. *et al.* Randomized benchmarking and process tomography for gate errors in a solid-state qubit. *Physical Review Letters* **102**, 090502 (2009).

[26] Liu, C., Dutton, Z., Behroozi, C. H. & Hau, L. V. Observation of coherent optical information storage in an atomic medium using halted light pulses. *Nature* **409**, 490–493 (2001).

[27] Phillips, D. F., Fleischhauer, A., Mair, A., Walsworth, R. L. & Lukin, M. D. Storage of light in atomic vapor. *Physical Review Letters* **86**, 783–786 (2001).

[28] de Riedmatten, H., Afzelius, M., Staudt, M. U., Simon, C. & Gisin, N. A solid-state light-matter interface at the single-photon level. *Nature* **456**, 773–777 (2008).

[29] Hedges, M. P., Longdell, J. J., Li, Y. & Sellars, M. J. Efficient quantum memory for light. *Nature* **465**, 1052–6 (2010).

[30] Reim, K. F. *et al.* Towards high-speed optical quantum memories. *Nature Photonics* **4**, 218–221 (2010).

[31] Bustard, P. J., Lausten, R., England, D. G. & Sussman, B. J. Toward quantum processing in molecules: A THz-bandwidth coherent memory for light. *Physical Review Letters* **111**, 083901 (2013).

[32] England, D. G., Bustard, P. J., Nunn, J., Lausten, R. & Sussman, B. J. From photons to phonons and back: A THz optical memory in diamond. *Physical Review Letters* **111**, 243601 (2013).

[33] Glauber, R. J. Optical Coherence and Photon Statistics. In Dewitt, C., Blandin, A. & Cohen-Tannoudji, C. (eds.) *Quantum Optics and Electronics*, 63 (1965).

[34] Resch, K. *Quantum optics: course notes* (University of Waterloo, 2016).

[35] Mandel, L. & Wolf, E. *Optical coherence and quantum optics* (Cambridge University Press, 2008).

[36] Hanbury Brown, R. & Twiss, R. Correlation between photons in two coherent beams of light. *Nature* **177**, 27–29 (1956).

[37] Clauser, J. F. Experimental distinction between the quantum and classical field-theoretic predictions for the photoelectric effect. *Physical Review D* **9**, 853–860 (1974).

[38] Chanelière, T. *et al.* Storage and retrieval of single photons transmitted between remote quantum memories. *Nature* **438**, 833–6 (2005).

[39] Zhao, B. *et al.* A millisecond quantum memory for scalable quantum networks. *Nature Physics* **5**, 95–99 (2008).

[40] Lee, K. C. *et al.* Macroscopic non-classical states and terahertz quantum processing in room-temperature diamond. *Nature Photonics* **6**, 41–44 (2011).

[41] Knill, E., Laflamme, R. & Milburn, G. J. A scheme for efficient quantum computation with linear optics. *Nature* **409**, 46–52 (2001).

[42] Rarity, J. G., Tapster, P. R. & Loudon, R. Non-classical interference between independent sources. *Journal of Optics B: Quantum and Semiclassical Optics* **7**, S171 (2005).

[43] Boyd, R. *Nonlinear Optics*. Academic Press (Academic Press, 2008).

[44] Grice, W. & Walmsley, I. Spectral information and distinguishability in type-II down-conversion with a broadband pump. *Physical Review A* **56**, 1627–1634 (1997).

[45] Kwiat, P. *et al.* New High-Intensity Source of Polarization-Entangled Photon Pairs. *Physical Review Letters* **75**, 4337–4341 (1995).

[46] URL http://www.newlightphotonics.com/.

[47] Weston, M. M. *et al.* Efficient and pure femtosecond-pulse-length source of polarization-entangled photons. *Optics Express* **24**, 10869–10879 (2016).

[48] URL https://www.semrock.com/.

[49] URL http://www.forealspectrum.com/.

[50] URL http://www.excelitas.com/.

[51] URL http://www.goochandhousego.com/.

[52] URL http://www.princetoninstruments.com/.

[53] Briegel, H.-J., Dür, W., Cirac, J. & Zoller, P. Quantum Repeaters: The Role of Imperfect Local Operations in Quantum Communication. *Physical Review Letters* **81**, 5932–5935 (1998).

[54] Duan, L. M., Lukin, M. D., Cirac, J. I. & Zoller, P. Long-distance quantum communication with atomic ensembles and linear optics. *Nature* **414**, 413–418 (2001).

[55] Pan, J.-W. *et al.* Multiphoton entanglement and interferometry. *Rev. Mod. Phys.* **84**, 777–838 (2012).

[56] Bennett, C. & Brassard, G. Quantum cryptography: Public key distribution and coin tossing. In *Proceedings of the IEEE International Conference on Computers, Systems, and Signal Processing*, 175–179 (1984).

[57] Ekert, A. Quantum Cryptography based on Bell's theorem. *Physical Review Letters* **67**, 661–663 (1991).

[58] Kocsis, S., Xiang, G. Y., Ralph, T. C. & Pryde, G. J. Heralded noiseless amplification of a photon polarization qubit. *Nature Physics* **9**, 23–28 (2012).

[59] Meyer-Scott, E. *et al.* Certifying the presence of a photonic qubit by splitting it in two. *Physical Review Letters* **070501**, 2–6 (2015).

[60] Dür, W., Briegel, H.-J., Cirac, J. I. & Zoller, P. Quantum repeaters based on entanglement purification. *Physical Review A* **59**, 169–181 (1999).

[61] Bennett, C. H. *et al.* Teleporting an unknown quantum state via dual classical and Einstein-Podolsky-Rosen channels. *Physical Review Letters* **70**, 1895–1899 (1993).

[62] Bouwmeester, D. *et al.* Experimental Quantum Teleportation. *Nature* **390**, 575–579 (1997).

[63] Deutsch, D. *et al.* Quantum privacy amplification and the security of quantum cryptography over noisy channels. *Physical Review Letters* **77**, 2818 (1996).

[64] Pan, J.-W., Simon, C., Brukner, C. & Zeilinger, A. Entanglement Purification for Quantum Communication. *Nature* **410**, 1067 (2001).

[65] Matsukevich, D. N. & Kuzmich, A. Quantum state transfer between matter and light. *Science (New York, N.Y.)* **306**, 663–6 (2004).

[66] Chou, C. W. *et al.* Measurement induced entanglement for excitation stored in remote atomic ensembles. *Nature* **438**, 828–832 (2005).

[67] Choi, K. S., Deng, H., Laurat, J. & Kimble, H. J. Mapping photonic entanglement into and out of a quantum memory. *Nature* **452**, 67–71 (2008).

[68] Lee, K. C. *et al.* Entangling Macroscopic Diamonds at Room Temperature. *Science* **334**, 1253–1256 (2011).

[69] Massar, S. & Popescu, S. Optimal extraction of information from finite quantum ensembles. *Physical Review Letters* **74**, 1259–1263 (1995).

[70] Lvovsky, A. I., Sanders, B. C. & Tittel, W. Optical quantum memory. *Nature Photonics* **3**, 706–714 (2009).

[71] Simon, C. *et al.* Quantum memories. *The European Physical Journal D* **58**, 1–22 (2010).

[72] Heshami, K. *et al.* Quantum memories: emerging applications and recent advances. *Journal of Modern Optics* **0**, 1–24 (0).

[73] Harris, S. Electromagnetically Induced Transparency. *Physics Today* **50** (1997).

[74] Zhang, H. *et al.* Preparation and storage of frequency-uncorrelated entangled photons from cavity-enhanced spontaneous parametric downconversion. *Nature Photonics* 1–5 (2011).

[75] Eisaman, M. D. *et al.* Electromagnetically induced transparency with tunable single-photon pulses. *Nature* **438**, 837–41 (2005).

[76] Longdell, J. J., Fraval, E., Sellars, M. J. & Manson, N. B. Stopped light with storage times greater than one second using electromagnetically induced transparency in a solid. *Physical Review Letters* **95**, 2–5 (2005).

[77] Bustard, P. J., Heshami, K., England, D. G., Spanner, M. & Sussman, B. J. Raman-induced slow-light delay of THz-bandwidth pulses. *Physical Review A* **93**, 043810 (2016).

[78] Kurnit, N., Abella, I. & Hartmann, S. Observation of a photon echo. *Physical Review Letters* **13**, 567 (1964).

[79] Alexander, A. L. *et al.* Photon Echoes Produced by Switching Electric Fields. *Physical Review Letters* **96**, 43602 (2006).

[80] Hosseini, M. *et al.* Coherent optical pulse sequencer for quantum applications. *Nature* **461**, 241–5 (2009).

[81] Afzelius, M., Simon, C., De Riedmatten, H. & Gisin, N. Multimode quantum memory based on atomic frequency combs. *Physical Review A - Atomic, Molecular, and Optical Physics* **79**, 1–9 (2009).

[82] Clausen, C. *et al.* Quantum storage of photonic entanglement in a crystal. *Nature* **469**, 508–11 (2011).

[83] Saglamyurek, E. *et al.* Broadband waveguide quantum memory for entangled photons. *Nature* **469**, 512–5 (2011).

[84] Saglamyurek, E. *et al.* A multiplexed light-matter interface for fibre-based quantum networks. *Nature Communications* **7**, 11202 (2016).

[85] Rieländer, D. *et al.* Quantum Storage of Heralded Single Photons in a Praseodymium-Doped Crystal. *Physical Review Letters* **112**, 040504 (2014).

[86] Reiserer, A., Kalb, N., Rempe, G. & Ritter, S. A quantum gate between a flying optical photon and a single trapped atom. *Nature* **508**, 237–40 (2014).

[87] Reiserer, A., Ritter, S. & Rempe, G. Nondestructive detection of an optical photon. *Science (New York, N.Y.)* **342**, 1349–51 (2013).

[88] Feizpour, A., Hallaji, M., Dmochowski, G. & Steinberg, A. M. Observation of the nonlinear phase shift due to single post-selected photons. *Nature Physics* **11**, 905–909 (2015).

[89] Specht, H. P. *et al.* A single-atom quantum memory. *Nature* **473**, 190–193 (2011).

[90] Ritter, S. *et al.* An elementary quantum network of single atoms in optical cavities. *Nature* **484**, 195–200 (2012).

[91] Kalb, N., Reiserer, A., Ritter, S. & Rempe, G. Heralded Storage of a Photonic Quantum Bit in a Single Atom. *Physical Review Letters* **114**, 1–5 (2015).

[92] Duan, L. M. & Kimble, H. J. Scalable photonic quantum computation through cavity-assisted interactions. *Physical Review Letters* **92**, 127902–1 (2004).

[93] Nunn, J. *et al.* Mapping broadband single-photon wave packets into an atomic memory. *Physical Review A - Atomic, Molecular, and Optical Physics* **75**, 011401 (2007).

[94] Reim, K. F. *et al.* Single-photon-level quantum memory at room temperature. *Physical Review Letters* **107**, 1–4 (2011).

[95] Sprague, M. R. *et al.* Broadband single-photon-level memory in a hollow-core photonic crystal fibre. *Nature Photonics* **8**, 287–291 (2014).

[96] Michelberger, P. S. *et al.* Interfacing GHz-bandwidth heralded single photons with a room-temperature Raman quantum memory. *New Journal of Physics* **17**, 43006 (2015). 1405.1470.

[97] Saunders, D. J. *et al.* Cavity-Enhanced Room-Temperature Broadband Raman Memory. *Physical Review Letters* **116**, 24–27 (2016).

[98] Ding, D.-S. *et al.* Raman quantum memory of photonic polarized entanglement. *Nature Photonics* **9** (2015).

[99] Kumar, P. Quantum frequency conversion. *Optics letters* **15**, 1476 (1990).

[100] Rakher, M. T. *et al.* Simultaneous wavelength translation and amplitude modulation of single photons from a quantum dot. *Physical Review Letters* **107**, 083602 (2011).

[101] McGuinness, H. J., Raymer, M. G., McKinstrie, C. J. & Radic, S. Quantum frequency translation of single-photon states in a photonic crystal fiber. *Physical Review Letters* **105**, 093604 (2010).

[102] Tanzilli, S. *et al.* A photonic quantum information interface. *Nature* **437**, 116–120 (2005).

[103] Ikuta, R. *et al.* Wide-band quantum interface for visible-to-telecommunication wavelength conversion. *Nature Communications* **2**, 1544 (2011).

[104] De Greve, K. *et al.* Quantum-dot spin-photon entanglement via frequency downconversion to telecom wavelength. *Nature* **491**, 421–425 (2012).

[105] Guerreiro, T. *et al.* Nonlinear interaction between single photons. *Physical Review Letters* **113**, 173601 (2014).

[106] Dudin, Y. O. *et al.* Entanglement of light-shift compensated atomic spin waves with telecom light. *Physical Review Letters* **105**, 1–4 (2010).

[107] Lavoie, J., Donohue, J. M., Wright, L. G., Fedrizzi, A. & Resch, K. J. Spectral compression of single photons. *Nature Photonics* **7**, 363–366 (2013).

[108] Sparkes, B. M. *et al.* Precision Spectral Manipulation: A Demonstration Using a Coherent Optical Memory. *Physical Review X* **2**, 021011 (2012).

[109] Saglamyurek, E. *et al.* An integrated processor for photonic quantum states using a broadband light-matter interface. *New Journal of Physics* **16** (2014).

[110] Reim, K. F. *et al.* Multipulse addressing of a Raman quantum memory: Configurable beam splitting and efficient readout. *Physical Review Letters* **108**, 1–5 (2012).

[111] Nunn, J. *et al.* Enhancing Multiphoton Rates with Quantum Memories. *Physical Review Letters* **110**, 133601 (2013).

[112] Humphreys, Peter C, Metcalf, Benjamin J., Spring, Justin B., Moore, Merrit, Jin, X.-M., Barbieri, Marco, Kolthammer, W. Steven, Walmsley, I. A. Linear Optical Quantum Computing in a Single Spatial Mode. *Physical Review Letters* **150501**, 1–5 (2013).

[113] Humphreys, P. C. *et al.* Continuous-variable quantum computing in optical time-frequency modes using quantum memories. *Physical Review Letters* **113**, 130502 (2014).

[114] Campbell, G. T. *et al.* Configurable Unitary Transformations and Linear Logic Gates Using Quantum Memories. *Physical Review Letters* **113**, 063601 (2014).

[115] Yao, X.-C. *et al.* Observation of eight-photon entanglement. *Nature Photonics* **6**, 225–228 (2012).

[116] Prawer, S. & Greentree, A. D. Diamond for Quantum Computing. *Science* **320**, 1601–1602 (2008).

[117] Ashcroft, N. & Mermin, N. *Solid State Physics* (W.B. Saunder Company, 1976).

[118] Kimball, G. E. The Electronic Structure of Diamond. *The Journal of Chemical Physics* **3**, 560 (1935).

[119] Saslow, W., Bergstresser, T. & Cohen, M. L. Band Structure and Optical Properties of Diamond. *Physical Review Letters* 354–356 (1966).

[120] Raman, C. & Rendall, G. Birefringence patterns in diamond. *Proceedings of the Indian Academy of ...* **273** (1944).

[121] Raman, C. The Diamond: Its Structure and Properties. *Proceedings of the Indian Academy of Sciences- ...* 231–246 (1968).

[122] Solin, S. & Ramdas, A. Raman spectrum of diamond. *Physical Review B* **1** (1970).

[123] Wigner, E. The elastic characterisitic vibrations of symmetrical systems. *Nachr. Ges. Wiss. Göttingen* 133 (1930).

[124] Birman, J. L. Space Group Selection Rules: Diamond and Zinc Blende. *Physical Review* **127**, 1093–1106 (1962).

[125] Crackwell, A. *Applied Group Theory.* Selected Readings in Physics (Permagon Press, 1968).

[126] Hayes, W. & Loudon, R. *Scattering of Light by Crystals* (Dove Publications Inc., 1974).

[127] Klemens, P. Anharmonic Decay of Optical Phonons. *Physical Review* **659** (1966).

[128] Kozhekin, A., Mølmer, K. & Polzik, E. Quantum memory for light. *Physical Review A* **62**, 1–5 (2000).

[129] Nunn, J. *Quantum Memory in Atomic Ensembles.* Ph.D. thesis, University of Oxford (2008).

[130] Giovannetti, V., Lloyd, S. & Maccone, L. Quantum-enhanced measurements: Beating the standard quantum limit. *Science* **306**, 1330–1336 (2004).

[131] Bussières, F. *et al.* Prospective applications of optical quantum memories. *Journal of Modern Optics* **60:18**, 1519–1537 (2013).

[132] Mosley, P. J. *et al.* Heralded generation of ultrafast single photons in pure quantum states. *Physical Review Letters* **100**, 133601 (2008).

[133] Lauk, N., O'Brien, C. & Fleischhauer, M. Fidelity of photon propagation in electromagnetically induced transparency in the presence of four-wave mixing. *Physical Review A* **88**, 013823 (2013).

[134] Hosseini, M. *et al.* Memory-enhanced noiseless cross-phase modulation. *Light: Science & Applications* **1**, e40 (2012).

[135] Simon, C. *et al.* Quantum repeaters with photon pair sources and multimode memories. *Physical Review Letters* **98**, 190503 (2007).

[136] Weiner, A. M. & Leaird, D. E. Generation of terahertz-rate trains of femtosecond pulses by phase-only filtering. *Optics Letters* **15**, 51–53 (1990).

[137] Hiscocks, M. P. *et al.* Diamond waveguides fabricated by reactive ion etching. *Optics Express* **16**, 19512–19519 (2008).

[138] Glauber, R. J. The quantum theory of optical coherence. *Phys. Rev.* **130**, 2529–2539 (1963).

[139] Grangier, P., Roger, G. & Aspect, A. Experimental evidence for a photon anticorrelation effect on a beam splitter: A new light on single-photon interferences. *Europhysics Letters* **1**, 173 (1986).

[140] Kimble, H. J. The quantum internet. *Nature* **453**, 1023–1030 (2008).

[141] Gündoğan, M., Ledingham, P. M., Almasi, A., Cristiani, M. & de Riedmatten, H. Quantum storage of a photonic polarization qubit in a solid. *Physical Review Letters* **108**, 1–5 (2012).

[142] Zhong, M. *et al.* Optically addressable nuclear spins in a solid with a six-hour coherence time. *Nature* **517**, 177–180 (2015).

[143] England, D. G. *et al.* Storage and retrieval of THz-bandwidth single photons using a room-temperature diamond quantum memory. *Physical Review Letters* **114**, 053602 (2015).

[144] Fisher, K. A. G. *et al.* Frequency and bandwidth conversion of single photons in a room-temperature diamond quantum memory. *Nature Communications* **7**, 11200 (2016).

[145] Kurtsiefer, C., Mayer, S., Zarda, P. & Weinfurter, H. Stable solid-state source of single photons. *Physical Review Letters* **85**, 290–293 (2000).

[146] Politi, A., Cryan, M. J., Rarity, J. G., Yu, S. & O'Brien, J. L. Silica-on-silicon waveguide quantum circuits. *Science* **320**, 646–649 (2008).

[147] Lita, A. E., Miller, A. J. & Nam, S. W. Counting near-infrared single-photons with 95% efficiency. *Optics Express* **16**, 3032–3040 (2008).

[148] Kielpinski, D., Corney, J. F. & Wiseman, H. M. Quantum optical waveform conversion. *Physical Review Letters* **106**, 130501 (2011).

[149] Weiner, A. M. Femtosecond pulse shaping using spatial light modulators. *Review of Scientific Instruments* **71**, 1929–1960 (2000).

[150] Rakher, M. T., Ma, L., Slattery, O., Tang, X. & Srinivasan, K. Quantum transduction of telecommunications-band single photons from a quantum dot by frequency upconversion. *Nature Photonics* **4**, 786–791 (2010).

[151] Raymer, M. G. & Srinivasan, K. Manipulating the color and shape of single photons. *Physics Today* **65**, 32–37 (2012).

[152] Brecht, B., Eckstein, A., Christ, A., Suche, H. & Silberhorn, C. From quantum pulse gate to quantum pulse shaper – dengineered frequency conversion in nonlinear optical waveguides. *New Journal of Physics* **13**, 065029 (2011).

[153] McKinstrie, C. J., Mejling, L., Raymer, M. G. & Rottwitt, K. Quantum-state-preserving optical frequency conversion and pulse reshaping by four-wave mixing. *Physical Review A* **85**, 053829 (2012).

[154] Brackett, C. A. Dense wavelength division multiplexing networks: Principles and applications. *IEEE Journal on Selected Areas in Communications* **8**, 948–964 (1990).

[155] Sinclair, N. *et al.* Spectral multiplexing for scalable quantum photonics using an atomic frequency comb quantum memory and feed-forward control. *Physical Review Letters* **113**, 3–4 (2014).

[156] Donohue, J. M., Lavoie, J. & Resch, K. J. Ultrafast Time-Division Demultiplexing of Polarization-Entangled Photons. *Physical Review Letters* **163602**, 1–5 (2014).

[157] Loudon, R. *The Quantum Theory of Light* (Oxford University Press, 2004).

[158] Eckbreth, A. C. BOXCARS: Crossed-beam phase-matched CARS generation in gases. *Applied Physics Letters* **32**, 421–423 (1978).

[159] Kowligy, A. S. *et al.* Quantum optical arbitrary waveform manipulation and measurement in real time. *Optics Express* **22**, 27942–57 (2014).

[160] Chang, D., Vuletic, V. & Lukin, M. Quantum nonlinear optics photon by photon. *Nature Photonics* **8**, 685–694 (2014).

[161] O'Brien, J. L. Optical quantum computing. *Science* **318**, 1567–1570 (2007).

[162] Pittman, T. B., Jacobs, B. C. & Franson, J. D. Single photons on pseudodemand from stored parametric down-conversion. *Physical Review A* **66**, 042303 (2002).

[163] Yuan, Z.-S. *et al.* Synchronized independent narrow-band single photons and efficient generation of photonic entanglement. *Physical Review Letters* **98**, 180503 (2007).

[164] Campbell, G., Hosseini, M., Sparkes, B. M., Lam, P. K. & Buchler, B. C. Time- and frequency-domain polariton interference. *New Journal of Physics* **14**, 033022 (2012).

[165] Pinel, O. *et al.* A mirrorless spinwave resonator. *Scientific Reports* **5** (2015).

[166] Ou, Z., Hong, C. & Mandel, L. Relation between input and output states for a beam splitter. *Optics Communications* **63**, 118–122 (1987).

[167] Hong, C. K., Ou, Z. Y. & Mandel, L. Measurement of subpicosecond time intervals between two photons by interference. *Physical Review Letters* **59**, 2044–2046 (1987).

[168] Rarity, J. G. & Tapster, P. R. Fourth-order interference in parametric downconversion. *Journal of the Optical Society of America B* **6**, 1221–1226 (1989).

[169] Mattle, K., Weinfurter, H., Kwiat, P. G. & Zeilinger, A. Dense coding in experimental quantum communication. *Physical Review Letters* **76**, 4656–4659 (1996). URL http://link.aps.org/doi/10.1103/PhysRevLett.76.4656.

[170] Miller, A. J., Nam, S. W., Martinis, J. M. & Sergienko, A. V. Demonstration of a low-noise near-infrared photon counter with multiphoton discrimination. *Applied Physics Letters* **83**, 791–793 (2003).

[171] Motes, K. R., Gilchrist, A., Dowling, J. P. & Rohde, P. P. Scalable boson sampling with time-bin encoding using a loop-based architecture. *Physical Review Letters* **113**, 120501 (2014).

[172] Dresselhaus, M., Dresselhaus, G. & Jorio, A. *Group Theory: Application to the Physics of Condensed Matter* (Springer, 2008).

Appendix A

List of publications during Ph.D.

Work included in this thesis

Refereed publications:

1. D.G. England, **K.A.G. Fisher**, J.-P. Maclean, P.J. Bustard, R. Lausten, K.J. Resch, B.J. Sussman, *Storage and retrieval of THz-bandwidth single photons using a room-temperature diamond quantum memory*, Physical Review Letters, **114**, 053602 (2015).

    - Performed experiment, analyzed data, and contributed to writing of manuscript.

2. **K.A.G. Fisher**, D.G England, J.-P. Maclean, P.J. Bustard, K.J. Resch, B.J. Sussman, *Frequency and bandwidth conversion of single photons in a room-temperature diamond quantum memory*, Nature Communications, **7**, 11200 (2016).

    - Performed experiment, analyzed data, and wrote initial manuscript.

3. D.G. England, **K.A.G. Fisher**, J.-P. W. MacLean, P. J. Bustard, K. Heshami, K.J. Resch, B.J. Sussman, *Phonon-mediated nonclassical interference in diamond*, Physical Review Letters, **117**, 073603 (2016), .

    - Performed experiment, analyzed data, and contributed to writing of manuscript.

Not yet published:

4. **K.A.G. Fisher**, D.G. England, J.-P. W. MacLean, P. J. Bustard, K. Heshami, K.J. Resch, B.J. Sussman, *Storage of polarization-entangled photons with THz-bandwidths in a diamond quantum memory*, manuscript in preparation.

    - Performed experiment, analyzed data, and wrote initial manuscript.

Contributions to additional work

5. **K.A.G. Fisher**, A. Broadbent, L.K. Shalm, Z. Yan, J. Lavoie, R. Prevedel, T. Jennewein, K.J. Resch, *Quantum computing on encrypted data*, Nature Communications **5**, 3074 (2014).

    - Performed experiment, analyzed data, and wrote initial manuscript.

6. C. Erven, E. Meyer-Scott, **K. Fisher**, J. Lavoie, B.L. Higgins, Z. Yan, C.J. Pugh, J.-P. Bourgoin, R. Prevedel, L.K. Shalm, L. Richards, N. Gigov, R. Laflamme, G. Weihs, T. Jennewein, K.J. Resch, *Experimental three-photon quantum nonlocality under strict locality conditions*, Nature Photonics **8**, 292–296 (2014).

    - Contributed to experiment, data analysis, and writing of manuscript.

7. E. Meyer-Scott, D. McCloskey, K. Gołos, J.Z. Salvail, **K.A.G. Fisher**, D.R. Hamel, A. Cabello, K.J. Resch, T. Jennewein, *Certifying the presence of a photonic qubit by splitting it in two*, Physical Review Letters, **116**, 070501 (2016).

    - Contributed to data analysis, and writing of manuscript.

8. D. Mahler, L. Rozema, **K. Fisher**, L. Vermeyden, K.J. Resch, H. Wiseman, A. Steinberg, *Experimental nonlocal and surreal Bohmian trajectories*, Science Advances, **2**, e1501466 (2016).

    - Contributed to experiment and writing of manuscript.

9. X. Ma, T. Jackson, H. Zhou, J. Chen, D. Lu, M.D. Mazurek, **K.A.G. Fisher**, X. Peng, D. Kribs, K.J. Resch, Z. Ji, B. Zeng, R. Laflamme, *Pure-state tomography with the expectation value of Pauli operators*, Physical Review A, **93**, 032140 (2016).

    - Contributed to writing of manuscript.

Appendix B

Quantization of the electric field

In this appendix we will begin with the well-known equations for electromagnetic fields travelling through free-space, and relate the the energy of the light to the energy of the harmonic oscillator. We will then make the connection with the quantum harmonic oscillator and use it to define a quantized electric field. The treatment here follows that of Ref. [34].

B.1 Maxwell's equations

Maxwell's equations in free-space are:

$$\vec{\nabla} \cdot \vec{E} = 0, \tag{B.1}$$

$$\vec{\nabla} \cdot \vec{B} = 0, \tag{B.2}$$

$$\vec{\nabla} \times \vec{E} = -\frac{\partial \vec{B}}{\partial t}, \tag{B.3}$$

$$\vec{\nabla} \times \vec{B} = \mu_0 \epsilon_0 \frac{\partial \vec{E}}{\partial t} \tag{B.4}$$

The speed of light c is related to the permittivity and permeability of free space by the relation $c = 1/\sqrt{\mu_0 \epsilon_0}$. We can introduce a vector potential $\vec{A}$ such that the magnetic field

is equals the curl of the vector potential,

$$\vec{B} = \vec{\nabla} \times \vec{A}. \tag{B.5}$$

In order for Maxwell's equations to still be satisfied some conditions need to be met. Eq. B.2 is still satisfied by the vector identity $\vec{\nabla} \cdot (\vec{\nabla} \times \vec{A}) = 0$ for any $\vec{A}$. To satisfy Eq. B.3 we require that

$$\vec{E} = -\frac{\partial \vec{A}}{\partial t}. \tag{B.6}$$

Plugging the magnetic field relation into Maxwell's 4th equation (Eq. B.4), and using the vector calculus identity $\vec{\nabla} \times (\vec{\nabla} \times \vec{A}) = \vec{\nabla}(\vec{\nabla} \cdot \vec{A}) - \nabla^2 \vec{A}$ we find that

$$\vec{\nabla} \times (\vec{\nabla} \times \vec{A}) = \frac{1}{c^2}\frac{\partial \vec{E}}{\partial t} \tag{B.7}$$

$$\nabla^2 \vec{A} = -\frac{1}{c^2}\frac{\partial \vec{E}}{\partial t} = \frac{1}{c^2}\frac{\partial^2 \vec{A}}{\partial t^2} \tag{B.8}$$

where we have used the Coulomb gauge condition $\vec{\nabla} \cdot \vec{A} = 0$. Let's consider $\vec{A}$ to be a superposition of forward and backward travelling plane waves labelled by modes k,

$$\vec{A} = \sum_{\vec{k}} \vec{A}_k(t) e^{i\vec{k}\cdot\vec{r}} + \vec{A}_k^*(t) e^{-i\vec{k}\cdot\vec{r}}. \tag{B.9}$$

Substituting this into Eq. B.8 looks daunting, but since the solution must work for all modes independently, we can just consider an arbitrary mode k:

$$\nabla^2 \vec{A}_k(t) e^{i\vec{k}\cdot\vec{r}} = \frac{1}{c^2}\frac{\partial^2}{\partial t^2}\vec{A}_k(t) e^{i\vec{k}\cdot\vec{r}} \tag{B.10}$$

$$\left(\frac{\partial^2}{\partial t^2} + (ck)^2\right)\vec{A}_k(t) = 0 \tag{B.11}$$

$$\vec{A}_k(t) = \vec{A}_k e^{-i\omega_k t} \tag{B.12}$$

where $\omega_k = ck$. This solution can be substituted back into Eq. B.9 to give the full solution for the vector potential as a function of space and time, $\vec{A}(r,t)$. Let's continue, however,

with the expressions of the electric and magnetic fields in a single mode k:

$$\begin{aligned}
\vec{E}_k &= -\frac{\partial}{\partial t}\left(\vec{A}_k e^{i(\vec{k}\cdot\vec{r}-\omega_k t)} + \vec{A}_k^* e^{-i(\vec{k}\cdot\vec{r}-\omega_k t)}\right) && \text{(B.13)}\\
&= i\omega_k\left(\vec{A}_k e^{i(\vec{k}\cdot\vec{r}-\omega_k t)} + \vec{A}_k^* e^{-i(\vec{k}\cdot\vec{r}-\omega_k t)}\right) && \text{(B.14)}\\
\vec{B}_k &= \vec{\nabla}\times\left(\vec{A}_k e^{i(\vec{k}\cdot\vec{r}-\omega_k t)} + \vec{A}_k^* e^{-i(\vec{k}\cdot\vec{r}-\omega_k t)}\right) && \text{(B.15)}\\
&= i\vec{k}\times\left(\vec{A}_k e^{i(\vec{k}\cdot\vec{r}-\omega_k t)} - \vec{A}_k^* e^{-i(\vec{k}\cdot\vec{r}-\omega_k t)}\right) && \text{(B.16)}
\end{aligned}$$

We can use these the expressions for $\vec{E}_k$ and $\vec{B}_k$ to find the energy of a single mode k,

$$\begin{aligned}
H_k &= \frac{1}{2}\int_V dV(\epsilon_0 E_k^2 + \frac{1}{\mu_0}B_k^2) && \text{(B.17)}\\
&= 2\epsilon_0 V\omega_k^2 \vec{A}_k\cdot\vec{A}_k^* && \text{(B.18)}
\end{aligned}$$

where V is volume of a single mode. Here, Eq. B.18 is where we can first see how we will quantize electric field. The energy of the electromagnetic field resembles that of the harmonic oscillator

$$H_k = \frac{1}{2}(P_k^2 + \omega_k^2 X_k^2), \qquad \text{(B.19)}$$

which we obtain by rewriting the vector potential $\vec{A}_k$ in terms of canonical positions X and momenta P, and a polarization vector $\vec{\varepsilon}_k$ as

$$\vec{A}_k = \frac{1}{\sqrt{4\epsilon_0 V\omega_k^2}}(iP_k + \omega_k X_k)\vec{\varepsilon}_k. \qquad \text{(B.20)}$$

B.2 Quantum harmonic oscillator

Recall that the quantum harmonic oscillator has the Hamiltonian

$$\begin{aligned}
\mathcal{H} &= \hbar\omega\left(\hat{p}^2 + \omega\hat{x}^2\right) && \text{(B.21)}\\
&= \hbar\omega\left(\hat{a}^\dagger\hat{a} + \frac{1}{2}\right), && \text{(B.22)}
\end{aligned}$$

where $\hat{a}$ and $\hat{a}^\dagger$ are the raising and lowering operators, defined as

$$\hat{a} = \frac{1}{\sqrt{2\hbar\omega}}\left(i\hat{p} + \omega\hat{x}\right), \tag{B.23}$$

$$\hat{a}^\dagger = \frac{1}{\sqrt{2\hbar\omega}}\left(-i\hat{p} + \omega\hat{x}\right). \tag{B.24}$$

We are now set to quantize the electric field. We do this by replacing the single mode position and momentum variables of Eq. B.20 with the position and momentum operators in a single mode $\hat{x}_k$ and $\hat{p}_k$,

$$\vec{A}_k \rightarrow \frac{1}{\sqrt{4\epsilon_0 V\omega_k^2}}(i\hat{p}_k + \omega_k\hat{x}_k)\vec{\varepsilon}_k \tag{B.25}$$

$$= \sqrt{\frac{\hbar}{2\epsilon_0 V\omega_k}}\hat{a}_k\vec{\varepsilon}_k \tag{B.26}$$

$$\vec{A}_k^* \rightarrow \sqrt{\frac{\hbar}{2\epsilon_0 V\omega_k}}\hat{a}_k^\dagger\vec{\varepsilon}_k. \tag{B.27}$$

The quantized electric field in a mode k is then

$$\vec{E}_k = i\sqrt{\frac{\hbar\omega_k}{2\epsilon_0 V}}\left(\hat{a}_k e^{i(\vec{k}\cdot\vec{r}-\omega_k t)} + \hat{a}_k^\dagger e^{-i(\vec{k}\cdot\vec{r}-\omega_k t)}\right)\vec{\varepsilon}_k. \tag{B.28}$$

Appendix C

HOM interference between a photon and coherent state

In this appendix we give a more complete treatment of Hong-Ou-Mandel (HOM) interference between a single photon and a weak coherent state of strength α. We will go through the cases for both the HOM dip and the HOM peak, deriving the interference visibilities when the wavepackets are coincident on a beamsplitter from different ports.

C.1 HOM dip

The initial state incident on the beamsplitter, $|\psi\rangle$, is a single photon with a spectral shape given by $f(\omega_1)$ in input port a, and a coherent state comprised of $|\alpha|^2$ photons with spectral shape $g(\omega_2)$ in port b. We write the separable joint spetrum as $F(\omega_1, \omega_2) = f(\omega_1)g(\omega_2)$. There is a time delay between the photon and coherent state given by $e^{i\omega\tau}$. Recall that the beamsplitter mappings are $\hat{a} \to t\hat{c} + r\hat{d}$, and $\hat{b} \to t\hat{d} - r\hat{c}$. The state after the beamsplitter is described by

$$
\begin{aligned}
|\psi\rangle &= \iint d\omega_1 d\omega_2 F(\omega_1,\omega_2) e^{i\omega_1\tau} |\omega_1\rangle_a \otimes |\alpha(\omega_2)\rangle_b \qquad \text{(C.1)} \\
&\rightarrow \iint d\omega_1 d\omega_2 F(\omega_1,\omega_2) e^{i\omega_1\tau} [t\hat{c}^\dagger(\omega_1) + r\hat{d}^\dagger(\omega_1)]| - r\alpha(\omega_2)\rangle_c \otimes |t\alpha(\omega_2)\rangle_d
\end{aligned}
$$

where the coherent state, being classical in nature, follows the convenient beamsplitter mapping $|\alpha\rangle_b \rightarrow |-r\alpha\rangle_c \otimes |t\alpha\rangle_d$. The expected coincidence detection rate between the two output ports is given by the integral over frequency ω of the expectation value of the number operators in ports c and d:

$$
\begin{aligned}
P_{c\&d} &= \iint d\omega d\omega' \left\langle \hat{c}^\dagger(\omega)\hat{c}(\omega)\hat{d}^\dagger(\omega')\hat{d}(\omega') \right\rangle \qquad \text{(C.2)} \\
&= \iint d\omega d\omega' \iiiint d\omega_1 d\omega_2 d\omega_1' d\omega_2' F^*(\omega_1',\omega_2') F(\omega_1,\omega_2) e^{i(\omega_1-\omega_1')\tau} \qquad \text{(C.3)} \\
&\quad \times \langle -r\alpha(\omega_2')|_c \otimes \langle t\alpha(\omega_1')|_d [t\hat{c}(\omega_1') + r\hat{d}(\omega_1')] \hat{c}^\dagger(\omega)\hat{c}(\omega)\hat{d}^\dagger(\omega')\hat{d}(\omega') [t\hat{c}^\dagger(\omega_1) + r\hat{d}^\dagger(\omega_1)] \\
&\quad \times |-r\alpha(\omega_2)\rangle_c \otimes |t\alpha(\omega_2)\rangle_d \\
&= \iint d\omega d\omega' \iiiint d\omega_1 d\omega_2 d\omega_1' d\omega_2' F^*(\omega_1',\omega_2') F(\omega_1,\omega_2) e^{i(\omega_1-\omega_1')\tau} \qquad \text{(C.4)} \\
&\quad \times \langle -r\alpha(\omega_2')|_c \otimes \langle t\alpha(\omega_1')|_d [t^2 \hat{c}(\omega_1')\hat{c}^\dagger(\omega)\hat{c}(\omega)\hat{c}^\dagger(\omega_1)\hat{d}^\dagger(\omega')\hat{d}(\omega') \\
&\qquad + rt\hat{c}(\omega_1')\hat{c}^\dagger(\omega)\hat{c}(\omega)\hat{d}^\dagger(\omega')\hat{d}(\omega')\hat{d}^\dagger(\omega_1) + rt\hat{c}^\dagger(\omega)\hat{c}(\omega)\hat{c}^\dagger(\omega_1)\hat{d}(\omega_1')\hat{d}^\dagger(\omega')\hat{d}(\omega') \\
&\qquad + r^2\hat{c}^\dagger(\omega)\hat{c}(\omega)\hat{d}(\omega_1')\hat{d}^\dagger(\omega')\hat{d}(\omega')\hat{d}^\dagger(\omega_1)] | - r\alpha(\omega_2)\rangle_c \otimes |t\alpha(\omega_2)\rangle_d
\end{aligned}
$$

We see here four terms to work out with the coefficients t^2, rt, rt, r^2. We can write each of

these terms in there normal-ordered form, remembering that $[c(\omega_i), c^\dagger(\omega_j)] = \delta(\omega_i - \omega_j)$,

$$\begin{aligned} t^2 \times \hat{c}(\omega_1')\hat{c}^\dagger(\omega)\hat{c}(\omega)\hat{c}^\dagger(\omega_1)\hat{d}^\dagger(\omega')\hat{d}(\omega') &= t^2 \times [\delta(\omega_1' - \omega)\delta(\omega - \omega_1) + \delta(\omega_1' - \omega)\hat{c}^\dagger(\omega_1)\hat{c}(\omega) \\ &+ \delta(\omega - \omega_1)\hat{c}^\dagger(\omega)\hat{c}(\omega_1') + \delta(\omega_1' - \omega_1)\hat{c}^\dagger(\omega)\hat{c}(\omega) \\ &+ \hat{c}^\dagger(\omega_1)\hat{c}^\dagger(\omega)\hat{c}(\omega)\hat{c}(\omega_1')] \times \hat{d}^\dagger(\omega')\hat{d}(\omega') \end{aligned} \tag{C.5}$$

$$\begin{aligned} rt \times \hat{c}(\omega_1')\hat{c}^\dagger(\omega)\hat{c}(\omega)\hat{d}^\dagger(\omega')\hat{d}(\omega')\hat{d}^\dagger(\omega_1) &= rt \times [\delta(\omega_1' - \omega)\hat{c}(\omega) + \hat{c}^\dagger(\omega)\hat{c}(\omega)\hat{c}(\omega_1')] \\ &\times [\delta(\omega' - \omega_1)\hat{d}^\dagger(\omega') + \hat{d}^\dagger(\omega_1)\hat{d}^\dagger(\omega')\hat{d}(\omega')] \end{aligned} \tag{C.6}$$

$$\begin{aligned} rt \times \hat{c}^\dagger(\omega)\hat{c}(\omega)\hat{c}^\dagger(\omega_1)\hat{d}(\omega_1')\hat{d}^\dagger(\omega')\hat{d}(\omega') &= rt \times [\delta(\omega - \omega_1)\hat{c}^\dagger(\omega) + \hat{c}^\dagger(\omega_1)\hat{c}^\dagger(\omega)\hat{c}(\omega)] \\ &\times [\delta(\omega_1' - \omega')\hat{d}(\omega') + \hat{d}^\dagger(\omega')\hat{d}(\omega')\hat{d}(\omega_1')] \end{aligned} \tag{C.7}$$

$$\begin{aligned} r^2 \times \hat{c}^\dagger(\omega)\hat{c}(\omega)\hat{d}(\omega_1')\hat{d}^\dagger(\omega')\hat{d}(\omega')\hat{d}^\dagger(\omega_1) &= r^2 \times \hat{c}^\dagger(\omega)\hat{c}(\omega) \times [\delta(\omega_1' - \omega')\delta(\omega' - \omega_1) \\ &+ \delta(\omega_1' - \omega')\hat{d}^\dagger(\omega_1)\hat{d}(\omega') + \delta(\omega' - \omega_1)\hat{d}^\dagger(\omega')\hat{d}(\omega_1') \\ &+ \delta(\omega_1' - \omega_1)\hat{d}^\dagger(\omega')\hat{d}(\omega') + \hat{d}^\dagger(\omega_1)\hat{d}^\dagger(\omega')\hat{d}(\omega')\hat{d}(\omega_1')] \end{aligned} \tag{C.8}$$

We can now evaluate the expectation value by acting the ladder operators to the left and

right, using the fact that $\hat{c}(\omega)|-r\alpha(\omega_2)\rangle_c = (-r\alpha)\delta(\omega-\omega_2)|-r\alpha(\omega_2)\rangle_c$, to give

$$
\begin{aligned}
P_{c\&d} &= \iint d\omega d\omega' \iiiint d\omega_1 d\omega_2 d\omega_1' d\omega_2' F^*(\omega_1',\omega_2') F(\omega_1,\omega_2) e^{i(\omega_1-\omega_1')\tau} \qquad \text{(C.9)}\\
&\times \{t^4|\alpha|^2\delta(\omega'-\omega_2')\delta(\omega'-\omega_2)\times[\delta(\omega_1'-\omega)\delta(\omega-\omega_1)\\
&\quad +r^2|\alpha|^2\delta(\omega_1'-\omega)\delta(\omega_1-\omega_2')\delta(\omega-\omega_2)\\
&\quad +r^2|\alpha|^2\delta(\omega-\omega_1)\delta(\omega-\omega_2')\delta(\omega_1'-\omega_2)\\
&\quad +r^2|\alpha|^2\delta(\omega_1'-\omega_1)\delta(\omega-\omega_2')\delta(\omega-\omega_2)\\
&\quad +r^4|\alpha|^4\delta(\omega_1-\omega_2')\delta(\omega-\omega_2')\delta(\omega-\omega_2)\delta(\omega_1'-\omega_2)]\\
&- r^2t^2|\alpha|^2\delta(\omega-\omega_2)\delta(\omega'-\omega_2')\times[\delta(\omega_1'-\omega)+r^2|\alpha|^2\delta(\omega-\omega_2')\delta(\omega_1'-\omega_2)]\\
&\quad \times[\delta(\omega'-\omega_1)+t^2|\alpha|^2\delta(\omega_1-\omega_2')\delta(\omega'-\omega_2)]\\
&- r^2t^2|\alpha|^2\delta(\omega-\omega_2')\delta(\omega'-\omega_2)\times[\delta(\omega-\omega_1)+r^2|\alpha|^2\delta(\omega-\omega_2)\delta(\omega_1-\omega_2')]\\
&\quad \times[\delta(\omega'-\omega_1')+t^2|\alpha|^2\delta(\omega'-\omega_2')\delta(\omega_1'-\omega_2)]\\
&+ r^4|\alpha|^2\delta(\omega-\omega_2')\delta(\omega-\omega_2)\times[\delta(\omega_1'-\omega')\delta(\omega'-\omega_1)\\
&\quad +t^2|\alpha|^2\delta(\omega_1-\omega_2')\delta(\omega'-\omega_2)\\
&\quad +t^2|\alpha|^2\delta(\omega'-\omega_1)\delta(\omega'-\omega_2')\delta(\omega_1'-\omega_2)\\
&\quad +t^2|\alpha|^2\delta(\omega_1'-\omega_1)\delta(\omega'-\omega_2')\delta(\omega'-\omega_2)\\
&\quad +t^4|\alpha|^4\delta(\omega_1-\omega_2')\delta(\omega'-\omega_2')\delta(\omega'-\omega_2)\delta(\omega_1'-\omega_2)]\}
\end{aligned}
$$

This looks awful, but as we evaluate some of the delta functions it will simplify a fair bit.

First, we integrate over ω_2 and ω_2' to find

$$\begin{aligned} P_{c\&d} &= \iint d\omega d\omega' \iint d\omega_1 d\omega_1' e^{i(\omega_1-\omega_1')\tau} \\ &\times \{t^4|\alpha|^2 F^*(\omega_1',\omega')F(\omega_1,\omega') \times [\delta(\omega_1'-\omega)\delta(\omega-\omega_1) \\ &\quad +r^2|\alpha|^2\delta(\omega_1'-\omega)\delta(\omega_1-\omega')\delta(\omega-\omega') \\ &\quad +r^2|\alpha|^2\delta(\omega-\omega_1)\delta(\omega-\omega')\delta(\omega_1'-\omega') \\ &\quad +r^2|\alpha|^2\delta(\omega_1'-\omega_1)\delta(\omega-\omega') \\ &\quad +r^4|\alpha|^4\delta(\omega_1-\omega')\delta(\omega-\omega')\delta(\omega_1'-\omega')] \\ &- r^2t^2|\alpha|^2 F^*(\omega_1',\omega')F(\omega_1,\omega)\delta(\omega_1'-\omega)\delta(\omega'-\omega_1) \\ &\quad \times[1+r^2|\alpha|^2\delta(\omega-\omega')] \times [1+t^2|\alpha|^2\delta(\omega'-\omega)] \\ &- r^2t^2|\alpha|^2 F^*(\omega_1',\omega)F(\omega_1,\omega')\delta(\omega-\omega_1)\delta(\omega'-\omega_1') \\ &\quad \times[1+r^2|\alpha|^2\delta(\omega-\omega')] \times [1+t^2|\alpha|^2\delta(\omega'-\omega)] \\ &+ r^4|\alpha|^2 F^*(\omega_1',\omega)F(\omega_1,\omega) \times [\delta(\omega_1'-\omega')\delta(\omega'-\omega_1) \\ &\quad +t^2|\alpha|^2\delta(\omega_1-\omega)\delta(\omega'-\omega) \\ &\quad +t^2|\alpha|^2\delta(\omega'-\omega_1)\delta(\omega'-\omega)\delta(\omega_1'-\omega) \\ &\quad +t^2|\alpha|^2\delta(\omega_1'-\omega_1)\delta(\omega'-\omega) \\ &\quad +t^4|\alpha|^4\delta(\omega_1-\omega)\delta(\omega'-\omega)\delta(\omega_1'-\omega)]\} \end{aligned} \tag{C.10}$$

Next, we integrate over ω_1 and ω_1' to get

$$\begin{aligned} P_{c\&d} &= \iint d\omega d\omega' \times \{ \\ &\quad t^4|\alpha|^2 \times [|F(\omega,\omega')|^2 \\ &\quad +3r^2|\alpha|^2 F^*(\omega,\omega')F(\omega',\omega')e^{i(\omega'-\omega)\tau}\delta(\omega-\omega') \\ &\quad +r^4|\alpha|^4|F(\omega',\omega')|^2\delta(\omega-\omega')] \\ &- 2r^2t^2|\alpha|^2 F^*(\omega,\omega')F(\omega',\omega)e^{i(\omega'-\omega)\tau} \\ &\quad \times[1+r^2|\alpha|^2\delta(\omega-\omega')] \times [1+t^2|\alpha|^2\delta(\omega'-\omega)] \\ &+ r^4|\alpha|^2 \times [|F(\omega',\omega)|^2 \\ &\quad +3t^2|\alpha|^2 F^*(\omega,\omega)F(\omega',\omega)e^{i(\omega'-\omega)\tau}\delta(\omega'-\omega) \\ &\quad +t^4|\alpha|^4 F(\omega,\omega)|^2\delta(\omega'-\omega)]\} \end{aligned} \tag{C.11}$$

The joint spectrum is normalized so that $\iint d\omega d\omega' |F(\omega,\omega')|^2 = 1$. We then perform the integrations over ω and ω' where possible, and write remaining spectral functions as $\mathcal{S} = \int d\omega |F(\omega,\omega)|^2$, which we take to be equal to 1 when perfect spectral overlap between $f(\omega)$ and $g(\omega)$ is attained. We write the simplified coincidence probability in orders of $|\alpha|^2$

$$\begin{aligned} P_{c\&d} &= |\alpha|^2 \times \left\{ t^4 + r^4 - 2r^2t^2 \iint d\omega d\omega' F^*(\omega,\omega') F(\omega',\omega) e^{i(\omega'-\omega)\tau} \right\} \\ &\quad + |\alpha|^4 \times r^2 t^2 \mathcal{S} \end{aligned} \tag{C.12}$$

where the $|\alpha|^6$ order terms have cancelled. For the $|\alpha|^2$ order term we have the same result as we saw for the HOM dip between single photon in Chapter 2. When the spectra of the two states perfectly match the spectral function is invariant under exchange of the arguments, $F(\omega,\omega') = F(\omega',\omega)$, and including a factor of 2 to compensate for double counting of each frequency during the integration, we get the result

$$\begin{aligned} P_{c\&d} &= |\alpha|^2 \times \left\{ t^4 + r^4 - 2r^2t^2 \iint d\omega d\omega' |F(\omega',\omega)|^2 \cos\left[(\omega'-\omega)\tau\right] \right\} \\ &\quad + |\alpha|^4 \times r^2 t^2 \mathcal{S} \end{aligned} \tag{C.13}$$

Here we can see the crux of what we wish to show. The HOM interference takes place in the $|\alpha|^2$ order which corresponds to a single photon from the coherent state. When $|\tau| \gg 0$ we see the frequency integrals will give fast oscillations that average to 0, resulting in a baseline coincidence rate of $|\alpha|^2(t^4 + r^4) + |\alpha|^4 r^2 t^2$, where we take $\mathcal{S} = 1$. When $\tau \approx 0$ the integral approaches 1 and we get a coincidence rate of $|\alpha|^2(t^2 - r^2)^2 + |\alpha|^4 r^2 t^2$, producing the characteristic dip. This results in a dip visibility of

$$\mathcal{V} = \frac{2r^2t^2|\alpha|^2}{(t^4 + r^4)|\alpha|^2 + r^2t^2|\alpha|^4} \tag{C.14}$$

When the coherent state is very weak, $|\alpha|^2 \ll 1$, when can neglect the $|\alpha|^4$ term and the visibility returns to that of HOM interference between two single photons. As the coherent state increases in photon number we can no longer neglect term and we see that it serves to degrade the dip visibility as expected.

C.2 HOM peak

Here we go through the same treatment as above to derive a formula for the visibility of the HOM peak, which we plot in Chapter 2. Recall that for the HOM peak we look at multi-photon events in just one of the beamsplitter output ports. The two-photon expectation value in mode c, P_{2c}, is given as

$$
\begin{aligned}
P_{2c} &= \iint d\omega d\omega' \left\langle \hat{c}^\dagger(\omega)\hat{c}(\omega)\hat{c}^\dagger(\omega')\hat{c}(\omega') \right\rangle && \text{(C.15)} \\
&= \iint d\omega d\omega' \iiint\!\!\int d\omega_1 d\omega_2 d\omega_1' d\omega_2' F^*(\omega_1', \omega_2') F(\omega_1, \omega_2) e^{i(\omega_1 - \omega_1')\tau} && \text{(C.16)} \\
&\quad \times \langle -r\alpha(\omega_2')|_c \otimes \langle t\alpha(\omega_2')|_d \times [t\hat{c}(\omega_1') + r\hat{d}(\omega_1')] \times \hat{c}^\dagger(\omega)\hat{c}^\dagger(\omega')\hat{c}(\omega)\hat{c}(\omega') \\
&\quad \times [t\hat{c}^\dagger(\omega_1) + r\hat{d}^\dagger(\omega_1)] \times |-r\alpha(\omega_2)\rangle_c \otimes |t\alpha(\omega_2)\rangle_d \\
&= \iint d\omega d\omega' \iiint\!\!\int d\omega_1 d\omega_2 d\omega_1' d\omega_2' F^*(\omega_1', \omega_2') F(\omega_1, \omega_2) e^{i(\omega_1 - \omega_1')\tau} && \text{(C.17)} \\
&\quad \times \langle -r\alpha(\omega_2')|_c \otimes \langle t\alpha(\omega_2')|_d \times [t^2\hat{c}(\omega_1')\hat{c}^\dagger(\omega)\hat{c}^\dagger(\omega')\hat{c}(\omega)\hat{c}(\omega')\hat{c}^\dagger(\omega_1) \\
&\qquad + rt\hat{c}(\omega_1')\hat{c}^\dagger(\omega)\hat{c}^\dagger(\omega')\hat{c}(\omega)\hat{c}(\omega')\hat{d}^\dagger(\omega_1) \\
&\qquad + rt\hat{d}(\omega_1')\hat{c}^\dagger(\omega)\hat{c}^\dagger(\omega')\hat{c}(\omega)\hat{c}(\omega')\hat{c}^\dagger(\omega_1) \\
&\qquad + r^2\hat{d}(\omega_1')\hat{c}^\dagger(\omega)\hat{c}^\dagger(\omega')\hat{c}(\omega)\hat{c}(\omega')\hat{d}^\dagger(\omega_1)] \times |-r\alpha(\omega_2)\rangle_c \otimes |t\alpha(\omega_2)\rangle_d
\end{aligned}
$$

In similar fashion to the HOM dip treatment, we find the normal-ordered expressions for

each of the four terms above, finding that

$$\begin{aligned} t^2 \times \hat{c}(\omega_1')\hat{c}^\dagger(\omega)\hat{c}^\dagger(\omega')\hat{c}(\omega)\hat{c}(\omega')\hat{c}^\dagger(\omega_1) &= t^2 \times [\delta(\omega-\omega_1')\delta(\omega'-\omega_1)\hat{c}^\dagger(\omega')\hat{c}(\omega) \\ &\quad +\delta(\omega-\omega_1')\delta(\omega-\omega_1)\hat{c}^\dagger(\omega')\hat{c}(\omega') \\ &\quad +\delta(\omega'-\omega_1)\delta(\omega'-\omega_1')\hat{c}^\dagger(\omega)\hat{c}(\omega) \\ &\quad +\delta(\omega'-\omega_1')\delta(\omega-\omega_1)\hat{c}^\dagger(\omega)\hat{c}(\omega') \\ &\quad +\delta(\omega-\omega_1')\hat{c}^\dagger(\omega')\hat{c}^\dagger(\omega_1)\hat{c}(\omega)\hat{c}(\omega') \\ &\quad +\delta(\omega'-\omega_1)\hat{c}^\dagger(\omega)\hat{c}^\dagger(\omega')\hat{c}(\omega_1')\hat{c}(\omega) \\ &\quad +\delta(\omega'-\omega_1')\hat{c}^\dagger(\omega)\hat{c}^\dagger(\omega_1)\hat{c}(\omega)\hat{c}(\omega') \\ &\quad +\delta(\omega-\omega_1)\hat{c}^\dagger(\omega)\hat{c}^\dagger(\omega')\hat{c}(\omega_1')\hat{c}(\omega') \\ &\quad +\delta(\omega_1-\omega_1')\hat{c}^\dagger(\omega)\hat{c}^\dagger(\omega')\hat{c}(\omega)\hat{c}(\omega') \\ &\quad +\hat{c}^\dagger(\omega)\hat{c}^\dagger(\omega')\hat{c}^\dagger(\omega_1)\hat{c}(\omega_1')\hat{c}(\omega)\hat{c}(\omega')] \end{aligned} \tag{C.18}$$

$$\begin{aligned} rt \times \hat{c}(\omega_1')\hat{c}^\dagger(\omega)\hat{c}^\dagger(\omega')\hat{c}(\omega)\hat{c}(\omega')\hat{c}^\dagger(\omega_1) &= rt \times [\delta(\omega-\omega_1')\hat{c}^\dagger(\omega')+\delta(\omega'-\omega_1')\hat{c}^\dagger(\omega) \\ &\quad +\hat{c}^\dagger(\omega)\hat{c}^\dagger(\omega')\hat{c}(\omega_1')] \times \hat{c}(\omega)\hat{c}(\omega')\hat{d}^\dagger(\omega_1) \end{aligned} \tag{C.19}$$

$$\begin{aligned} rt \times \hat{d}(\omega_1')\hat{c}^\dagger(\omega)\hat{c}^\dagger(\omega')\hat{c}(\omega)\hat{c}(\omega')\hat{c}(\omega_1) &= rt \times \hat{c}^\dagger(\omega)\hat{c}^\dagger(\omega')\hat{d}(\omega_1') \times [\delta(\omega'-\omega_1)\hat{c}(\omega) \\ &\quad +\delta(\omega-\omega_1)\hat{c}(\omega')+\hat{c}^\dagger(\omega_1)\hat{c}(\omega)\hat{c}(\omega')] \end{aligned} \tag{C.20}$$

$$\begin{aligned} r^2 \times \hat{c}^\dagger(\omega)\hat{c}^\dagger(\omega')\hat{c}(\omega)\hat{c}(\omega')\hat{d}(\omega_1')\hat{d}^\dagger(\omega_1) &= r^2 \times \hat{c}^\dagger(\omega)\hat{c}^\dagger(\omega')\hat{c}(\omega)\hat{c}(\omega') \\ &\quad \times[\delta(\omega_1-\omega_1')+\hat{d}^\dagger(\omega_1)\hat{d}(\omega_1')] \end{aligned} \tag{C.21}$$

The two-photon rate in mode c is then,

$$
\begin{aligned}
P_{2c} \;=\; & \iint d\omega d\omega' \iiiint d\omega_1 d\omega_2 d\omega_1' d\omega_2' F^*(\omega_1', \omega_2') F(\omega_1, \omega_2) e^{i(\omega_1 - \omega_1')\tau} \times \{ \qquad \text{(C.22)} \\
& t^2 \times [r^2|\alpha|^2 \times \delta(\omega - \omega_1')\delta(\omega' - \omega_1)\delta(\omega' - \omega_2')\delta(\omega - \omega_2) \\
& \quad + r^2|\alpha|^2 \times \delta(\omega - \omega_1')\delta(\omega - \omega_1)\delta(\omega' - \omega_2')\delta(\omega' - \omega_2) \\
& \quad + r^2|\alpha|^2 \times \delta(\omega' - \omega_1)\delta(\omega' - \omega_1')\delta(\omega - \omega_2')\delta(\omega - \omega_2) \\
& \quad + r^2|\alpha|^2 \times \delta(\omega' - \omega_1')\delta(\omega - \omega_1)\delta(\omega - \omega_2')\delta(\omega' - \omega_2) \\
& \quad + r^4|\alpha|^4 \times \delta(\omega - \omega_1')\delta(\omega' - \omega_2')\delta(\omega' - \omega_1)\delta(\omega - \omega_2)\delta(\omega - \omega') \\
& \quad + r^4|\alpha|^4 \times \delta(\omega' - \omega_1)\delta(\omega - \omega_2')\delta(\omega - \omega_2)\delta(\omega - \omega_1')\delta(\omega - \omega') \\
& \quad + r^4|\alpha|^4 \times \delta(\omega' - \omega_1')\delta(\omega - \omega_2')\delta(\omega - \omega_1)\delta(\omega - \omega_2)\delta(\omega - \omega') \\
& \quad + r^4|\alpha|^4 \times \delta(\omega - \omega_1)\delta(\omega - \omega_2')\delta(\omega' - \omega_2)\delta(\omega' - \omega_1')\delta(\omega - \omega') \\
& \quad + r^4|\alpha|^4 \times \delta(\omega_1 - \omega_1')\delta(\omega - \omega_2')\delta(\omega - \omega_2)\delta(\omega - \omega') \\
& \quad + r^6|\alpha|^6 \times \delta(\omega - \omega_2')\delta(\omega - \omega')\delta(\omega - \omega_1)\delta(\omega - \omega_2)\delta(\omega - \omega_1')] \\
- \;\; & r^4 t^2|\alpha|^4 \times \delta(\omega - \omega_2)\delta(\omega - \omega')\delta(\omega_1 - \omega_2') \times [\delta(\omega - \omega_1')\delta(\omega' - \omega_2') \\
& \quad + \delta(\omega' - \omega_1')\delta(\omega - \omega_2') + r^2|\alpha|^2 \times \delta(\omega - \omega_2')\delta(\omega' - \omega_2')\delta(\omega_1' - \omega_2)] \\
- \;\; & r^4 t^2|\alpha|^4 \times \delta(\omega - \omega_2')\delta(\omega - \omega')\delta(\omega_1' - \omega_2) \times [\delta(\omega' - \omega_1)\delta(\omega - \omega_2) \\
& \quad + \delta(\omega - \omega_1)\delta(\omega' - \omega_2) + r^2|\alpha|^2 \times \delta(\omega_1 - \omega_2')\delta(\omega - \omega_2)\delta(\omega - \omega')] \\
+ \;\; & r^6|\alpha|^4 \times \delta(\omega - \omega_2')\delta(\omega - \omega_2)\delta(\omega - \omega') \\
& \quad \times [\delta(\omega_1 - \omega_1') + t^2|\alpha|^2 \times \delta(\omega_1 - \omega_2')\delta(\omega_1' - \omega_2)]\}
\end{aligned}
$$

We can start to simplify this beast by integrating over ω_2 and ω_2'. This produces,

$$
\begin{aligned}
P_{2c} \;=\; & \iint d\omega d\omega' \iint d\omega_1 d\omega_1' e^{i(\omega_1-\omega_1')\tau} \times \{ \\
& t^2 \times [r^2|\alpha|^2 \times \delta(\omega-\omega_1')\delta(\omega'-\omega_1) \times F^*(\omega_1',\omega')F(\omega_1,\omega) \\
& \quad + r^2|\alpha|^2 \times \delta(\omega-\omega_1')\delta(\omega-\omega_1) \times F^*(\omega_1',\omega')F(\omega_1,\omega') \\
& \quad + r^2|\alpha|^2 \times \delta(\omega'-\omega_1)\delta(\omega'-\omega_1') \times F^*(\omega_1',\omega)F(\omega_1,\omega) \\
& \quad + r^2|\alpha|^2 \times \delta(\omega'-\omega_1')\delta(\omega-\omega_1) \times F^*(\omega_1',\omega)F(\omega_1,\omega') \\
& \quad + r^4|\alpha|^4 \times \delta(\omega-\omega_1')\delta(\omega'-\omega_1)\delta(\omega-\omega') \times F^*(\omega_1',\omega')F(\omega_1,\omega) \\
& \quad + r^4|\alpha|^4 \times \delta(\omega'-\omega_1)\delta(\omega-\omega')\delta(\omega-\omega_1') \times F^*(\omega_1',\omega)F(\omega_1,\omega) \\
& \quad + r^4|\alpha|^4 \times \delta(\omega'-\omega_1')\delta(\omega-\omega_1)\delta(\omega-\omega') \times F^*(\omega_1',\omega)F(\omega_1,\omega) \\
& \quad + r^4|\alpha|^4 \times \delta(\omega-\omega_1)\delta(\omega-\omega')\delta(\omega'-\omega_1') \times F^*(\omega_1',\omega)F(\omega_1,\omega') \\
& \quad + r^4|\alpha|^4 \times \delta(\omega_1-\omega_1')\delta(\omega-\omega') \times F^*(\omega_1',\omega)F(\omega_1,\omega) \\
& \quad + r^6|\alpha|^6 \times \delta(\omega-\omega')\delta(\omega-\omega_1)\delta(\omega-\omega_1') \times F^*(\omega_1',\omega)F(\omega_1,\omega)] \\
- \;& r^4t^2|\alpha|^4 \times \delta(\omega-\omega') \times [\delta(\omega-\omega_1')\delta(\omega'-\omega_1) \\
& \quad + \delta(\omega'-\omega_1')\delta(\omega-\omega_1) + r^2|\alpha|^2 \times \delta(\omega-\omega_1)\delta(\omega'-\omega_1)\delta(\omega_1'-\omega)] \\
& \times F^*(\omega_1',\omega_1)F(\omega_1,\omega) \\
- \;& r^4t^2|\alpha|^4 \times \delta(\omega-\omega') \times [\delta(\omega'-\omega_1)\delta(\omega-\omega_1') \\
& \quad + \delta(\omega-\omega_1)\delta(\omega'-\omega_1') + r^2|\alpha|^2 \times \delta(\omega_1-\omega)\delta(\omega-\omega_1')\delta(\omega-\omega')] \\
& \times F^*(\omega_1',\omega)F(\omega_1,\omega_1') \\
+ \;& r^6|\alpha|^4 \times \delta(\omega-\omega') \times [\delta(\omega_1-\omega_1') + t^2|\alpha|^2 \times \delta(\omega_1-\omega)\delta(\omega_1'-\omega)] \\
& \times F^*(\omega_1',\omega)F(\omega_1,\omega)\}
\end{aligned}
\tag{C.23}
$$

Next, we can perform integrations over ω_1 and ω_1' to give

$$
\begin{aligned}
P_{2c} \;=\; & \iint d\omega d\omega' \times \{ \\
& t^2 \times [r^2|\alpha|^2 \times |F(\omega,\omega')|^2 e^{i(\omega'-\omega)\tau} \\
& \quad + r^2|\alpha|^2 \times |F(\omega,\omega')|^2 \\
& \quad + r^2|\alpha|^2 \times |F(\omega',\omega)|^2 \\
& \quad + r^2|\alpha|^2 \times |F(\omega,\omega')|^2 e^{i(\omega-\omega')\tau} \\
& \quad + r^4|\alpha|^4 \times \delta(\omega-\omega') \times |F(\omega,\omega')|^2 e^{i(\omega'-\omega)\tau} \\
& \quad + r^4|\alpha|^4 \times \delta(\omega-\omega') \times |F(\omega,\omega')|^2 e^{i(\omega'-\omega)\tau} \\
& \quad + r^4|\alpha|^4 \times \delta(\omega-\omega') \times |F(\omega,\omega')|^2 e^{i(\omega-\omega')\tau} \\
& \quad + r^4|\alpha|^4 \times \delta(\omega-\omega') \times |F(\omega,\omega')|^2 e^{i(\omega-\omega')\tau} \\
& \quad + r^4|\alpha|^4 \times \delta(\omega-\omega') \times \int d\omega_1 |F(\omega_1,\omega)|^2 \\
& \quad + r^6|\alpha|^6 \times \delta(\omega-\omega') \times |F(\omega,\omega)|^2] \\
- \;& r^4 t^2 |\alpha|^4 \times \delta(\omega-\omega') \times [F^*(\omega,\omega')F(\omega',\omega)e^{i(\omega'-\omega)\tau} \\
& \quad + F^*(\omega',\omega)F(\omega,\omega)e^{i(\omega-\omega')\tau} + r^2|\alpha|^2 \times |F(\omega,\omega)|^2] \\
- \;& r^4 t^2 |\alpha|^4 \times \delta(\omega-\omega') \times [F^*(\omega,\omega)F(\omega',\omega)e^{i(\omega'-\omega)\tau} \\
& \quad + F^*(\omega',\omega)F(\omega,\omega')e^{i(\omega-\omega')\tau} + r^2|\alpha|^2 \times |F(\omega,\omega)|^2] \\
+ \;& r^6|\alpha|^4 \times \delta(\omega-\omega') \times \left[\int d\omega_1 |F(\omega_1,\omega)|^2 + t^2|\alpha|^2 \times |F(\omega,\omega)|^2 \right] \}
\end{aligned}
\tag{C.24}
$$

where we have made the assumption that the spectral function is invariant under exchange of its arguments $F(\omega_i,\omega_j) = F(\omega_j,\omega_i)$. Evaluating some of the ω and ω' integrals, and using the fact that the spectral function is normalized $\iint d\omega_i d\omega_j |F(\omega_i,\omega_j)|^2 = 1$, we get

the simplified expression

$$\begin{aligned} P_{2c} &= t^2 \times [2r^2|\alpha|^2 \times \iint d\omega d\omega' |F(\omega,\omega')|^2 e^{i(\omega'-\omega)\tau} \\ &\quad +2r^2|\alpha|^2 \times \mathcal{S} \\ &\quad +4r^4|\alpha|^4 \times \mathcal{S} \\ &\quad +r^4|\alpha|^4 \\ &\quad +r^6|\alpha|^6 \times \mathcal{S}] \\ &- r^4t^2|\alpha|^4 \times [2+r^2|\alpha|^2] \times \mathcal{S} \\ &- r^4t^2|\alpha|^4 \times [2+r^2|\alpha|^2] \times \mathcal{S} \\ &+ r^6|\alpha|^4 \times \left[1+t^2|\alpha|^2 \times \mathcal{S}\right]\} \end{aligned}$$

where we have again labelled the integral $\mathcal{S} = \int d\omega F(\omega,\omega)$, which we take equal to 1 when the spectral function $f(\omega)$ and $g(\omega)$ are overlapped. The first term in this expression carries the time-dependent interference pattern. Collecting terms we find,

$$P_{2c} = 2r^2t^2|\alpha|^2 \times \left[1 + \iint d\omega d\omega' |F(\omega,\omega')|^2 e^{i(\omega'-\omega)\tau}\right] + r^4|\alpha|^4 \tag{C.25}$$

From here we can see the effect of the HOM peak. When τ is large, i.e., the delay is far from zero, the $e^{i(\omega'-\omega)\tau}$ term will oscillate quickly and average to zero over the ω and ω' integrations. This leaves a baseline two-photon rate of $2r^2t^2|\alpha|^2 + r^4|\alpha|^4$. When the delay $\tau = 0$, the integral is equal to 1 and we get a two-photon rate of $4r^2t^2|\alpha|^2 + r^4|\alpha|^4$, the $|\alpha|^2$ portion doubles. This returns a HOM peak visibility of

$$V = \frac{2r^2t^2|\alpha|^2}{2r^2t^2|\alpha|^2 + r^4|\alpha|^4} \tag{C.26}$$

as we saw in Section 2.5.

Appendix D

Classical memory fidelity

In this appendix we would like to discuss the fidelity bound that a quantum memory must surpass for the process to be worthwhile. By this we mean that the quantum memory must outperform a measure-and-resend technique. In this appendix we derive the average fidelity for a measure-and-resend strategy on qubits which provides the fidelity bound on memory storage to be 2/3.

Suppose we have a given qubit $|\psi\rangle = \cos\frac{\theta}{2}|0\rangle + e^{i\phi}\sin\frac{\theta}{2}|1\rangle$. The measure-and-resend straregy is to perform a measurement in the computational basis and to re-emit the of the measurement result. Here, the angle θ is measured from the z-axis of the Bloch sphere, $0 < \theta < \pi$, and the angle ϕ $0 < \phi < 2\pi$. One can see how this constitutes a type of memory: we can wait any amount of time before preparing the new qubit. All that remains is if the re-emitted qubit is a faithful recreation of the input. If turns out that 2/3 of the time it will be. The re-emitted qubit is given by

$$\rho = \cos^2\frac{\theta}{2}|0\rangle\langle 0| + \sin^2\frac{\theta}{2}|1\rangle\langle 1| \tag{D.1}$$

The fidelity with original state is calculated as

$$\begin{aligned}
\mathcal{F}(\rho, |\psi\rangle\langle\psi|) &= \langle\psi|\rho|\psi\rangle && \text{(D.2)}\\
&= \cos^2\frac{\theta}{2}\langle\psi|(|0\rangle\langle 0|)|\psi\rangle + \sin^2\frac{\theta}{2}\langle\psi|(|1\rangle\langle 1|)|\psi\rangle && \text{(D.3)}\\
&= \cos^4\frac{\theta}{2} + \sin^4\frac{\theta}{2} && \text{(D.4)}
\end{aligned}$$

Next we want to find the average fidelity over all pure states $|\psi\rangle$, i.e., those on the surface of the Bloch sphere,

$$\mathcal{F}_{avg} = \frac{1}{4\pi}\int_0^{\pi} d\theta \sin\theta \int_0^{2\pi} d\phi \mathcal{F}\left(\rho, |\psi\rangle\langle\psi|\right) \tag{D.5}$$

$$= \frac{1}{4\pi}\int_0^{\pi} d\theta \sin\theta \int_0^{2\pi} d\phi \left(\cos^4\frac{\theta}{2} + \sin^4\frac{\theta}{2}\right) \tag{D.6}$$

Evalauting the integral over ϕ we find

$$\mathcal{F}_{avg} = \frac{1}{2}\int_0^{\pi} d\theta \sin\theta \left(\cos^4\frac{\theta}{2} + \sin^4\frac{\theta}{2}\right) \tag{D.7}$$

$$= \frac{1}{2}\int_0^{\pi} d\theta \sin\theta \cos^4\frac{\theta}{2} + \frac{1}{2}\int_0^{\pi} d\theta \sin\theta \sin^4\frac{\theta}{2} \tag{D.8}$$

Using the trigonometric identity $\sin\theta = 2\sin\frac{\theta}{2}\cos\frac{\theta}{2}$ we get

$$\mathcal{F}_{avg} = \int_0^{\pi} d\theta \sin\frac{\theta}{2}\cos^5\frac{\theta}{2} + \int_0^{\pi} d\theta \cos\frac{\theta}{2}\sin^5\frac{\theta}{2} \tag{D.9}$$

The first term can be evaulated using the chain rule: $\frac{d}{d\theta}\cos^6\theta = -3\cos^5\frac{\theta}{2}\sin\frac{\theta}{2}$. Similarly for the second term $\frac{d}{d\theta}\sin^6\frac{\theta}{2} = 3\sin^5\frac{\theta}{2}\cos\frac{\theta}{2}$. This produces

$$\mathcal{F}_{avg} = \left[-\frac{1}{3}\cos^6\frac{\theta}{2}\right]_{\theta=0}^{\pi} + \left[\frac{1}{3}\sin^6\frac{\theta}{2}\right]_{\theta=0}^{\pi} \tag{D.10}$$

$$= \frac{1}{3} + \frac{1}{3} \tag{D.11}$$

$$= \frac{2}{3} \tag{D.12}$$

We have shown that the output from the measure-and-resend memory will, on average, have 2/3 overlap with the original qubit. Any implementation of a quantum memory must outperform this to be worthwhile.

Appendix E

Maxwell-Bloch equations for three-level system

The three-level Hamiltonian for the relevant process in diamond is

$$\begin{aligned} \mathcal{H} &= \mathcal{H}_{\text{atom}} + \mathcal{H}_{\text{light}} + \mathcal{H}_{\text{dip}} && \text{(E.1)} \\ &= \sum_i \hbar\omega_i |i\rangle\langle i| + \int d\omega \hbar\omega \left(\hat{a}^\dagger \hat{a} + \frac{1}{2}\right) - \vec{E}\cdot\vec{d} && \text{(E.2)} \end{aligned}$$

where the electric field $\vec{E}$ is

$$\begin{aligned} \vec{E} &= \vec{E}_c + \vec{E}_s && \text{(E.3)} \\ \vec{E}_c &= \tilde{\alpha} e^{i\omega_c \tau} \vec{\varepsilon}_c + \text{c.c.} && \text{(E.4)} \\ \vec{E}_s &= i\mathcal{A}_s \hat{a}_s e^{i\omega_s \tau} \vec{\varepsilon}_s + \text{h.c.} && \text{(E.5)} \end{aligned}$$

where $\tau = t - z/c$. Recall that $k_s = \omega_s/c$, which relates to the form we are used to. We also have the slowly-varying envelope term labelled as $\mathcal{A}_s = \sqrt{\hbar\omega_s/2\epsilon_0}$. We are also only considering a single frequency mode – the result can be integrated over the frequency ω_s to consider finite spectra. Refer to Chapter 2 for the full expression of quantized electric field. The dipole moment can be expressed as $\vec{d} = \vec{d}_{02}\sigma_{02} + \vec{d}_{21}\sigma_{21} + \text{h.c.}$, where we ignore the $|0\rangle \to |1\rangle$ transition since it is forbidden by parity. We have introduced the notation

$\sigma_{jk} = |j\rangle\langle k|$. We want to find out how these operators σ_{jk} evolve in our system, and so we use the Heisenberg equation of motion

$$i\hbar\partial_t\sigma_{jk} = [\sigma_{jk}, \mathcal{H}] \tag{E.6}$$

where ∂_t is shorthand for $\partial/\partial t$. We need to work out all the cases σ_{jk} for $j, k = 0, 1, 2$.

$$\begin{aligned}
i\hbar\partial_t\sigma_{00} &= [\sigma_{00}, \mathcal{H}_{\text{atom}}] + [\sigma_{00}, \mathcal{H}_{\text{light}}] + [\sigma_{00}, \mathcal{H}_{\text{dip}}] && \text{(E.7)}\\
&= 0 + 0 + \vec{E}\cdot\left(\vec{d}_{02}\sigma_{02} - \vec{d}^*_{02}\sigma_{20}\right) && \text{(E.8)}\\
i\hbar\partial_t\sigma_{11} &= \vec{E}\cdot\left(\vec{d}_{21}\sigma_{21} - \vec{d}^*_{21}\sigma_{12}\right) && \text{(E.9)}\\
i\hbar\partial_t\sigma_{22} &= \vec{E}\cdot\left[\vec{d}_{21}\sigma_{21} + \vec{d}^*_{02}\sigma_{20} - (\vec{d}_{02}\sigma_{02} + \vec{d}^*_{21}\sigma_{10})\right] && \text{(E.10)}\\
&= -i\hbar(\partial_t\sigma_{00} + \partial_t\sigma_{11}) && \text{(E.11)}\\
i\hbar\partial_t\sigma_{02} &= \omega_{20}\sigma_{02} - \vec{E}\cdot\left[\vec{d}^*_{02}(\sigma_{00} - \sigma_{22}) + \vec{d}_{21}\sigma_{01}\right] && \text{(E.12)}\\
i\hbar\partial_t\sigma_{01} &= \omega_{10}\sigma_{01} - \vec{E}\cdot\left[\vec{d}^*_{21}\sigma_{02} - \vec{d}^*_{02}\sigma_{21}\right] && \text{(E.13)}\\
i\hbar\partial_t\sigma_{21} &= -\omega_{21}\sigma_{21} - \vec{E}\cdot\left[\vec{d}^*_{21}(\sigma_{22} - \sigma_{11}) - \vec{d}_{02}\sigma_{01}\right] && \text{(E.14)}
\end{aligned}$$

Here we used $\omega_{jk} = \omega_j - \omega_k$, and keep the ordering such that this term is positive. Now we make the approximation that the crystal starts, and stays, predominately in the ground state, such that $\sigma_{00} \to 1, \sigma_{22} \to 0, \sigma_{11} \to 0$. This is justified by the 40 THz splitting between states $|0\rangle$ and $|1\rangle$. This simplifies the coupled equations to

$$\begin{aligned}
i\hbar\partial_t\sigma_{02} &= \omega_{20}\sigma_{02} - \vec{E}\cdot\left[\vec{d}^*_{02} + \vec{d}_{21}\sigma_{01}\right] && \text{(E.15)}\\
i\hbar\partial_t\sigma_{01} &= \omega_{10}\sigma_{01} - \vec{E}\cdot\left[\vec{d}^*_{21}\sigma_{02} - \vec{d}^*_{02}\sigma_{21}\right] && \text{(E.16)}\\
i\hbar\partial_t\sigma_{21} &= -\omega_{21}\sigma_{21} + \vec{E}\cdot\vec{d}_{02}\sigma_{01} && \text{(E.17)}
\end{aligned}$$

Next we switch to the rotating frame and make the rotating wave approximation, which states that high frequency terms oscillate so fast that they average out and do not contribute. Therefore we only keep the lower frequency terms, and make the substitution

$\tilde{\sigma}_{jk} = \sigma_{jk} e^{i\omega_{jk}\tau}$. Our three equations become

$$
\begin{aligned}
i\hbar\partial_t \tilde{\sigma}_{02} &= -\vec{E}\cdot\left[\vec{d}^*_{02} e^{-i\omega_{20}\tau} + \vec{d}_{21}\tilde{\sigma}_{01} e^{-i\omega_{21}\tau}\right] && \text{(E.18)}\\
i\hbar\partial_t \tilde{\sigma}_{01} &= -\vec{E}\cdot\left[\vec{d}_{21}\tilde{\sigma}_{02} e^{i\omega_{21}\tau} - \vec{d}^*_{02}\tilde{\sigma}_{21} e^{-i\omega_{20}\tau}\right] && \text{(E.19)}\\
i\hbar\partial_t \tilde{\sigma}_{21} &= \vec{E}\cdot\vec{d}_{02}\tilde{\sigma}_{01} e^{i\omega_{20}\tau} && \text{(E.20)}
\end{aligned}
$$

Now we are in a position to plug in our electric field terms, $\vec{E} = \vec{E}_c + \vec{E}_s$.

$$
\begin{aligned}
i\hbar\partial_t \tilde{\sigma}_{02} &= -\vec{d}^*_{02}\cdot\{\vec{\varepsilon}_c\left[\tilde{\alpha}e^{-i(\omega_{20}-\omega_c)\tau} + \tilde{\alpha}^* e^{-i(\omega_{20}+\omega_c)\tau}\right]\\
&\qquad +i\vec{\varepsilon}_s\mathcal{A}_s\left(\hat{a}_s e^{-i(\omega_{20}-\omega_s)\tau} - \hat{a}^\dagger_s e^{-i(\omega_{20}+\omega_s)\tau}\right)\}\\
&\quad -\vec{d}_{21}\cdot\{\vec{\varepsilon}_c(\tilde{\alpha}e^{-i(\omega_{21}-\omega_c)\tau} + \tilde{\alpha}^* e^{-i(\omega_{21}+\omega_c)\tau})\\
&\qquad +i\vec{\varepsilon}_s\mathcal{A}_s\left[\hat{a}_s e^{-i(\omega_{21}-\omega_s)\tau} - \hat{a}^\dagger e^{-i(\omega_{21}+\omega_s)\tau}\right]\}\tilde{\sigma}_{01} && \text{(E.21)}
\end{aligned}
$$

$$
\begin{aligned}
i\hbar\partial_t \tilde{\sigma}_{01} &= -\vec{d}_{21}\cdot\{\vec{\varepsilon}_c(\tilde{\alpha}e^{i(\omega_{21}+\omega_c)\tau} + \tilde{\alpha}^* e^{i(\omega_{21}-\omega_c)\tau})\\
&\qquad +i\varepsilon_s\mathcal{A}_s\left[\hat{a}_s e^{i(\omega_{21}+\omega_s)\tau} - \hat{a}^\dagger e^{i(\omega_{21}-\omega_s)\tau}\right]\}\tilde{\sigma}_{02}\\
&\quad -\vec{d}^*_{02}\cdot\{\vec{\varepsilon}_c\left[\tilde{\alpha}e^{-i(\omega_{20}-\omega_c)\tau} + \tilde{\alpha}^* e^{-i(\omega_{20}+\omega_c)\tau}\right]\\
&\qquad +i\vec{\varepsilon}_s\mathcal{A}_s\left[\hat{a}_s e^{-i(\omega_{20}-\omega_s)\tau} - i\hat{a}^\dagger_s e^{-i(\omega_{20}+\omega_s)\tau}\right]\}\tilde{\sigma}_{21} && \text{(E.22)}
\end{aligned}
$$

$$
\begin{aligned}
i\hbar\partial_t \tilde{\sigma}_{21} &= \vec{d}_{02}\cdot\{\vec{\varepsilon}_c\left[\tilde{\alpha}e^{i(\omega_{20}+\omega_c)\tau} + \tilde{\alpha}^* e^{i(\omega_{20}-\omega_c)\tau}\right]\\
&\qquad +i\vec{\varepsilon}_s\mathcal{A}_s\left[\hat{a}_s e^{i(\omega_{20}+\omega_s)\tau} - \hat{a}^\dagger_s e^{i(\omega_{20}-\omega_s)\tau}\right]\}\tilde{\sigma}_{01} && \text{(E.23)}
\end{aligned}
$$

In the same vein as the rotating wave approximation, we can neglect terms that are sums of frequencies since they will oscillate much faster than the terms that are differences of frequencies. At the same time we define

$$
\begin{aligned}
\Delta_c &= \omega_{21} - \omega_c && \text{(E.24)}\\
\Delta_s &= \omega_{20} - \omega_s && \text{(E.25)}\\
\Delta_1 &= \omega_{20} - \omega_c && \text{(E.26)}\\
\Delta_2 &= \omega_{21} - \omega_s && \text{(E.27)}
\end{aligned}
$$

Since we are concerned with two-photon resonance here, we take $\Delta_c = \Delta_s = \Delta$. Our coupled equations become

$$\begin{aligned} i\hbar\partial_t\tilde{\sigma}_{02} &= -\vec{d}_{02}^{*}\cdot\left[\vec{\varepsilon}_c\tilde{\alpha}e^{-i\Delta_1\tau} + i\vec{\varepsilon}_s\mathcal{A}_s\hat{a}_s e^{-i\Delta\tau}\right] \\ &\quad -\vec{d}_{21}\cdot\left[\vec{\varepsilon}_c\tilde{\alpha}e^{-i\Delta\tau} + i\vec{\varepsilon}_s\mathcal{A}_s\hat{a}_s e^{-i\Delta_2\tau}\right]\tilde{\sigma}_{01} \qquad \text{(E.28)} \\ i\hbar\partial_t\tilde{\sigma}_{01} &= -\vec{d}_{21}\cdot\left[\vec{\varepsilon}_c\tilde{\alpha}^{*}e^{i\Delta\tau} - i\vec{\varepsilon}_s\mathcal{A}_s\hat{a}_s^{\dagger}e^{i\Delta_2\tau}\right]\tilde{\sigma}_{02} \\ &\quad -\vec{d}_{02}^{*}\cdot\left[\vec{\varepsilon}_c\tilde{\alpha}e^{-i\Delta_1\tau} + i\vec{\varepsilon}_s\mathcal{A}_s\hat{a}_s e^{-i\Delta\tau}\right]\tilde{\sigma}_{21} \qquad \text{(E.29)} \\ i\hbar\partial_t\tilde{\sigma}_{21} &= \vec{d}_{02}\cdot\left[\vec{\varepsilon}_c\tilde{\alpha}^{*}e^{i\Delta_1\tau} - i\vec{\varepsilon}_s\mathcal{A}_s\hat{a}_s^{\dagger}e^{i\Delta\tau}\right]\tilde{\sigma}_{01} \qquad \text{(E.30)} \end{aligned}$$

Terms with Δ_2 are associated with the photon as the pump for spontaneous anti-Stokes emission. This process is very weak and can be neglected. Terms with Δ_1 are associated with the control beam pump spontaneous Stokes emission. While this process does occur we will neglect it here in order to focus on the memory dynamics. We therefore set $\vec{d}_{02}\cdot\vec{\varepsilon}_c = 0$ and $\vec{d}_{21}\cdot\vec{\varepsilon}_s = 0$. Our equations simplify to

$$\begin{aligned} i\hbar\partial_t\tilde{\sigma}_{02} &= -i\vec{d}_{02}^{*}\cdot\vec{\varepsilon}_s\mathcal{A}_s\hat{a}_s e^{-i\Delta\tau} - \vec{d}_{21}\cdot\vec{\varepsilon}_c\tilde{\alpha}e^{-i\Delta\tau}\tilde{\sigma}_{01} \qquad \text{(E.31)} \\ i\hbar\partial_t\tilde{\sigma}_{13} &= -\vec{d}_{21}\cdot\vec{\varepsilon}_c\tilde{\alpha}^{*}e^{i\Delta\tau}\tilde{\sigma}_{02} - i\vec{d}_{02}^{*}\cdot\vec{\varepsilon}_s\mathcal{A}_s\hat{a}_s e^{-i\Delta\tau}\tilde{\sigma}_{21} \qquad \text{(E.32)} \\ i\hbar\partial_t\tilde{\sigma}_{21} &= -i\vec{d}_{02}\cdot\vec{\varepsilon}_s\mathcal{A}_s\hat{a}_s^{\dagger}e^{i\Delta\tau}\tilde{\sigma}_{01} \qquad \text{(E.33)} \end{aligned}$$

The last simplication we do is another linear approximation. We assume that both the photon ladder operators and the crystal coherences are weak perturbations on the system, which is predominately in the ground state. Then terms that have both a ladder operator and a crystal coherence term are higher order perturbations which are safe to neglect. The equations simplify once more to

$$\begin{aligned} i\hbar\partial_t\tilde{\sigma}_{02} &= -i\vec{d}_{02}^{*}\cdot\vec{\varepsilon}_s\mathcal{A}_s\hat{a}_s e^{-i\Delta\tau} - \vec{d}_{21}\cdot\vec{\varepsilon}_c\tilde{\alpha}e^{-i\Delta\tau}\tilde{\sigma}_{01} \qquad \text{(E.34)} \\ i\hbar\partial_t\tilde{\sigma}_{01} &= -\vec{d}_{21}\cdot\vec{\varepsilon}_c\tilde{\alpha}^{*}e^{i\Delta\tau}\tilde{\sigma}_{02} \qquad \text{(E.35)} \end{aligned}$$

where the equation for $\partial_t\tilde{\sigma}_{21}$ is neglected entirely.

We can now consider the propagation of the electric fields in the medium. Recall that the electric field is related to the material polarization $\vec{P}$ by

$$\left(\frac{\partial^2}{\partial z^2} - \frac{1}{c^2}\frac{\partial^2}{\partial t^2}\right)\vec{E} = \mu_0\frac{\partial^2}{\partial t^2}\vec{P} \qquad \text{(E.36)}$$

We will assume that the strong control field is largely unaffected by propagation through the medium, and so we just consider the wave equation for the signal field $\vec{E}_s$,

$$\left(\frac{\partial^2}{\partial z^2} - \frac{1}{c^2}\frac{\partial^2}{\partial t^2}\right)\left(i\vec{\varepsilon}\mathcal{A}_s\hat{a}_s e^{i\omega_s(t-z/c)}\right) = \mu_0\frac{\partial^2}{\partial t^2}\vec{\tilde{P}}_s e^{i\omega_s(t-z/c)} \tag{E.37}$$

where $\vec{\tilde{P}}_s = \vec{P}_s e^{-i\omega_s\tau}$ and $\vec{P}_s$ is the source term for the signal field. We have only written the positive frequency component of the electric here since it was the only one included in the coupling equation. Taking the derivatives we find

$$\begin{aligned}
&\vec{\varepsilon}_s\left[\left(\frac{\partial^2}{\partial z^2}\hat{a}_s\right) - 2i\frac{\omega_s}{c}\left(\frac{\partial}{\partial z}\hat{a}_s\right) - \frac{\omega_s^2}{c^2}\hat{a}_s\right]e^{i\omega_s(t-z/c)} \\
&-\frac{1}{c^2}\vec{\varepsilon}_s\left[\left(\frac{\partial^2}{\partial t^2}\hat{a}_s\right) + 2i\omega_s\left(\frac{\partial}{\partial t}\hat{a}_s\right) - \omega_s^2\hat{a}_s\right]e^{i\omega_s(t-z/c)} \\
&\qquad = \frac{-i\mu_0}{\mathcal{A}_s}\left[\left(\frac{\partial^2}{\partial t^2}\vec{\tilde{P}}_s\right) + 2i\omega_s\left(\frac{\partial}{\partial t}\vec{\tilde{P}}_s\right) - \omega_s^2\vec{\tilde{P}}_s\right]e^{i\omega_s(t-z/c)}
\end{aligned} \tag{E.38}$$

Next we will divide both sides by $e^{i\omega_s(t-z/c)}$ and make the slowly-varying envelope approximation, in the same manner as in Section 2.6.1, and drop the terms involving $\partial^2/\partial z^2$ and $\partial^2/\partial t^2$ from both sides, and the $\partial/\partial t$ term from the right-hand-side. This results in the simplified wave equation,

$$\vec{\varepsilon}_s\frac{\omega_s}{c}\left[\frac{\partial}{\partial z} + \frac{1}{c}\frac{\partial}{\partial t}\right]\hat{a}_s = -\frac{\mu_0\omega_s^2}{2\mathcal{A}_s}\vec{\tilde{P}}_s \tag{E.39}$$

Now we want to relate this to the coupled equations we derived from the Hamiltonian. The material polarization is related to the dipole moment $\vec{d}$, taking the form $\vec{P} = \sum_{ij}\vec{d}_{ij}\sigma_{ij}$. Recall that only the $\vec{d}_{02}$ term will appear since $\vec{d}_{01} = 0$ and the coherence σ_{21} was neglected in Eq. E.35. The polarization vector is then simply $\vec{\tilde{P}}_s = \vec{d}_{02}\hat{P} = \vec{d}_{02}\tilde{\sigma}_{02}e^{i\Delta\tau}$. Before plugging this into the coupled equations will be also define a ladder operator for the phonon "spin wave" which is equal to the coherence term, $\hat{b} = \tilde{\sigma}_{01}$. The ladder operator $\hat{b}$ follows the usual commutation relations. We can now connect the wave equation to the coupled equations for the coherences $\tilde{\sigma}_{02}$ and $\tilde{\sigma}_{01}$.

$$\left[\frac{\partial}{\partial z}+\frac{1}{c}\frac{\partial}{\partial t}\right]\hat{a}_s = -\frac{\mu_0\omega_s^2}{2\mathcal{A}_s k_s}(\vec{\varepsilon}_s)^*\cdot\vec{d}_{02}\hat{P} \tag{E.40}$$

$$\partial_t\hat{P} = i\Delta\hat{P}-\frac{\vec{d}_{02}^*\cdot\vec{\varepsilon}_s\mathcal{A}_s}{\hbar}\hat{a}_s+i\frac{\vec{d}_{21}\cdot\vec{\varepsilon}_c}{\hbar}\tilde{\alpha}\hat{b} \tag{E.41}$$

$$\partial_t\hat{b} = i\frac{\vec{d}_{21}\cdot\vec{\varepsilon}_c}{\hbar}\tilde{\alpha}^*\hat{P} \tag{E.42}$$

We can clean it up by defining a few constants such as the control Rabi frequency $\Omega_c = \vec{d}_{21}\cdot\vec{\varepsilon}_c\tilde{\alpha}/\hbar$, and a signal coupling constant $\kappa = \vec{d}_{02}^*\cdot\vec{\varepsilon}_s\mathcal{A}_s/\hbar$, resulting in

$$\left[\frac{\partial}{\partial z}+\frac{1}{c}\frac{\partial}{\partial t}\right]\hat{a}_s = -\kappa^*\hat{P} \tag{E.43}$$

$$\partial_t\hat{P} = i\Delta\hat{P}-\kappa\hat{a}_s+i\Omega_c\hat{b} \tag{E.44}$$

$$\partial_t\hat{b} = i\Omega_c^*\hat{P} \tag{E.45}$$

These coupled field equations can be numerically solved, as in Ref. [93] which shows that high storage efficiencies are possible in this system.

Appendix F

Group theory explanation for selection rules

We can use elements of group theory and representation theory to understand a great deal about the vibrational modes in diamond by considering the symmetries of the physical system. It will take some work to get there, but will hopefully be quite insightful. Most of what we will cover here is outlined in "Applied Group Theory" by Crackwell.

A *group* is defined by a set of group elements $\{E, P, Q, R, ...\}$ (here E refers to the identity operation), and a group operation $\circ$, such that:

1. The product of any two group elements is itself a group element, e.g., $Q = P \circ R$.
2. The product of any group element with the identity is itself, $E \circ P = P$.
3. Every group element has an inverse which is also in the group, $P^{-1} \circ P = E$.
4. Multiplication is associative, $P \circ (Q \circ R) = (P \circ Q) \circ R$.
5. (Bonus!) A group is called Abelian if all elements commute, $P \circ Q = Q \circ P$.

An example of a group is invariance of a square under rotations. Another example is the integers from 0 to 3 under addition modulo 4. As an in-depth example, let's look at the invariance of a square under rotations and reflections.

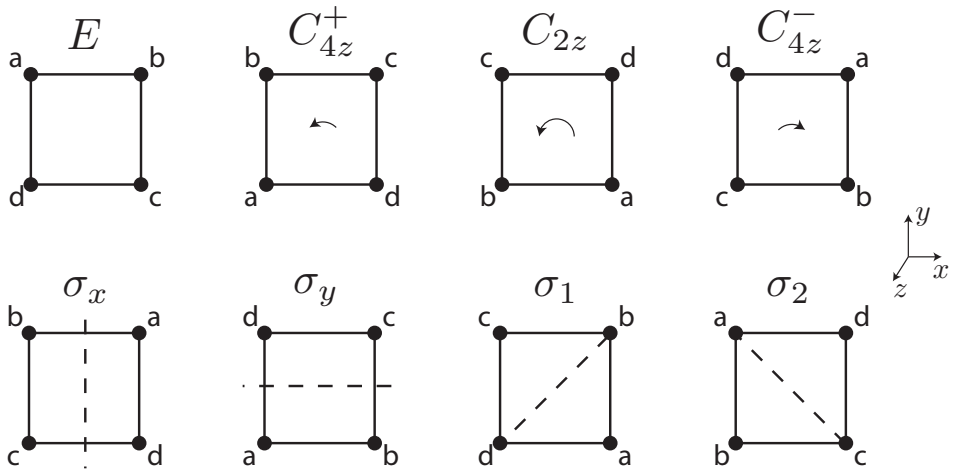

Figure F.1: The elements of the group describing the square are: E, the identity, where no change occurs to the square; C_{4z}^{+}, a 90 degree rotation about the z-axis (out of the page); C_{2z}, a 180 degree rotation about z; , C_{4z}^{-}, a 90 degree rotation the other direction about z; σ_x, a reflection about the y-axis (an inversion of x-coordinates); σ_y, a reflection about the x-axis (inversion of y-coordinates); σ_1, a reflection about the line joining b-d; and σ_2, a reflection about the line joining a-c.

F.1 Symmetries of the square

Fig. F.1 shows all the possible rotation and reflection operations on the square (corners labelled a, b, c, d) that leave the square invariant except for re-labelling of its corners. The multiplicative property of the group can be seen: any two operations (rotations/reflections on the square) in succession give another operation on the square. For example, a 90 degree rotation (C_{4z}^{+}) followed by a reflection in x (σ_x) equals a reflection about the line a-c ($\sigma_x \circ C_{4z}^{+} = \sigma_2$). In this manner we can build a group multiplication table where the elements in rows and columns are ordered to match with their inverses giving the identity (E) along the diagonal. Table F.1 can be read as the element in the i^{th} row acting on the element in the j^{th} column.

There are some things that pop out at us from looking at Table F.1. First, notice that each group element appears only once in each row and column. This is true in general, and

	E	C_{4z}^+	C_{4z}^-	C_{2z}	σ_x	σ_y	σ_1	σ_2
E	E	C_{4z}^+	C_{4z}^-	C_{2z}	σ_x	σ_y	σ_1	σ_2
C_{4z}^-	C_{4z}^-	E	C_{2z}	C_{4z}^+	σ_1	σ_2	σ_y	σ_x
C_{4z}^+	C_{4z}^+	C_{2z}	E	C_{4z}^-	σ_2	σ_1	σ_x	σ_y
C_{2z}	C_{2z}	C_{4z}^-	C_{4z}^+	E	σ_y	σ_x	σ_2	σ_1
σ_x	σ_x	σ_1	σ_2	σ_y	E	C_{2z}	C_{4z}^+	C_{4z}^-
σ_y	σ_y	σ_2	σ_1	σ_x	C_{2z}	E	C_{4z}^-	C_{4z}^+
σ_1	σ_1	σ_y	σ_x	σ_2	C_{4z}^-	C_{4z}^+	E	C_{2z}
σ_2	σ_2	σ_x	σ_y	σ_1	C_{4z}^+	C_{4z}^-	C_{2z}	E

Table F.1: Multiplication table for the square's symmetry group

is quite helpful to know when filling out a group multiplication table. Second, notice that the table has structure: the rotational elements appear in either the top-left or bottom-right blocks, and the reflection elements appear in the other quadrants. This type of behaviour can tell us a lot about how the group symmetry works in different scenarios, which we will come back to later.

F.2 Operations for the diamond group

The diamond crystal has two-interpenetrating face-centred cubic (FCC) lattices. This means it has two Carbon atoms in each until cell. It can be thought of as a single FCC lattice with a basis, i.e., an atom at the origin and one displaced by a vector $\vec{r} = a/4(\hat{x} + \hat{y} + \hat{z})$. To find the symmetries of the FCC lattice we go about a similar process as with the square. It turns out that the FCC lattice symmetry falls into the octahedral group, denoted O_h. This group combines all the rotation operations on a cube with an inversion operation about the centre of the cube. The group has 48 elements (24 rotations times 2 with inversion). Fig. F.2 gives some examples of these operations.

The multiplication table for this group has 2308 elements so we won't write it out. Instead we note that, just as for the square, the table will have distinct patterns which we discuss next.

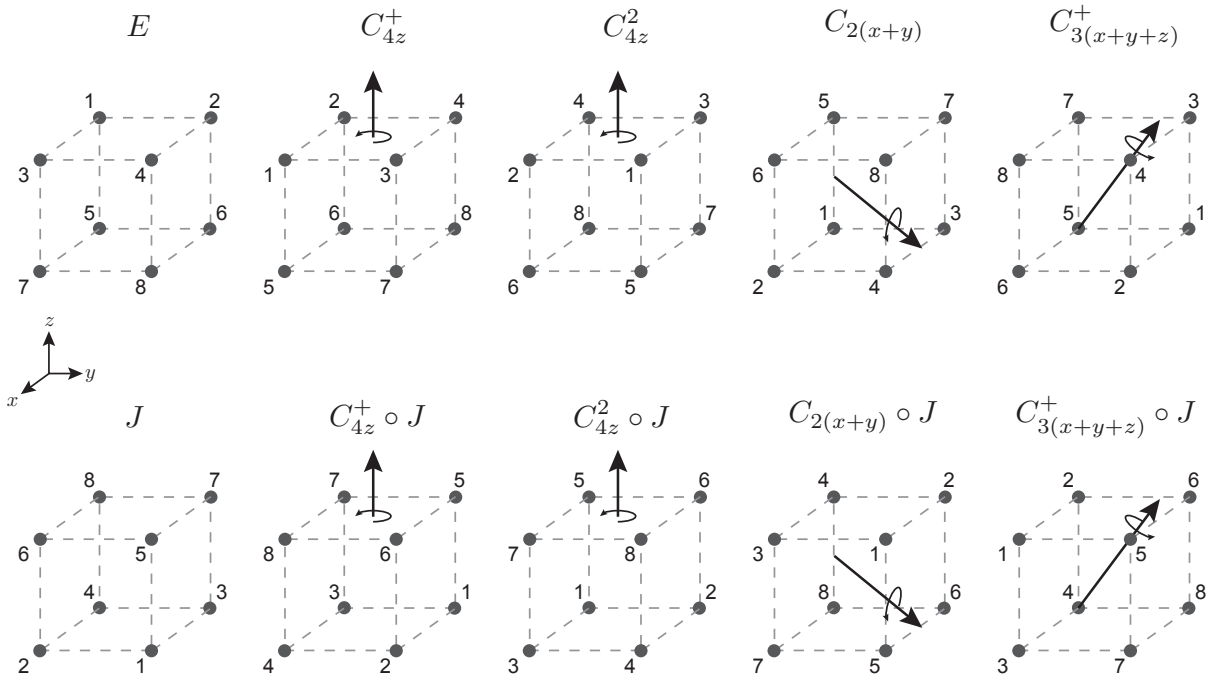

Figure F.2: 10 of the 48 group operations in the O_h group, each from a different conjugacy class. E is the identity; C_{4z}^{+} is a 90 degree rotation about the z axis; C_{4z}^{2} is a 180 degree rotation about z; $C_{2(x+y)}$ is a 180 degree rotation about $\hat{x} + \hat{y}$; $C_{3(x+y+x)}^{+}$ is a 120 degree rotation about $\hat{x} + \hat{y} + \hat{z}$; J is an inversion about the centre of the cube; the remaining operations are rotations on the previously inverted cube.

F.3 Conjugacy classes

Suppose we pick a group element R and look at the product $P^{-1} \circ R \circ P$, where P is any other element in the group. What we find is something interesting. If we let P run through all the group elements the product gives only a select few outcomes. These outcomes, together with R, form a *conjugacy class*. Each element in a conjugacy class uses a similar symmetry, so that we can often just look at one element in a class to gain intuition on the system. There are some important results from representation theory involving conjugacy classes that we will use shortly.

Let's work out an example with the square. Take $R = C_{4z}^{+}$. Then for any P in the group we find $P \circ C_{4z}^{+} \circ P$ to be equal to either C_{z4}^{+} or C_{4z}^{-}. So the group elements C_{4z}^{+} and C_{4z}^{-} form a conjugacy class. There are 5 conjugacy classes in total for the square group,

$$E = \{E\} \tag{F.1}$$
$$C_{4z} = \{C_{z4}^{+}, C_{4z}^{-}\} \tag{F.2}$$
$$C_{2z} = \{C_{2z}\} \tag{F.3}$$
$$\sigma = \{\sigma_x, \sigma_y\} \tag{F.4}$$
$$\sigma' = \{\sigma_1, \sigma_2\} \tag{F.5}$$

The breakdown of the group elements into classes matches with some of our intuition. The rotations and reflections are separated into different classes as could be expected by the group multiplication table. That the 180 degree and 90 degree rotations fall into separate classes might be surprising, but they are fundamentally different in that the C_{2z} commutes with every element in the group, while $C_{4z}^{\pm}$ do not.

There are a few important factors to make note of here. The number of conjugacy classes in a group is meaningful. Also the *order* of a class, which is the number of group elements within it. Commonly, when seeing a list of all the classes in a group, the order is often written in front of the name. For example, the list of conjugacy classes for the square is $\{E, 2C_{4z}, C_{2z}, 2\sigma, 2\sigma'\}$.

The conjugacy classes for the O_h group, the symmetry group of the diamond lattice, are

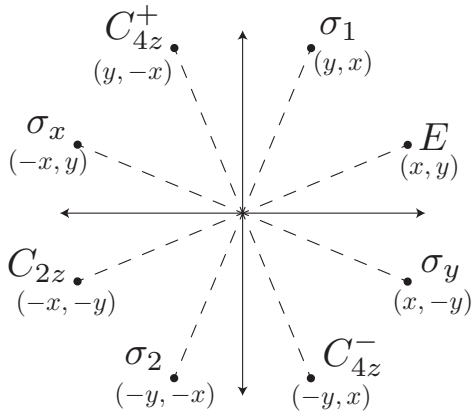

Figure F.3: Operations from the symmetry group of the square acting on a two-dimensional vector

$\{E, 6C_4, 3C_4^2, 6C_2, 8C_3, J, 6C_4 \circ J, \}$, where an example operation from each class is shown in Fig. F.2.

F.4 Representations of a group

So far, we have kept the discussion strictly pictorial. While we know how some group elements might transform a square or a cube, we cannot yet write down an expression for them. The same is true for the group operation, $\circ$. We might know what $C_{4z}^{+} \circ \sigma_x$ does to the square, but beyond that the group operation seems confusing. Giving the group a context to work in, or a *representation*, is our next topic of discussion. Representations of groups can vary from being a scalar quantity to a three-dimensional (or higher) system. The commonality between representations is that they are all invariant in the same manner. There are infinitely many representations of a group. It is the subject of representation theory to find an expression for any them as a linear combination of some base set called the *irreducible representations*. By decomposing the symmetries of a physical system into its irreducible representations we can learn which processes can occur, like the normal modes of vibration in molecules and crystals, and even selection rules for them.

We are usually interested in representing group elements by matrices, with the group operation then being matrix multiplication. Let's work out a two-dimensional representation for the square. Consider a vector (x, y). Each of the group operations on (x, y) can be found in a straightforward way, see Fig. F.3,

$$\begin{aligned} E &= \begin{pmatrix} 1 & 0 \\ 0 & 1 \end{pmatrix}, \quad C_{4z}^{+} = \begin{pmatrix} 0 & 1 \\ -1 & 0 \end{pmatrix}, \quad C_{4z}^{-} = \begin{pmatrix} 0 & -1 \\ 1 & 0 \end{pmatrix}, \quad C_{2z} = \begin{pmatrix} -1 & 0 \\ 0 & -1 \end{pmatrix}, \\ \sigma_x &= \begin{pmatrix} -1 & 0 \\ 0 & 1 \end{pmatrix}, \quad \sigma_y = \begin{pmatrix} 1 & 0 \\ 0 & -1 \end{pmatrix}, \quad \sigma_1 = \begin{pmatrix} 0 & -1 \\ 1 & 0 \end{pmatrix}, \sigma_2 = \begin{pmatrix} 1 & 0 \\ 0 & 1 \end{pmatrix}. \end{aligned} \tag{F.6}$$

It is straightforward to verify that these matrices produce the same multiplication table as shown in Table F.1. Something we can make note of here is that matrices within the same conjugacy class have the same trace, which we call its *character*. Following the notation of Ref. [125], we label the character of a conjugacy class p by $\chi_p^{(i)}$, where i labels which representation we used. For the two-dimensional matrices above we have the characters

$$\chi_E^{\text{2-dim}} = 2, \quad \chi_{C_{4z}}^{\text{2-dim}} = 0, \quad \chi_{C_{2z}}^{\text{2-dim}} = -2, \quad \chi_{\sigma}^{\text{2-dim}} = 0, \quad \chi_{\sigma'}^{\text{2-dim}} = 0 \tag{F.7}$$

The character of a class is very much dependent on the representation being used. If fact, the character of the conjugacy classes will play a vital role in finding the irreducible representations of a group. There are some important results from representation theory that we will state here, but not prove. (For a non-intimidating explanation see Ref. [125]).

1. The number of conjugacy classes = the number of irreducible representations.

2. The dimensions of the irreducible representations can be found using the formula $\sum_k l_k^2 = N$, where N is the total number of elements in the group and l_k is the dimension of the k^{th} representation. The dimension of a representation implies we are expressing the elements as matrices.

3. Irreducible representations follow an orthogonality relation $\sum_{p=1}^{r} h_p (\chi_p^{(i)})^* \chi_p^{(j)} = \delta_{ij} N$. Here the sum is over the conjugacy classes p, of which there are r, and lastly h_p is the order of the class.

	E	C_{4z}	C_{2z}	σ	σ'
$\chi^{(1)}$	1	1	1	1	1
$\chi^{(2)}$	1	1	1	-1	-1
$\chi^{(3)}$	1	-1	1	1	-1
$\chi^{(4)}$	1	-1	1	-1	1
$\chi^{(5)}$	2	0	-2	0	0

Table F.2: Character table for the square

F.4.1 Character table for the square

For the square we know there are 8 group elements and 5 conjugacy classes. This means there are 5 irreducible representations and using item 2 in the list above we find their dimensions

$$l_1^2 + l_2^2 + l_3^2 + l_4^2 + l_5^2 = 8 \tag{F.8}$$

From this we see that 4 of the irreducible representations are one-dimensional, and 1 will be two-dimensional. One-dimensional representations of group elements are just equal to their characters, the trace of a 1×1 matrix. Using the orthogonality condition, we can construct a table to find what the characters of each class in each irreducible representation will be. For the square this is shown in Table F.2.

Notice that the first representation $\chi^{(1)}$ has characters of 1 in every class. As it turns out, every group will have this irreducible representation. Also notice that in every representation the character of the identity operation E is simply the dimension of the representation. As we might have anticipated, the identity operation in any matrix representation is the identity matrix, $\mathbb{1}$. Lastly, notice that the two-dimensional irreducible representation, $\chi^{(5)}$, is the same as our two-dimensional matrix representation from above.

A simple example of a reducible representation is the *regular* representation. To express a group element in the regular representation we take the Table F.1 and set every entry equal to zero, except the element we are representing which we set to 1. For example, the

C_{4z}^{+} element is

$$C_{4z}^{+} = \begin{pmatrix} 0 & 1 & 0 & 0 & 0 & 0 & 0 & 0 \\ 0 & 0 & 0 & 1 & 0 & 0 & 0 & 0 \\ 1 & 0 & 0 & 0 & 0 & 0 & 0 & 0 \\ 0 & 0 & 1 & 0 & 0 & 0 & 1 & 0 \\ 0 & 0 & 0 & 0 & 0 & 0 & 0 & 1 \\ 0 & 0 & 0 & 0 & 0 & 1 & 0 & 0 \\ 0 & 0 & 0 & 0 & 1 & 0 & 0 & 0 \end{pmatrix}. \tag{F.9}$$

By looking at the multiplication table we can imagine the other elements and see that they will all have a trace of zero, except the identity which gives a trace of 8. In this representation χ^{reg} the classes have the following characters,

	E	C_{4z}	C_{2z}	σ	σ'
χ^{reg}	8	0	0	0	0

By staring at the character table (Table F.2) we can find that $\chi^{\text{reg}} = \chi^{(1)} + \chi^{(2)} + \chi^{(3)} + \chi^{(4)} + 2\chi^{(5)}$. This can be confirmed by adding up the characters of each class.

F.4.2 Character table for the diamond, O_h group

In the case of the O_h group we have 10 irreducible representations (4 one-dimensional, 2 two-dimensional, 3 three-dimensional), found using the relation stated in the second list item above. Table F.3 shows the characters of the conjugacy classes in each irreducible representation.

F.4.3 Basis functions

We have seen both pictorial and matrix representations for groups. Next we will discuss representing group symmetries with functions. Knowing how a function correspond to the irreducible representations of a group is extremely useful, as it gives us a tool to understand

	E	$6C_4$	$3C_4^2$	$6C_2$	$8C_3$	J	$6C_4 \circ J$	$3C_4^2 \circ J$	$6C_2 \circ J$	$8C_3 \circ J$
$\chi^{(1)}$	1	1	1	1	1	1	1	1	1	1
$\chi^{(2)}$	1	-1	1	-1	1	1	-1	1	-1	1
$\chi^{(3)}$	2	0	2	0	-1	2	0	2	0	-1
$\chi^{(4)}$	3	1	-1	-1	0	3	1	-1	-1	0
$\chi^{(5)}$	3	-1	-1	1	0	3	-1	-1	1	0
$\chi^{(6)}$	1	1	1	1	1	-1	-1	-1	-1	-1
$\chi^{(7)}$	1	-1	1	-1	1	-1	1	-1	1	-1
$\chi^{(8)}$	2	0	2	0	-1	-2	0	-2	0	1
$\chi^{(9)}$	3	1	-1	-1	0	-3	-1	1	1	0
$\chi^{(10)}$	3	-1	-1	1	0	-3	1	1	-1	0

Table F.3: Character table for the O_h group.

the physical processes that can occur in the system. What does it mean for a function to possess symmetries? A simple example are even and odd functions, which when inverted about the origin are either invariant or have a sign change.

Examples basis functions in the square symmetry

Consider the function $x^2 + y^2$, which describes a circle, and is an even function. Since all the symmetry operations of the square leave this function invariant, they all act as the identity. This means the $x^2 + y^2$ is associated with the first representation $\chi^{(1)}$.

Next consider the vector (x, y). We already know that the operations $(x, y) \to (x', y')$ are described by the two-dimensional matrix representation $\chi^{(5)}$. If we take a function $f(x, y)$, we can look at $f(x', y')$ for each group operation, and determine the character of each operation. Knowing the characters we can find a linear combination of irreducible representations which describe the function. As an example, let's consider the function $f(x, y) = xy$. Recall from the two-dimensional matrix representation, Eq. F.6, that $C_{4z}^+(x, y) = (y, -x)$. We then have that $f(x', y') = f(y, -x) = -xy$, and so $C_{4z}^+ f(x, y) = -f(x, y)$. By doing the same using a group operation from each of the conjugacy classes

we find the characters of the representation for $f(x, y) = xy$, denoted χ^{xy},

	E	C_{4z}	C_{2z}	σ	σ'
χ^{xy}	1	-1	1	-1	1

These are the same characters as the $\chi^{(4)}$ representation. This means that the function $f(x, y) = xy$ transforms in the same way as the represention $\chi^{(4)}$ under the group operations. Next let's find some basis functions for the diamond symmetry group, O_h, using the same logic outlined here.

Basis functions for O_h

Just as the circle function, $x^2 + y^2$, remained invariant under the symmetries of the square, the spherical function $x^2 + y^2 + z^2$ will remain invariant for the cube symmetries. We can see this by the fact that the O_h operations map between corners of the cube, all of which have the same distance from the origin, $x^2 + y^2 + z^2$. The spherical function transforms according to the $\chi^{(1)}$ irreducible representation from Table F.3.

To find the representation of a general function $f(x, y, z)$, or a vector of functions $(f(x, y, z), g(x, y, z), h(x, y, z))$, we follow the same logic as for the square. First, we want to find how a three-dimensional vector (x, y, z) transforms in the O_h group. Below we write out the 3×3 matrix representations for one group operation from each conjugacy class (we

will only need to look at 1 per class to determine the character),

$$E = \begin{pmatrix} 1 & 0 & 0 \\ 0 & 1 & 0 \\ 0 & 0 & 1 \end{pmatrix}, \quad C_{4z}^{+} = \begin{pmatrix} 0 & -1 & 0 \\ 1 & 0 & 0 \\ 0 & 0 & 1 \end{pmatrix}, \quad C_{4z}^{2} = \begin{pmatrix} -1 & 0 & 0 \\ 0 & -1 & 0 \\ 0 & 0 & 1 \end{pmatrix},$$

$$C_2 = \begin{pmatrix} -1 & 0 & 0 \\ 0 & 0 & -1 \\ 0 & -1 & 0 \end{pmatrix}, \quad C_3 = \begin{pmatrix} 0 & 0 & -1 \\ 1 & 0 & 0 \\ 0 & -1 & 0 \end{pmatrix}, \quad J = \begin{pmatrix} -1 & 0 & 0 \\ 0 & -1 & 0 \\ 0 & 0 & -1 \end{pmatrix},$$

$$C_{4z}^{+} \circ J = \begin{pmatrix} 0 & 1 & 0 \\ -1 & 0 & 0 \\ 0 & 0 & -1 \end{pmatrix}, \quad C_{4z}^{2} \circ J = \begin{pmatrix} 1 & 0 & 0 \\ 0 & 1 & 0 \\ 0 & 0 & -1 \end{pmatrix}, C_2 \circ J = \begin{pmatrix} 1 & 0 & 0 \\ 0 & 0 & 1 \\ 0 & 1 & 0 \end{pmatrix},$$

$$C_3 \circ J = \begin{pmatrix} 0 & 0 & 1 \\ -1 & 0 & 0 \\ 0 & 1 & 0 \end{pmatrix}. \tag{F.10}$$

This produces the character table

	E	$6C_4$	$3C_4^2$	$6C_2$	$8C_3$	J	$6C_4 \circ J$	$3C_4^2 \circ J$	$6C_2 \circ J$	$8C_3 \circ J$
$\chi^{\text{3-dim}}$	3	1	-1	-1	0	-3	-1	1	1	0

which is equal to the $\chi^{(9)}$ irreducible representation. Let's work out one more example, which will be important for us. Consider the vector of functions $\vec{f} = (yz, xz, xy)$. The operation C_{4z}^{+} maps $x \to y$, $y \to -x$ and $z \to z$, so our functions become

$$\vec{f'} = \begin{pmatrix} xz \\ -yz \\ -xy \end{pmatrix} = \begin{pmatrix} 0 & 1 & 0 \\ -1 & 0 & 0 \\ 0 & 0 & -1 \end{pmatrix} \begin{pmatrix} yz \\ xz \\ xy \end{pmatrix}. \tag{F.11}$$

The 3×3 matrix written is the expression for the C_{4z}^{+} element in this representation. Below we have worked out the 3×3 matrix representations, for one group element from each class,

for how our vector $\vec{f} = (yz, xz, xy)$ transforms.

$$
\begin{aligned}
E &= \begin{pmatrix} 1 & 0 & 0 \\ 0 & 1 & 0 \\ 0 & 0 & 1 \end{pmatrix}, \quad C_{4z}^{+} = \begin{pmatrix} 0 & 1 & 0 \\ -1 & 0 & 0 \\ 0 & 0 & -1 \end{pmatrix}, \quad C_{4z}^{2} = \begin{pmatrix} -1 & 0 & 0 \\ 0 & -1 & 0 \\ 0 & 0 & 1 \end{pmatrix}, \\
C_2 &= \begin{pmatrix} 1 & 0 & 0 \\ 0 & 0 & 1 \\ 0 & 1 & 0 \end{pmatrix}, \quad C_3 = \begin{pmatrix} 0 & 0 & -1 \\ 1 & 0 & 0 \\ 0 & 1 & 0 \end{pmatrix}, \\
J &= E, \quad C_{4z}^{+} \circ J = C_{4z}^{+}, \quad C_{4z}^{2} \circ J = C_{4z}^{2}, \quad C_2 \circ J = C_2, \quad C_3 \circ J = C_3. \quad \text{(F.12)}
\end{aligned}
$$

We construct the character table for this representation as follows,

	E	$6C_4$	$3C_4^2$	$6C_2$	$8C_3$	J	$6C_4 \circ J$	$3C_4^2 \circ J$	$6C_2 \circ J$	$8C_3 \circ J$
$\chi^{(yz,xz,xy)}$	3	-1	-1	1	0	3	-1	-1	1	0

which is equal to the irreducible representation $\chi^{(5)}$. We have covered what will be useful for our discussion on the vibration in diamond, so let's get to it.

F.5 Application to diamond lattice

Fig. F.4 shows the diamond crystal lattice. As stated previously, it is an FCC lattice with a two-atom basis. We would like to consider the normal modes of vibration for the atoms in the lattice. By considering mappings between the atom sites along with displacements of each atom we can find which irreducible representations form the normal modes of vibration. Before we combine them we need a representation for the atom sites, denoted $\chi^{\text{atom sites}}$, and a representation for displacement $\chi^{\text{3-dim}}$. A good resource for this discussion is Ref. [172].

F.5.1 Representation for mapping between atom sites, $\chi^{\text{atom sites}}$

We have a few things to consider when searching for the irreducible representations that map between atom sites. The first is the periodicity of the crystal lattice. While we are

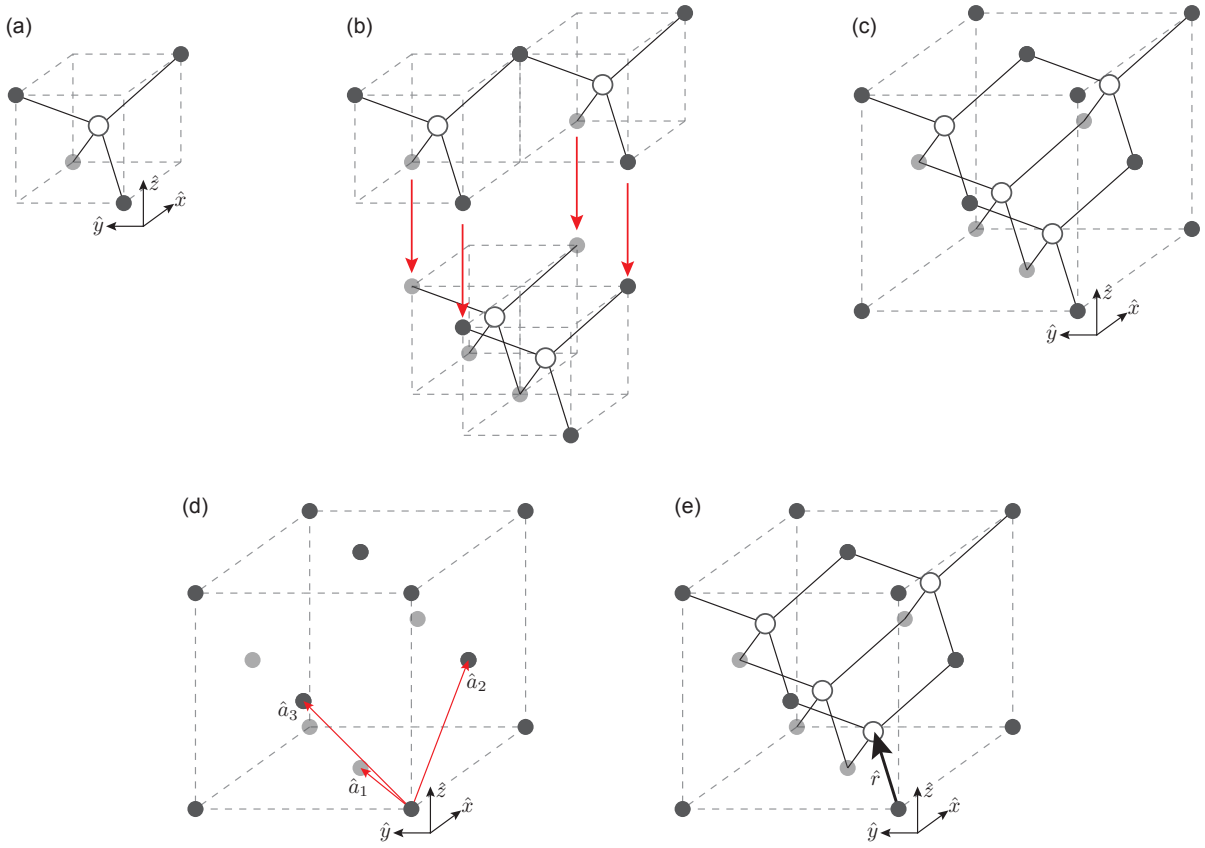

Figure F.4: (a) A tetrahedral arrangement of Carbon atoms (half transparent black dots imply depth). (b) Stacking four of the tetrahedral blocks form the diamond lattice, (c). The diamond is two inter-lacing face-centred cubic lattices, one marked with black dots, the other with white dots. (d) The primitive lattice vectors, $\hat{a}_1, \hat{a}_2, \hat{a}_3$ for a face-centred cubic lattice. Translation by a vector $\vec{R}_n = n_1\hat{a}_1 + n_2\hat{a}_2 + n_3\hat{a}_3$ will land on another atom for any integers $n_{1,2,3}$. (e) The two face-centred cubic sub-lattices in diamond are separated by a basis vector $\vec{r} = a/4(\hat{x} + \hat{y} + \hat{z})$.

considering the unit cell of an FCC lattice, we should remember that the bulk crystal is comprised of a vast amount of these cells. We consider atom sites equivalent if we translate by a lattice vector $\vec{R}_n = n_1\hat{a}_1 + n_2\hat{a}_2 + n_3\hat{a}_3$ to get back to the original site, where the primary lattice vectors $\hat{a}_1$, $\hat{a}_2$, $\hat{a}_3$ define the FCC lattice (shown in Fig. F.4(d)).

Second, each point on the FCC lattice is two atoms, joined by the basis vector $\vec{r} = a/4(\hat{x} + \hat{y} + \hat{z})$. As can be seen in Fig. F.4(e), each Carbon atom in sub-lattice 1, marked by the black dots, has 4 bonds to neighbouring Carbon atoms in sub-lattice 2, marked by white dots. As we can see in Fig. F.5 each group operation will then either preserve the lattice orientation (i.e., the identity), up to translation by $\vec{R}_n$, or invert the orientation. The inversion is equivalent to a switch of the sub-lattices, i.e., mapping from sub-lattice $1 \to 2$, or vice versa. This makes our representation $\chi^{\text{atom sites}}$ two-dimensional, with the group operations acting on a vector representing the order of the sub-lattices $(1, 2)$. The group operations are either the identity, or have 0 on the diagonal and 1 on the anti-diagonal. The character table for the representation is

	E	$6C_4$	$3C_4^2$	$6C_2$	$8C_3$	J	$6C_4 \circ J$	$3C_4^2 \circ J$	$6C_2 \circ J$	$8C_3 \circ J$
$\chi^{\text{atom sites}}$	2	0	2	0	2	0	2	0	2	0

We have that $\chi^{\text{atom sites}} = \chi^{(1)} + \chi^{(7)}$. Let's think about these two irreducible representations. The first, $\chi^{(1)}$, we expect from an FCC lattice with a single atom at each point. This is the representation for mapping between atoms on the same sub-lattice. The second irreducible representation, $\chi^{(7)}$, can be thought of as which way the basis vector $\vec{r}$ is pointing, i.e., from sub-lattice $1 \to 2$ or $2 \to 1$. We can see this from the group operations in Fig. F.5. Operations which invert the whole unit cell are equivalent to ones that change the direction of $\vec{r}$, and will be equal to -1 in the representation $\chi^{(7)}$.

F.5.2 Displacement

We have already solved this. In our basis function section we asked how a displacement vector $\vec{d} = x\hat{x} + y\hat{y} + z\hat{z}$ would transform in the symmetry group. We found that it is associated with the $\chi^{(9)}$ irreducible representation which is odd under inversion about the origin.

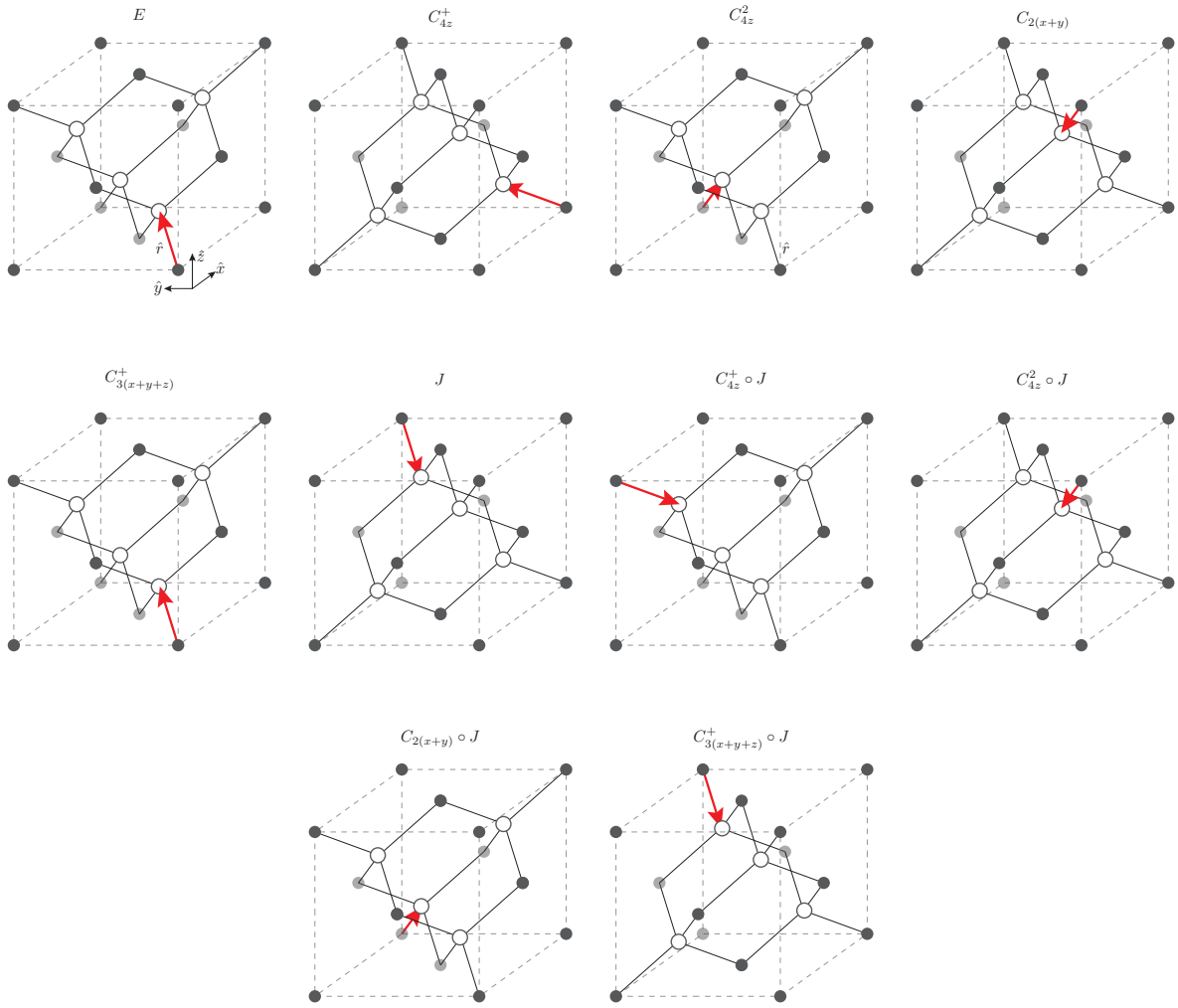

Figure F.5: One group operation from each conjugacy class acting on the diamond lattice. Half of the operations change the orientation of the lattice which can be thought of as an inversion, or more simply a switch from one sub-lattice to another (swap of black and white dots, plus translation).

F.5.3 Lattice vibrations and selection rules

Our goal is to find the irreducible representations that describe vibrations between the atom sites on the lattice. We find these by building a representation, χ^{vibe} that combines the mapping between atom sites, $\chi^{\text{atom sites}}$, and that which describes a displacement vector, $\chi^{(9)}$.

We build the new representation by taking the tensor product of each group operation in $\chi^{\text{atom sites}}$ with the corresponding group operation in $\chi^{(9)}$. Thankfully we don't need to crunch all that math out. Since all we really care for is the character, i.e., the trace of each group operation, we can use the property of the trace that $\text{Tr}(P \otimes Q) = \text{Tr}P \times \text{Tr}Q$. We can then simply multiply the characters of corresonding conjugacy classes together from each representation to find the new one. We have the following relation for the character of the i^{th} conjugacy class,

$$\chi_i^{\text{vibe}} = \chi_i^{\text{atom sites}} \times \chi_i^{(9)} \tag{F.13}$$

$$= (\chi_i^{(1)} + \chi_i^{(7)}) \times \chi_i^{(9)} \tag{F.14}$$

$$= \chi_i^{(1)} \times \chi_i^{(9)} + \chi^{(7)} \times \chi_i^{(9)} \tag{F.15}$$

Using the character table of the O_h group (Table F.3), we can see that the first term results again in the $\chi^{(9)}$ irreducible representation, and the second term has the character table

	E	$6C_4$	$3C_4^2$	$6C_2$	$8C_3$	J	$6C_4 \circ J$	$3C_4^2 \circ J$	$6C_2 \circ J$	$8C_3 \circ J$
$\chi^{(7)}$	1	-1	1	-1	1	-1	1	-1	1	-1
$\chi^{(9)}$	3	1	-1	-1	0	-3	-1	1	1	0
$\chi^{(7)} \otimes \chi^{(9)}$	3	-1	-1	1	0	3	-1	-1	1	0

This equals the $\chi^{(5)}$ representation, and so we have our answer $\chi^{\text{vibe}} = \chi^{(9)} + \chi^{(5)}$. We know that the $\chi^{(9)}$ representation describes displacements of the atoms within the same sub-lattice. This corresponds to the acoustic phonon branch which take the form of travelling vibrational waves through the lattice.

We know that the second term $\chi^{(5)}$ describes displacements between the two sub-lattices. This representation describes the optical phonon branch, the two sub-lattices

beating against each other out of phase. Strictly speaking there are three normal modes describing the optical phonon branch, one for a vibration in each direction. Because the $\chi^{(5)}$ representation is invariant under inversion about the origin, a property it shares with the crystal ground state (all atoms stationary) it is "Raman-active". A Raman involves two electric dipole terms, each of which changes sign under inversion, and so is invariant under inversion. In general, Raman processes can map between states that have the same parity. (Levels with opposite parities can be addressed with a single electric dipole transition.) The Raman process requires two electric dipole terms.

F.5.4 Polarization selection rules

Lastly, we return to our brief discussion on basis functions. We have found that the $\chi^{(5)}$ irreducible representation describes the Raman process we wish to use in diamond. We found above that the vector $\vec{f} = yz\hat{x} + xz\hat{y} + xy\hat{z}$ is associated with the $\chi^{(5)}$ representation. Each component of the vector is then associated with the optical phonon vibration in that direction. This tells us that the two electric dipole moments which excite the optical phonon mode in the z-direction must be polarized along the x- and y-directions. This gives the polarization selection rule for our quantum memory.